TECHNICAL UNIVERSITY OF MUNICH

TUM School of Engineering and Design

Method Development for the Numerical Wind Tunnel in Applied Structural Engineering

Máté-Tamás Péntek

Complete reprint of the dissertation approved by the TUM School of Engineering and Design of the Technical University of Munich for the award of the

Doktor der Ingenieurwissenschaften (Dr.-Ing.).

Chair:

Priv.-Doz. Dr.-Ing. habil. Stefan Kollmannsberger

Examiners:

1. Prof. Dr.-Ing. Kai-Uwe Bletzinger
2. Prof. Girma Bitsuamlak, Ph.D.
3. Prof. Félix Nieto Mouronte, Ph.D.

The dissertation was submitted to the Technical University of Munich on 28 September 2023 and accepted by the TUM School of Engineering and Design on 30 November 2023.

Schriftenreihe des Lehrstuhls für Statik
TU München

Band 61

Máté-Tamás Péntek

METHOD DEVELOPMENT FOR THE NUMERICAL WIND TUNNEL IN APPLIED STRUCTURAL ENGINEERING

München 2023

Veröffentlicht durch

Kai-Uwe Bletzinger
Lehrstuhl für Statik
Technische Universität München
Arcisstr. 21
80333 München

Telefon: +49(0)89 289 22422
Telefax: +49(0)89 289 22421
E-Mail: kub@tum.de
Internet: www.cee.ed.tum.de/st

ISBN: 978-3-943683-74-5

Kurzfassung

Diese Arbeit konzentriert sich auf zahlreiche computerbasierte Entwicklungen von Methoden für fortgeschrittene Analysen im numerischen Windkanal. Sie geht zunächst auf spezifische Definitionen ein und gibt einen Überblick, um die allgemeinen theoretischen Grundlagen zu schaffen. Im rechnergestützten Windingenieurwesen werden die Verbesserungen sowohl durch Fortschritte in der Software als auch in der Hardware vorangetrieben, hier mit Schwerpunkt auf strukturbezogene Effekte, die spezifisch für das Bauwesen sind. Zu den entsprechenden Inhalten gehören die Besonderheiten der Open-Source-Programmierung für Hochleistungsrechner. Moderne numerische Ansätze bieten somit eine brauchbare Alternative für die Beurteilung komplexer Phänomene.

Im Weiteren wird ein Rahmenwerk vorgestellt, um windinduzierte Schwingungen mithilfe zusätzlicher Dämpfungseinrichtungen am Beispiel eines Hochhauses zu behandeln. Bei einer schmalbandigen Anregung, wie zum Beispiel Wirbelablösungen, ist dies ein gängiger Ansatz zur Begrenzung der Strukturbewegungen auf ein sicheres Maß. Rechenmodelle und -methoden erlauben eine flexible Erweiterung der Simulation von Windströmung und Strukturantwort, sodass weitere Module, die Dämpfersysteme darstellen, einbezogen werden können. Von besonderem Vorteil ist dabei, dass diese Komponenten nach einer partitionierten Strategie zusammenwirken. Die untersuchten Szenarien zeigen, dass die gekoppelte Physik richtig erfasst wird, während das Schema robust und skalierbar bleibt.

Darüber hinaus konzentriert sich die Dissertation auf Verbesserungen im Zusammenhang mit der Identifizierung des Antritts von Flattern bei Brückenüberbauten. Zunächst werden verschiedene Aspekte zur Validierung des Arbeitsablaufs behandelt. Danach richtet sich der Fokus auf eine innovative Verbesserungsmöglichkeit der indirekten Flattererkennung mittels erzwungener Bewegung. Dies wird durch Kombinationen von mehreren Anregungsfrequenzen und -richtungen erreicht, um die Rechenkosten zu senken. Die Ergebnisse zeigen, dass durch solche Handlungen Flatterbeiwerte ermittelt werden können, indem die erforderlichen Ressourcen erheblich reduziert werden. Es werden mehrere theoretische und praktische Überlegungen skizziert, die den Einsatz dieser Fortschritte in numerischen Arbeitsabläufen kommentieren.

Die Verwendung des numerischen Windkanals zur Bewertung der Auswirkungen auf Leichtbaustrukturen wird dargestellt. Das mechanische Verhalten solcher Konstruktionen definiert Betrachtungen und Werkzeuge, die für die Untersuchung notwendig sind. Die Form verknüpft die Struktureigenschaften mit den aus dem Wind resultierenden Kräften. Repräsentative Bauwerke sind oft Unikate, für die nur selten Referenzdaten verfügbar sind. Bei der Analyse einer beispielhaften Dachkonstruktion für ein Stadion werden rechnerische Ansätze bis an ihre Grenzen getrieben. Mit solchen Werkzeugen lassen sich die Last- und Verformungszustände angemessen bewerten. Entsprechende Simulationen verdeutlichen verschiedene Methodenentwicklungen, die auch Aspekte der realitätsnahen Modellierung sowie die Möglichkeiten des Hochleistungsrechnens berücksichtigen.

Abstract

This work focuses on numerous computational method developments for advanced analyses using the numerical wind tunnel. It first addresses specific definitions and includes an overview to set the general theoretical basis. In computational wind engineering, enhancements are driven by advances in software and hardware alike, here focusing on effects that are specific to civil engineering structures. The corresponding content includes particularities of open-source programming for high-performance computing environments. Modern numerical approaches propose themselves as a viable alternative for assessing complex phenomena.

In continuation, a framework is presented that aims to deal with wind-induced vibrations using devices for added damping, with the example of a highrise building. For a narrowband excitation such as vortex shedding, this is a common approach to limit structural motions to safe levels. Computational models and methods permit a flexible way to extend the simulation of wind flow and structural response, such that it includes further modules representing damper systems. It is a particular advantage that these components interact by following a partitioned strategy. The investigated scenarios show that the coupled physics is captured properly, while the scheme remains robust and scalable.

Additionally, the dissertation focuses on improvements related to identifying flutter onset for bridge decks. Various aspects dedicated to validating the workflow are addressed first. Thereafter, the novelty lies in enhancements to indirect flutter detection by means of forced motion. This is achieved using combinations of multiple excitation frequencies and directions in an attempt to reduce computational cost. The results indicate that such measures lead to obtaining flutter derivatives while significantly lowering the necessary resources. Multiple theoretical and practical considerations are outlined, commenting on the applicability of these advances in numerical workflows.

Using the numerical wind tunnel for assessing effects on lightweight structures is also highlighted. The mechanical behavior of such constructions defines deliberations and tools necessary for investigation. Shape interlinks structural properties with the forces arising from wind. Representative constructions are often unique, for which reference data is seldom available. Computational approaches are driven to their limit during the analysis of an exemplary stadium structure. With such tools, the load and deformation states can be adequately assessed. Corresponding simulations highlight various developments in methods, including considering aspects for realistic modeling as well as leveraging the possibilities offered by high-performance computing.

Acknowledgements

I handed in my Bachelor's thesis on bridge engineering in the summer of 2012, which already focused on aspects related to wind effects. Since then, I have spent more than a decade working on various topics, the majority being related to computational wind engineering. This timeframe also marks my presence in Munich, during which many of my activities have been linked to the Technical University. I was fortunate enough to embark on a very fruitful journey and meet incredible people.

First and foremost, I would like to express my gratitude to Kai-Uwe Bletzinger. In his role as a host, head of institute, advisor and mentor, he has critically helped my path and supported my progress. He entrusted me with multiple roles and provided me with necessary freedom in my actions. I thank Roland Wüchner for mentoring me on a variety of topics. I would especially like to highlight our collaboration on building up the Structural Wind Engineering course, which rewarded me greatly in many ways. The Chair of Structural Analysis – aka Statik – provided an environment in which I enjoyed spending time. My colleagues critically contributed to this with a pleasant yet intellectually challenging atmosphere, ranging from eureka moments to silly laughs. I value the collegiality with Veronika Singer, Bianca Einfalt and Johann Rippel during all of the administrative tasks we worked on.

This dissertation is a recollection of my most representative activities. I was fortunate enough to contribute to multiple topics, work on many challenges, and be part of several projects. All of these fall into the broader topic of computational wind engineering, a selection of which I label as advances to the numerical wind tunnel. I spent considerable time on analyzing structures vibrating in wind, including the possibilities of modeling various added devices to mitigate their motion. The collaboration on this topic with Andreas Winterstein, Michael Vogl, Péter Kupás, Andreas Riedl and Felix Weber, who is affiliated with Maurer SE, is greatly appreciated. For various related investigations, I additionally thank Giovanni Frison, Thomas Boekels and Anoop Kodakkal. Bridge aeroelasticity was one of the subjects that lured me into research. As a group, we improved many aspects of numerical investigations and came up with practical and pragmatic solutions, which I value. This would not have been possible without Guillermo Martínez-López, Michael Andre, Iñigo López and Norbert Sárközi. A specific project involved collaboration between our research institute and two companies. Here, I would like to remark on the presence of Christian Seiler and Andreas Neureuther from Grassl GmbH, as well as Alexander Michalski and Sami Bidier from str.ucture GmbH. Munich celebrated the 50th anniversary of the 1972 Summer Olympics in 2022. While the city was preparing with festive events and organizing the 2022 European Championships, we were investigating the wind effects acting on the stadium. This was symbolic as the engineering community recalled all of the necessary advances to host the Olympic Games, as well as many topics in science that this landmark site still influences. Together with Philipp Bucher, we pushed our software and hardware to its limits. The fact that it works is a showcase of what numerics are capable of, despite giving the impression of being nothing short of a wonder. I thank him for the camaraderie between us in solving some of the most challenging simulation cases I have ever encountered. Klaus Sautter and Ann-Kathrin Goldbach kindly supported the discussion on lightweight structures. In a broader context, I had the great opportunity to work together with Suneth Warnakulasuriya, Carlos Lázaro and Jordi Cotela Dalmau, learning a lot from each of them. Daniel Hackett proved to be a valuable sparring partner on various topics, for which I thank him as well as his colleagues at RWDI Consulting Engineers and Scientists. They were open to discussions in supporting me as well as our group. My activities greatly benefitted from the collaboration with many researchers from the International Centre for Numerical Methods in Engineering (CIMNE) in Barcelona, which I duly note. I kindly recount various activities with members of the Department of Structural Mechanics, Faculty of Civil Engineering of the Technical University of Cluj-Napoca, and highlight the encounters with Zsongor Gobesz.

This research would not have been possible without the financial support of the German Academic Exchange Service (DAAD) and Collegium Talentum, which funded my activities during its early years. Their scholarships additionally provided a broad and valuable network for researchers, as well as numerous occasions to travel. Various developments were further funded by the Central Innovation Programme for SMEs on behalf of the Federal Ministry for Economic Affairs and Climate Action, as part of the collective research project AiF-ZIM ZF 4066103MC8. I gratefully acknowledge the Gauss Centre for Supercomputing e.V. (www.gauss-centre.eu) for funding this project by providing computing time on the GCS supercomputer SuperMUC-NG at the Leibniz Supercomputing Centre (www.lrz.de) in Garching near Munich. I would especially like to remark on the support of Wolfram Hesse in assisting our two dedicated projects on this facility.

I dearly thank my partner and family for their encouragement during all of these years. Their support was unconditional and remains highly appreciated. Every one of you contributed to making this dissertation happen by simply being there, part of everything else that happened. It surely has to do with the butterfly effect and how interconnected everything is, or something along those lines. I will invite your for a beer, repair your bicycle, file a complaint for you. Whatever makes you happy!

Máté Péntek
Technical University of Munich
September 2023

Contents

Abbreviations

ABL	Atmospheric Boundary Layer
ALE	Arbitrary Lagrangian-Eulerian
AMD	Added Mass Damper
AoA	Angle of Attack
BARC	Benchmark on the Aerodynamics of a Rectangular 5:1 Cylinder
BC	Boundary Condition
CAARC	Commonwealth Advisory Aeronautical Research Council
CAD	Computer-Aided Design
CAE	Computer-Aided Engineering
CFD	Computational Fluid Dynamics
CSD	Computational Structural Dynamics
CSM	Computational Structural Mechanics
CWE	Computational Wind Engineering
DoF	Degree of Freedom
EIE	Extraneously Induced Excitation
EoM	Equation of Motion
FE	Finite Element
FEM	Finite Element Method
FIV	Flow-Induced Vibration
FSI	Fluid-Structure Interaction
FVM	Finite Volume Method
HPC	High-Performance Computing
IBVP	Initial Boundary Value Problem
IC	Initial Condition

IIE	Instability-Induced Excitation
LES	Large Eddy Simulation
LEV	Leading-Edge Vortex
LHS	Left-Hand Side
MIE	Movement-Induced Excitation
MPI	Message-Passing Interface
NSEs	Navier-Stokes Equations
OMP	Open Multi-Processing
OWC	One-Way Coupling
PVW	Principle of Virtual Work
RHS	Right-Hand Side
RMS	Root Mean Square
SD	Standard Deviation
SDoF	Single-Degree of Freedom
TDoF	Two-Degree of Freedom
TEV	Trailing-Edge Vortex
TMD	Tuned Mass Damper
TSD	Tuned Sloshing Damper
TWC	Two-Way Coupling
URANS	Unsteady Reynolds-Averaged Navier-Stokes
VMS	Variational Multiscale
WIV	Wind-Induced Vibration
WT	Wind Tunnel

Chapter 1

Introduction

1.1 Motivation

Numerical approaches play an increasing role in every engineer's toolbox. Recent computationally-enabled developments critically contribute to expanding the usage of the so-called *numerical Wind Tunnel (WT)*. Such activities are supported and strongly influenced by concurrent advancements in software and hardware. Consequently, I share this dissertation under the motto:

> "First we shape our tools, thereafter our tools shape us."*

The work focuses on selected topics that are considered particularly relevant for structural engineers. In a more general sense, improvements will be highlighted and commented upon from the broader perspective of Computational Wind Engineering (CWE). These discussions will continuously relate this toolbox to what is more traditionally known as the *experimental WT*. I will include comparisons and various remarks on differences, as well as the complementary nature between this established device and its computer-oriented counterpart.

From my perspective, the broadly used nomenclature is somewhat flawed. In this work, I propose the labeling *analog* instead of experimental, and *digital* instead of numerical, at least as conceptual substitutes. The reason is twofold. First, both approaches are by definition experimental, with investigations based on assumptions and chosen models. As such, they represent a well-defined and limited excerpt of reality. This is a trivial aspect that we often overlook. Reality is to be understood as the phenomenon that we want to investigate, assess or plan for, at its own time and spatial scale, with all intricacies of its complex

---

* Quote attributed to Father John Culkin and Marshall McLuhan.

physics. Engineers can all but employ certain scenarios that are a reduced yet representative snapshot of this. Second, the device called WT holds historic relevance, with early attempts already being used for scientific purposes in the 18th and 19th centuries. They gained more recognition at the beginning of the 20th century, notably with versions being built by the Wrights brothers (using blowing and introducing a collector, in 1901), with later improved designs by Eiffel (using suction and introducing a diffuser, in 1909) and Prandtl (first closed-circuit, in 1909). Chanetz (2017) provides a review of the chronology, with Solari (2019, Ch. 7) placing developments in an enlarged compendium. These tunnel-like devices had air being moved through them by fans. The timeline corresponds to the period when the fluorescent lamp was invented and the principles of television were laid out at the beginning of the century (see Dummer, 1997, Ch. 2). Therefore, the term experimental was established in this historic context. Its usage comes somewhat naturally, as at that time the distinction between analog and digital was futile.

The collapse of the Tacoma Narrows Bridge in 1940 critically influenced how structural engineers had to approach investigating the effect of wind on constructions, as remarked by Olson et al. (2015) and Solari (2019, Ch. 9). Yet again, experimental WT testing continued to play a crucial role, including influencing the development of methods and tools. Therefore, the analog device is backed up by more than a century of usage, with its worthy part in assisting challenging investigations. Meanwhile, the theoretical foundations of the Finite Element Method (FEM) are linked to variational calculus and the Principle of Virtual Work (PVW) dating back to the 17th and 18th centuries. Nonetheless, more established developments occurred at the beginning of the 20th century, with usage for structural analysis gaining traction between the 1940s and 1960s. Historical overviews (Stein, 2014; Sabat and Kundu, 2021) remark on the works of Ritz, Galerkin, Courant, Turner, Argyris, Clough and Zienkiewicz[*] during those decades. Here, particular activities related to Finite Element Analysis (FEA) and Computational Structural Mechanics (CSM) should be considered. For Computational Fluid Dynamics (CFD), the first numerical weather prediction system is linked to Richardson at the beginning of the 20th century. In the modern sense, digital computation for flow problems appeared – similarly to those related to structures – by the 1960s, with first commercial codes being present in the 1980s. Historical reviews (Jameson, 2012; Bhattacharyya et al., 2021) also note a clear connection between this progress and the advances of adequate hardware. As most CFD simulation (to date) rely on the Finite Volume Method (FVM), developments are co-dependent. Practical widespread usage and maturation of Computer-Aided Engineering (CAE) (implying design as well) thus result in 50 years of experience. Gustafsson (2018, Ch. 5) describes this technical evolution in detail, calling it the “Establishment of Scientific Computing as a New Discipline”. Blocken (2014) provides an additional snapshot of the state of CWE, discussing competing and complementary aspects of available WT approaches.

---

[*] This list is non-exhaustive.

Current computational development of methods supporting various analyses are representative of the increased rate of digital workflows and respective environments. For this dissertation, I highlight the role of the *Kratos Multiphysics*[*] open-source research software. This toolbox enabled the simulation work presented, as well as hosting the majority of newly contributed advancements. Crucially, it is a community-driven project in a transparent manner with trackable changes and technologically-influenced updates. I believe this is a key difference compared to proprietary software, whether commercial or for research, which not only impacted my way of work but also establishes a good premise for the sustainable and modern growth of the project. Such developments need to be attuned to the hardware used. In particular, the presented simulations leveraged High-Performance Computing (HPC) infrastructures. SuperMUC-NG[†] was the host system for the bulk of the work. Technological advances for such environments have to comply with multiple prerequisites, linked to scalability and robustness, not only of input/output data handling but also the efficiency of the core part of the numerical simulations. Correspondingly, any new additions need to extend beyond the traditional premise of sound mathematical and algorithmic considerations. Additionally, typical programming aspects that are suitable for standard workstations will not suffice. Careful considerations are required, which concern the development of digital tools for parallel computing on distributed memory machines. Load balancing and job bundling (or farming) are further aspects determining the success and efficiency of complex simulations on such dedicated infrastructures. As on-demand cloud-based HPC becomes increasingly available, future usage and evolution should be expected to considerably increase.

This thesis represents my experience and contributions, the respective advancement of many processes and procedures from the perspective outlined in the previous paragraphs. Insights will be substantiated by selected topics with technical discussions in the upcoming chapters. I included the brief historical overview with the purpose of being able to comment on the context in which my work is placed. Advances have to be interpreted with this timeline in mind, with recent developments being jointly made possible by the state-of-the-art progress in software and hardware. The terms analog and digital WT make sense from this standpoint, including naturally leading to the notion of a hybrid version, which implies a strong complementary aspect in the era of modern tools.

1.2 Outline

Chapter 2 provides an *overview of the numerical WT* by synthesizing its components as part of recent developments. Here, I describe the building blocks, how these are connected and what current advances render it a modern tool. It represents the metamodel, as a collection of multiple aspects in CWE. All following

---

[*] Kratos Multiphysics (www.github.com/KratosMultiphysics/Kratos) is to be seen as an example project, with other alternatives available, such as: OpenFOAM (ESI OpenFOAM, www.openfoam.com, The OpenFOAM Foundation, www.openfoam.org), FEniCS (www.fenicsproject.org).

[†] Refers to the supercomputing facility SuperMUC-NG, at the Leibniz Supercomputing Centre www.lrz.de.

content relies on this part.

In Chapter 3, the work focuses on the *mitigation of wind-induced vibrations by added devices*. Loading from gusts or vortex shedding results in fluctuating forces, which can often trigger an unwanted structural response. I contribute with a generic framework and related developments to enable the inclusion of an arbitrary number and type of damping systems. After laying out the fundamentals, various considerations of an extended partitioned coupling scheme are highlighted. Robustness and scalability are key aspects, showcased on a generic highrise-type construction in smooth flow. With these steps, I establish a prototype that includes passive and semi-active dampers. Their effectiveness is displayed in fully-coupled simulations. Whereas the first part limits its scope to investigating the effect of a Tuned Mass Damper (TMD) (and a certain variation of it), further work broadens this. The approach displays its flexibility in dealing with additional devices, such as a Tuned Sloshing Damper (TSD). My aim is to substantiate that such coupled schemes are generic yet accurate for and accommodating in capturing the proper function of any additional module. While the effect of a TMD on a building could be investigated with simpler approaches, models describing how a TSD works are more prohibitive for traditional experimental means and simplified or scaled models. The showcased numerical approach presents a detailed investigation, including approaching turbulent Atmospheric Boundary Layer (ABL) wind on a high-resolution structure model. Mitigating vibrations is achieved with the aid of both types of dampers.

Chapter 4 includes key enhancements to the *analysis of the transient wind loading on bridge decks*. In particular, the work aims to improve the indirect identification of flutter onset, specifically the forced-motion approach. I add insights from a vast validation campaign. This is carried out on two shapes that represent cross-sections for generic bridge decks. The first part of the study focuses on the aerodynamic force coefficients and flutter derivatives obtained by the traditional way. Such effort is necessary to ensure the quality and trustworthiness of the computational tools including its recent developments, while running on the target HPC infrastructure. Moreover, the work incorporates relevant observations on geometry- and mesh-related aspects in case of such simulations. The second part deals with improvements to the forced-motion approach by combining multiple prescribed frequencies and directions. A major contribution lies in establishing limits of usability and accuracy. Further enhancements take place on a technical level, related to computational details on distributed memory machines. This vast simulation campaign is concluded by direct flutter identification through Fluid-Structure Interaction (FSI) simulations, achieved by a partitioned fully-coupled approach. As a result, an entire numerical workflow is obtained by covering steps ranging from aerodynamic insights leading up to identifying the onset of the movement-induced instability. The novelty is critically linked to the enabling and impact of the combined multi-frequency forced motion approach.

Chapter 5 is about the complex modeling of *wind-structure interaction for lightweight structures*. Such constructions, in particular those incorporating large technical membranes or cable-net systems with cladding, are critically influenced by their properties. This implies that the shapes are mechanically-defined, predominantly by their (pre)stress-state. The preliminary work outlines the need for a more systematic study of double-curved free-standing roof structures. Such an endeavor should address aspects related to aerodynamic loading, levels of interaction as a function of prestress and added-mass ratio, as well as typical patterns for expected structural behavior. I also include contributions focused on a unique stadium, for which a realistic setup requires complex modeling considerations. A digital workflow is outlined that supports the Computer-Aided Design (CAD) of the geometry, and additionally enables properly defining a feasible prestress-state of the construction by CAE. As form and force (internal as well as external) are strongly interlinked, the process is often iterative. The work provides insights into the structural behavior undergoing ABL wind loading, as well as all necessary developments and analysis steps to make this happen. Such a case study drives simulation capabilities to its current limits, which in turn highlights multiple required advances for the workflow to function properly.

In Chapter 6, the *conclusions and outlook* wrap up the dissertation. In this segment, I include a summary of the thesis and provide a preview of subsequent activities.

Chapters 3, 4 and 5 are derived from specific topics and particular projects in which I was involved, and consequently, these are similarly structured. They begin with the *fundamentals*, containing the theoretical basis. Insights related to *research and development* follow, showcasing advances and including key results. A dedicated *summary* reflects the main achievements, including addressing a concise outlook. This structuring of the dissertation is presented in Fig. 1.1.

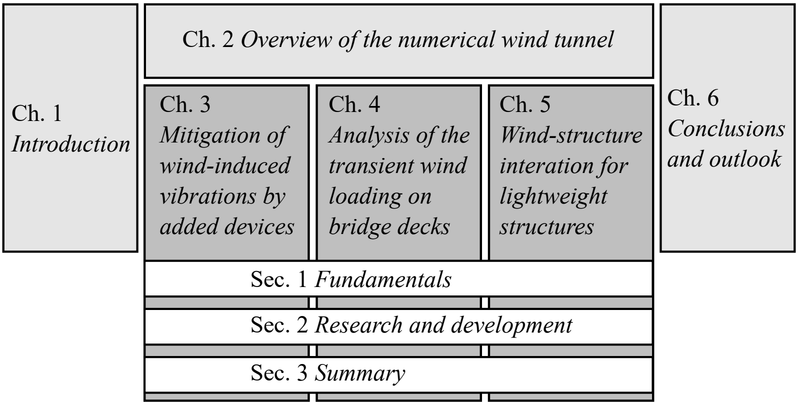

Figure 1.1: Organization of the thesis content.

1.3 Main contributions

In this section, I emphasize key contributions of my thesis to CWE. As many related activities were part of an extended team effort, my role is highlighted for each topic.

In Chapter 2: My contribution to the numerical WT is represented by the development of multiple features and modules, here placed into the broad context of CWE. Related advances were supplemented by substantial simulation campaigns, with particular technical aspects linked to HPC environments. Such insights led to a metamodel, as formally described in this part.

In Chapter 3: I dedicated effort to developing a numerical framework for adding mitigation devices as a countermeasure for Wind-Induced Vibrations (WIVs). The focus was twofold. For one, I was interested in a flexible scenario to include various modules, which led to a multiply-partitioned scheme. Additionally, it was key to establish whether various components with altering numerical models could be coupled in a stable and efficient way. Correspondingly, investigations containing TMDs as well as TSDs were carried out, such that linear as well as nonlinear behavior was covered. Whereas the former component can be numerically described by a rigid body model, the latter involved exploring and improving various formulations for the sloshing motion. I conceptualized the study and drove methodological advances. Research included identifying relevant scenarios and preparing appropriate prototypes. A large simulation campaign was necessary to substantiate these findings.

In Chapter 4: I focused on establishing the entire workflow for numerical bridge analysis as part of an endeavor relying on FEM-based methodological developments at our institute. It was based on two characteristic cross-sections, that were particularly chosen for their resemblance in the aspect ratio, as well as the distinction between the geometries related the bluffness. These were selected for the vast availability of literature to properly validate each step of the workflow. I laid out the key simulation functionalities, beginning with investigations related to bridge aerodynamics. This involved using a parametrization of mesh motion to systematically explore each Angle of Attack (AoA) in an automated manner, starting from the same base setup. Analyses by forced motion was enabled by an improved formulation to flexibly permit assessments for an arbitrary combination of amplitudes, frequencies and type of Degree of Freedom (DoF). Free vibration simulations concluded the key components, such that a direct identification using FSI became possible with a partitioned scheme. Here, certain developments were concurrent to those enabling multiple coupling. The methodological novelty focused on multi-frequency and -direction forced motion simulations to efficiently obtain flutter derivatives. My interest additionally covered particular aspects related to shape, meshing, geometric scale and related numerical quality metrics, which resulted in a review of recommendations and practical considerations. These efforts contributed to establishing an investigation layout with algorithmic enhancements tuned for HPC systems.

In Chapter 5: My work on the Olympic Stadium in Munich aimed at recreating a realistic and detailed model of the structure as well as its surroundings to enable advanced FSI simulations. This work is symbolic for various topics of interest at our institute, such as lightweight structures, form finding and optimization, coupled simulations and structural wind engineering. The timeline of numerical developments is simbolically linked to the 50th anniversary of the Summer Olympics in 1972, and all of the scientific and engineering challenges it has triggered. In particular, I established the geometry and relevant properties based on multiple sources. The geometry was supported by archived plans and recent digital data. Wind conditions were derived from measurements and historical accounts. Structural properties resulted from considerations dating to the early design phase and backed up by optimization efforts. The complexity of the model and simulations of interest required multiple preparatory steps. My work included developments for ensuring a realistic and smooth discrete geometry of the surface, optimization for finding an appropriate stress state, as well as additional steps for improving the mesh quality. Moreover, realistic wind conditions implied a thorough investigation of the site, matching topology in the model, resulting in the generation of a representative ABL wind inlet. The complexity and size of the data recurrently led to technical adaptations, such as for (re)meshing, surface smoothing, and in general data handling throughout the process. Computations were tailored to HPC needs and requirements.

1.4 Further contributions

Here, I highlight various contributions to the broader context of CWE. These encompass multiple outcomes of my research leading up to this dissertation, all of which have significantly influenced the structure, content, and commentary in the current document.

Publications:

1. S. Warnakulasuriya, **M. Péntek**, D. Hackett, R. Wüchner: *Investigating the applicability of shape sensitivities for improved wind comfort in balcony regions*, extended abstract in the conference proceedings of the 8th European-African Conference on Wind Engineering, Bucharest, Romania, 2022, URL: eacwe2022.utcb.ro/wp-content/uploads/8EACWE2022-Proceedings.pdf;

2. **M. Péntek**, G. Martínez-López, S. Warnakulasuriya, K.-U. Bletzinger: *Discussing the appropriate ranges of y+ for the accuracy of CFD simulations at high Reynolds numbers*, extended abstract in the conference proceedings of the 8th European-African Conference on Wind Engineering, Bucharest, Romania, 2022, URL: eacwe2022.utcb.ro/wp-content/uploads/8EACWE2022-Proceedings.pdf;

3. **M. Péntek**, P. Bucher, K. Sautter, K.-U. Bletzinger: *The 50-year anniversary of the Olympic Stadium in Munich as a motivator for advances in computational wind engineering*, extended abstract in the conference proceedings of the 8th European-African Conference on Wind Engineering, Bucharest,

Romania, 2022, URL: eacwe2022.utcb.ro/wp-content/uploads/8EACWE2022-Proceedings.pdf;

4. **M. Péntek**, A.-K. Goldbach, K. B. Sautter and K.-U. Bletzinger: *Numerical modeling and simulation of lightweight structures – using the example of the Olympic Stadium in Munich on its 50th anniversary*, full paper in the conference proceedings of the 33. Forum Bauinformatik, Munich, Germany, 2022, DOI: 10.14459/2022md1686600;

5. **M. Péntek**, A. Riedl, K.-U. Bletzinger and F. Weber: *Investigating the Vibration Mitigation Efficiency of Tuned Sloshing Dampers Using a Two-Fluid CFD Approach*, in Applied Sciences, 12, 7033, 2022, DOI: 10.3390/app12147033;

6. P. Bucher, **M. Péntek**, K. Sautter, R. Wüchner, K.-U. Bletzinger: *Detailed FSI modeling and HPC simulation of the Olympic Stadium roof in Munich under wind loading*, regular abstract in the conference proceedings of Structural Membranes, Munich, Germany, 2021, DOI: 10.23967/membranes.2021.039;

7. R. Wüchner, **M. Péntek**, A. Winterstein, P. Bucher, K.-U. Bletzinger: *Coupled numerical simulations in wind engineering – Potentials and application cases [Orig. Gekoppelte numerische Simulationen im Windingenieurwesen – Potenziale und Anwendungsszenarien]*, full paper in the conference proceedings of the Baustatik-Baupraxis 14, Stuttgart, Germany, 2020, DOI: 10.18419/opus-10762;

8. A. Winterstein, **M. Péntek**, K.-U. Bletzinger, R. Wüchner: *Coupled numerical simulations for the evaluation of mitigation methods in case of wind-induced vibrations [Orig. Gekoppelte numerische Simulation zur Bewertung von Reduktionsmassnahmen bei windinduzierten Schwingungen]*, full paper in the conference proceedings of the WTG-Berichte Nr. 16: Aufbruch zu neuen Methoden im Windingenieurwesen, Windtechnologische Gesellschaft e.V., ISBN: 3-928909-15-0, Munich, Germany, 2019;

9. **M. Péntek**, A. Winterstein, M. Vogl, P. Kupás, K.-U. Bletzinger, R. Wüchner: *A multiply-partitioned methodology for fully-coupled computational wind-structure interaction simulation considering the inclusion of arbitrary added mass dampers*, in the Journal of Wind Engineering & Industrial Aerodynamics, 177, 117–135, 2018, DOI: 10.1016/j.jweia.2018.03.010;

10. **M. Péntek**, R. Wüchner, K.-U. Bletzinger: *A novel fully-coupled computational wind-structure interaction approach for the design of added mass dampers*, full paper in the conference proceedings of the 7th European-African Conference on Wind Engineering, Liège, Belgium, 2017;

11. M. Andre, **M. Péntek**, R. Wüchner, K.-U. Bletzinger: *Aeroelastic simulation of the wind-excited torsional vibration of a parabolic trough solar collector*, in the Journal of Wind Engineering & Industrial Aerodynamics, 165, 67–78, 2017, DOI: 10.1016/j.jweia.2017.03.005;

12. K.-U. Bletzinger, R. Wüchner, M. Andre, **M. Péntek**, A. Michalski: *The Numerical Wind Tunnel – Potentials and Challenges in case of Flexible Structures [Orig. Der numerische Windkanal im Bauwesen – Potentiale und Herausforderungen am Beispiel flexibler Tragwerke]*, full paper in the conference proceedings of the 20. Dresdner Baustatik-Seminar: Realität – Modellierung – Tragwerksplanung, Institut für Statik und Dynamik der Tragwerke, TU Dresden, ISSN: 1615-9705, Dresden, Germany, 2016;
13. **M. Péntek**, M. Andre, R. Wüchner, K.-U. Bletzinger: *Shape-Optimal Design of Wind-Excited Structures*, regular abstract in the conference proceedings of the Baustatik-Baupraxis Forschungskolloquium, Döllnsee, Germany, 2015;
14. **M. Péntek**: *Shape Optimization of Structures Subjected to Wind Load [Orig. Szerkezetek alak-optimalizálása szélterhelés mellett]*, in the Intelligent Network 2015 Research Topics from Young Scientists Abroad [Orig. Intelligens háló 2015 – Határon túli fiatal kutatók tanulmányai], Edutus Főiskola, ISBN: 978-963-8445-76-6, Tatabánya, Hungary, 2015.

Presentations:

1. *The 50-year anniversary of the Olympic Stadium in Munich as a motivator for advances in computational wind engineering*, regular presentation at the 8th European-African Conference on Wind Engineering, Bucharest, Romania, September 2022;
2. *Investigating the applicability of shape sensitivities for improved wind comfort in balcony regions*, regular presentation at the 8th European-African Conference on Wind Engineering, Bucharest, Romania, September 2022;
3. *Numerical modeling and simulation of lightweight structures – using the example of the Olympic Stadium in Munich on its 50th anniversary*, keynote presentation at the 33. Forum Bauinformatik, Munich, Germany, September 2022;
4. *Wind-induced vibrations of structures: Modeling and numerical simulation*, invited presentation from the Graduiertenkolleg at the TU Braunschweig, online, Germany, March, 2022;
5. *Multiphysics: Coupling and data transfer on a simple example*, regular presentation at the V. Kratos Workshop, organized by the Technical University of Munich and the International Center for Numerical Methods in Engineering, Munich, Germany, March 2019;
6. *Open-Source Research Development: Example of the Numerical Wind Tunnel [Orig. Nyílt forráskódú kutatásfejlesztés: A numerikus szélcsatorna példája]*, small plenary at Hungarian Science Day in Transylvania, Transylvanian Museum Society, Cluj-Napoca, Romania, November 2018;
7. *Added devices to mitigate wind-induced vibrations simulated by multiply-coupled schemes*, regular presentation at the FE im Schnee Seminar, Hirschegg, Austria, March 2018;

8. *A novel fully-coupled computational wind-structure interaction approach for the design of added mass dampers*, regular presentation at 7th European-African Conference on Wind Engineering, Liège, Belgium, July 2017;
9. *Shape-Optimal Design in Computational Wind Engineering*, regular presentation at the FE im Schnee Seminar, Hirschegg, Austria, March 2016;
10. *Shape-Optimal Design of Wind-Excited Structures*, regular presentation at the Forschungskolloquium Baustatik-Baupraxis, Döllnsee, Germany, September 2015.

Projects:

1. Research project: *WENSS – Wind Effects on Non-Standard Shapes and Structures*, with the role of the initiator and co-applicant, Engineering Research Infrastructures for European Synergies[*], funded under the Horizon Europe Framework Programme, 2023–2024;
2. Supercomputing project: *Resource-efficiency and resilience of the built environment to natural hazards: Advanced technologies, special investigations and dedicated numerical models for wind effects on structures*, with the role of the principal investigator, Gauss Centre for Supercomputing[†], 10 million CPU-hours, 2022–2024;
3. Supercomputing project: *Wind-structure interaction simulations for high-rise, wide-span and slender civil engineering structures*, with the role of the principal investigator, Gauss Centre for Supercomputing, 15 million CPU-hours, 2019–2023;
4. Teaching project: *iWindlab – Interactivity as the driving force behind the learning process*, with the role of the project owner, funded as part of the excellence strategy of the university[‡], Technical University of Munich, 2022–2023;
5. Research project: *Research into the theoretical-conceptual basis for the performant computation of complex wind-structure interactions of engineering structures [Orig. Erforschung der theoretisch-konzeptionellen Grundlagen für die performante Berechnung komplexer Wind-Struktur-Interaktionen von Ingenieurbauten]*, with the role of the project responsible, a specific subproject as part of the industry collaboration on *Numerical methods for optimization, fast variant calculation and the aeroelastic verification of bridges [Orig. Numerisches Verfahren für Optimierung, schnelle Variantenberechnung und den aeroelastischen Nachweis von Brücken]*, Central Innovation Programme for SMEs on behalf of the Federal Ministry for Economic Affairs and Climate Action, ZIM[§] AiF Projekt GmbH[¶], 2018–2021.

---

[*] www.eries.eu.

[†] www.gauss-centre.eu.

[‡] www.tum.de/studium/lehre/chancen-fuer-die-lehre/ideenwettbewerb.

[§] www.zim.de.

[¶] www.aif-projekt-gmbh.de.

Chapter 2

Overview of the numerical wind tunnel

This chapter provides a general overview of the numerical WT, to be considered as a metamodel. Its aim is to deliver the definition of the nomenclature specific to the context in which it is used for this work. I also outline the setting where the developments and investigations presented in further chapters were carried out. Typical components of the numerical WT are addressed, with their governing equations and particular numerical formulations. I mention various assumptions for and characteristics of the models used. Relevant developments take place in an open-source environment. Modules of the respective software project are highlighted, and linked to the methodology. Furthermore, I include specific features of numerical methods, which characterize the applications used. As simulations heavily relied on HPC, technical aspects are mentioned accordingly. These incorporate notions on the treatment of numerical procedures on distributed memory architectures. For computations to be carried out properly, robustness and accuracy must be maintained, along with appropriate scalability. Concluding thoughts reveal particularities in data handling and bundling of jobs in a well-balanced manner.

2.1 Components and formulations

In this section, the main definitions are outlined. These are to be related to the numerical WT used for investigating corresponding effects on constructions. Consequently, the context is that of structural analysis, which implies certain peculiarities. Fig. 2.1 depicts the main components.

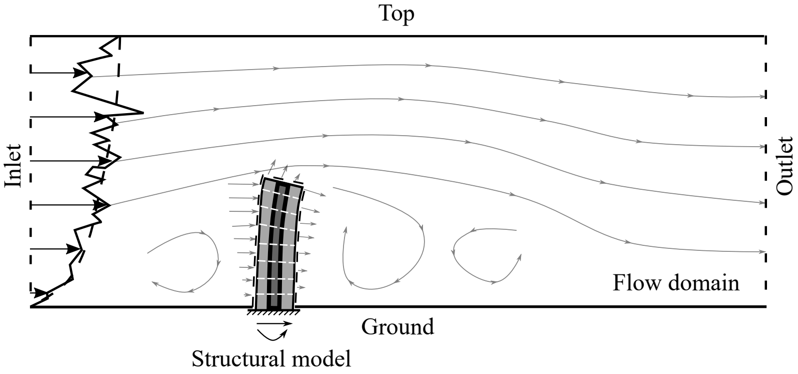

Figure 2.1: Main components of a numerical WT.

These are as follows:

- *Flow domain*: This is the region where wind flow is simulated, which is determined by means of CFD. In the current work, all developments and investigations imply the transient nature of the flow in three-dimensional space. Consequently, the Navier-Stokes Equations (NSEs) are addressed based on the assumptions of the Large Eddy Simulation (LES) turbulence model. Governing equations are solved by a stabilized formulation using the FEM (see Wall, 1999, Ch. 3 and Oñate, 2000). This is a Variational Multiscale (VMS) approach, based on Algebraic Subgrid Scales (ASGS). A detailed description of it and its use for modeling turbulence for civil engineering applications is detailed in Cotela et al. (2016, Chs. 2 and 3). The basic formulation relies on an Eulerian view of the mesh. It is fixed and acts as a background grid, while the change of quantities is tracked on it. Main unknown variables to be solved for are velocities and pressures, as the work implies an incompressible single-phase flow. Relevant Boundary Conditions (BCs) include:
  - *Inlet*: In the inflow region, certain simulations assume low (practically zero) turbulence. This is achieved by defining the wind inlet profile using a function that represents the temporal mean. It will result in zero turbulence intensity incoming onto the structure. Numerically, this definition is of Dirichlet type, by prescribing velocity values on the proper surface. Other simulations aim to model ABL turbulence by a pregenerated synthetic wind (Yan and Li, 2015;

  Melaku and Bitsuamlak, 2021) for providing the time-dependent content. In this case, the mean profile is defined as previously noted, on which these fluctuating components are superposed. This generation follows the procedure proposed by Mann (1998).

  - *Outlet*: At the outlet, the value of pressure (i.e. the difference from the inside region to the ambient pressure outside) is fixed to zero, again a condition typically of Dirichlet type*.
  - *Sides (and top or bottom)*: On these surfaces, the velocity component perpendicular to the plane is fixed to zero, whereas all other components are free. It is labeled as a slip condition.
  - *Ground*: For certain simulations, the region close to the ground is governed by a wall function. This aims to locally correct flow patterns. It is particularly useful when near-surface zones should be captured correctly, despite a coarse mesh. Wall functions are based on empirical considerations, and the exact formulation is specific to the methodology and problem-dependent.
  - *Structure*: The outer hull of the construction is relevant to the flow. This surface is finely meshed to capture patterns accordingly. A no-slip condition is used, which fixes all velocity components to zero. In the context of LES with VMS, the formulation is known to have an additional wall-function-like effect near the boundaries. This can be beneficial for sharp-edged geometries with clear separation and reattachment points.

- *Structural model*: In this work, two types are used. For certain geometries that are not expected to deform, a rigid body is modeled. This will be termed as low-resolution or low-fidelity. Other investigations rely on a highly detailed depiction – high-fidelity or -resolution – of the assessed construction. Here, the FEM serves as the basis, with a formulation including geometric nonlinearities, while not considering any higher-order material behavior. For the FEA of structures, it is typically of interest to obtain displacements as the primal quantity. Reaction forces are recovered, with velocities and accelerations being the results of further postprocessing. A Lagrangian viewpoint of the mesh serves this purpose well. Relevant BCs include:

  - *Load*: In the context of transient wind simulations, these are time-dependent signals. The low-resolution model needs as an input resulting forces and moments, whereas the detailed structure is acted upon on multiple mesh nodes. Here, these are of Neumann type. Additionally, self-weight is considered, and in particular cases the internal prestress force is also accounted for.
  - *Ground*: For the high-resolution models, this means a fixed connection to specific points. Hereby, nodal displacements (and, in certain

---

* Where the pressure gradient is known rather than an absolute value, or when there is a preference for certain numerical formulations, a Neumann-type condition can be formulated using the gradient, which represents the flux across the boundary.

cases, rotations) are set to zero. When working with rigid bodies, some motions are also fixed. These conditions are of Dirichlet type. For others, one needs to assign stiffness and damping values to enable every necessary DoF.

- *Interface between structure and wind flow*: This is represented by the surface of the structure, upon which the wind acts. In the numerical context, one has to distinguish between simulated effects, and what approaches are used. In this work, I follow a partitioned (Piperno et al., 1995; Wall et al., 2000; Degroote et al., 2010) strategy, which implies that the numerics for the structure and fluid are segregated. Each has its own computational model, formulation, as well as dedicated solver. In the following, I include typical aspects to consider, which represent general parts of FSI schemes:

  - *Mapping*: At its base, it is a data transfer operation (Farhat et al., 1998; Bungartz et al., 2016; Bucher, 2017). The wind pressure on the outer hull is exchanged into nodal forces or a surface load for the structure. Apart from this coherence in physics, the mesh topology is also accounted for, as the transfer will typically happen between non-matching grids. In case of forces, the exchange needs to happen in a conservative manner, such that equilibrium is achieved in an integral sense. When structural deformations need to be captured in the fluid domain, the physics is related to this kinematic quantity. Equilibrium here means that the deformation on one side needs to be consistent with the other side. In case of the rigid body oscillator, there is a particular formulation to reduce forces to a particular point, as well as distributing a concentrated deformation to a contour.
  - *Coupling*: This can be seen as the sequence of solving various partitions, or generically the communication pattern between them. The effect of wind on constructions is very often assessed by applying the time history of pressures on them. It has the implication of determining the flow condition, and transferring loads from one model to the other, without the structural deformations having an impact. Essentially, wind acts on the same undeformed configuration, independent of the actual state of the construction. This is known as One-Way Coupling (OWC). By contrast, Two-Way Coupling (TWC) permits the communication in both directions, with various modules having an effect on each other. This can be further categorized into strong – additionally known asiterative, as in Matthies and Steindorf (2003) and Küttler and Wall (2008) – and weak – also called staggered, as in Felippa and Park (1980) and Dettmer and Perić (2012) – schemes, depending on whether further inner iterations for convergence need to take place or not. Accordingly, components such as predict, check and accelerate convergence will be involved. In the current context, this means that the wind acts on the structures, which in turn deforms and triggers a corresponding update in the flow field. Most simulations within this work use the Aitken underrelaxation.

The last enumerated aspect needs further detailing. Previously, I highlighted that CFD typically uses a background-mesh type approach. In case such mesh topologies need to enable a deformation, this shall be treated in the so-called Arbitrary Lagrangian-Eulerian (ALE) way (Donea et al., 1982). It means that the numerical grid can behave in both ways. On the one hand, the CFD mesh can continue recording velocities and pressures describing wind flow. On the other hand, the same grid can deform. This change in shape can be achieved using a structural similarity model, whereby a desired change in geometry is treated as a prescribed deformation to a typical structure (Mini, 2014). It is a complementary problem, with its own Initial Conditions (ICs) and BCs, as well as a dedicated solving procedure.

In Fig. 2.2, an exemplary solving procedure of FSI with TWC is highlighted. This depicts the previous components and how these are interconnected during a transient analysis between two time steps, specifically in case of strong coupling.

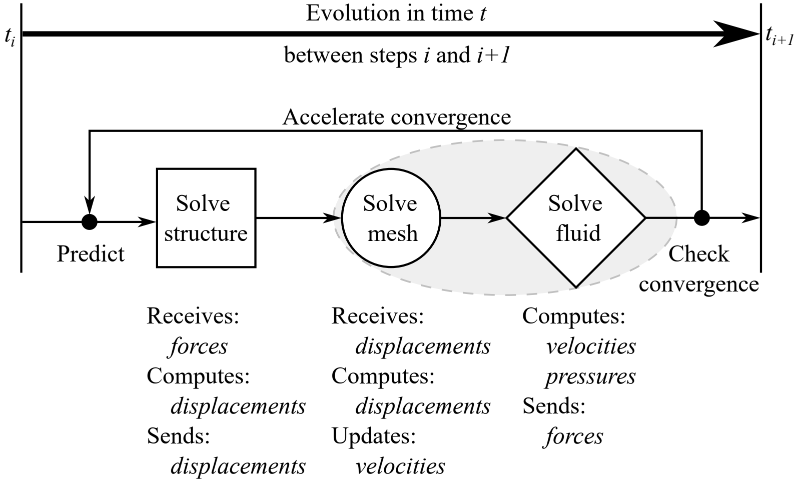

Figure 2.2: Generic strong TWC solving procedure for FSI.

The numerical WT is to be viewed at the highest level of abstraction as a meta-model. Consequently, it provides a framework with a related set of rules and underlying theoretical concepts. In essence, it is a collection of various numerical models (or modules) interacting for a specific purpose, in the current scope that of investigating the effect of wind on structures.

2.2 Governing equations

Governing equations complement the presentation of the components and respective numerical formulations. These represent the physical and mathematical foundation in a continuous and a discrete sense. For the current thesis, the main discussion revolves around transient problems, which involves solving dynamic processes within multiphysics. In particular, I include some peculiarities related to the FEM, for Computational Structural Dynamics (CSD) and CFD. Consequently, deriving the dynamic equilibrium for structures relies on ensuring the momentum balance. Herein, the linear momentum $\mathbf{L}$ is defined by integrating the mass density ρ_S and the velocity field $\dot{\mathbf{d}}_S$ over the considered structural domain Ω_S:

$$\mathbf{L} = \int_{\Omega} \rho_S \dot{\mathbf{d}}_S d\Omega_S. \tag{2.1}$$

Newton's Second Law of Motion relates the total force $\mathbf{F}$ acting on an object to the acceleration $\ddot{\mathbf{d}}_S$ of the mass. Applying the Reynolds Transport Theorem and the Law of Conservation of Mass defines the time derivative of the linear momentum, with the result shown in Eq. (2.2):

$$\dot{\mathbf{L}} = \int_{\Omega} \rho_S \ddot{\mathbf{d}}_S d\Omega_S = \mathbf{F}. \tag{2.2}$$

The total force is also equal to the traction $\mathbf{t}_S$ and body force $\mathbf{b}_S$ applied on the boundary Γ_S and domain Ω_S, respectively:

$$\left.\begin{aligned} \mathbf{F} &= \int_{\Omega} \rho_S \ddot{\mathbf{d}}_S d\Omega_S \\ \mathbf{F} &= \int_{\Gamma} \mathbf{t}_S d\Gamma_S + \int_{\Omega} \mathbf{b}_S d\Omega_S \end{aligned}\right\} \Rightarrow \int_{\Gamma} \mathbf{t}_S d\Gamma_S + \int_{\Omega} \mathbf{b}_S d\Omega_S - \int_{\Omega} \rho_S \ddot{\mathbf{d}}_S d\Omega_S = \mathbf{0}. \tag{2.3}$$

Using the Divergence Theorem, the integral of traction $\mathbf{t}_S$ over the surface Γ_S can be equated to a volume integral over Ω_S, now expressed by the Cauchy stress tensor $\boldsymbol{\sigma}$. As the relation holds for any arbitrary domain Ω_S, it can also be expressed locally:

$$\begin{aligned} \text{Over a domain:} \quad & \int_{\Omega} \left(\nabla \cdot \boldsymbol{\sigma} + \mathbf{b}_S - \rho_S \ddot{\mathbf{d}}_S\right) d\Omega_S = \mathbf{0}, \\ \text{Local form:} \quad & \nabla \cdot \boldsymbol{\sigma} + \mathbf{b}_S - \rho_S \ddot{\mathbf{d}}_S = \mathbf{0}. \end{aligned} \tag{2.4}$$

The local form represents the governing equation. This notation is extended by time (instance t_i within the total duration T) information, as well as the ICs and BCs. It results in the strong form expression of:

$$
\begin{aligned}
&\text{Equilibrium:} \\
&\qquad \nabla \cdot \boldsymbol{\sigma} + \mathbf{b}_S - \rho_S \ddot{\mathbf{d}}_S = \mathbf{0} \quad \text{in } \Omega_S \times (t_0, T), \\
&\text{ICs:} \\
&\qquad \mathbf{d}_S = \mathbf{d}_S^{init} \quad \text{in } \Omega_S \times \{t_0\}, \\
&\qquad \dot{\mathbf{d}}_S = \dot{\mathbf{d}}_S^{init} \quad \text{in } \Omega_S \times \{t_0\}, \\
&\text{BCs:} \\
&\qquad \mathbf{d}_S = \mathbf{d}_S^{D} \quad \text{on } \Gamma_{S,D} \times (t_0, T), \\
&\qquad \boldsymbol{\sigma} \cdot \mathbf{n} = \mathbf{t}_S^{N} \quad \text{on } \Gamma_{S,N} \times (t_0, T),
\end{aligned}
\tag{2.5}
$$

where the boundary of the domain must satisfy BCs, expressed as $\partial\Omega_S = \Gamma_{S,D} \cup \Gamma_{S,N}$, with the former term representing Dirichlet conditions and the latter those of Neumann type. Furthermore, such conditions should not be conflicting, i.e. $\Gamma_{S,D} \cap \Gamma_{S,N} = \emptyset$. $\mathbf{n}$ represents the normal to the boundary $\Gamma_{S,N}$. This manner of expressing equilibrium is known as the strong form, which implies that the relations hold at every point in the domain. A general analytic solution to this problem is typically not possible. Consequently, according to the variational principle of the FEM, this Initial Boundary Value Problem (IBVP) can be expressed in the weak form based on the Galerkin approach. This implies satisfying the equations in an integral sense. An arbitrary test function, $\delta\mathbf{d}$, is introduced, and the local form in Eq. (2.4) is integrated over the domain:

$$\int_{\Omega} \left(\nabla \cdot \boldsymbol{\sigma} + \mathbf{b}_S - \rho_S \ddot{\mathbf{d}}_S \right) \delta\mathbf{d} \, d\Omega_S = \mathbf{0}. \tag{2.6}$$

By this, the differential equations governing the physical problem are transformed into a form that can be better approximated numerically. The proper choice of the test function ensures the minimization of the error introduced by this step using the Galerkin method. This function is selected to represent the virtual displacement field, which is the necessary premise for the PVW. The procedural details of reaching this form are discussed in the work of Zienkiewicz and R. L. Taylor (2006, Chs. 1 and 2). The resulting derived equations must respect the physical principles of the system regarding the balance of forces. Correspondigly, the total virtual work δW can be expressed as the condition of equilibrium:

$$\delta W = \delta W_{int} + \delta W_{kin} - \delta W_{ext} = 0. \tag{2.7}$$

Subparts of the virtual work, internal, kinematic (or dynamic) and external, are marked by appropriate subscripts. These are defined as:

$$\begin{aligned}
\delta W_{int} &= \int_{\Omega} (\boldsymbol{\sigma} + \boldsymbol{\sigma}_0) : \delta \mathbf{e} d\Omega_S, \\
\delta W_{kin} &= \int_{\Omega} \rho_S \ddot{\mathbf{d}}_S \cdot \delta \mathbf{d} d\Omega_S, \\
\delta W_{ext} &= \int_{\Omega} \mathbf{b}_S \cdot \delta \mathbf{d} d\Omega_S + \int_{\Gamma} \mathbf{t}_S \cdot \delta \mathbf{d} d\Gamma_{S,N}.
\end{aligned} \tag{2.8}$$

where $\delta\mathbf{e}$ notes the appropriate virtual strain and $\boldsymbol{\sigma}_0$ the contribution of prestress.

In conclusion, the balance of momentum is used to derive the equilibrium of forces, which holds in the strong sense, i.e. globally as well as locally inside the domain. Using the variational principle and assuming a particular choice of the test function results in the expression of the virtual work. This is the weak form, which holds in an integral sense. The FEM implies an additional step, such that the relations do not hold in continuous space but rather in a discrete sense. An appropriate transformation includes an approximate vector field $\tilde{\mathbf{d}}_S$, which is achieved by interpolating discrete nodal displacement values $\hat{\mathbf{d}}_S$ by shape functions $\mathbf{N}$. Eq. (2.9) highlights this:

$$\mathbf{d}_S \approx \tilde{\mathbf{d}}_S = \mathbf{N}\hat{\mathbf{d}}_S. \tag{2.9}$$

We arrive at the Equation of Motion (EoM), in a semi-discrete form, from Eq. (2.7):

$$\begin{array}{rcl}
\delta W_{kin} & \rightarrow & \mathbf{M}\ddot{\hat{\mathbf{d}}}_S, \\
\delta W_{int} & \rightarrow & \hat{\mathbf{F}}_{int}\left(\hat{\mathbf{d}}_S\right), \\
\delta W_{ext} & \rightarrow & \hat{\mathbf{F}}_{ext}, \\
 & \Downarrow & \\
\multicolumn{3}{c}{\mathbf{M}\ddot{\hat{\mathbf{d}}}_S + \hat{\mathbf{F}}_{int}\left(\hat{\mathbf{d}}_S\right) = \hat{\mathbf{F}}_{ext}.}
\end{array} \tag{2.10}$$

The internal virtual work essentially leads to the stiffness contribution, being a nonlinear function of $\hat{\mathbf{d}}_S$. One can further extend the relation to include damping, for example based on the Rayleigh model, introducing the velocity-dependent part. Consequently, the complete EoM is expressed as:

$$\mathbf{M}\ddot{\hat{\mathbf{d}}}_S + \mathbf{C}\dot{\hat{\mathbf{d}}}_S + \hat{\mathbf{F}}_{int}\left(\hat{\mathbf{d}}_S\right) = \hat{\mathbf{F}}_{ext}. \tag{2.11}$$

For geometric linear elements, the last term is generally denoted as $\mathbf{K}\hat{\mathbf{d}}_S$. These steps cover key insights related to the equilibrium of structures, from a continuous strong sense to a weak, approximated and discrete form, as characteristic of the FEM.

Fluid flow is governed by the NSEs. The first relation marks the balance of momentum (in the convective form), similarly to how this was previously described for the structure. Additionally, a statement about the mass conservation is needed. For incompressible flow, this leads to a condition on the divergence of the velocity field. These can be summarized as follows:

$$
\begin{aligned}
&\text{Balance of momentum:} && \\
& && \frac{\partial \mathbf{u}_F}{\partial t} + (\mathbf{u}_F \cdot \nabla)\,\mathbf{u}_F + \frac{1}{\rho_F}\nabla p_F - \nu_F \nabla^2 \mathbf{u}_F = \mathbf{f}_F \\
& && \text{in } \Omega_F \times (t_0, T), \\
&\text{Conservation of mass:} && \\
& && \nabla \cdot \mathbf{u}_F = \mathbf{0} \quad \text{in } \Omega_F \times (t_0, T), \\
&\text{ICs:} && \\
& && \mathbf{u}_F = \mathbf{u}_F^{init} \quad \text{in } \Omega_F \times \{t_0\}, \\
&\text{BCs:} && \\
& && \mathbf{u}_F = \mathbf{u}_F^{D} \quad \text{on } \Gamma_{F,D} \times (t_0, T), \\
& && \boldsymbol{\sigma}\left(\mathbf{u}_F, p_F\right) \cdot \mathbf{n} = \mathbf{t}_F^{N} \quad \text{on } \Gamma_{F,N} \times (t_0, T),
\end{aligned}
\tag{2.12}
$$

where ρ_F and ν_F are fluid properties, representing density and kinematic viscosity. Ω_F and Γ_F mark the flow domain and its boundary. The main variables are noted by the vector field of velocities $\mathbf{u}_F$ and scalar field of pressures p_F. $\mathbf{f}_F$ stands for the body force applied to the fluid. With pressure being a main variable, either an indirect imposition of the BC through traction is possible, or, if of Dirichlet type, directly through fixing the absolute values. Consequences related to stability and accuracy depend on the actual implementation, also guiding the choice of an option. Similar rules hold for the domain boundaries, where and how various types of BCs are applied, as for the observations related to CSD. Analogously, in the context of the FEM for CFD, the actual field of variables in the continuous sense is approximated and later interpolated from nodal variables and shape functions. This leads to:

$$
\begin{cases}
\mathbf{u}_F \approx \tilde{\mathbf{u}}_F = \mathbf{N}_{\mathbf{u}} \hat{\mathbf{u}}_F \\
p_F \approx \tilde{p}_F = N_p \hat{p}_F
\end{cases} .
\tag{2.13}
$$

$\mathbf{N}_{\mathbf{u}}$ and N_p denote the different choices for shape functions in the case of velocity and pressure (Bazilevs et al., 2012, Ch. 2). This is predominantly necessary to ensure stability and accuracy conditions, as well as to optimize computational efficiency, particularly in incompressible flow problems. The numerical challenge also arises from the difference in the physical quantities related to their magnitude and distribution.

Certain details have been omitted for the sake of brevity. Similarly, detailing the temporal discretization lies beyond the current scope. Nonetheless, the IBVP for CSD as well as CFD require the numerical solution for a nonlinear problem. The residual form of the derivation is included for transient structural analysis with the FEM, as presented by Dieringer (2014, Ch. 4). This leads to an iterative solution procedure in between time steps. Instead of solving for $\hat{\mathbf{d}}_S$, the unknown is the incremental deformation $\mathbf{\Delta}\hat{\mathbf{d}}_S$. Moreover, the notion of effective stiffness $\mathbf{K}_{eff}$ is introduced, whereas the residual is noted $\mathbf{R}_S$. The simplified EoM results in:

$$\mathbf{K}_{eff}\mathbf{\Delta}\hat{\mathbf{d}}_S = \mathbf{R}_S. \tag{2.14}$$

Assuming a temporal discretization by the Generalized-α scheme (Chung and Hulbert, 1993), the detailed form is expressed as:

$$\left[\frac{1-\alpha_m}{\beta\Delta t^2}\mathbf{M} + \frac{\left(1-\alpha_f\right)\gamma}{\beta\Delta t}\mathbf{C} + \left(1-\alpha_f\right)\mathbf{K}\right]\mathbf{\Delta}\hat{\mathbf{d}}_S^{n,i} = \mathbf{R}_S\left(\hat{\mathbf{d}}_S^{n,i}\right), \tag{2.15}$$

where α_m, α_f, γ and β are parameters of the time integration, including the time step δt. n indexes the temporal increments, whereas i reflects the nonlinear iterations for reaching convergence within a time step. In the same manner, the NSEs can be linearized. With a Finite Element (FE) formulation for fluids, and assuming the Bossak time integration scheme, a similar relation can be derived. Herein, the result of the detailed steps in Cotela et al. (2016, Ch. 2) is included:

$$-\left(\frac{1-\alpha_B}{\gamma_N\Delta t}\mathbf{M} + \mathbf{C}\right)\begin{bmatrix}\mathbf{\Delta}\hat{\mathbf{u}}_F^{n,i}\\ \mathbf{\Delta}\hat{p}_F^{n,i}\end{bmatrix} = \mathbf{R}_F\left(\hat{\mathbf{u}}_F^{n,i}, \hat{p}_F^{n,i}\right), \tag{2.16}$$

with α_B and γ_N being coefficients related to time integration. Consequently, a clear similarity between the formulations for structural analysis and flow problems is outlined. This can be summarized in a *gen*eric (symbolic and simplified) notation of the EoM, with the unknown $\mathbf{\Delta}\hat{\mathbf{x}}_{gen}$:

$$\mathbf{K}_{gen}\mathbf{\Delta}\hat{\mathbf{x}}_{gen} = \mathbf{R}_{gen}. \tag{2.17}$$

Additionally, FSI requires linking the formulations for CFD and CSD together, as the numerically discretized domains interact at their interface. In an ALE framework, the total nodal velocity $\hat{\mathbf{u}}_F$ of the fluid is composed of a relative component and the mesh velocity (Bazilevs et al., 2012, Chs. 4 and 5). This latter term must be equal to the structural motion, which is the time derivative of the displacements $\hat{\mathbf{d}}_S$ on the interface. Properly computing the total nodal velocity is crucial for ensuring accurate coupling between these subsystems, especially in regions where significant deformations are expected.

2.3 Open-source software development

Computational developments are based on open-source software. Relevant advances cover multiple areas of coupled multiphysics. These are part of a larger, community-driven effort, mostly belonging to the *Kratos Multiphysics* project. This software was designed to tackle various simulation challenges, with its framework enabling a modern and modular implementation environment. As stated in Dadvand et al. (2010), it is intended for building multidisciplinary programs based on the FEM[*]. One of its strengths lies in providing a common platform in achieving this. The structure of the code is shown in Fig. 2.3.
Core functionalities are those required and shared by multiple use cases. These represent the typical implementational aspects for the FEM. *Applications* contain specific developments for focused use cases, such as CFD or CSM. Many of the enhancements contributed by this dissertation happen at this latter level. The following enumeration highlights parts of *Kratos Multiphysics*, which the work heavily relies on.

- General functionalities:
    - *Core*: To be seen as a collection of basics, for algorithms and datastructures, related to input/output, geometry, as well as common aspects of the FEM.
    - *LinearSolversApplication*: Provides additional solving functionalities, including an interface to the MKL[†]. These contain many capabilities to simulate the behavior of structures. Apart from direct solutions for sparse systems, it permits dealing with eigenvalue problems.
    - *MeshingApplication*: Has functionalities to create and manipulate meshes. It interfaces to external libraries.
    - *StatisticsApplication*: It includes a collection of utilities to calculate spatial or temporal statistics efficiently.
    - *HDF5Application*: Provides additional input/output functionalities based on the H5[‡] format.
- Particular applications for simulations:
    - *FluidDynamicsApplication*: Represents most of the content for CFD. In particular, this thesis implies simulations with the fractional step scheme for solving the NSEs. Consequently, the main unknowns of the problem – velocities and pressures – are uncoupled and solved for separately, while still satisfying the incompressibility constraint.
    - *StructuralMechanicsApplication*: Contains relevant functionalities for CSM simulations. This includes the eigenvalue problem to determine vibration mode shapes and frequencies. Furthermore, it permits static and dynamic (i.e. time history) analysis.

---

[*] Various other discretization methods are implemented as part of different applications.

[†] Intel MKL, www.intel.com/content/www/us/en/docs/onemkl/get-started-guide/2023-0/overview.html.

[‡] www.hdfgroup.org/solutions/hdf5.

  - *CoSimulationApplication*: It is a generic coupling tool to be used in multidisciplinary numerical investigations. Herein, it coordinates the coupling scheme, according to the OWC or TWC pattern. For the latter case, further key components – such as type (weak or strong) as well as predictors and accelerators – need to be defined.
  - *MappingApplication*: This application is responsible for enabling the transfer of data, including between non-matching numerical grids. Most cases use the nearest element approach.
  - *MeshMovingApplication*: Is required for the ALE formulation used by CFD when the numerical mesh needs to be moved. An updating strategy based on structural similarity is a typical choice.

- Specific requirements for HPC:
  - *MetisApplication*: Subdividing computational models for computing on distributed memory machines requires this building block. This is permitted by an interface to the METIS[*] library. Base functionalities are presented in Karypis and Kumar (1997).
  - *TrilinosApplication*: Provides various linear algebra utilities to solve problems on specific parallel architectures[†]. An overview is provided in Heroux et al. (2003).

Furthermore, the fluctuating components of the ABL flow are determined using *WindGen*[‡]. This is a synthetic wind generation library, implementing the model described in Mann (1998) according to the technical details in Andre (2018, Ch. 2). It creates the time-dependent velocity field, in an H5 format, with its frequency content matching one of the well-established assumptions. In this case, it is the one based on the spectral density distribution proposed by Kaimal (see Simiu and Yeo, 2019, Ch. 2). MMG tools[§] are additionally used for certain treatments of the numerical mesh. Output data is typically in H5 or ASCII formats. Postprocessing happens in Paraview[¶], which is a well-established open-source software for data visualization. Custom Python[‖]-based scripts are used for data science and engineering purposes. They are employed either to handle or post-process results, or to implement new functionalities. GiD[**] is the only component in the workchain that is proprietary. It is a software aiding the preparatory steps for numerical simulations, such as geometry creation, most meshing tasks and creating the initial computational models based on a predefined problemtype. I kindly remark on the solution-oriented stance of its developers and their prompt response in providing updates. In this sense, it strives to follow the positive community attitude.

---

[*] www.github.com/KarypisLab/METIS.

[†] trilinos.github.io.

[‡] www.github.com/msandre/WindGen.

[§] www.mmgtools.org.

[¶] www.paraview.org.

[‖] www.python.org.

[**] www.gidsimulation.com.

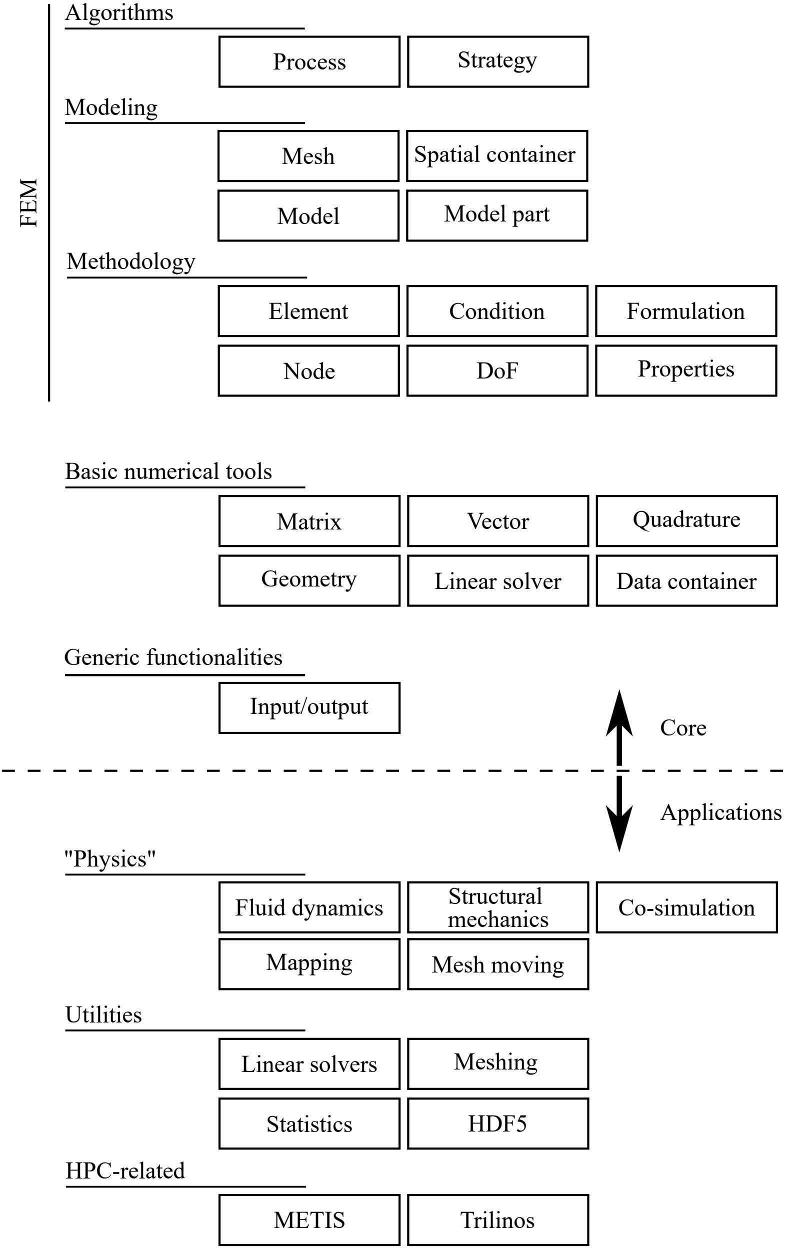

Figure 2.3: Code structure of *Kratos Multiphysics*, adapted from Dadvand et al. (2010) and Baumgärtner et al. (2015, Ch. 5).

2.4 High-performance computing

HPC systems assist activities in CAD and CAE, which involve memory- and compute-bound processes, also known as Random-Access Memory (RAM)-intensive and Central Processing Unit (CPU)-intensive, respectively. It is a generic term that describes specific hardware architectures required for working on complex and large-scale numerical problems. Similar to how scientific computing and numerical analysis became an important pillar of science in the 1950s, new prerequisites require dedicated discussions.

Herein, shared-memory machines permit the direct access of processors to the main memory. Most personal computers are of this kind. During the current work, particular meshing-related activities, data-handling tasks and manipulating computational models required appropriately high RAM. At an algorithmic and coding level, this meant serial processes, or exploiting Open Multi-Processing (OMP) parallelization. The latter is a programming standard that acts as an add-on for the compiler. Its usage results in improving the performance of algorithms when possible. Respective libraries act as an Application Programming Interface (API), providing compiler directives that guide how certain parts of the code need to be run, such as single-threaded, concurrent or parallel on multiple threads, etc.

Conversely, distributed-memory machines should be thought of as a network of connected shared-memory units. This adds a technical level that is characteristic of the topology defining communication between them. In case of large numerical problems, respective models (and corresponding systems of equations) can be split up and handled separately. Accordingly, data partitioning becomes relevant, and explicit message parsing needs to take place between the computing modules. Working on these architectures implies a series of processes working independently, having their own memory space. These are coordinated by a set of rules and procedures, according to the standard definitions provided by the Message-Passing Interface (MPI). Numerical simulations included in this thesis heavily rely on this approach.

The conceptual difference between shared and distributed memory architectures is depicted in Fig. 2.4. Most current personal computers will have a shared (UMA[*]-type) layout, whereas modern supercomputers are characterized by a hybrid one. It is up to the software to properly exploit the hardware architecture. An exemplary pseudocode reflects main steps and typical keywords, comparing the OMP and MPI protocols showcased in Fig. 2.5. OMP relies on multithreading. There is a master process and workers can be dynamically activated as necessary. Respective directives are typically marked in the code with `#pragma omp <directive>`. In case of MPI, all processes need to be initialized from the start, with resources allocated appropriately. These need to be available at the beginning and will be blocked during execution. Corresponding functions usually have the structure `#MPI_<function>`[†]. Hybrid parallelism is also possible.

SuperMUC-NG provides the hardware infrastructure for most of the presented simulation work. Corresponding numerical models are large, and require the usage of the MPI for analyses on distributed-memory machines. The challenge is

---

[*] Shared memory can be further categorized into uniform memory access (UMA) or non-UMA (NUMA).

[†] The exact definition and detailing of the presented commands is out of scope.

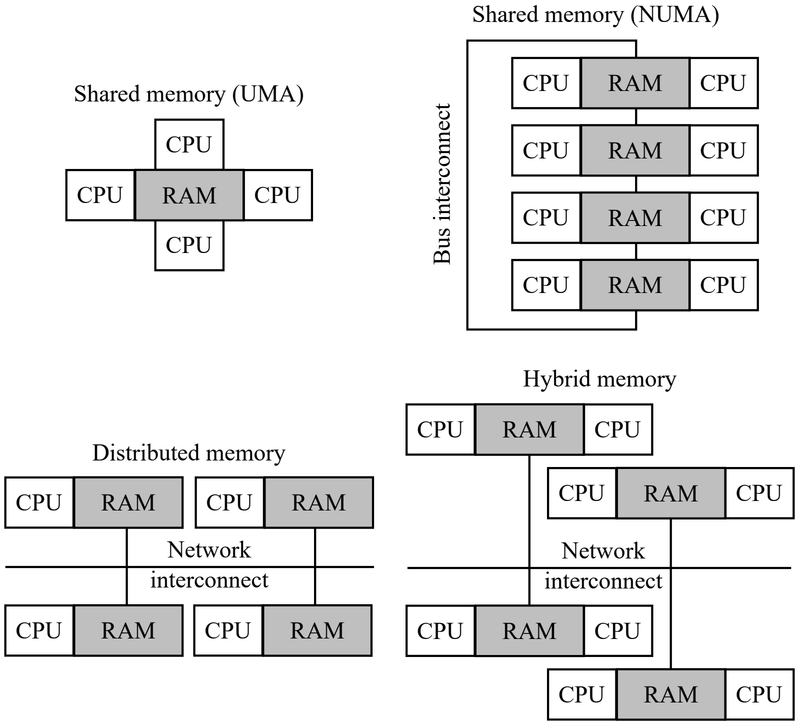

Figure 2.4: Conceptual difference between shared- and distributed-memory architectures, adapted from Ploskas and Samaras (2016, Ch. 1).

not only to parallelize single large jobs but also to bundle multiple of them appropriately. SLURM* is the system used for managing and scheduling jobs on this Linux cluster. It sets the rules for the submission of numerical simulations, including prioritization. These considerations define the proper choice of resources, such that runs are well balanced. Fig. 2.6 highlights such aspects for bundled jobs. Hereby, the computer cluster system relies on its scheduler, which prioritizes large jobs in terms of both computational resource (provided in the number of compute nodes or cores) and maximum allowable time. For users, a planned submission to the queue should respect recommendations. A well-balanced plan of bundled jobs implies tasks of similar size and with similar duration, using checkpointing†. A poorly thought-through one does not follow these best practices, which results in unnecessarily blocking computational resources.

---

[*] Simple Linux Utility for Resource Management (SLURM), a job scheduler typically used on HPC systems, www.github.com/SchedMD/slurm.

[†] Checkpointing in numerical simulations can be compared to the concepts of Recovery Time Objective (RTO) and Recovery Point Objective (RPO) in cloud services.

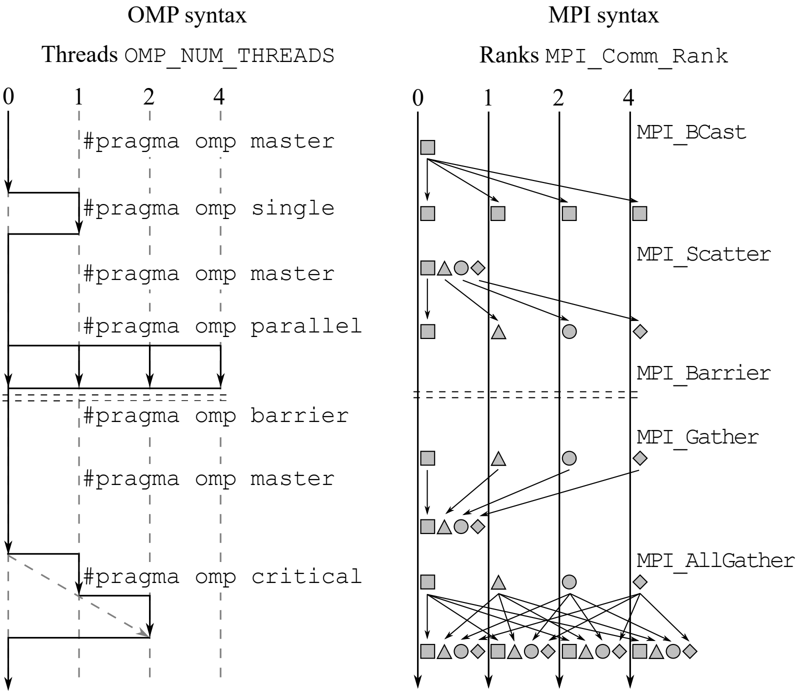

Figure 2.5: Exemplary process flow with typical keywords, comparing the OMP and MPI protocols.

I remark on the importance of considering runtime and job limits, for which a checkpointing mechanism is a necessity. This enables the restart of simulations, while minimizing losses of resources and data in case of failure or arriving at the time cap. The software used should exhibit proper scaling performance, with the user being aware of the relevant settings and appropriate properties. Consequently, simulations requiring different computational resources can be grouped together.

Technical characteristics of the hardware need to be linked to certain aspects related to software. In *Kratos Multiphysics*, the *MetisApplication* is in charge of the partitioning operation. This divides the computational model such that it can be evaluated on a distributed-memory machine. It is a serial operation that should be executed a priori for file-based input, or directly in memory as a more failproof approach for certain use cases where multiple processes need access to the same input data during runtime. The entire simulation routine implements MPI requirements. Using the *TrilinosApplication* is required for solving the linear systems in parallel. A restart mechanism ensures that a simulation can be reinitiated from a certain checkpoint. This is important for resource efficiency, whether

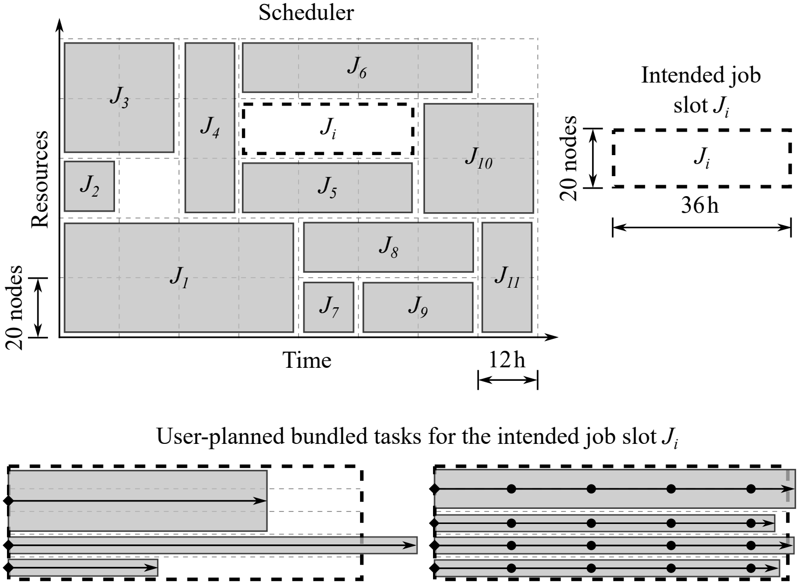

Three poorly-balanced tasks

Four well-balanced tasks with checkpointing ●

Figure 2.6: Typical HPC job planning based on available and required resources.

a job needs to be continued after a failure or time limit. One can enable or suppress output data or adapt simulation parameters, such that it avoids an identified failure. Smart data formats such as H5 support these numerical investigations. In particular, this chosen type permits the efficient storage of data, as well as input/output operations with multiprocess read and write access. The operating system is SUSE Linux[*], having Spack[†] as a package management framework. This provides a modular concept to flexibly allow the usage of various software.

Numerical developments and advances in software are closely linked to the HPC infrastructure. These need to be modular, robust and scalable. In my work, I emphasize these technical aspects and the links between them, as respective knowledge is key for adequate enhancements and proper simulations. These insights are also fundamental in establishing the numerical WT.

---

[*] SUSE Linux Enterprise Server (SLES), www.suse.com/products/server.

[†] www.spack.io.

Chapter 3

Mitigation of wind-induced vibrations by added devices

The mitigation of WIVs is a challenging aspect, and the possible use of added devices in achieving this is addressed here. As part of the preliminary insights, the sources and types of relevant excitation mechanisms are highlighted first. The content includes characterizing the external force, which is followed by models of oscillators for typical structures. I cover basics related to the amplification of corresponding vibrations, and how this can be counteracted using added dampers. These generalities are followed by a detailed study on a framework that permits the inclusion of an arbitrary number and type of such devices. Developments enable the modeling and simulation of a fully-coupled scenario, with feedback between wind and structure, as well as structure and added damper. Further advances cover computational means for modeling sloshing motion, and its usage as a mitigation device. In this second part, an additional wind flow case is addressed by explicitly capturing ABL turbulence. Such an approach can support development and assist in making design decisions related to the placement, number, and type of damping devices.

3.1 Fundamentals

3.1.1 Narrowband aerodynamic excitations

Wind loading on a typical tall building is presented in Fig. 3.1.

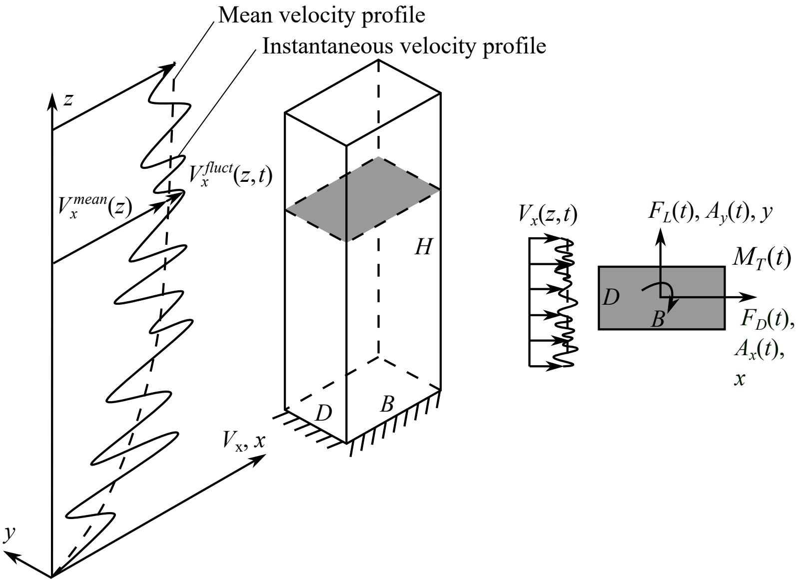

Figure 3.1: Wind loading on a typical tall building, adapted from Flay (2013).

The streamwise velocity component V_x is defined along height z and time t. It can be decomposed in a mean (time-averaged) V_x^{mean} – often denoted simply as V – and a fluctuating (or instantaneous) V_x^{fluct} component, as follows in Eq. (3.1):

$$V_x(z,t) = V_x^{mean}(z) + V_x^{fluct}(z,t). \tag{3.1}$$

For a horizontal cut at a specific height z, the acting wind force components are defined as drag F_D and lift F_L. These are given according to the standard nomenclature in bluff body aerodynamics. Herein, we distinguish between the body-attached axis (x–y) and the flow-attached one (drag–lift). For the given example, these reference systems overlap. Along- and cross-wind components are defined by their respective force coefficients C_D and C_L, and a chosen reference area A^{ref}. $\rho_{(a)}$ reprsents the density of air. Corresponding relations are shown in Eqs. (3.2), (3.3), and (3.4). The torsion moment-related term C_M is included for completeness:

$$F_D(t) = C_D \frac{1}{2} \rho A^{ref} V_x^2(z,t), \tag{3.2}$$

$$F_L(t) = C_L \frac{1}{2} \rho A^{ref} V_x^2(z,t), \tag{3.3}$$

$$M_T(t) = C_M \frac{1}{2} \rho A^{ref} B V_x^2(z,t). \tag{3.4}$$

The reference area A^{ref} is typically chosen to be the projected one in streamwise direction, the same for all force components. However, this depends on the domain of application, and there are differences in definition between bridge engineering, airfoils and tall buildings. For the current discussion, a unit length is considered for corresponding sectional forces, defining the relations over height, as provided in Eq. (3.5), here for a unit length:

$$A^{ref} = H^{seg} D, \tag{3.5}$$

with the height of the segment often $H^{seg} = 1\,\mathrm{m}$. The formulas in this form imply that C_D and C_L do not depend on the velocity. Corresponding structural response is of interest, which is typically characterized by displacements or accelerations. They are noted generically by their amplitude A_x and A_y along the body-attached axis, with the overall magnitude represented as A_{xy} in Eq. (3.6):

$$A_{xy}(t) = \sqrt{A_x^2(t) + A_y^2(t)}. \tag{3.6}$$

Three typical response types can be observed. Based on the nomenclature by Naudascher and Rockwell (1994, Ch. 1), these can be labelled as Extraneously Induced Excitations (EIEs), Instability-Induced Excitations (IIEs) and Movement-Induced Excitations (MIEs). A corresponding categorization is detailed in Fig. 3.2. This is best showcased linked to body oscillators, which are simplified representations of common structural types and their dominant response. Main directions are to be distinguished. Additionally, a row of plots show the time-history of the amplitude $A_{xy}(t)$ for a given mean velocity V_x^{mean}. Another row highlights the dependency of this amplitude on various ranges of the velocity. To obtain these insights, it is relevant to consider the evolution of the fluctuating component as either the Root Mean Square (RMS) value or the Standard Deviation (SD). Structural response depends on several factors. First, the characteristics of the flow, particularly the wind velocity spectrum, are crucial. Corresponding forces arise primarily from the shape of the bodies, initially considered motionless and undeformable. Aerodynamic admittance defined these. Additionally, the response is affected by the spectrum of the applied action and the properties of the structure, linked through mechanical admittance. Both connections act as filters, one based on geometry and the other on mechanical aspects. Davenport (1964) proposed a model for along-wind flow, corresponding forces and resulting response. Fig. 3.3 presents this relation, whereby the upper row shows the time-based dependence (marking the mean and SD), whereas the lower part includes the characterization in frequency domain, using the Power Spectral Density (PSD). According to Parseval's Theorem, the square of SD in the time-signal is equal to the area under the curve in the spectral representation, which is a statement of conservation of energy. The actual depiction has to be interpreted based on how the results were scaled.

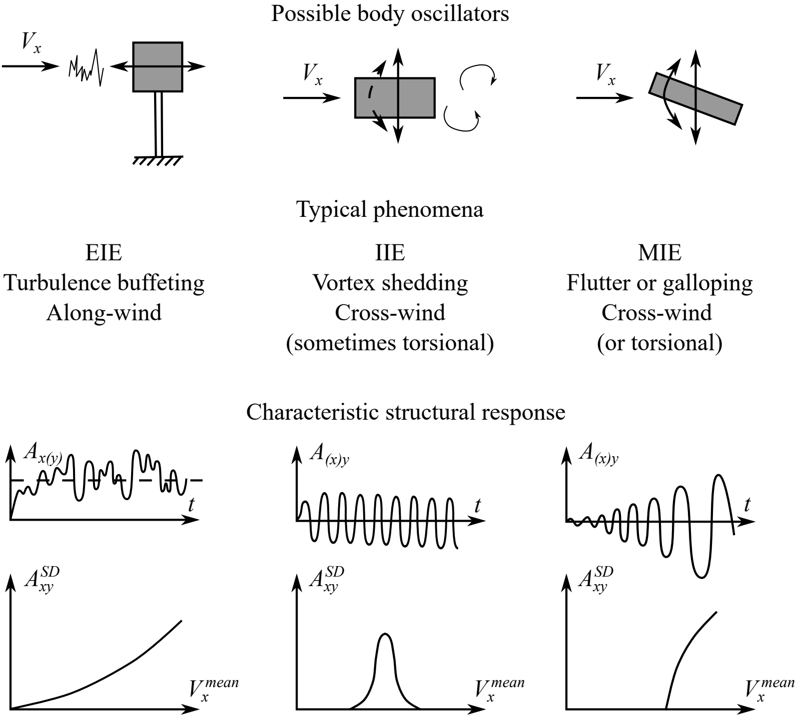

Figure 3.2: Categorization of structural response in case of Flow-Induced Vibrations (FIVs), based on Naudascher and Rockwell (1994, Ch. 1) and Davenport and Novak (2002).

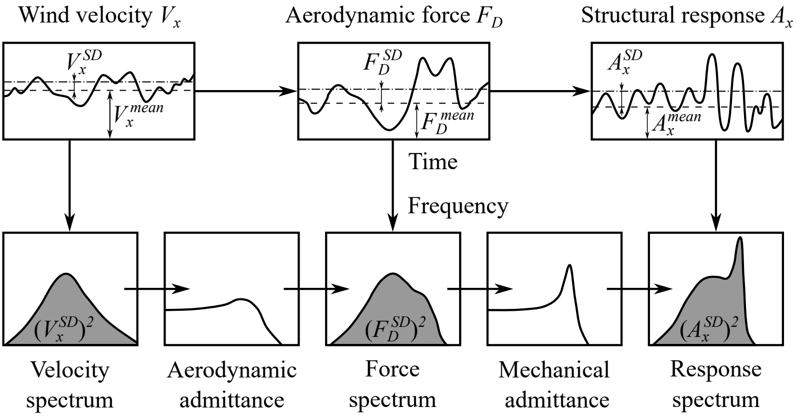

Figure 3.3: Along-wind response chain, as proposed by Davenport (1964).

Previous content presented responses categorized as if these would tend to happen separately. According to Strømmen (2006, Ch. 1), for most civil engineering structures corresponding phenomena occur at their strongest in fairly separate wind velocity regions. This is rather a matter of convenience in thought and representation, as various excitation mechanisms can interfere and overlap. Fig. 3.4 connects all velocity regions, indicating the critical velocity V_x^{crit} for the onset of instability, as well as the value for resonance V_x^{res}. While here only one location for the latter is marked, multiple such peaks can exist for various lower eigenmodes. The depiction also highlights that the response can be split into a time-invariant (quasi-steady or -static) and a fluctuating (dynamic) part. This division is possible, as design scenarios for ABL-type flow conditions reach statistic stationarity. Additional considerations are needed for special wind conditions, i.e. non-synoptic (tornadoes, downbursts, etc.) scenarios.

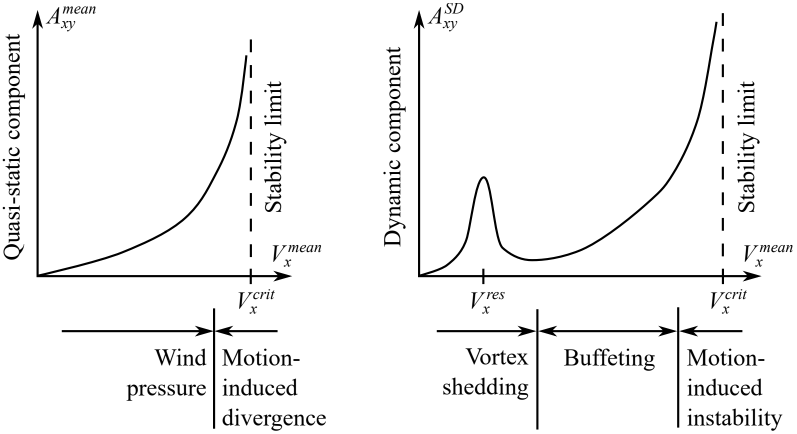

Figure 3.4: Static and dynamic response, with velocity regions distinguished, adapted from Strømmen (2006, Ch. 6).

Strong vortex shedding tends to be pronounced in low atmospheric turbulence. Moreover, the characteristic frequency range is narrow, which is different from typical conditions of ABL flow conditions. The spectral content is compared in Fig. 3.5, highlighting the differences in frequency content (wide versus narrow) and using the surface roughness length z_0 for normalizing. Common values are linked to the inverse wavelength, which in turn can be connected to reference length scales. Here, the height of a building H or the length L characterizing its surroundings can be decisive for approaching flow, whereas the cross-sectional dimension B or a generic diameter D will influence shedding.

This narrow-banded excitation due to vortex shedding will hold further interest. The Strouhal number St defines the dimensionless frequency. For this purpose, the excitation force (lift for bluff-body aerodynamics, acting cross-wind) can be assumed to be a pure harmonic, an accepted simplification according Simiu and Yeo (2019, Ch. 19). In Eqs. (3.7), (3.8), and (3.9), the definitions are shown:

$$St = \frac{f_{sh} D}{V_x}, \tag{3.7}$$

$$\omega_{sh} = 2\pi f_{sh}, \tag{3.8}$$

$$F_L(t) = \frac{1}{2} \rho A^{ref} V_x^2 C_L \sin(\omega_{sh} t). \tag{3.9}$$

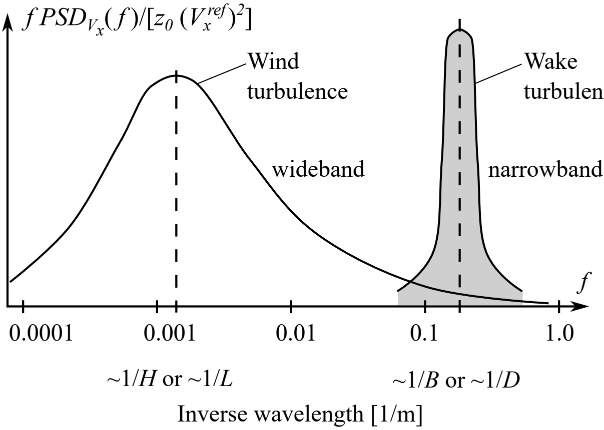

Figure 3.5: Universal spectrum for along-wind (ABL turbulence) and cross-wind (wake turbulence) fluctuations, according to Davenport and Novak (2002).

The amplitude of the acting force is denoted as C_L in Eq. (3.9). Certain specialized approaches for cross-wind response assume this to be $C_L^{RMS}(t)$. These represent the basic models for typical design, based on norms and standards. Once a body oscillator starts vibrating, motion-dependent changes will occur. Thus, a purely aerodynamic scenario will need considerations from aeroelasticity. Lock-in will exhibit itself such that shedding rate above the natural frequency of the structure will remain at the value defined by the latter, within a considerable range (order of magnitude +20% possible), as in Fig. 3.6. Here, a clear distinction between classical mechanical resonance and that caused by wind-induced vortices on slender structures is remarked on. More advanced considerations are covered by Vickery and Basu (1983) and Ruscheweyh (1990).

The normalized amplitude of the cross-wind response A_y^{SD}/D depends on the Scruton number Sc, a parameter symbolizing dimensionless mass characterizing a vibration mode, as shown in Eq. (3.10). Herein, $m_{i,e}$ is the equivalent generalized mass (per unit length) for a certain mode shape i and δ the logarithmic decrement for damping:

$$Sc = \frac{2\delta m_{i,e}}{\rho D^2}. \tag{3.10}$$

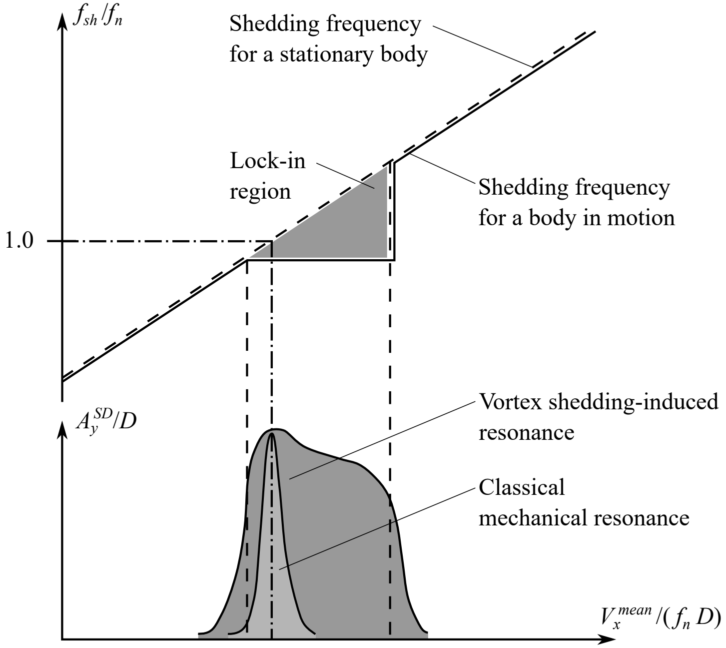

Figure 3.6: Lock-in of an oscillating cylinder, adapted from Ruscheweyh (1994).

Kwok (2013) propose a relation specifically for the fluctuating component characterizing the shedding force F_{sh}^{fluct}. Eq. (3.11) introduces a particular coefficient, C_{sh}, as follows:

$$F_{sh}^{fluct}(t) = \frac{1}{2}\rho A^{ref} V^2 C_{sh} \sin(\omega_{sh} t). \tag{3.11}$$

This is nonlinear and depends on multiple parameters: cross-sectional shape, level of turbulence, magnitude of deformation, and operating velocity. The discussion in this thesis continues assuming the simplified, linear relation.
I have highlighted the narrow-banded nature of cross-wind excitations due to vortex shedding. The next steps focus on this specific aspect and how it can be mitigated, including what role numerics play in it. In a general sense, there are three standard approaches for counteracting WIVs, as summarized in Fig. 3.7. The usage of added devices will be further detailed.

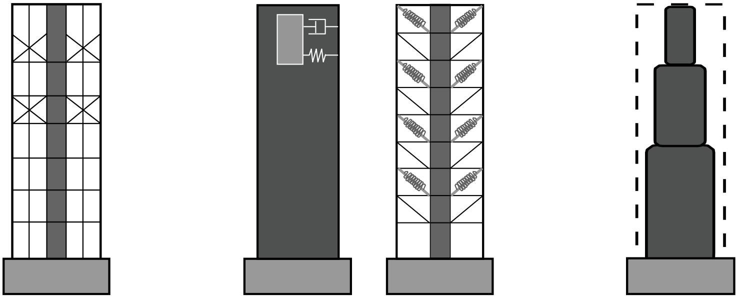

Structural system modifications

Auxiliary damping devices

Aerodynamic modifications

Figure 3.7: Measures to mitigate WIVs, adapted from Kareem et al. (2013).

It is important to note the frequently interchangeable usage of WIVs and FIVs. While they share many similarities, key differences arise depending on the context and the specific phenomena being described. The former term primarily characterizes usage in this work, whereas the latter refers more broadly to oscillations induced by any fluid (liquid or gas), including those related to internal flows, such as in pipes.

3.1.2 Structural response of body oscillators

The response of structures subject to wind is complex yet can be represented using simplified models in many scenarios. In case of dynamic loading, preliminary thoughts based on modal analysis and decomposition can assist appropriate choices. These typically highlight which mode shapes are relevant to capture, making a considerate contribution to how the real construction would react. Fig. 3.8 shows that common structures including tall buildings and long bridges can be modeled as continuous beams.

These are characterized by mode shapes, of which the first few are highly relevant due to their contribution to mass participation during oscillations. Ordering usually follows the increase in eigenfrequency. Often, the first mode can be approached by a lumped-mass model. Using this assumption, an equivalency with a Single-Degree of Freedom (SDoF) system can be established. Petersen and Werkle (2017, Ch. 18) provide a consistent approach to set up such a model. It assumes kinetic equivalency between the particular mode shape of the real structure and that of the simplified system. Fig. 3.9 graphically highlights these considerations. The reasoning is that for a given real structure and a selected mode shape, the kinetic energy is computed using Eq. (3.12), considering the mass distribution along the heigh $\mu(x)$, and the amplitude of the mode shape $\eta_i(x)$ during one period T, as shown in:

$$E_{cont}^{kin} = \frac{1}{2}\int_0^L \mu(x)\dot{y}^2(x,t)\,dx. \tag{3.12}$$

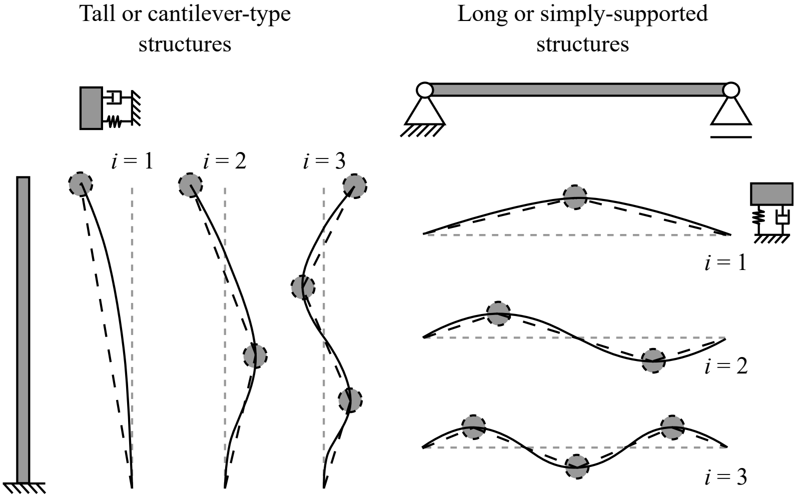

Figure 3.8: Line-like models of typical structures, with continuous eigenmodes and their lumped-mass (piecewise linear) equivalent.

The amplitude of the mode during one oscillation is $y(x,t)$, defined as:

$$y(x,t) = y(x)\sin(\omega_i t) = Y\eta_i(x)\sin(\omega_i t). \tag{3.13}$$

For the SDoF system, the energy content is formulated as:

$$E^{kin}_{equiv} = \frac{1}{2}M\dot{y}^2 = \frac{1}{2}M\left(\frac{Y\sin(\omega_i t)}{dt}\right)^2 = \frac{1}{2}M\omega_i^2 Y^2\cos^2(\omega_i t). \tag{3.14}$$

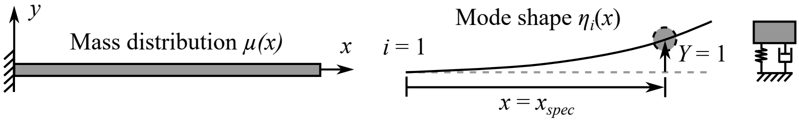

Figure 3.9: From a continuous beam to a kinetically-equivalent SDoF system, adapted from Petersen and Werkle (2017, Ch. 18).

The unknown is the equivalent mass M. A solution is provided by setting an equality between Eqs. (3.12) and (3.14), requiring the amplitude of deformation Y to be the same for both systems. This results in the consistent setup of an SDoF oscillator, representing the kinematics at a specific location x_{spec} for a certain mode shape of a continuous system, showcased in Fig. 3.9. This approach adheres to the reasoning using the generalized modal properties of mass, damping and stiffness (Lago et al., 2018, Ch. 5). The described modeling steps advantageously lead to body oscillators, represented as SDoF systems. Consequently, the focus now shifts to describing such equivalent structures, and analyzing their behavior under harmonic loading. This typically arises from vortex shedding. Fig. 3.10 highlights the model including the amplification curve under external excitation. Eq. (3.15) presents the EoM:

$$m_s \ddot{x} + c_s \dot{x} + k_s x = F_s = F_{s,0} \sin(\omega_{ext} t). \tag{3.15}$$

m_s, c_s and k_s represent the structural properties of mass, (equivalent viscous) damping and stiffness. This is excited by a harmonic force of amplitude F_0 and angular frequency (also known as pulsatance) ω_{ext}. Eq. (3.16) leads to the angular frequency $\omega_{n,s}$ and frequency $f_{n,s}$ of the structure:

$$\omega_{n,s} = 2\pi f_{n,s} = \sqrt{\frac{k_s}{m_s}}. \tag{3.16}$$

Additionally, c_{crit} denotes the critical damping, $x_{s,0}$ the (stationary) amplitude of the harmonic response, whereas $x_{s,static}$ is the static deflection considering the force $F_{s,0}$ and stiffness k_s.

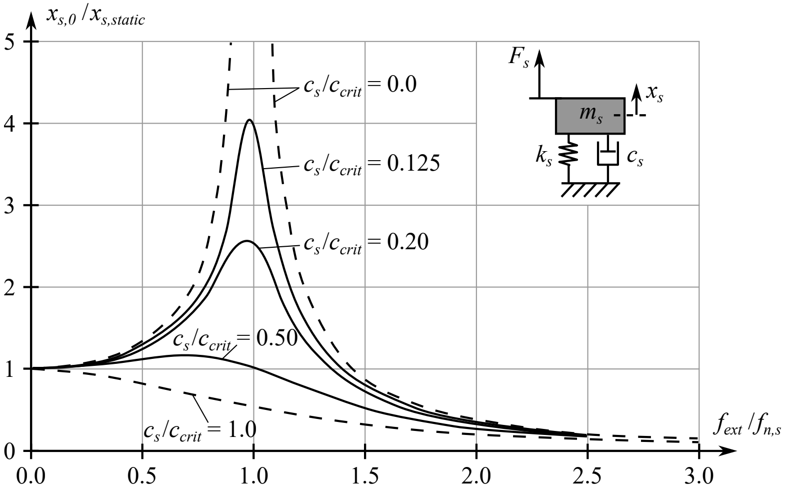

Figure 3.10: Dynamic amplification of the response for an SDoF system, according to Den Hartog (1985, Ch. 2).

Extending the SDoF to a Two-Degree of Freedom (TDoF) model by adding a rigid body oscillator represents the basis of added damping devices. The coupled behavior is highlighted by the amplification curve, as in Fig. 3.11. Here, only the original SDoF is still excited by a harmonic force. The added device is directly linked to this but does not undergo any outside influence. Essentially, it is subject to the movement of its base, as described in Eq. (3.17).

$$\begin{cases} m_s\ddot{x}_s + \left(c_s + c_d\right)\dot{x}_s - c_d\dot{x}_d + \left(k_s + k_d\right)x_s - k_d x_d & = F_{s,0}\sin\left(\omega_{ext} t\right) \\ m_d\ddot{x}_d + c_d\dot{x}_d - c_s\dot{x}_s + k_d x_d - k_s x_s & = 0 \end{cases} \tag{3.17}$$

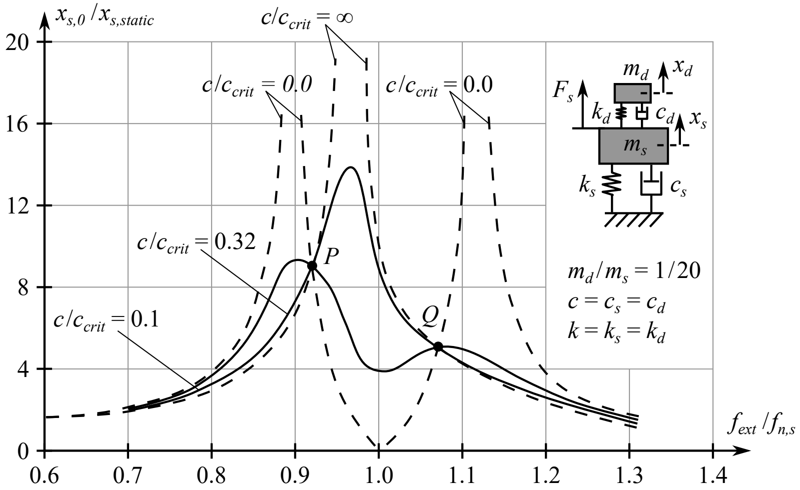

Figure 3.11: Dynamic amplification of the response for a TDoF system, according to Den Hartog (1985, Ch. 3).

Den Hartog (1985, Ch. 3) and Petersen and Werkle (2017, Ch. 18) note the importance of points P and Q through which all curves pass. Finding the optimal parameters for a TDoF setup relies on optimizing the location of these points. Both referenced works provide a detailed workflow and particular values depending on the maximum type of mitigation to be achieved. These lead to the dimensioning of a TMD, also called a Dynamic Vibration Absorber (DVA).

3.1.3 Partitioned numerical solutions

The goal is to find a proper numerical solution strategy to solve the EoM for a TDoF system. This is best represented by the matrix form in Eq. (3.18), which is an alternative for the relations in Eq. (3.17). It is an inhomogenous linear system of second-order ordinary differential equations. This monolithic formulation can be solved trivially.

$$\begin{bmatrix} m_s & 0 \\ 0 & m_d \end{bmatrix}\begin{pmatrix} \ddot{x}_s \\ \ddot{x}_d \end{pmatrix} + \begin{bmatrix} c_s + c_d & -c_d \\ -c_d & c_d \end{bmatrix}\begin{pmatrix} \dot{x}_s \\ \dot{x}_d \end{pmatrix} + \begin{bmatrix} k_s + k_d & -k_d \\ -k_d & k_d \end{bmatrix}\begin{pmatrix} x_s \\ x_d \end{pmatrix} = \begin{pmatrix} F_{s,0}\sin\left(\omega_{ext} t\right) \\ 0 \end{pmatrix} \tag{3.18}$$

Reorganizing these governing equations leads to Eq. (3.19). On the Left-Hand Side (LHS) both SDoF solvers are present, whereas the Right-Hand Side (RHS) denotes the input forces for each. Here, in addition to the external force $F_{s,ext}$, two further components appear, which are the coupling terms $F_{s,coupl}$ and $F_{d,coupl}$ for the structure and damper, respectively.

$$\begin{cases} \underbrace{m_s\ddot{x}_s + c_s\dot{x}_s + k_s x_s}_{EoM_s} & = \underbrace{F_{s,0}\sin(\omega_{ext}t)}_{F_{s,ext}} \underbrace{-\left(c_d\dot{x}_s + k_d x_s\right) + \left(c_d\dot{x}_d + k_d x_d\right)}_{F_{s,coupl}} \\ \underbrace{m_d\ddot{x}_d + c_d\dot{x}_d + k_d x_d}_{EoM_d} & = \underbrace{\left(c_d\dot{x}_s + k_d x_s\right)}_{F_{d,coupl}} \end{cases} \tag{3.19}$$

The kinematics of both bodies are time dependent, such that $x_s = x_s(t)$, and $x_d = x_d(t)$. The same holds for the external $F_{s,ext} = F_{s,ext}(t)$ and coupling forces $F_{s,coupl} = F_{s,coupl}(t)$, $F_{d,coupl} = F_{d,coupl}(t)$. A partitioned approach assumes solving for the two SDoF systems separately. In a time-discrete setting, one can apply the Jacobi procedure or follow the Gauss-Seidel approach (Ford, 2014, Ch. 20) for iterating. The latter provides faster convergence as the intermediate solutions are already used. Coupling forces represent the unknowns, for which these inner iterations are needed.Respective flow charts for possible solution procedures are provided in Fig. 3.12.

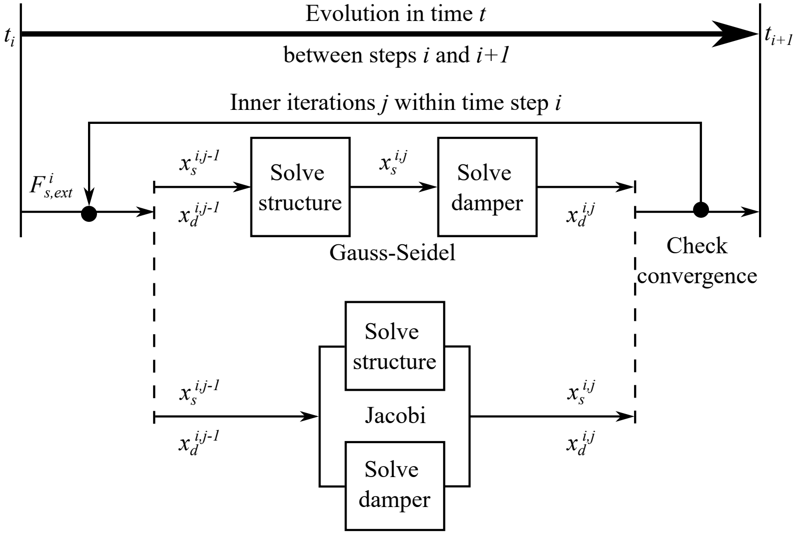

Figure 3.12: Time-stepping and inner iterations in case of a partitioned solution.

Indexing time steps with i and internal loops by j, the relations (here checking absolute difference) are shown in Eq. (3.20):

$$\begin{aligned} (a) \quad &\Rightarrow \quad EoM_s^{i,j} = F_{s,ext}^{i} + F_{s,coupl}^{i,j-1}, \\ (b) \quad &\Rightarrow \quad EoM_d^{i,j} = F_{d,coupl}^{i,j}. \end{aligned} \tag{3.20}$$

The solution is to be deemed converged once the residual of (coupling) forces or displacements for t^i between interim iterations $(j-1) \rightarrow j$ are below a certain tolerance ε, according to Eq. (3.21):

$$\begin{aligned} \left|F_{s,coupl}^{i,j} - F_{s,coupl}^{i,j-1}\right| < \varepsilon_s^{force} \quad &\text{or} \quad \left|F_{d,coupl}^{i,j} - F_{d,coupl}^{i,j-1}\right| < \varepsilon_d^{force}, \\ \left|x_s^{i,j} - x_s^{i,j-1}\right| < \varepsilon_s^{disp} \quad &\text{or} \quad \left|x_d^{i,j} - x_d^{i,j-1}\right| < \varepsilon_d^{disp}. \end{aligned} \tag{3.21}$$

These partitioning steps clearly show various considerations in splitting physics and solving systems separately. For the particular case of a TDoF, it should be viewed as an exercise to highlight such aspects. Nonetheless, the strength lies in the generality of the method. Fig. 3.12 depicts the time discrete iteration, as well as the inner loop needed to achieve the numerical equilibrium between two segregated solvers, which can be seen as black box systems. The Jacobi and Gauss-Seidel approaches use similar input and output types. These will be different in actual value for a specific iteration, as convergence will be achieved at different rates. Using the notation in the flowchart does not explicitly highlight this property. It should be observed that the scheme is almost identical to that in Fig. 2.2. This is generally assumed in multiphysics for the numerical solution strategy of coupled problems, which will permit the extension to multiple solvers and various nesting combinations.

3.2 Research and development

My contributions aim at showcasing a developed framework, in an initial step ensuring the proof of concept, whereas the versatility is revealed on a complex setup. Methodologically, multiply-partitioned schemes are of interest. Coupled phenomena are often approached with an attempt to simplify treatment by identifying subsystems and focusing on these separately. There is a physical (Felippa et al., 2001) and mathematical reasoning for this. Wind flow patterns and structural motions can be viewed and modeled on their own, as can any additional devices enriching such a setup. The governing equations are formulated in a particular way for each of these components. While CSM is mainly interested in the deformation in time, CFD captures the deformation rate on a fixed grid. The linearized solution is provided by solving a system of equations. Appropriate matrices usually depict each physical system separately, even if a monolithic large system could be built. The reasons for decomposition are manyfold. In multiphysics, computational approaches tend to favor well-conditioned matrices for fast and robust solving. This can imply a separation based on the type of variables (and magnitude of the numerical entries), such as pressures and velocities for fluids (Hines, 2008). Rotations and displacements could represent a similar reasoning in case of structures. Partitioning is also be relevant when running on distributed memory systems, as a result of domain decomposition. Equilibrium still needs to be achieved in a global sense for the entire system. This leads to various coupling considerations and appropriate technical solutions.

In my work, I highlight key concepts and results in the domain of vibration mitigation. An exemplary wind flow setup was chosen, with loading arising on a generic highrise. Conditions and the respective building geometry were selected to trigger specific types of oscillation patterns. The investigation covered simplified models as well as well-detailed ones. Functioning of the partitioned scheme on HPC systems was revealed by examining the mitigation efficiency of various added devices.

3.2.1 Definition and modeling of the wind flow

Wind flow is defined based on the prescriptions for the Commonwealth Advisory Aeronautical Research Council (CAARC) study (Wardlaw and Moss, 1970; Melbourne, 1980). Herein, two scenarios were proposed, of which the setup for *Building B* (International Association for Wind Engineering, 2007) is chosen. This implies a rectangular, generic tall building in appropriate flow conditions for a suburban terrain. The study was designed and is still often used to validate experimental and numerical approaches. Structural behavior is only described by the density and the main vibration characteristics, namely the type of mode and the fundamental frequencies for weak bending, strong bending and torsion. Fig. 3.13 summarizes the setup.

A CFD study was established as part of this work to ensure realistic flow conditions. The base scenario is of ABL turbulent wind, as originally prescribed by the study, with the AoA of interest being 0°. On the wide face of the building, the incoming fluctuations are expected to lead to larger forces. At the reference height $h^{ref} = 180\,\mathrm{m}$, mean speeds of up to $V_x^{mean} = 40\,\mathrm{m/s}$ are to be accounted for. This

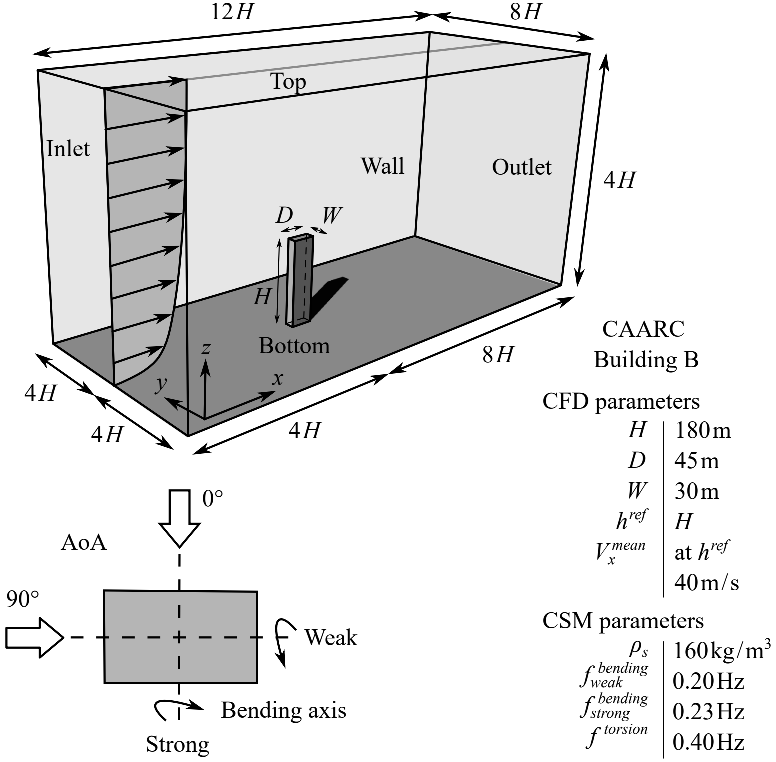

Figure 3.13: Showcasing the simulation setup for the CAARC Building B.

is accompanied by the streamwise turbulence intensity $TI_{V_x} = 14\,\%$ and the integral turbulence length scale $L_{V_x} = 175\,\text{m}$. A modified case only captures the mean velocity profile, with practically zero upstream turbulence for the building. Moreover, this profile is increased to the point to trigger resonance, leading to a characteristic mean velocity that is approximately double the original considerations, at almost $V_x^{mean} = 80\,\text{m/s}$. For this latter scenario, the turbulence intensity is zero, whereas the length scale is very high (in theory up to infinity). An AoA of 90° should lead to strong oscillations around the weak bending axis. The outcome of CFD simulation in an empty channel is depicted in Fig. 3.14. This includes the evaluation of the turbulent energy spectrum at the reference height, marking the cutoff frequency at $f^{co} = 1\,\text{Hz}$, as well as noting the target Kaimal spectrum (Kaimal et al., 1972) in the lower-right subplot. Data represents $t = 200\,\text{s}$ of simulation duration for the smooth flow, and $t = 600\,\text{s}$ for the ABL turbulent conditions, after an initial ramp-up phase. Dots indicate the previously mentioned reference values for mean velocity, turbulence intensity, and integral turbulence length scale.

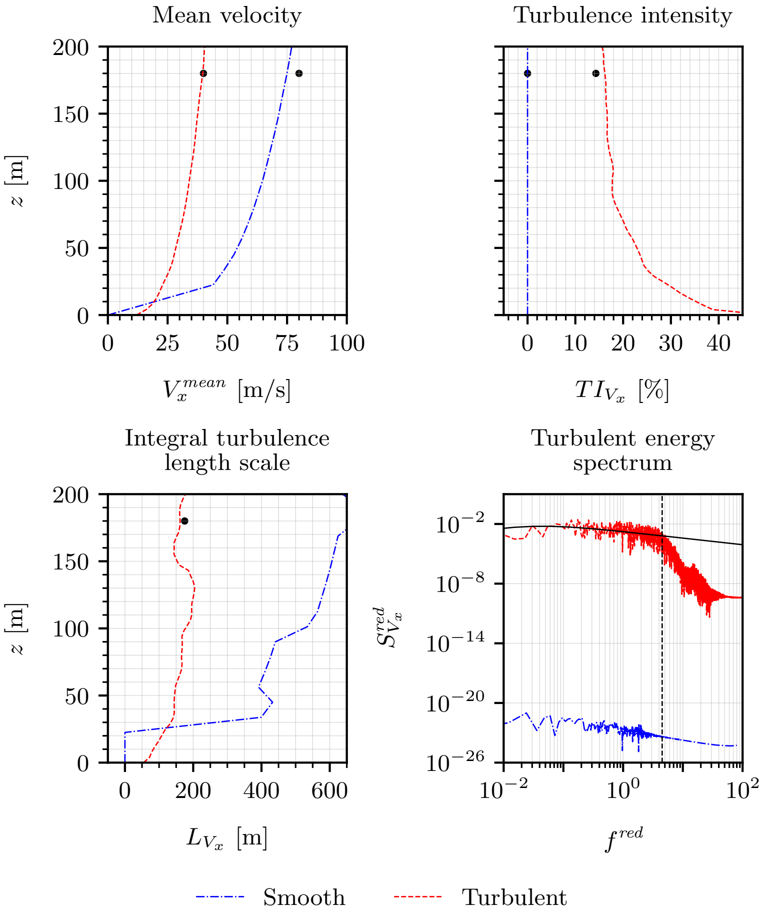

Figure 3.14: Flow parameters under smooth and ABL turbulent conditions.

Turbulent energy is shown in a spectral representation, with a normalized axis. The reduced frequency f^{red} is defined as:

$$f^{red} = \frac{f h^{ref}}{V_x^{ref}}, \tag{3.22}$$

with the reduced power spectrum for the streamwise velocity $S_{V_x}^{red}$ obtained by:

$$S_{V_x}^{red} = \frac{f S_{V_x}}{\left(V_x^{ref}\right)^2}. \tag{3.23}$$

3.2.2 Investigated prototypical structural models

Various structural models were considered as part of the investigation. During the initial phase, the aim was to trigger resonance around the weak bending axis. For this, the building was modeled in a three-dimensional space with solid elements, once using plane shells, even with further reductions to a beam model as well as an SDoF oscillator. All were chosen to reproduce the weak bending characteristics. This line of thought is shown in Fig. 3.15.

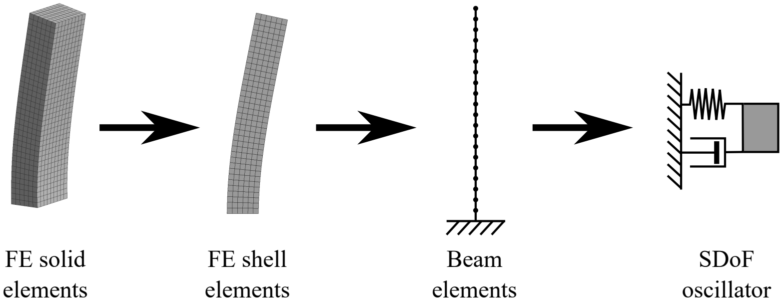

Figure 3.15: Investigated model hierarchy according to the FEM, adapted from Péntek et al. (2018).

Model simplification as in Fig. 3.16 implies reproducing the main structural characteristics while reducing the geometrical complexity of the element types. Conversely, during this process the number of assumptions increases, and the numerical formulation for a four-node tetrahedron is more straightforward than the similar relations for beam element. Nonetheless, the usage of line-like models in structural engineering is widespread.

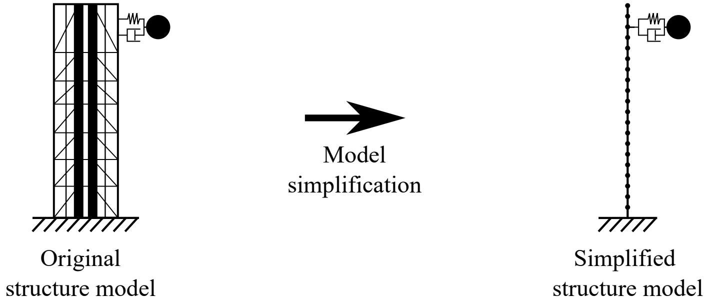

Figure 3.16: Structural model simplification during the investigation, adapted from Péntek et al. (2018).

It is crucial to follow appropriate steps to maintain the target modal behavior. A properly normalized eigenform of a more complex model serves as the basis in setting up a simpler one. This process is described in Sec. 3.1, with the main steps highlighted in Fig. 3.17. This depiction shows the inclusion of an Added Mass Damper (AMD) as the main reason for the developments.

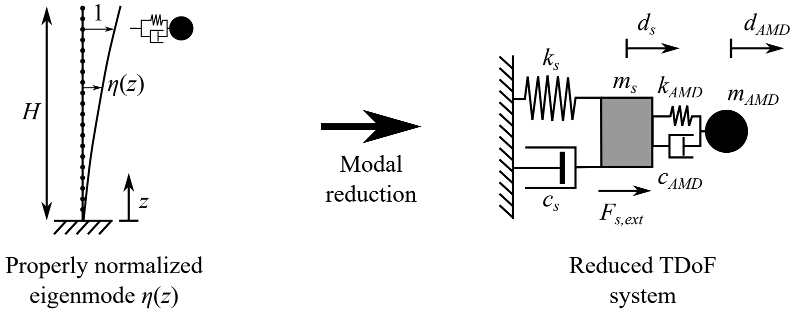

Figure 3.17: Modal reduction during the investigation, adapted from Péntek et al. (2018).

3.2.3 Multiply-partitioned schemes

Partitioning in multiphysics is further detailed, starting with the example of FSI. Hereby, the interaction between fluid and structure has to be addressed at a conceptual level. Additional insights related to the symbolic representation of the complementing linear system are included, as in case of the monolithic formulation in Fig. 3.18. The physical fields are color-coded, and the properties of the model comprise the total stiffness k, primarily from the structure, and the damping c, mostly attributed to the fluid. The variable m represents the total mass in motion, with its characteristic deformation over time denoted as $d(t)$.

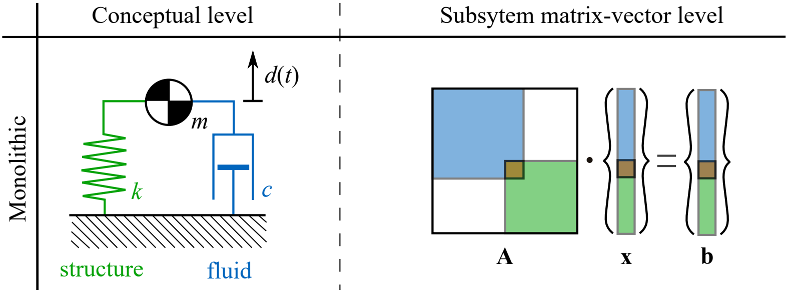

Figure 3.18: One-dimensional model consideration for the monolitic formulation of two physical subsystems, adapted from Dettmer et al. (2015) and Winterstein et al. (2016).

Whereas the monolithic view implies considering this system as a whole, a partitioning leads to a clear interface between the split subsystems. Dedicated coupling is now needed to ensure the equilibrium, as hinted in Fig. 3.19.

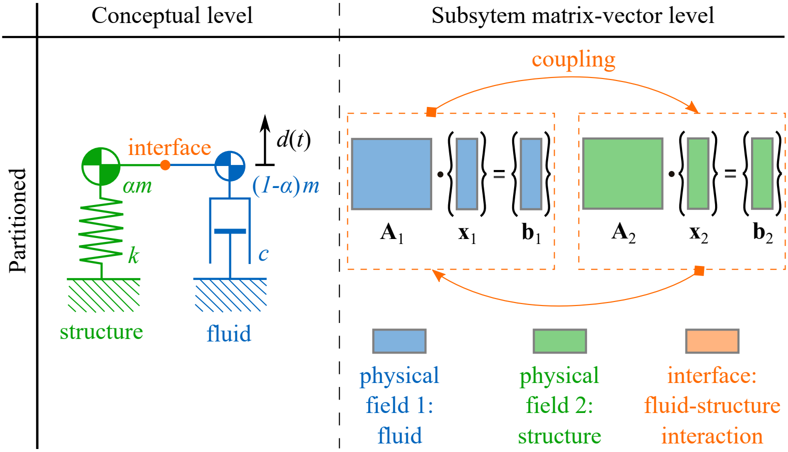

Figure 3.19: One-dimensional model consideration for partitioning two physical subsystems, adapted from Dettmer et al. (2015) and Winterstein et al. (2016).

Bungartz et al. (2015) also refer to this type of partitioned scheme as bi-coupling. The subdomains can be fluid and structure as well as structure and AMD. Various possibilities exist for combining three systems. However, in the current work, the encapsulation shown in Fig. 3.20 is adopted.

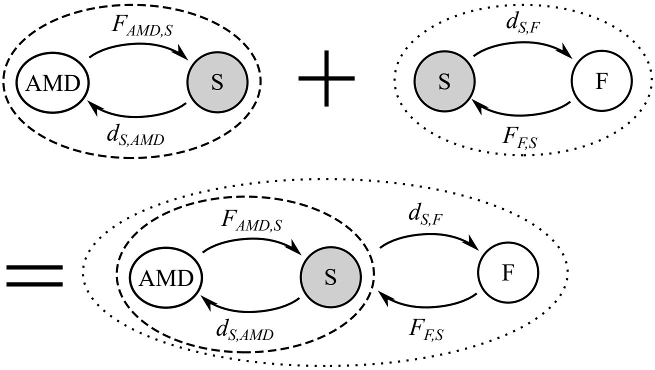

Figure 3.20: Expansion of bi-coupling through inclusion into multi-coupling, adapted from Bungartz et al. (2015).

A practical reason would be that the fluid acts on the outer hull of the structure, whereas the added devices could be seen as an extension inside the structure. Moreover, the outer loop for FSI is computationally more demanding, which results in favoring less of such iterations. Data needs to be transferred in between, with F generically noting force and d displacement, with the subscripts remarking the specific subsystems.

Partitioning into three physical subsystems is highlighted by expanding the previous one-dimensional problem, as shown in Fig. 3.21. The number of interfaces increases, with the structure now communicating alternately with the fluid and the AMD. This setup introduces both inner and outer iterations through encapsulation, as depicted in Fig. 3.20.

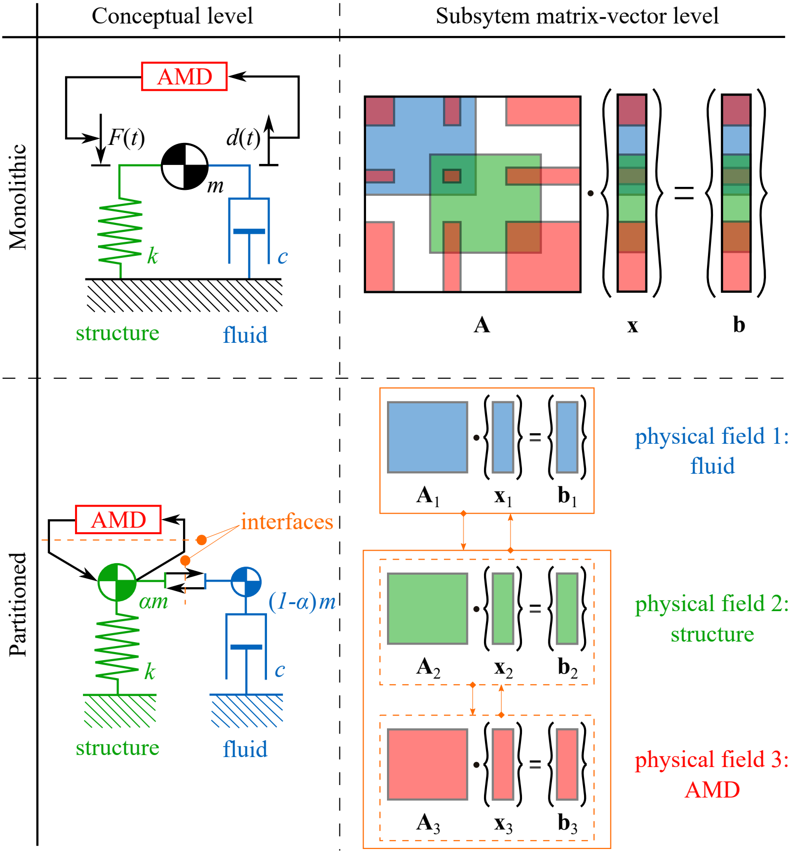

Figure 3.21: One-dimensional model consideration for partitioning three physical subsystems.

3.2.4 Proof of concept for a prototype

The baseline study considers the prototype, i.e. the CAARC Building B, at 90° AoA with flow conditions to trigger resonance around the weak bending axis. Along- and cross-wind moments are shown for CFD and FSI, respectively, in Fig. 3.22. The results for the latter component substantiate an interaction that tends to increase the arising forces, thereby supporting the use of FSI for investigating wind-induced resonance and lock-in. Not only does the magnitude of the bending moment increase, but the frequency of it also exhibits a more distinct harmonic pattern. These characteristics can be accurately assessed computationally, provided that the movement of the structure is modeled and captured, which is not achievable with pure CFD alone. A vertical dashed line at $t = 25\,\mathrm{s}$ denotes the end of the ramp-up for the inlet velocity.

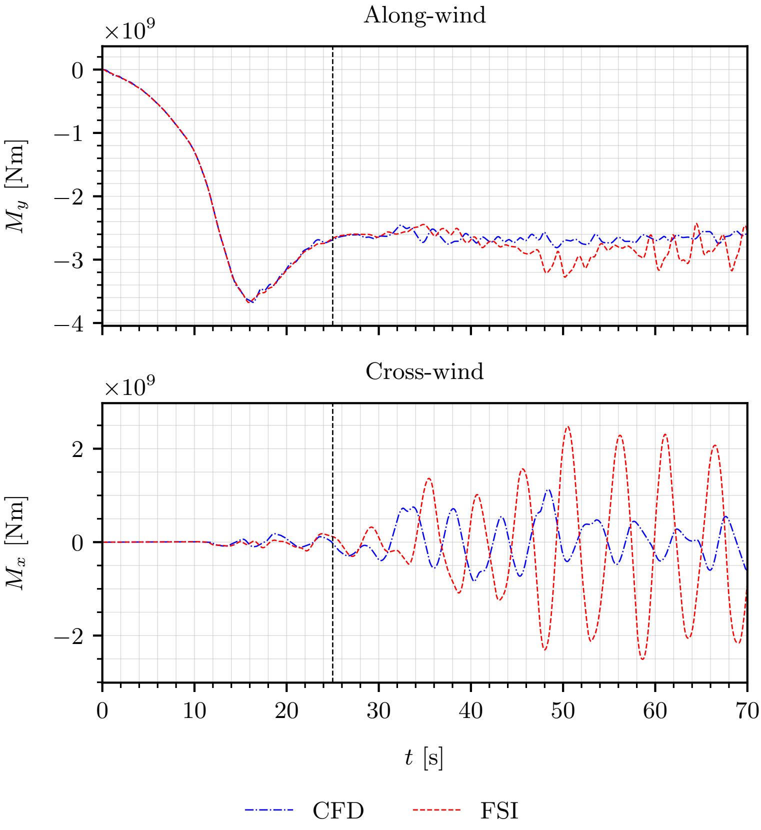

Figure 3.22: Comparing the aerodynamic moments in case of CFD and FSI.

Moments acting on the structure and respective displacements over time are shown in Fig. 3.23. The structure without any damping devices is considered as a baseline, with amplitude growing unboundedly as part of the resonant amplification in lack of structural damping. Such an assumption was considered to trigger the worst case scenario. Both added devices, a TMD and a Semi-Active TMD (SATMD), perform well, limiting oscillation similarly to a reasonable degree.

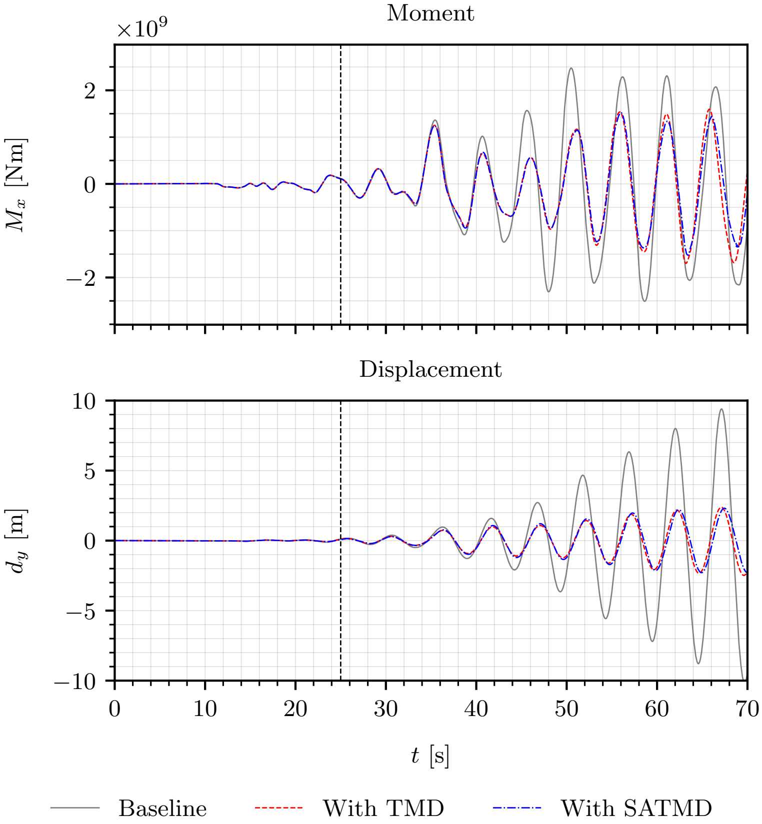

Figure 3.23: Evolution of the aerodynamic moment as well as displacement of the point of connection in cross-wind direction, during an FSI simulation.

3.2.5 Generic inclusion of added devices

Exploratory steps substantiate the ability to generically include any type and potentially number of devices. The respective conditions are provided by the robust and flexibly numerical framework. This has practical implications, as various design scenarios may include multiple additional dampers. Such a situation can arise when splitting the amount of added weight for Tuned Liquid Dampers (TLDs) over multiple floors, or counteracting the vibrations of a bridge spanning several openings. Fig. 3.24 visually aids this consideration.

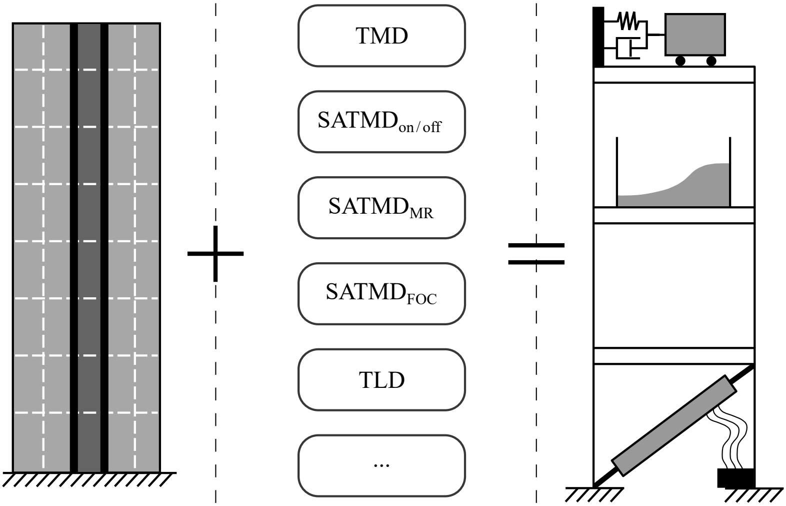

Figure 3.24: Possibility of coupling various types of AMDs and multiple devices concurrently*.

Including a TMD into a computational structural model can be straightforward and may not require a dedicated partitioned approach. Nonetheless, considering either more complex devices, or with the aim of not directly modifying existing structural models, coupling subsystems is a proper way to proceed. In particular, devices with vastly different governing equations, such as sloshing motion in case of TSDs, can be adequately handled with partitioning. The basic definition of a container filled with liquid is presented in Fig. 3.25. Multiple numerical models permit capturing sloshing waves as described by the evolution of the wave height in time $h(x,t)$ inside a container of dimensions $L \times W \times H$. These range from shallow water theory over particle methods to so-called two-fluid CFD approaches. My research focuses on the latter, as thoroughly described in Péntek et al. (2022). The setup was thereby enhanced to counter vibrations along two perpendicular axes. Modeling was achieved by superposing the effect along each direction

---

* SATMDs may imply solutions based on Magnetorheological (MR) dampers or Fractional-Order Controllers (FOCs).

contributed by a dedicated TMD or TSD. An exemplary placement is shown in the horizontal plane, with devices located inside the building at a top floor, as in Fig. 3.26.

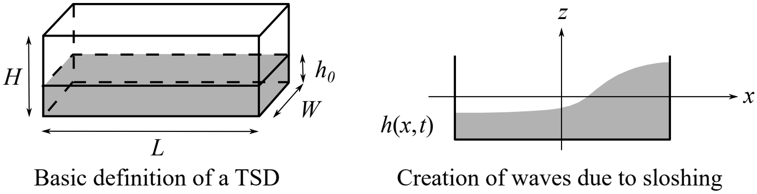

Figure 3.25: Brief definition of a TSD.

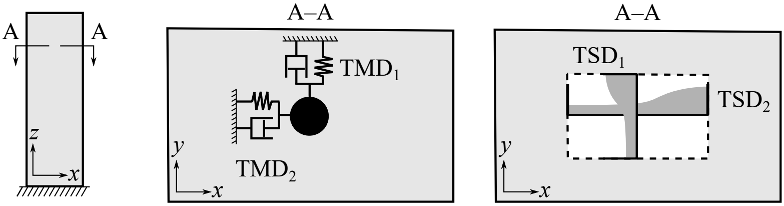

Figure 3.26: Placement of multiple TMDs or TSDs in a plane view, adapted from Péntek et al. (2022).

3.2.6 Case study on a complex setup

The complex setup implied appropriate wind conditions at high spatial and temporal resolution. Similarly, instead of a generic structure discretized by either purely solid, shell or beam elements, a detailed model was established. Respective efforts ensured that the developments were not only tested in a limited scope and under heavily simplified circumstances, but in conditions with practical relevance. The reaction of the highrise building is depicted by the arising bending moments. Fig. 3.27 substantiates the notion that for the along-wind direction no significant energy content can be observed, with the vertical lines simply marking the bending modes 0.20 Hz and 0.23 Hz. Conversely, cross-wind reactions in the form of moments have notable energy content for 0.08 Hz and 0.20 Hz, the latter of which coincides with the lowest eigenmode in case of smooth flow. It should be noted that the orientation of the building for the ABL turbulent conditions is 0° AoA, i.e. with flow perpendicular to the wide face. For smooth flow, the structure is rotated by 90°, with wind parallel with the wide side. The magnitude of bending moments are shown as a function of frequencies resulting from the Fast Fourier Transform (FFT).

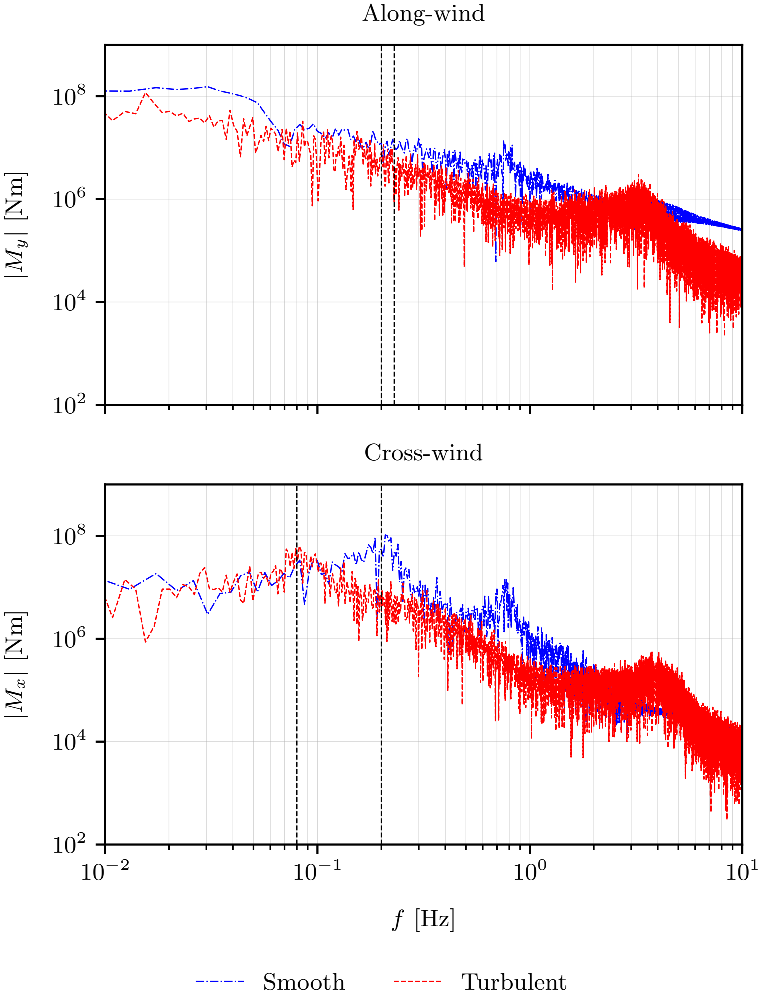

Figure 3.27: Comparison of aerodynamic moments under smooth and ABL turbulent conditions.

Structural accelerations at the top of the building represent a metric to highlight the performance of various AMDs. Vibration mitigation can be seen in the time domain in Fig. 3.28. Qualitatively, both devices reduce peak oscillations to a similar degree.

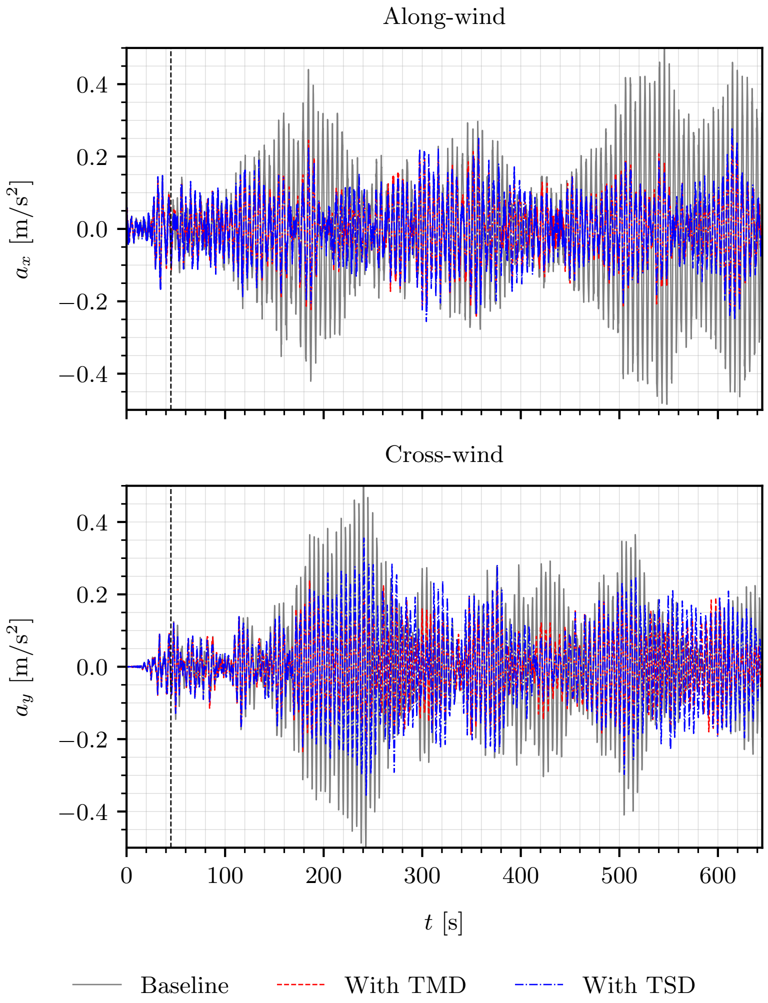

Figure 3.28: Comparison of structural accelerations under ABL turbulent flow conditions.

Tab. 3.1 summarizes the performance in case of upstream turbulence. Here, the TMD and TSD result in comparable outcomes, with the former performing marginally better in cross-wind, as measured by the RMS and max of the time series. This relatively good efficiency is obtained despite the broadband nature of the incoming flow.

Table 3.1: Statistics of the accelerations of the top point under ABL turbulent flow conditions.

Case		Along-wind [m/s^2]			Cross-wind [m/s^2]		
		Mean	RMS	Max	Mean	RMS	Max
Baseline		0.00	0.17	0.52	0.00	0.16	0.47
With TMD		0.00	0.08	0.23	0.00	0.08	0.25
Diff. to baseline	[%]	*0.0*	*−52.9*	*−55.8*	*0.0*	*−50.0*	*−46.8*
With TSD		0.00	0.08	0.25	0.00	0.11	0.33
Diff. to baseline	[%]	*0.0*	*−52.9*	*−51.9*	*0.0*	*−31.3*	*−29.5*
Diff. to TMD	[%]	*0.0*	*0.0*	*8.7*	*0.0*	*37.5*	*32.0*

The added devices are tuned to mitigate a particular frequency, with the optimal parameters depending on the targeted performance measure. Whether minimizing displacements, velocities or accelerations, slightly different recommendations apply (Petersen and Werkle, 2017, Ch. 18). Accelerations in time are provided in Fig. 3.29. While along-wind values are only slightly reduced, the highest mitigation is achieved for cross-wind oscillations under practically turbulence-free inflow conditions. In Tab. 3.2, the outcome is summarized quantitatively. Herein, the evaluation substantiates the TMD achieving almost twice as good a performance, whereas both devices critically mitigate vibrations.

Table 3.2: Statistics of the accelerations of the top point under smooth flow conditions.

Case		Along-wind [m/s^2]			Cross-wind [m/s^2]		
		Mean	RMS	Max	Mean	RMS	Max
Baseline		0.00	0.24	0.72	0.00	2.58	7.75
With TMD		0.00	0.10	0.30	0.00	0.21	0.62
Diff. to baseline	[%]	*0.0*	*−58.3*	*−58.3*	*0.0*	*−91.9*	*−92.9*
With TSD		0.00	0.18	0.53	0.00	0.41	1.22
Diff. to baseline	[%]	*0.0*	*−25.0*	*−26.4*	*0.0*	*−84.1*	*−84.3*
Diff. to TMD	[%]	*0.0*	*80.0*	*76.7*	*0.0*	*95.2*	*96.8*

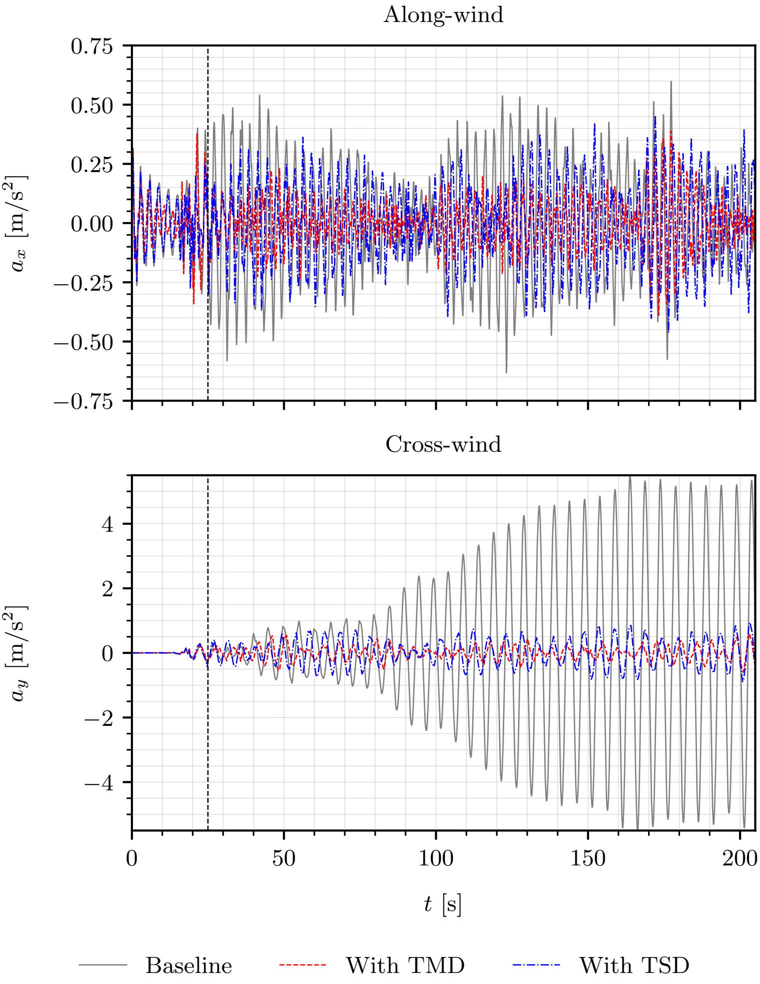

Figure 3.29: Comparison of structural accelerations under smooth flow conditions.

All of the developments happened aligned to requirements of modern programming and HPC. Relevant figures for required resources can be seen in Tab. 3.3. In particular, the compute times in CPU-hours are recorded for various simulations. Reproducing smooth flow conditions is approximately half the effort as for the CFD run with ABL turbulence, due to mesh refinement from the inlet to the building. A typical TWC-FSI computation needs at least twice the resources when compared to only modeling the flow. Including AMDs will further increase the effort by up to a factor of two, depending on the actual number of inner iterations and the complexity of the additional subsystem. These numbers are linked to the specific detailing of the models and numerical formulations, as outlined in Tabs. A.1 and A.2.

Table 3.3: Numerical effort required for assessment.

Type of Simulation		CPU-hours
Turbulent wind CFD		12,000
Smooth flow CFD		7,000
Diff. to wind turbulent CFD	[%]	*−41.6*
Smooth flow FSI		15,000
Diff. to smooth flow CFD	[%]	*114.3*
Smooth flow FSI + TMD		23,000
Diff. to smooth flow FSI	[%]	*53.3*
Smooth flow FSI + TSD		32,000
Diff. to smooth flow FSI	[%]	*113.3*

[*] Using MPI distributed memory parallelism on Intel Skylake–Xeon Platinum 8174 processors with a base frequency of 3.10 GHz and 33 MB cache.

A further advantage of the numerical workflow lies in enabling visual insight into multiple aspects of the considered phenomenon. Deformation patterns or stress distributions can be highlighted for the structural model. Wind flow can be shown as statistics or for specific time frames, either as maps for pressures or velocities, or in the form of streamlines. These can help to identify zones of high turbulence. Similarly, in the case of a TSD, the sloshing motion can be captured in multiple ways, such as through wave contours and vorticity or the separation between air and water, which can aid design decisions. Shaping the container by rounding off corners or including vertical slat screens based on the gained insights will help optimize water motion and enhance the damping effect. Some of these potentials are collected in Fig. 3.30.

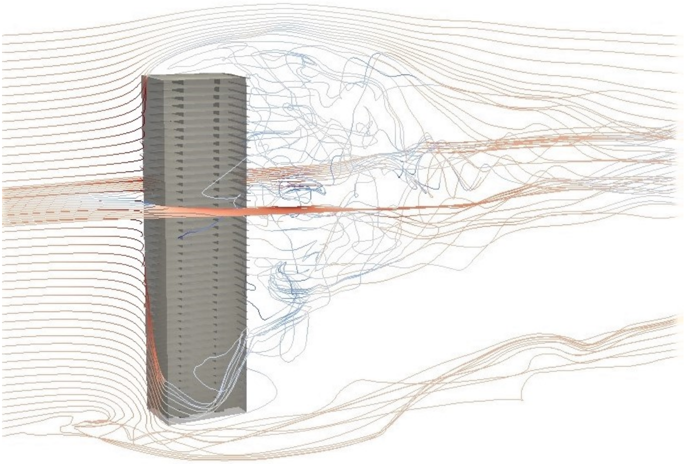

Visualization of the wind flow field using CFD

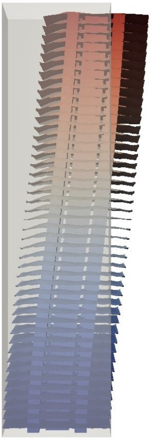

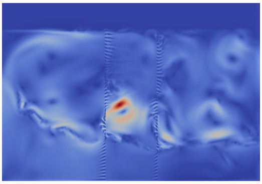

Velocity magnitude

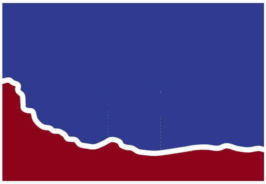

Visualization of the structural deformations using CSD

and density
in the TSD using CFD

Figure 3.30: Showcasing some visualization potentials enabled by computational multiphysics, adapted from Péntek et al. (2022).

3.3 Summary

My research focused on narrowband cross-wind forces inducing resonance, where recreating adequate flow conditions was part of the necessary effort. The proper choice of meshing and respective sizing, including the time step, influenced the quality of the simulated flow. Using FSI could enable capturing synchronization between oscillating systems, as long as wind characteristics and structural properties were adequately accounted for. The inclusion of AMDs was of clear focus, particularly passive devices, with differing underlying physics. TMDs and TSDs functioned in different ways, with data types and transfer operations having to be dedicated for each. Methodologically, the main achievements were linked to coupling multiple subsystems together in a robust and scalable manner. The resulting framework clearly highlighted that numerical models of altering complexity could be successfully combined and used for various research as well as design purposes. Showcasing simulations on an HPC environment substantiated this approach for being technologically mature. This could be seen as a prerequisite for as well as a valuable property of the numerical WT. Consequently, simulations were not bound by geometric scales or manufacturing limitations. Moreover, all systems could be fine-tuned individually, further developed depending on needs, with a large variety of insights to be captured.

Future work should cover more detailed added devices, such as an explicitly modeled pendulum damper. Furthermore, in case of sloshing motion, the full three-dimensional wave motion and its possible interference between the two perpendicular directions should be investigated. As a follow-up use case, the inverse of vibration mitigation may be worth exploring. Correspondingly, energy harvesting from specific WIVs could be investigated by exploiting the potentials of numerical methods.

Chapter 4

Analysis of the transient wind loading on bridge decks

Transient wind loading on bridge decks represents a key interest in my work. Various enhancements for analyses via a numerical workflow constitute related additions. Some of these permit the investigation by established means as part of a validation campaign, while other improvements help to achieve better computational efficiency. Preliminaries outline the typical approach for assessing the effect of wind flow on bridge decks, including necessary theoretical considerations. These lay out relevant definitions as well as prepare the discussion for flutter identification. The validation campaign implies transient simulations for determining aerodynamics coefficients and flutter derivatives. I include various observations commenting on the chosen numerical setup, investigated geometries and certain mesh-related aspects. New developments focus on indirect flutter identification by forced motion simulations. Herein, combining multiple frequencies and directions of excitations enable improvements in efficiency, while maintaining accuracy. The workflow is concluded with FSI investigations capturing the direct onset of flutter.

4.1 Fundamentals

4.1.1 Bridge aerodynamics

Wind loading on a bridge depends on a certain flow state at a respective height above the ground. Whereas for large structures it is often necessary to additionally consider a distribution along the longitudinal axes, a two-dimensional sectional model is used for most analysis purposes, as this sufficiently represents the base scenario. A possible wind flow is depicted in Fig. 4.1, marking the time-averaged and instantaneous state. One should bear in mind that the deformation pattern of an elongated structure, in this particular case similar to a simply-supported beam, will respond with appropriate deformations. These in turn can also be split into a stationary and a fluctuating part. Local flow will correspondingly be affected by such movements, as well as being influenced by the main modal contributions of the bridge.

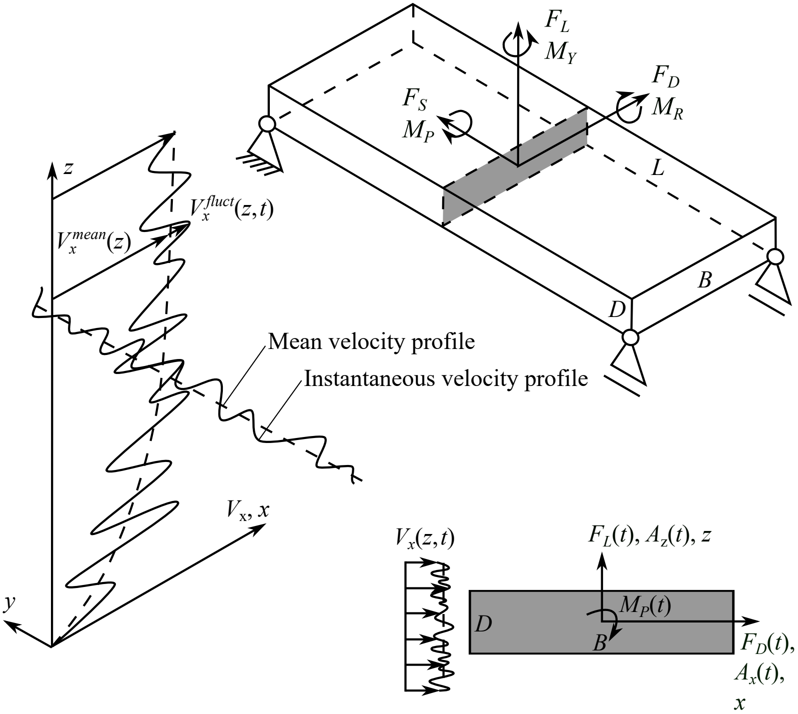

Figure 4.1: Wind loading on a typical long bridge, adapted from Strømmen (2006, Ch. 6).

In the most generic case, any three-dimensional bluff body will have the following static force C_D, C_F and moment C_M coefficients attributed to it. The components are presented in Eqs. (4.1) and (4.2):

$$C_{F_i} = \frac{F_i}{QB} \quad \text{for} \quad F_i = F_D, F_L, F_S \quad \text{with} \quad Q = \frac{1}{2}\rho V^2, \tag{4.1}$$

$$C_{M_i} = \frac{M_i}{QB^2} \quad \text{for} \quad M_i = M_R, M_P, M_Y, \tag{4.2}$$

where F_D, F_L, F_S denote the drag, lift and side forces, and M_R, M_Y, M_P the rolling, yawing and pitching moments. Q defines the dynamic pressure associated with the mean streamwise flow velocity V. As highlighted by dimensional analysis, these coefficients are based on the reference projected area of the section, typically along a unit length. Depending on the specific application, the normalization may be done using either the width B or the height D of the bridge deck. Most of the discussion will focus on a sectional model, both conceptually as well as for the methodological development including analyses. Consequently, the notation is simplified to drag F_D, lift F_L, and pitching $M_{(P)}$, with the coefficients C_D, C_L, $C_{M_{(P)}}$ (dropping the subscript of the moment for brevity).
The previous definitions describe a time-averaged snapshot, also known as a steady (or static) state. Forces and coefficients are presented as a function of the AoA. Reducing the geometry adheres to the strip theory assumption, which is rooted in the aerodynamics of airfoils and often used for bridges. Another level of approximation takes this representative cross-section and outlines a quasi-steady aerodynamic view. Herein, the notation by Ge and Tanaka (2013) is followed. The relations now become dependent on the current deformation state. Consequently, all quantities are function of this instantaneous position. However, the time history of the motion (i.e. memory-effect) is ignored. A series of assumptions are involved, which lead to simplifying the equations by linearization. Many of these are discussed in detail by Strømmen (2006, Ch. 5).

Eq. (4.3) displays the relevant force components:

$$F_D = QBC_D \quad \text{and} \quad F_L = QBC_L \quad \text{and} \quad M = QB^2C_M, \tag{4.3}$$

where Q denotes the dynamic pressure considering the streamwise velocity fluctuations, clearly illustrating the time-dependent nature of unsteadiness through time derivative of the static pressure p, as given by:

$$Q = \frac{\rho}{2}\left(V_x^{mean} + V_x^{fluct}\right)^2 = \frac{\rho}{2}\left(V_x^{mean} - \frac{1}{\rho}\frac{p}{t}\right)^2. \tag{4.4}$$

These coefficients depend on the AoA as well as the first approximation of the change around this position, as in:

$$C_i(\alpha) = C_i\left(\alpha^{mean}\right) + \alpha_{rel}\frac{dC_i\left(\alpha^{mean}\right)}{d\alpha} = C_i^{mean} + \alpha_{rel}\frac{dC_i\left(\alpha^{mean}\right)}{d\alpha}. \tag{4.5}$$

α_{rel} is the relative AoA and i denotes the enumeration of drag, lift and pitch. These basic assumptions are graphically illustrated in Fig. 4.2, which shows a flow-attached system with a positive moment (corresponding to pitch) in the clockwise direction. A generic rectangle is depicted alongside hypothetical qualitative plots of coefficients as a function of the AoA.

The steady and quasi-steady theories represent certain simplifications. When considering full unsteadiness, the force components are generally expressed in their entirety as:

$$\begin{aligned}
&\text{total} = \text{static} + \text{motion-dependent} + \text{buffeting-related}\\
&\Downarrow\\
F_D &= F_D^{stat} + F_D^{md} + F_D^{br},\\
F_L &= F_L^{stat} + F_L^{md} + F_L^{br},\\
M &= M^{stat} + M^{md} + M^{br}.
\end{aligned} \tag{4.6}$$

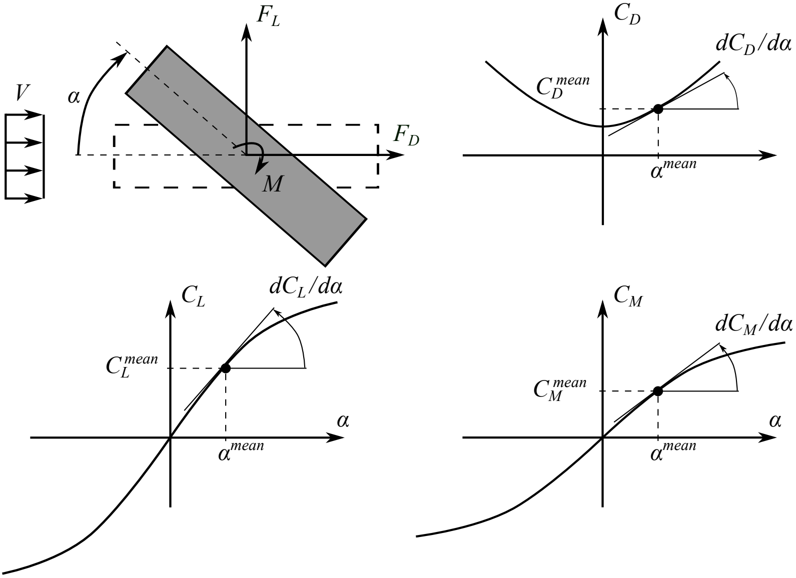

Figure 4.2: Aerodynamic coefficients and their dependency on the AoA, adapted from Strømmen (2006, Ch. 5).

The proper choice of the underlying theory must be determined based on the specific application. To make this choice, it is necessary to discuss the relevance of the forces arising in the context of FIVs by wind. In bridge engineering, it is accepted that vortex shedding-related excitations, including motion-dependent lock-in, are more pronounced in the case of low ABL turbulence, and often occuring at lower streamwise velocity. Appropriate conditions are remarked by Naudascher and Rockwell (1994, Ch. 6) and Holmes (2015, Ch. 12), and detailed in

Ch. 3. Similar scenarios are usually considered to have a favorable effect on flutter, which tend to occur in fairly stable conditions, albeit at high flow velocities. This usually implies a reduced significance of buffeting in turbulent wind, as it can contribute to breaking the spatial and temporal correlation of the shedding pattern as well as the dominant vibration mode of the structure. Assuming this simplification, the drag-related component will be treated with less significance, or even omitted. Yet again, this is a conceptual assumption and is applied to the subsequent two-dimensional analysis. Simiu and Yeo (2019, Ch. 21) rightfully note that turbulence can in some instances affect flutter unfavorable, i.e. its onset appearing earlier. Diana et al. (1993) investigate such a dependency of aeroelastic behavior in certain cases, whereas the works of Andre et al. (2017) and Z. J. Taylor and Browne (2020) highlight the relative importance of buffeting and self-excited forces in case of structures that are somewhat similar in geometry to bridge decks but closer to the ground (such as parabolic trough collectors or solar panels). As modeling assumptions and investigation methods inherently mean simplifications and corresponding limitations of the possible outcome, these need to be chosen carefully and appropriately.

The mean flow with its characteristic patterns conclude the aerodynamic discussion. Fig. 4.3 highlights the effect of the aspect ratio of a bluff body on the development of a shear layer and the mechanism for vortex creation.

While the separation point is primarily defined by the first corner (sharp edge), the reattachment (or lack thereof) depends on various factors, particularly the degree of elongation of the body. The morphology of vortex creation is directly linked to the dimensions of the cross-section, and the following three basic types are defined (see Hémon and Santi, 2002): Leading-Edge Vortex (LEV) for $B/D < (2-3)$, impinging leading-edge vortex (ILEV) for $(2-3) < B/D < (5-9)$, and Trailing-Edge Vortex (TEV) for $(5-9) < B/D$. Most bridge decks will fall into the second or sometimes third category. Dealing with vortical structures and assessing flow patterns have been some of the most challenging aspects in fluid dynamics.

Patterns around various shapes have been thoroughly studied, with Van Dyke (1982) providing a gallery of "fluid in motion". While key characteristics of most sharp-edged cross-sections can typically be easily defined, the difficulty increases with greater roundness. To better highlight dependencies on scale, insights are generally presented as a function of the Reynolds number *Re*, which is defined as:

$$Re = \frac{VD}{\nu}, \tag{4.7}$$

where ν represents the kinematic viscosity of the fluid. While the actual meaning of this metric is that it measures the ratio of inertial to viscous forces, it can also be interpreted as a dimensionless velocity. The reference dimension may be chosen according to the application and is usually either D or B. As a result, *Re* often receives the appropriate subscript to reflect which measure was used to define itmay receive an appropriate subscript to reflect which measure was used to define it, analogous to other dimensionless numbers such as *St* and *Sc*.

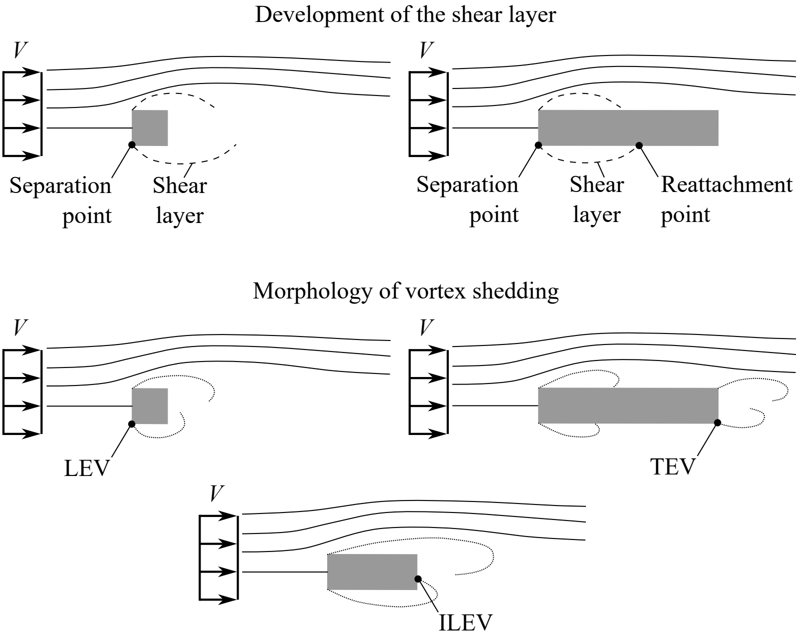

Figure 4.3: Mean flow around a rectangular cross-section, with separation highlighted in the top row and vortex shedding depicted in the lower row, adapted from Hémon and Santi (2002).

4.1.2 Movement-induced instabilities

4.1.2.1 Lock-in as an aeroelastic phenomenon

For a flexible body around which vortex shedding arises, the lift force will be additionally amplified. This phenomenon is movement-induced. Simiu and Yeo (2019, Ch. 19) propose the following EoM for an oscillating cylinder in cross-wind direction:

$$
\begin{aligned}
m\ddot{y} + c\dot{y} + ky &= F\left(y, \dot{y}, \ddot{y}, \ldots, t\right) \\
&\text{or} \\
m\left(\ddot{y} + 2\zeta\omega_s\dot{y} + \omega_s^2 y\right) &= \\
&= \frac{1}{2}\rho V^2 D \left[Y_1(K)\left(1 - \epsilon\frac{y^2}{D^2}\right)\frac{\dot{y}}{D} + Y_2(K)\frac{y}{D} + C_L(K)\sin(\omega_{sh}t + \phi) \right].
\end{aligned}
\tag{4.8}
$$

where the force depends on the respective displacement and its time derivatives.

The contribution of higher-order terms (more than second-order) is neglected. A more detailed model was proposed by Simiu and Scanlan (1996, Ch. 6). At lock-in, the angular frequency of the structure ω_s and that of shedding ω_{sh} are approximately equal. Eq. (4.8) includes the additional terms of Y_1, Y_2, C_L and ϵ, which are adjustable parameters, to be fitted to experimental results. The reduced frequency and velocity are denoted as K and V^{red}, respectively:

$$K = \frac{fD}{V}, \tag{4.9}$$

$$V^{red} = \frac{V}{fD}. \tag{4.10}$$

Certain works may use the angular frequency ω or the dimension B for normalizing. It is also crucial to remark that there are multiple models of these self-excited forces, each to be used for the purpose for which it was determined, but not beyond. Moreover, the introduced functions Y_1 and Y_2 dependent on K remark a linear combination for the definition of the excitation force, linked to $\dot{y}$ and y. This line of thought is typically used to mathematically model aeroelastic excitations.

Vortex shedding leads to oscillating cross-wind forces on a body in flow. For bluff cross-sections, this is generally of a purely harmonic nature. Shapes frequently found in civil engineering, including symmetric bridge decks with a specific aspect ratio, trigger this pattern. In case of IIE, these vortices will be the cause of corresponding movements if the body is flexible. Vortices are present and are the main cause of possible vibrations and oscillating forces. The phenomenon becomes aeroelastic in the presence of such motions, which tend to amplify it.

4.1.2.2 Galloping

Naudascher and Rockwell (1994, Ch. 7) define galloping when MIE occurs without a phase shift between the cross-wind force and the instantaneous velocity of the oscillator. This typically happens for structures characterized as shorter bluff bodies, where the separated shear layers do not reattach, at least when at rest. Furthermore, the motion is often modeled as an SDoF system for torsional or transversal direction. Whereas coupled modes can occur, literature typically presents in detail vibrations perpendicular to the flow. Ge and Tanaka (2013) describe this type of phenomenon as often being very violent, strongly nonlinear as well as with drastic effects of turbulence contributing to it. Simiu and Yeo (2019, Ch. 20) propose the following EoM and expression of the excitation force:

$$m\left(\ddot{y} + 2\zeta\omega_s\dot{y} + \omega_s^2 y\right) = F_y = -\frac{1}{2}\rho V^2 B \left(\frac{dC_L}{d\alpha} + C_D\right)_{\alpha=0} \frac{\dot{y}}{V}. \tag{4.11}$$

where its RHS contributes to the overall system damping, being linked to the velocity of the oscillator $\dot{y}$. Assuming the structural damping $\zeta > 0$ yet small, the occurrence of the instability requires the following term to become negative:

$$2m\zeta\omega_s + \frac{1}{2}\rho V B \left(\frac{dC_L}{d\alpha} + C_D\right)_{\alpha=0} < 0 \quad \Rightarrow \quad \left(\frac{dC_L}{d\alpha} + C_D\right)_{\alpha=0} < 0. \tag{4.12}$$

Eq. (4.12) marks the Glauert–Den Hartog necessary condition for incipient galloping. Den Hartog (1985, Ch. 7) states that “a section is dynamically unstable if the negative slope of the lift curve is greater than the ordinate of the drag curve”. For slender prismatic bodies, this susceptibility can be assessed by the mean lift and drag coefficients, evaluated as a function of the AoA, and thus by a quasi-steady assumption. This holds as long as the critical velocity for onset is rather large (see Naudascher and Rockwell, 1994, Ch. 7). It also follows that circular cylinders, for which $dC_L/d\alpha = 0$, cannot gallop. Examples prone to this phenomenon are short rectangular prisms, cables with icing and various open profiles for structural elements. Onset limits are high for large values of *Sc*. In the body-attached axis, the criteria for instability can be expressed by Eq. (4.13):

$$A_1 = \left.\frac{dC_{F_y}}{d\alpha}\right|_{\alpha=0} = -\left(\frac{dC_L}{d\alpha} + C_D\right)_{\alpha=0} > 0, \tag{4.13}$$

where the cross-wind force F_y can be measured directly or determined from the lift and drag components, i.e. the expression in the flow-attached reference system. Simiu and Yeo (2019, Ch. 20) reflect on the significance of this ratio and call it the steady-state aerodynamic (lift coefficient) derivative. A model for the forcing term in case of galloping is provided by Novak (1972). An example truncated series of this is included, as in Eq. (4.14):

$$C_{F_y} = A_1\left(\frac{\dot{y}}{V}\right) - A_2\left(\frac{\dot{y}}{V}\right)^2 \frac{\dot{y}}{|\dot{y}|} - A_3\left(\frac{\dot{y}}{V}\right)^3 + A_5\left(\frac{\dot{y}}{V}\right)^5 - A_7\left(\frac{\dot{y}}{V}\right)^7. \tag{4.14}$$

Here, a linear combination can again be observed, using the coefficients A_1 to A_7, which are multiplied by powers of $\dot{y}/V$. This term signifies that the relative AoA is equal to $\tan\alpha$ when considering small angles in the context of fluid dynamics. A procedure based on various signs and values for A_1 is part of the analysis for galloping, while the choice of powers is to be perceived as a function of desired stability.

4.1.2.3 Divergence

The concept of aeroelastic instability is showcased by the EoM for an SDoF system. Taking the example of a rotational DoF α, the expression is as follows:

$$I\ddot{\alpha} + c_\alpha\dot{\alpha} + k_\alpha\alpha = \frac{1}{2}\rho V^2 B^2 C_M(\alpha, \dot{\alpha}, \ddot{\alpha}, \ldots). \tag{4.15}$$

According to the steps presented in Ge and Tanaka (2013), the coefficient of the pitching moment can assume a simple expression, which is a linear combination on α and $\dot{\alpha}$, with the coefficients A and B, as in:

$$C_M = A\alpha + B\dot{\alpha}. \tag{4.16}$$

Reorganizing leads to:

$$\ddot{\alpha} + 2\zeta_\alpha\omega_\alpha\dot{\alpha} + \omega_\alpha^2\alpha = \frac{\rho V^2 B^2}{2I}(A\alpha + B\dot{\alpha}). \tag{4.17}$$

Noting:

$$\omega_\alpha = \sqrt{\frac{k_\alpha}{I}}, \quad \zeta_\alpha = \frac{c_\alpha}{2I\omega_\alpha} \quad \text{and} \quad V^{red} = \frac{V}{B\omega_\alpha},$$

results in:

$$\ddot{\alpha} + 2\,(\zeta_\alpha + \zeta_a)\,\omega_\alpha\,\dot{\alpha} + \omega_\alpha^2(1 - S_a)\alpha = 0, \tag{4.18}$$

where damping and stiffness contributions are added by the flow:

$$\zeta_a = -\frac{\rho V^2 B^2}{4I\omega_\alpha} B\left(V^{red}\right), \tag{4.19}$$

$$S_a = -\frac{\rho V^2 B^2}{4I\omega_\alpha^2} A\left(V^{red}\right). \tag{4.20}$$

A and B are functions of the V^{red}, which need to be determined. The following conditions lead to flutter and divergence, respectively:

$$\text{negative damping: } \zeta_\alpha + \zeta_a < 0 \Rightarrow \text{ flutter}, \tag{4.21}$$

$$\text{negative stiffness: } 1 - S_a < 0 \Rightarrow \text{ divergence}. \tag{4.22}$$

Of initial interest is divergence, here assumed as torsional. This is a purely static instability (see Strømmen, 2006, Ch. 8) related to losing stiffness due to interaction effects with the flow. A quasi-steady approach can provide an appropriate solution. Simiu and Yeo (2019, Ch. 20) give the following expression for the pitching moment per unit span:

$$M(\alpha) = \frac{1}{2}\rho V^2 B^2 C_M(\alpha), \tag{4.23}$$

which for small values of the rotation α can be linearized to:

$$M(\alpha) \approx \frac{1}{2}\rho V^2 B^2 \left(C_M(0) + \left.\frac{dC_M}{d\alpha}\right|_{\alpha=0} \alpha\right). \tag{4.24}$$

Eq. (4.24) leads to a closed-form expression to determine the critical velocity. Naudascher and Rockwell (1994, Ch. 2) remark that static stability is ensured as long as the total stiffness of the system is positive. Conversely, instability is characterized by a negative value of the square of the natural frequency. This also leads to the conclusion that for large values of stiffness the likelihood of divergence is reduced. References note classical examples for the appearance of this phenomenon in the form of buckling of pipes, plates and shells, with flow through or over them. For most civil engineering structures, wind conditions typically remain well below the critical velocity. The static relation is as follows:

$$k_\alpha \alpha = M(\alpha). \tag{4.25}$$

Using the notation:

$$\lambda = \frac{1}{2}\rho V^2 B^2 > 0, \tag{4.26}$$

which, reorganized, leads to instability condition, when the denominator becomes zero:

$$\alpha = \frac{\lambda C_M(0)}{k_\alpha - \lambda \left.\frac{dC_M}{d\alpha}\right|_{\alpha=0}} \rightarrow \infty. \tag{4.27}$$

It could be symbolically seen as negative stiffness. Strømmen (2006, Ch. 8) remarks on this unstable behavior of static type and interprets the rotation-linked coefficient. As the premultiplying factor is a rotation-dependent term in the pitching moment, this can be seen as a quasi-steady version of the aerodynamic coefficient A_3^*, which is detailed in 4.1.2.4 as part of the flutter-related discussion.

4.1.2.4 Flutter

Flutter can be linked to negative damping, as previously highlighted in Eq. (4.21). It is crucial to consider the various descriptions and nomenclature available. Naudascher and Rockwell (1994, Ch. 7) claim that "stall flutter in cross-flow [for which the essential ingredient] is the existence of a phase shift between the fluid force and the body velocity". This is a similar characteristic to nonstall flutter, and the opposite to what can be said about galloping. However, here large LEVs additionally characterize the event. For the nonstall case, these would rather be linked to TEVs. Typical cross-sections for bridges, which are considered long bluff bodies, can exhibit dynamic stall at zero mean incidence (i.e. AoA). Simiu and Yeo (2019, Ch. 21) note that "although it is accompanied at all times by vortex shedding with frequency equal to the flutter frequency, flutter is a phenomenon distinct from vortex-induced oscillation". The frequent misunderstanding can be attributed to the presence of vortices as the cause or effect of vibrations. Distinction is aided by a more differentiated view, which considers the type of structural response. Typical vortex-induced motions around the lock-in wind velocity are pronounced and only bounded by the structural damping, with oscillations being much weaker below or above this value. In case of flutter, once above the critical limit, movements only increase with velocity, leading to a dynamic instability and ultimately failure or collapse. This distinction, and the corresponding misunderstanding due to the lack of it, represents the basis for incorrect claims related to the failure of the Tacoma Narrows bridge in 1940. Solari (2019, Ch. 9) highlights the importance of this historic event for the evolution of suspension bridges, and new design considerations as well as analysis techniques. These cover the investigation of aeroelastic phenomena, including flutter.

Respective behaviour involves nonlinear aerodynamics. However, engineering experience shows that linearization is successfully applicable to detect the onset of flutter. This is generally the main goal, such that a potential dynamic instability can be identified and avoided. Civil engineering structures will tend to exhibit deformations within the linear elastic limit, characterized by relative small motions at the level of the considered cross-section. Characteristic sinusoidal deformations and their combinations will influence the structural response. Corresponding aeroelastic forces will be affected accordingly. As explained by Simiu and Yeo (2019, Ch. 21), these are valid reasons to assume small amplitudes of action and reaction, characterizing the system up until the starting condition of the dynamic instability, i.e. the limit between the stable and unstable region. Further content within this work relies on this consideration, with postcritical flutter being out of scope.

Szabó (2013, Ch. 2) highlights the dependency on the degree of elongation B/D of a bridge cross-section in Fig. 4.4. This depiction shows the relation of flutter onset to this geometric property. In particular, for ratios of $B/D \approx (5-9)$ two categories of flutter can be distinguished, high- (a) and low-speed (b), depending on the development of the shear layer. Case (c) marks values $B/D < 3$, for which typically no reattachment happens, and the recirculation bubble entirely surrounds the cross-section. This corresponds to low critical onset velocities, which is unfavorable. For $B/D > 12$, the geometry approaches the behavior of a flat plate in case (b), characterized by a clear reattachment of LEVs.

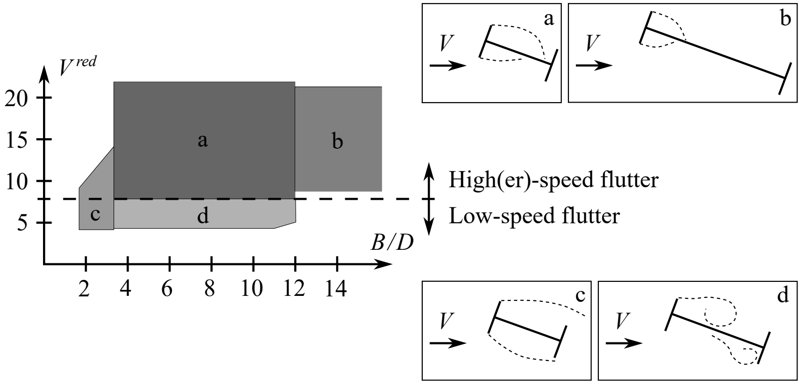

Figure 4.4: Flutter onset (marked by the critcal V^{red}) depending on the aspect ratio of an H-shaped bridge cross-section, adapted from Matsumoto (2000).

Försching (1974, Ch. 6) presents a conceptual model of flutter, remarking on phase shift, as in Fig. 4.5. In particular, the coupling between the heaving and pitching mode shape of a long bridge is mentioned, where corresponding motions can appear delayed with respect to each other. This also triggers a shift in the arising aeroelastic forces. The coupled behavior of the flow-structure system is characterized by the positive energy input. For torsion and bending appearing in phase, the total energy is null, which becomes positive for a certain shift. Negative damping can be explained as an energy input to the oscillating system, leading to an unbounded increase rather than reducing the vibrations of the structure. The resulting scenario is called classical flutter, of type bending-torsion coupled.

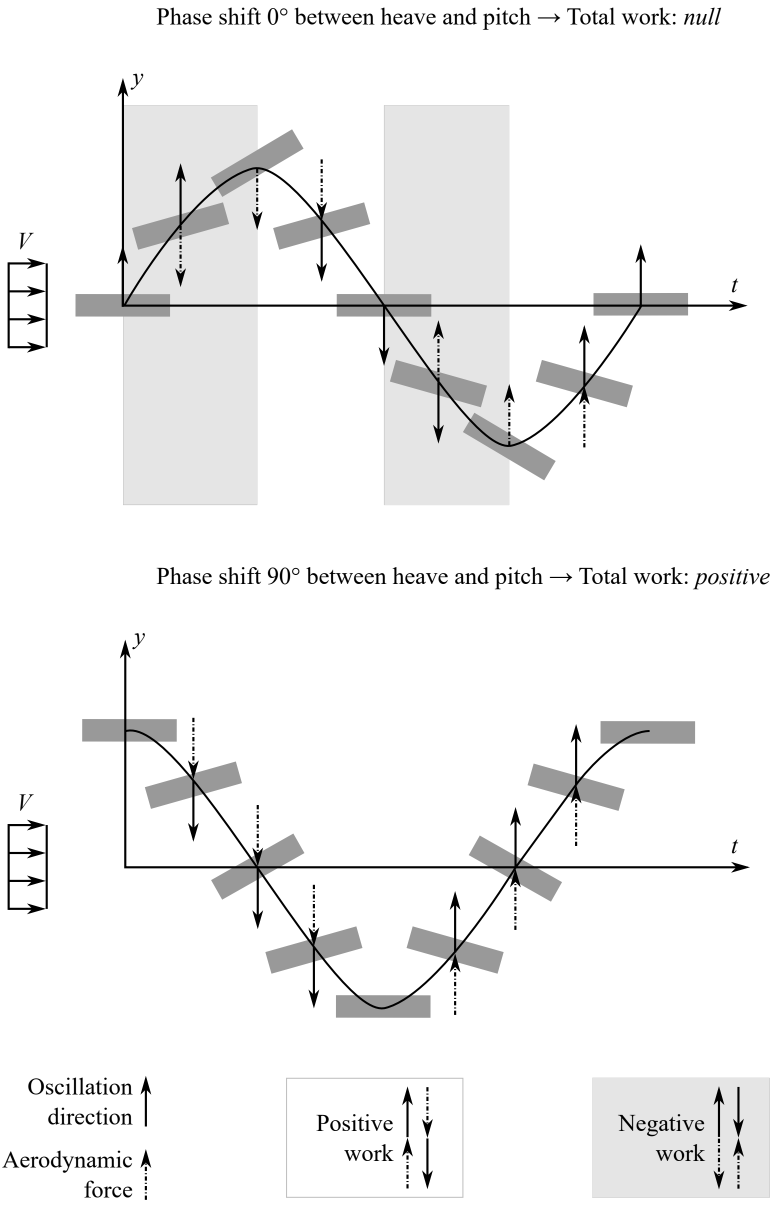
Phase shift 0° between heave and pitch → Total work: *null*

Phase shift 90° between heave and pitch → Total work: *positive*

Figure 4.5: Total work during flutter oscillations, adapted from Försching (1974, Ch. 6).

In the most general case, three DoFs are possible: movements in heave h, pitch α and streamwise sway p directions. Depending on the set of assumptions, some of these may be neglected. For example, in the case of a flat plate, the underlying theory of aeroelastic forces is based on the work of Theodorsen (1949), which assumes a linear dependency of the force and moment on the kinematics. This concept yields the following expressions for a two-dimensional airfoil. Eqs. (4.28) and (4.29) present the lift force and pitching moment for an oscillating cross-section:

$$F_L^{ae} = \frac{1}{2}\rho V^2 B C_L\left(\dot{h}, \ddot{h}, \alpha, \dot{\alpha}, \ddot{\alpha}\right), \tag{4.28}$$

$$M^{ae} = \frac{1}{2}\rho V^2 B^2 C_M\left(\dot{h}, \ddot{h}, \alpha, \dot{\alpha}, \ddot{\alpha}\right). \tag{4.29}$$

The absence of the heave h should be noted, whereas the acceleration terms $\ddot{h}$ and $\ddot{\alpha}$ appear. These higher-order contributions shall be linked to the mass m and pitching inertia I. Scanlan and Tomko (1971) proposed similar relations, by analogy, to express the aeroelastic lift, drag and moment acting on bridge decks. Mass-proportional terms $\ddot{h}$, $\ddot{p}$ and $\ddot{\alpha}$ are considered negligible for this use case. However, the significance of the terms h and p is accounted for, which relate to changes in the frequency of the vibrating body (as they are associated to the total stiffness). Eqs. (4.30), (4.31), and (4.32) note this accordingly:

$$F_D^{ae} = \frac{1}{2}\rho V^2 B C_D\left(h, \dot{h}, \alpha, \dot{\alpha}, p, \dot{p}\right), \tag{4.30}$$

$$F_L^{ae} = \frac{1}{2}\rho V^2 B C_L\left(h, \dot{h}, \alpha, \dot{\alpha}, p, \dot{p}\right), \tag{4.31}$$

$$M^{ae} = \frac{1}{2}\rho V^2 B^2 C_M\left(h, \dot{h}, \alpha, \dot{\alpha}, p, \dot{p}\right). \tag{4.32}$$

In the original notation by Scanlan and Tomko (1971), the dependency on $\dot{\alpha}$ was neglected. Subsequent works introduced the along-wind influence (see Scanlan, 1988), as well as the reliance on the rate of rotation. This resulted in eighteen so-called flutter derivatives P_i^*, H_i^* and A_i^* for $i = 1$ to 6, for the most general scenario. By omitting the effect of drag, the formulas are simplified, leading to a well-accepted form with eight such coefficients, namely H_i^* and A_i^* for $i = 1$ to 4:

$$F_L^{ae} = \frac{1}{2}\rho V^2 B C_L\left(h, \dot{h}, \alpha, \dot{\alpha}\right), \tag{4.33}$$

$$M^{ae} = \frac{1}{2}\rho V^2 B^2 C_M\left(h, \dot{h}, \alpha, \dot{\alpha}\right), \tag{4.34}$$

where the force and moment coefficients are expressed as linear combinations of the flutter derivatives with heave h and pitch α, and their first-order time derivatives:

$$C_L = K H_1^*(K)\frac{\dot{h}}{V} + K H_2^*(K)\frac{B\dot{\alpha}}{V} + K^2 H_3^*(K)\alpha + K^2 H_4^*(K)\frac{h}{B}, \tag{4.35}$$

$$C_M = KA_1^*(K)\frac{\dot{h}}{V} + KA_2^*(K)\frac{B\dot{\alpha}}{V} + K^2A_3^*(K)\alpha + K^2A_4^*(K)\frac{h}{B}. \tag{4.36}$$

Herein, $\dot{h}/V$ and $B\dot{\alpha}/V$ are considered effective AoAs. Furthermore, contributions multiplied by the first derivatives add to aerodynamic damping. In case only those associated with H_1^* and A_2^* are significant, the total damping coefficients can be expressed as (see Simiu and Yeo, 2019, Ch. 21):

$$c_h^{tot} = c_{h,s} - \frac{1}{2}\rho VBKH_1^*, \tag{4.37}$$

$$c_\alpha^{tot} = c_{\alpha,s} - \frac{1}{2}\rho VB^3KA_2^*. \tag{4.38}$$

H_i^* and A_i^* are called motional aerodynamic derivatives, to be evaluated on an oscillating bridge deck. These are different from the steady-state ones, such as those used to characterize galloping. A respective assessment determines these coefficients as a function of the reduced velocity or stiffness. The outcome characterizes a particular bridge deck shape independent of its actual structural properties. Scanlan and Tomko (1971) outline the fundamental considerations, including typical values for the aerodynamic derivatives characterizing flutter. Fig. 4.6 depicts a selection, in particular highlighting A_2^*, the torsion-related component of added damping. This includes an airfoil, the H-shaped Tacoma Narrows cross-section, a selection of truss-stiffened and box girder sections. Whereas all shapes are present in the legend, only the results of a few are included. The two regions, stable and unstable, are essentially separated by the horizontal axes and defined by the positive and negative regions of the vertical axes. Furthermore, $+\Delta c_{\alpha,s}$ signifies an increase in structural damping, and its effect on the critical onset velocity. This is negligible, signalling the minor contribution of this structural property in avoiding flutter. The main message is the importance of shape and how it can critically lead to unstable behavior or prevent it through a proper choice.

In case of an SDoF system with a rotational DoF, the A_2^* derivative would be the primary parameter for identifying the onset of flutter. Similarly, for a pure-heave oscillator, the instability would be driven by H_1^*. The onset of instability can be related to the region where these curves change signs. Real structures can exhibit coupled modes, such that the identification of critical flutter velocity becomes more challenging. One of the previous isolated modes will nonetheless tend to trigger and drive the instability. Moreover, for long span bridges additional three-dimensional effects, mode shapes and other considerations will apply. This thesis continues to focus on the two-dimensional cross-section assuming a TDoF model, at practically zero incoming turbulence.

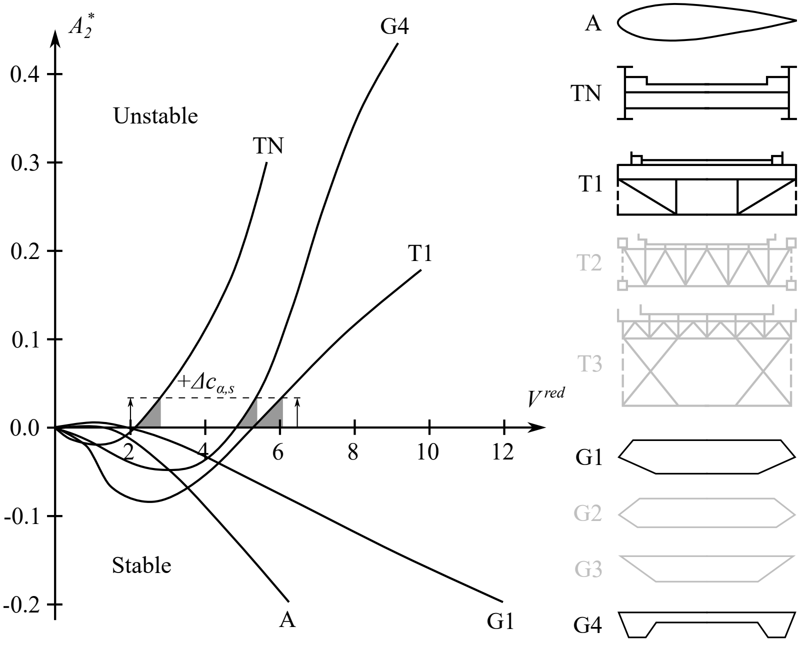

Figure 4.6: Examples for the A_2^* flutter derivative for various cross-sections, adapted from Scanlan and Tomko (1971).

4.1.3 Flutter identification

4.1.3.1 Direct identification

Various underlying analytical models and methods support the identification of flutter. For a specific design scenario where all conditions are known, here referring to the local wind as well as the structural properties, the onset of such an instability can be directly determined. Fig. 4.7 presents this principle, including a two-dimensional view and the evolution of the characteristic response, which grows unboundedly once above the critical value. Such results can be obtained using numerical means, which would imply a fully-coupled FSI simulation, typically assuming a strong TWC setup. In the most generic sense, the elastic axis could be offset from the center of gravity, which would introduce an eccentricity. This would require considering a coupling term, called static imbalance, usually noted as S. Resulting factors would arise, introducing $S\ddot{h}$ into the EoM for heave, and $S\ddot{\alpha}$ into the one for pitch (see Naudascher and Rockwell, 1994, Ch. 7). Due to symmetry conditions characterizing most bridge decks, this aspect is neglected for the further discussion. Governed by the EoM for a TDoF system, the critical onset velocity V^{crit} is identified based on the SD values for the response, recorded for heave h and pitch α.

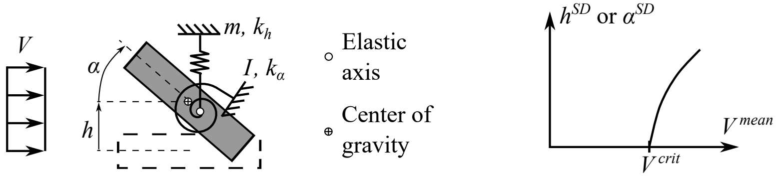

Figure 4.7: Principle of direct identification of flutter onset.

Fig. 4.8 shows a sectional model setup – representing a three-dimensional object that behaves predominantly in a two-dimensional manner – and its typical use in an experimental WT. Herein, the wind condition is usually defined by low turbulence and characterized by a uniform mean value. A representative cross-section of the model is constructed, which foremost captures the geometry of the bridge deck. Structural properties such as mass, torsional inertia and stiffness are typically tuned using a set of springs and point masses, assuming various distances and placements. Often explicit structural damping is neglected, only being represented by that inherent to the material of spring. Corresponding measurements are recorded using position sensors. This setup is especially advantageous, as only kinematics need to be captured, but not forces directly. In the experimental context, this implies a simpler arrangement, since only one type of variable is monitored.

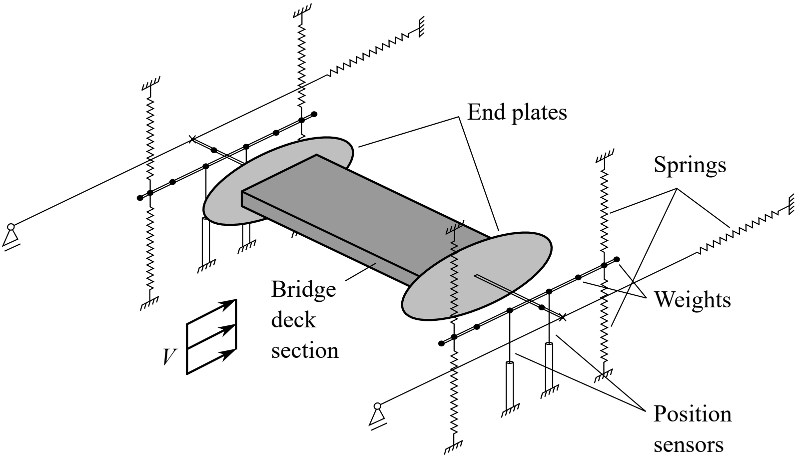

Figure 4.8: Axonometric depiction of a spring-mounted sectional bridge deck model, adapted from Avşar (2003, Ch. 4).

4.1.3.2 Indirect identification by free vibrations

Using an identical setup as for the direct identification, the indirect approach based on free vibration implies an initial displacement (typically both in heave h_0 and pitch α_0) with the system let to oscillate and the kinematics recorded. Tests with zero wind flow represent the baseline measurement to identify the structural model. Analytic models or numerical investigation of mode shapes can provide complementary data, where there is no medium around, i.e. vibrations take place in a vacuum. Additionally, various wind velocities V_i are applied. During these, the total response is captured, with the added effect of the flow, i.e. changes in mass (negligible, even less influence in case heavier cross-sections are chosen), damping and stiffness. The latter two provide the total effective values, consisting of the mechanical damping of the structure and the aerodynamic surplus from the flow. While the initial displacement conditions can be ensured in the experimental WT, for example, by electromagnets, applying these these in a numerical approach is trivial. The solution procedure is once again an FSI simulation assuming TWC. While the design and construction of such setups is straightforward, the key component of the solution procedure is the proper assessment of the added aerodynamic components. This boils down to system identification, which can be carried out with various methods. Among many available options, the Ibrahim Time Domain (ITD) (see Ibrahim and Mikulcik, 1977) and its modification (see Sarkar et al., 1992; Sarkar et al., 1994), which uses a recursive version of the former, are mentioned. The main idea of indirect means by free vibrations is visually supported by Fig. 4.9.

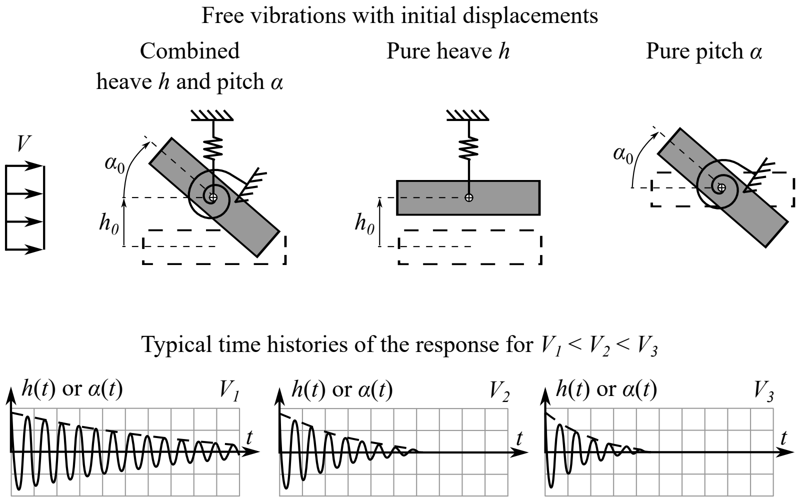

Figure 4.9: Principle of indirect flutter identification via free vibration tests.

For a specific initial displacement and various wind velocities (below an estimated critical value that triggers onset), the amplitude – particularly its decay

– and frequency of the response will differ. It is notable that the length of the acquired data decreases at higher wind velocities, leading to challenges in fitting and system parameter identification.

Eqs. (4.33), (4.34), (4.35), and (4.36) can be rewritten, using the reduced frequency K and the angular frequency ω, which leads to:

$$F_L^{ae} = \frac{1}{2}\rho B^3\omega^2\left[H_1^*(K)\frac{\dot{h}}{B\omega} + H_2^*(K)\frac{\dot{\alpha}}{\omega} + H_3^*(K)\alpha + H_4^*(K)\frac{h}{B}\right], \tag{4.39}$$

$$M^{ae} = \frac{1}{2}\rho B^4\omega^2\left[A_1^*(K)\frac{\dot{h}}{B\omega} + A_2^*(K)\frac{\dot{\alpha}}{\omega} + A_3^*(K)\alpha + A_4^*(K)\frac{h}{B}\right]. \tag{4.40}$$

As the model is characterized by heave and pitch vibration modes, Eqs. (4.39) and (4.40) need to be expanded for the respective components, characterized by ω_h and ω_α. This results in:

$$\begin{aligned}F_L^{ae} = {} & \frac{1}{2}\rho B^3\omega_h^2\left[H_1^*(K_h)\frac{\dot{h}}{B\omega_h} + H_2^*(K_h)\frac{\dot{\alpha}}{\omega_h} + H_3^*(K_h)\alpha + H_4^*(K_h)\frac{h}{B}\right]\\ & + \frac{1}{2}\rho B^3\omega_\alpha^2\left[H_1^*(K_\alpha)\frac{\dot{h}}{B\omega_\alpha} + H_2^*(K_\alpha)\frac{\dot{\alpha}}{\omega_\alpha} + H_3^*(K_\alpha)\alpha + H_4^*(K_\alpha)\frac{h}{B}\right],\end{aligned} \tag{4.41}$$

$$\begin{aligned}M^{ae} = {} & \frac{1}{2}\rho B^4\omega_h^2\left[A_1^*(K_h)\frac{\dot{h}}{B\omega_h} + A_2^*(K_h)\frac{\dot{\alpha}}{\omega_h} + A_3^*(K_h)\alpha + A_4^*(K_h)\frac{h}{B}\right]\\ & + \frac{1}{2}\rho B^4\omega_\alpha^2\left[A_1^*(K_\alpha)\frac{\dot{h}}{B\omega_\alpha} + A_2^*(K_\alpha)\frac{\dot{\alpha}}{\omega_\alpha} + A_3^*(K_\alpha)\alpha + A_4^*(K_\alpha)\frac{h}{B}\right],\end{aligned} \tag{4.42}$$

where $K_h = B\omega_h/V$ and $K_\alpha = B\omega_\alpha/V$. This introduces $H_i^*(K_h)$ and $A_i^*(K_h)$ related to heave, $H_i^*(K_\alpha)$ and $A_i^*(K_\alpha)$ related to pitch. There are more unknowns to be determined as relations to enable this. According to the findings of Sarkar et al. (1992) and Iwamoto and Fujino (1995), observations at the level of coupling between modes at intermediate wind speeds allow H_1^*, H_4^*, A_1^* and A_4^* to be associated with the angular frequency of heave ω_h, and H_2^*, H_3^*, A_2^* and A_3^* to be associated with the one corresponding to that of pitch ω_α. These referenced works show that the influence of SDoF-EoMs for these respective movements separately approximate the TDoF consideration well, which confirms the effect of coupling being weak, i.e. negligible. Eqs. (4.43) and (4.44) mark this simplification:

$$F_L^{ae} = \frac{1}{2}\rho B^3\left\{\omega_h^2\left[H_1^*(K_h)\frac{\dot{h}}{B\omega_h} + H_4^*(K_h)\frac{h}{B}\right] + \omega_\alpha^2\left[H_2^*(K_\alpha)\frac{\dot{\alpha}}{\omega_\alpha} + H_3^*(K_\alpha)\alpha\right]\right\}, \tag{4.43}$$

$$M^{ae} = \frac{1}{2}\rho B^4 \left\{\omega_h^2 \left[A_1^*(K_h)\frac{\dot{h}}{B\omega_h} + A_4^*(K_h)\frac{h}{B}\right] + \omega_\alpha^2 \left[A_2^*(K_\alpha)\frac{\dot{\alpha}}{\omega_\alpha} + A_3^*(K_\alpha)\alpha\right]\right\}. \tag{4.44}$$

H_1^*, H_4^*, A_2^* and A_3^* are also called direct-flutter derivatives, which can be obtained by analysis assuming an SDoF system for each DoF. Meanwhile, H_2^*, H_3^*, A_1^* and A_4^* are also labeled as cross-flutter, signalling the coupling effect. A generalized expression for the free vibration of the TDoF system can be achieved by moving the RHS terms in Eqs. (4.43) and (4.44) to the LHS. The EoM arrives at the form:

$$\ddot{X} + \overline{C}^{eff}\dot{X} + \overline{K}^{eff}X = 0, \tag{4.45}$$

where $X = [h, \alpha]^T$. The effective (or total) damping $\overline{C}^{eff}$ and stiffness $\overline{K}^{eff}$ of the system are formed as:

$$\overline{C}^{eff} = \overline{C}^{mech} - \overline{C}^{ae} = \begin{bmatrix} \overline{c}_{11}^{mech} - \frac{\rho B^2 \omega_h}{2m} H_1^* & \overline{c}_{12}^{mech} - \frac{\rho B^3 \omega_\alpha}{2m} H_2^* \\ \overline{c}_{21}^{mech} - \frac{\rho B^3 \omega_h}{2I} A_1^* & \overline{c}_{21}^{mech} - \frac{\rho B^4 \omega_\alpha}{2I} A_2^* \end{bmatrix}, \tag{4.46}$$

$$\overline{K}^{eff} = \overline{K}^{mech} - \overline{K}^{ae} = \begin{bmatrix} \overline{k}_{11}^{mech} - \frac{\rho B^2 \omega_h^2}{2m} H_4^* & \overline{k}_{12}^{mech} - \frac{\rho B^3 \omega_\alpha^2}{2m} H_3^* \\ \overline{k}_{21}^{mech} - \frac{\rho B^3 \omega_h^2}{2I} A_4^* & \overline{k}_{21}^{mech} - \frac{\rho B^4 \omega_\alpha^2}{2I} A_3^* \end{bmatrix}, \tag{4.47}$$

where $\overline{C}^{mech} = M_s^{-1}C_s$ and $\overline{K}^{mech} = M_s^{-1}K_s$ characterize the mechanical properties of the structure. The solving procedure determines the flutter derivatives through system identification for various values of the reduced velocity V^{red}, which corresponds to the reduced frequency K. Hereby, the following functions result:

$$\begin{aligned} H_1^*(K) &= -\frac{2m}{\rho B^2 \omega_h}\left(\overline{c}_{11}^{eff} - \overline{c}_{11}^{mech}\right), & A_1^*(K) &= -\frac{2I}{\rho B^3 \omega_h}\left(\overline{c}_{21}^{eff} - \overline{c}_{21}^{mech}\right), \\ H_2^*(K) &= -\frac{2m}{\rho B^3 \omega_\alpha}\left(\overline{c}_{12}^{eff} - \overline{c}_{12}^{mech}\right), & A_2^*(K) &= -\frac{2I}{\rho B^4 \omega_\alpha}\left(\overline{c}_{22}^{eff} - \overline{c}_{22}^{mech}\right), \\ H_3^*(K) &= -\frac{2m}{\rho B^3 \omega_\alpha^2}\left(\overline{k}_{12}^{eff} - \overline{k}_{12}^{mech}\right), & A_3^*(K) &= -\frac{2I}{\rho B^4 \omega_\alpha^2}\left(\overline{k}_{22}^{eff} - \overline{k}_{22}^{mech}\right), \\ H_4^*(K) &= -\frac{2m}{\rho B^2 \omega_h^2}\left(\overline{k}_{11}^{eff} - \overline{k}_{11}^{mech}\right), & A_4^*(K) &= -\frac{2I}{\rho B^3 \omega_h^2}\left(\overline{k}_{21}^{eff} - \overline{k}_{21}^{mech}\right). \end{aligned} \tag{4.48}$$

This approach is well established for the experimental WT due to its simplicity of the requirements, as far as the sectional model and the setup goes. No forces need to be measured, only kinematics recorded using the mounting rig. Data acquisition is straightforward, yet the challenge lies in the postprocessing, which implies accurate system identification. More inaccuracy is to be expected for higher velocity ranges and test specimens of lower mass, as noted by Iwamoto and Fujino (1995). Chowdhury and Sarkar (2003) describe the extension for using a three DoF model for eighteen derivatives. Although the numerical WT may offer more precise control over ICs and BCs (even allowing for the isolation of one DoF at a time), potentially leading to a more accurate assessment and fitting of data, the computational effort is significant. This is due to the need to solve a fully-coupled FSI simulation multiple times.

4.1.3.3 Indirect identification by forced vibrations

Forced vibrations provide another approach to determine flutter derivatives. As such, they are indirect means that rely on observing the phase shift between a well-defined imposed motion and the arising forces. The resulting data leads to the derivatives. Generally, a sectional model is assumed, which undergoes pure harmonic oscillations. The underlying principle is visually aided by Fig. 4.10, where θ marks the phase shift.

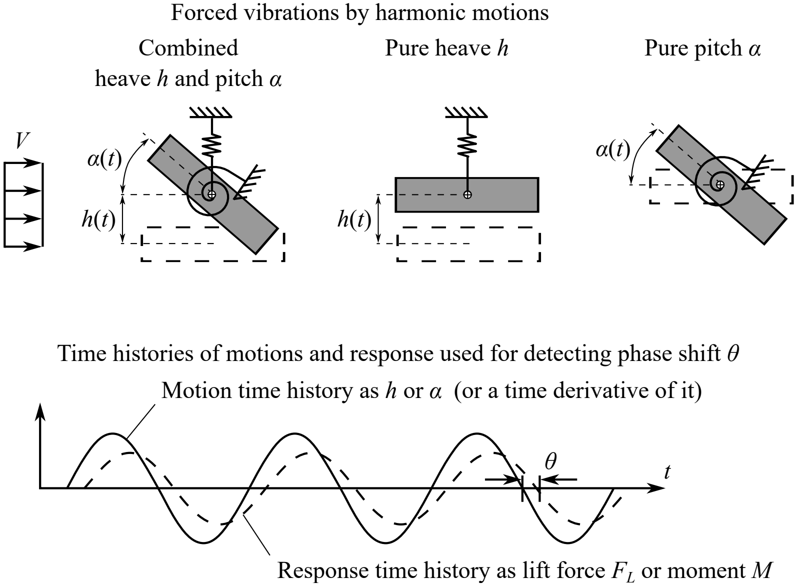

Figure 4.10: Principle of indirect flutter identification via forced vibration tests.

In case of addressing one DoF at a time, the expression of total aerodynamic forces simplify, as in Eqs. (4.49) and (4.50):

$$\begin{aligned}
&\text{pure heave: } h(t) = h_0 \sin\left(\omega_h t\right) \quad \Rightarrow \quad H_1^*, H_4^*, A_1^*, A_4^* \\
&\qquad\qquad \Updownarrow \\
&F_{L,h} = \frac{1}{2}\rho V^2 B \left[K H_1^*(K)\frac{\dot{h}}{V} + \cancelto{0}{(\dots)} + \cancelto{0}{(\dots)} + K^2 H_4^*(K)\frac{h}{B} \right], \\
&M_h = \frac{1}{2}\rho V^2 B^2 \left[K A_1^*(K)\frac{\dot{h}}{V} + \cancelto{0}{(\dots)} + \cancelto{0}{(\dots)} + K^2 A_4^*(K)\frac{h}{B} \right],
\end{aligned} \tag{4.49}$$

$$\begin{aligned}
&\text{pure pitch: } \alpha(t) = \alpha_0 \sin\left(\omega_\alpha t\right) \quad \Rightarrow \quad H_2^*, H_3^*, A_2^*, A_3^* \\
&\qquad\qquad \Updownarrow \\
&F_{L,\alpha} = \frac{1}{2}\rho V^2 B \left[\cancelto{0}{(\dots)} + K H_2^*(K)\frac{B\dot{\alpha}}{V} + K^2 H_3^*(K)\alpha + \cancelto{0}{(\dots)} \right], \\
&M_\alpha = \frac{1}{2}\rho V^2 B^2 \left[\cancelto{0}{(\dots)} + K A_2^*(K)\frac{B\dot{\alpha}}{V} + K^2 A_3^*(K)\alpha + \cancelto{0}{(\dots)} \right].
\end{aligned} \tag{4.50}$$

By imposing a harmonic motion, corresponding forces are searched for, of the generic form in time $F(t)$ as:

$$F(t) = a + b\cos(\omega t) + c\sin(\omega t), \tag{4.51}$$

where the phase shift is $\theta = \tan^{-1}(b/c)$. This leads to the respective flutter derivatives:

$$\begin{aligned}
H_1^*(K) &= \frac{2b_{lift}^{heave}}{\rho B^2 h_0 \omega_h}, & A_1^*(K) &= \frac{2b_{moment}^{heave}}{\rho B^3 h_0 \omega_h}, \\
H_2^*(K) &= \frac{2b_{lift}^{pitch}}{\rho B^3 \alpha_0 \omega_\alpha}, & A_2^*(K) &= \frac{2b_{moment}^{pitch}}{\rho B^4 \alpha_0 \omega_\alpha}, \\
H_3^*(K) &= \frac{2c_{lift}^{pitch}}{\rho B^3 \alpha_0}, & A_3^*(K) &= \frac{2c_{moment}^{pitch}}{\rho B^4 \alpha_0}, \\
H_4^*(K) &= \frac{2c_{lift}^{heave}}{\rho B^2 h_0}, & A_4^*(K) &= \frac{2c_{moment}^{heave}}{\rho B^3 h_0}.
\end{aligned} \tag{4.52}$$

In conclusion, indirect identification means determining these coefficients as a function of the reduced velocity or frequency, which are inversely related. This either happens based on system identification with free vibrations under different (wind-)flow settings, or by detecting phase shift. Mathematically, both involve

signal processing and parameter or curve fitting. The former method seems to be better suited for the experimental WT, and the latter for the numerical one. Using the computational approach in this context involves solving the flow and managing mesh motion, without the need for a structural solver or additional coupling iterations, so the overhead compared to a typical CFD simulation case is minimal.
Certain flutter derivatives can be attempted to be expressed in function of others, depending on the use case. Moreover, H_4^* and A_4^* are considered more difficult to assess accurately, while their influence on the critical flutter seems to be reduced (even being omitted in the original work of Scanlan and Tomko, 1971). Additional care should be taken for the notation, with the main ones being those presented in Starossek (1991, Ch. 2) or Simiu and Scanlan (1996, Ch. 6).

4.1.3.4 Instability condition for flutter onset

These flutter derivatives characterize the added damping and stiffness of the air on the bridge deck, while oscillating, assuming a dependence on the motion and its first time derivative, for heave and pitch. It is a concept that leads to the computation of the critical onset velocity. Once these are derived, a generic expression for the steady state solution of the displacement $h(t)$ of the EoM under a sustained external excitation force $F_L(t)$ can be deduced. This leads to a snapshot of the forcing term and the response. Herein, a harmonic forcing term can be assumed, which leads to a harmonic response, as in Petersen and Werkle (2017, Ch. 5):

$$\text{Real notation:} \quad F_L = F_{L,0} \sin(\omega t) \quad \Rightarrow \quad h = h_0 \sin\left(\omega t - \phi\right), \tag{4.53}$$

Complex notation:

$$F_L = F_{L,0} e^{i\omega t} = F_{L,0} \left[\cos(\omega t) + i \sin(\omega t)\right] \quad \Rightarrow \quad h = h_0 e^{i(\omega t - \phi)}. \tag{4.54}$$

One can observe that the action and reaction (i.e. response) are a function of the angular frequency ω, whereas ϕ denotes the phase lag. With the system being linear, the equilibrium also holds for combining forcing terms, due to the principle of superposition, similarly for the respective response. Analysis is possible by focusing on either one frequency or the effect of multiple at once. These observations are in line with the considerations for identifying critical flutter, with the help of derivatives. For heave h and pitch α, the complex solution is assumed, leading to:

$$\begin{aligned} h &= h_0 e^{i\omega t}, & \alpha &= \alpha_0 e^{i\omega t}, \\ \dot{h} &= h_0 i\omega e^{i\omega t}, & \dot{\alpha} &= \alpha_0 i\omega e^{i\omega t}, \\ \ddot{h} &= -h_0 \omega^2 e^{i\omega t}, & \ddot{\alpha} &= -\alpha_0 \omega^2 e^{i\omega t}. \end{aligned} \tag{4.55}$$

The LHS of the EoM for flutter can be rewritten as:

$$
\begin{aligned}
&m\left(\ddot{h}+2\omega_h\zeta_h\dot{h}+\omega_h^2 h\right)=F_L^{ae},\\
&I\left(\ddot{\alpha}+2\omega_\alpha\zeta_\alpha\dot{\alpha}+\omega_\alpha^2 h\right)=M^{ae},\\
&\qquad\qquad\Downarrow\\
&mh_0\omega^2 e^{i\omega t}\left[\left(\frac{\omega_h}{\omega}\right)^2+2i\zeta_h\frac{\omega_h}{\omega}-1\right]=F_L^{ae},\\
&I\alpha_0\omega^2 e^{i\omega t}\left[\left(\frac{\omega_\alpha}{\omega}\right)^2+2i\zeta_\alpha\frac{\omega_\alpha}{\omega}-1\right]=M^{ae}.
\end{aligned}
\tag{4.56}
$$

The RHS follows accordingly:

$$
\begin{aligned}
F_L^{ae}&=\frac{1}{2}\rho V^2 B\left[KH_1^*\frac{\dot{h}}{V}+KH_2^*\frac{B\dot{\alpha}}{V}+K^2H_3^*\alpha+K^2H_4^*\frac{h}{B}\right],\\
M^{ae}&=\frac{1}{2}\rho V^2 B^2\left[KA_1^*\frac{\dot{h}}{V}+KA_2^*\frac{B\dot{\alpha}}{V}+K^2A_3^*\alpha+K^2A_4^*\frac{h}{B}\right],\\
&\qquad\qquad\Downarrow\\
F_L^{ae}&=\frac{1}{2}\rho B^3\omega^2 e^{i\omega t}\left[\frac{h_0}{B}\left(iH_1^*+H_4^*\right)+\alpha_0\left(iH_2^*+H_3^*\right)\right],\\
M^{ae}&=\frac{1}{2}\rho B^4\omega^2 e^{i\omega t}\left[\frac{h_0}{B}\left(iA_1^*+A_4^*\right)+\alpha_0\left(iA_2^*+A_3^*\right)\right].
\end{aligned}
\tag{4.57}
$$

Combining and reorganizing Eqs. (4.56) and (4.57) leads to a homogenous system of equations. There is a trivial solution for $h_0/B=0$ and $\alpha_0=0$, which we are not interested in. By searching for the non-trivial solution for the unknown ω, which marks the common oscillation frequency for heave and pitch in case of flutter, the matrix E is formed. The corresponding notation and steps are properly detailed in Strømmen (2006, Ch. 8). In this dissertation, only the significant remarks from this reference are noted and the relevant formulas presented. For a long span bridge, the torsional and heave mode shapes will typically be the first two relevant. These are usually shape-wise similar. Observations show that the torsional component often triggers flutter, such that corresponding aeroelastic forces are driving the phenomenon. Instability is characterized by infinitely large structural response, which can be mathematically expressed by the determinant of the impedance matrix E becoming zero, stated as:

$$
\begin{gathered}
\det\left(E(\omega,V)\right)=0\\
\Downarrow\\
\begin{vmatrix}
\frac{2m}{\rho B^2}\left[\left(\frac{\omega_h}{\omega}\right)^2+2i\zeta_h\frac{\omega_h}{\omega}-1\right]-\left(iH_1^*+H_4^*\right) & -\left(iH_2^*+H_3^*\right)\\
-\left(iA_1^*+A_4^*\right) & \frac{2I}{\rho B^4}\left[\left(\frac{\omega_\alpha}{\omega}\right)^2+2i\zeta_\alpha\frac{\omega_\alpha}{\omega}-1\right]-\left(iA_2^*+A_3^*\right)
\end{vmatrix}=0.
\end{gathered}
\tag{4.58}
$$

This relation formally reveals stability limits associated to all mode shapes, here for a two-dimensional section model pitch and heave. A dependency on the flow velocity is included in the flutter derivatives. In general, such an approach can be used for static and dynamic considerations and including complex quantities. Consequently, the previous relation results in the simultaneous fulfillment for the real $\mathscr{R}e$ and imaginary $\mathscr{I}m$ parts:

$$\mathscr{R}e(\det(E)) = 0 \quad \text{and} \quad \mathscr{I}m(\det(E)) = 0. \tag{4.59}$$

For the case of dynamic stability limit of flutter, the solution leads to an eigenvalue problem. Each root contains a pair of the angular frequency ω and flow velocity V, of which the lowest V^{crit} and its corresponding ω^{res} hold interest. As the two motions are assumed to be coupled into joint oscillations, the common (also called resonant) frequency ω^{res} is noted:

$$\omega^{res} = \omega_h\left(V^{crit}\right) = \omega_\alpha\left(V^{crit}\right). \tag{4.60}$$

These considerations are followed by the expansion of the determinant for the real and imaginary parts. Including the obtained flutter derivatives yields the formulas that define the critical state. This is found by identifying the lowest identical roots in a third- and fourth-order polynomial in ω, as follows:

$$\mathscr{I}m(\det(E)) = 0 \Longleftrightarrow I_3\omega^3 + I_2\omega^2 + I_1\omega + I_0 = 0, \tag{4.61}$$

$$\mathscr{R}e(\det(E)) = 0 \Longleftrightarrow R_4\omega^4 + R_3\omega^3 + R_2\omega^2 + R_1\omega + R_0 = 0. \tag{4.62}$$

It is crucial that a common solution exists to satisfy both conditions, only then being a result with physical relevance. The stability condition can be additionally highlighted by a certain property of the solution for ω. Namely, it depends on the sign of the imaginary part. The generic response (either heave or pitch) is noted as $x(t)$ for brevity. Herein, it is clear that the system becomes unstable as soon as ω has a negative imaginary part. The flutter onset is marked by the respective wind speed. Eq. 4.63 defines the complex frequency in terms of its real $\mathscr{R}e$ and imaginary $\mathscr{I}m$ parts in the standard notation, and utilizes Euler's formula in exponential form to emphasize how the stability (described by $x(t)$) depends on the sign change.

$$\omega = \omega_{\mathscr{R}e} + i\omega_{\mathscr{I}m} \quad \Rightarrow \quad x(t) = x_0 e^{i(\omega_{\mathscr{R}e}+i\omega_{\mathscr{I}m})t} = x_0\left(e^{i\omega_{\mathscr{R}e}t}\cdot e^{-\omega_{\mathscr{I}m}t}\right)$$

$$\Rightarrow \begin{cases} \omega_{\mathscr{I}m} > 0 & \rightarrow \quad x(\infty) = 0 \quad \rightarrow \quad \text{stable} \\ \omega_{\mathscr{I}m} < 0 & \rightarrow \quad x(\infty) = \infty \quad \rightarrow \quad \text{unstable} \end{cases} \tag{4.63}$$

Assuming a particular structural model characterized by m, I, ω_h, ω_α, ζ_h and ζ_α, the relations can be generated for any value of K or V^{red}. The formulas highlight the relevance of flutter derivatives in leading to the onset velocity V^{crit}. While the direct approach identifies the instability limit within one simulation setup, indirect methods sweep through various configurations. For a certain combination of ω and V, the aeroelastic force F_L^{ae} and moment M^{ae}, as well as the kinematics can be retrieved. These would be in the form of harmonics that are specific to a certain steady state dynamic forcing. Consequently, the relations relying on $H_i^*(K)$ and $A_i^*(K)$ are used to characterize a specific cross-sectional shape for a range of (reduced) velocities. This is very helpful in assisting design iterations. Nonetheless, the challenge lies in determining the necessary coefficients, while properly dealing with signal processing and data fitting.

4.2 Research and development

I focused research and development efforts for improving the indirect approach imposing forced motions to determine flutter derivatives. This led to the critical onset velocity of the instability. Additionally, the activities implied covering the entire workflow, starting with assessing the main aerodynamic coefficients at various static angles, and concluding with FSI for direct identification. For this reason, one of the chosen geometries was the Benchmark on the Aerodynamics of a Rectangular 5:1 Cylinder (BARC), with important aspects for computational simulations enumerated in Bartoli et al. (2020). It is a thoroughly studied and documented case, with multiple contributions since 2010. However, this is not a realistic shape for bridges. Another cross-section was additionally selected due to being more appropriate for such considerations. This is the shape described in detail and assessed in Šarkić et al. (2012), Šarkić (2014), and Šarkić et al. (2015). Multiple variations exist among various authors, such as Starossek et al. (2009) and Nieto et al. (2015). Its dimensions are almost identical to that of the Hardanger Bridge, with flutter-related research and data in Siedziako (2018).

4.2.1 Chosen geometries

The geometries are similar in aspect ratio, although differences in flow patterns and local loads (i.e. pressures) are expected due to variations in edge detailing. Nonetheless, the workflow aimed to follow many of the prescriptions used in the initial BARC study, while also evaluating the transferability and comparability to this second, more realistic cross-section. Concrete dimensions are applied to the small-scale model, with sizing based on actual values used in various investigations. In this work, I consistently refer to these shapes as *Rectangle* and *Bridge*, as shown in Fig. 4.11.

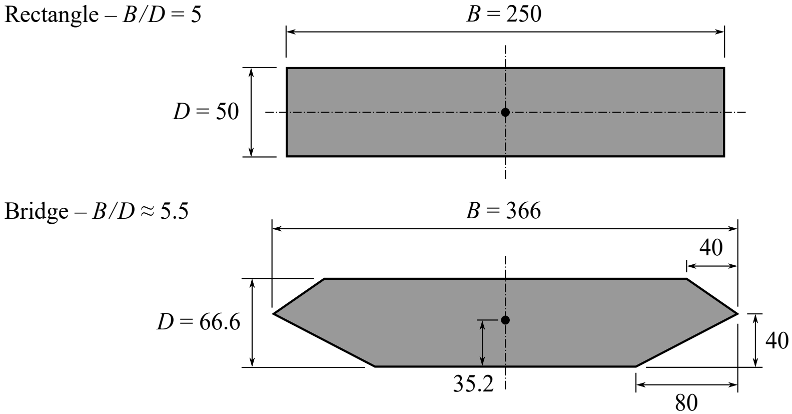

Figure 4.11: Dimensions in [mm] for the cross-sections at small scale.

4.2.2 Static aerodynamic coefficients

Proper domain sizing is the prerequisite for quality numerical simulations. Here, the findings of various authors were followed, accompanied by a mesh convergence study, including two choices for the domain width. The research aimed at establishing an appropriate setup for the sectional models of the cross-sections. Most insights and the bulk of the results included in the main body of the text refer to the Rectangle, due to the availability of data for this shape. Outcomes related to static angle investigations on the Bridge are included in App. B. Both geometries are immersed in the domain, as specified in Fig. 4.12. Between the outer surfaces and the structure, there are five refinement zones to best control the mesh transition. Details related to this sizing are contained in Tab. B.1. A summary of the convergence study can be seen in Fig. B.1.

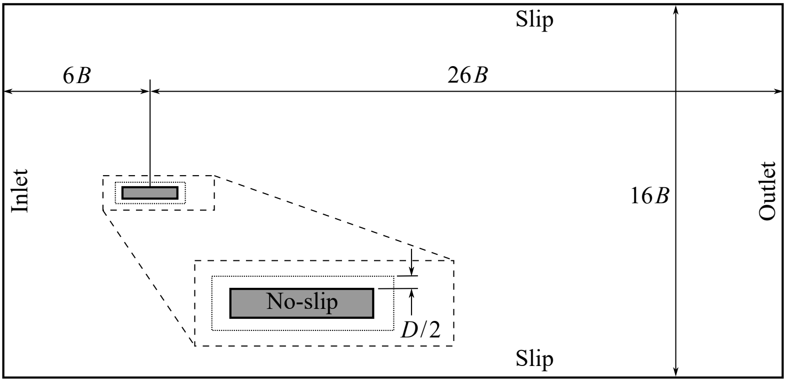

Figure 4.12: Domain sizing by relative measure for the cross-sections.

Investigations at various AoAs provide a snapshot of the aerodynamic performance of a cross-section in certain orientations. Essentially, it results in curves, with the coefficients as a function of the AoA. However, it does not include any insight into the change of these metrics based on the change of the position. It is also necessary to distinguish between flow-attached forces, with the axes being oriented along and perpendicular to the flow, and a body-attached reference system. For the latter, the system is rotated with the cross-section, typically coinciding with the main inertia axes. Moreover, computing such coefficients assumes a certain reference length, which usually alternates between the width or height of the bridge deck. Fig. 4.13 presents the time-averaged mean drag C_D^{mean}, lift C_L^{mean} and moment coefficients C_M^{mean}. A flow-attached system is considered, with force values normalized by the section height D. This is the typical approach for the Rectangle. Accordingly, reference results for the Bridge were converted by the factor B/D so that the magnitudes can be better compared along the y-axis range. It is clearly visible that drag is lower for the more streamlined body, lift is comparable, while the aerodynamic moment shows significantly different behavior.

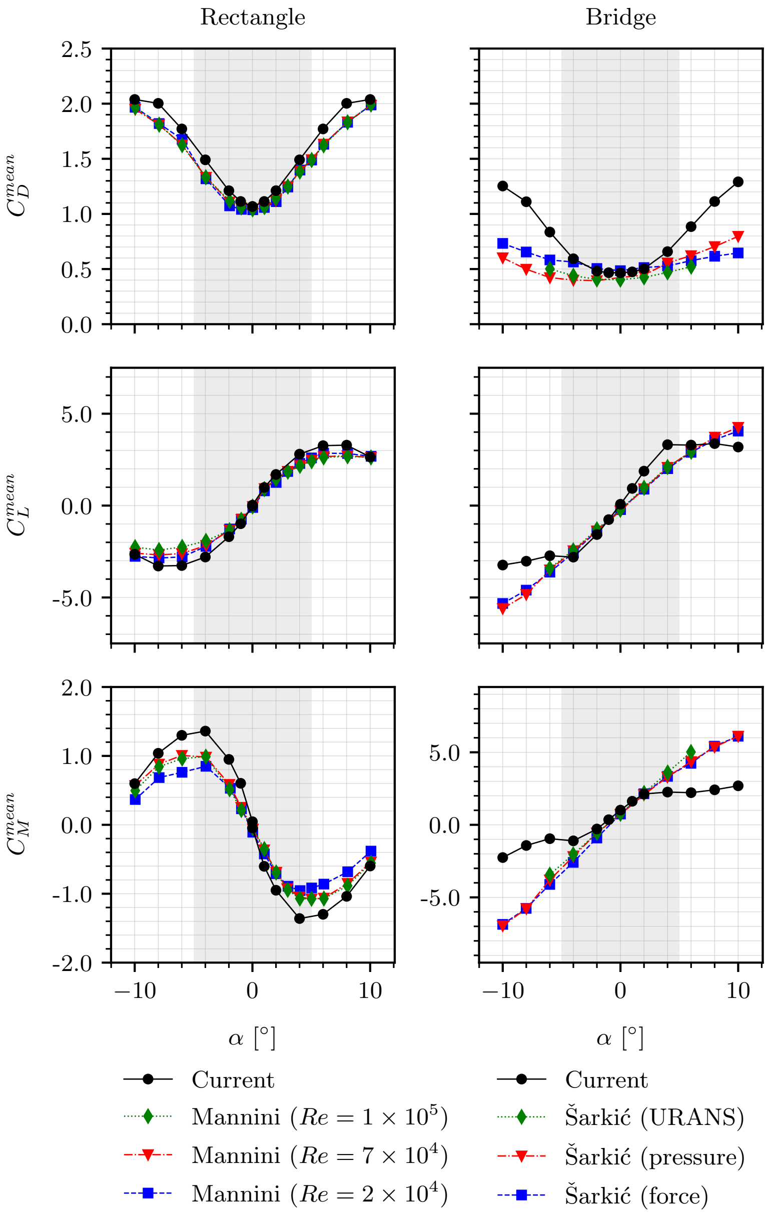

Figure 4.13: Time-averaged aerodynamic force coefficients.

Mannini et al. (2017) assess data using force measurements in an experimental WT, whereas Šarkić et al. (2012) use a combined approach with numerics. Aerodynamic force coefficients show good agreement with referenced values, in particular for the AoA $\alpha = -5°$ to $5°$. This is the range that is later relevant during indirect flutter analysis. Beyond these values, the second shape – Bridge – may exhibit flow patterns characterized by vortical structures that could be challenging to capture with the current setup. A comparable discrepancy can be observed in drag at a high AoA in Nieto et al. (2015). In addition to these global forces, local pressures are depicted in Figs. B.3 and B.4, as part of the broader validation effort.

4.2.3 Effect of shape and geometric scaling

Certain shape effects can often be highlighted when scaling the geometry. Traditionally, the majority of studies are carried out in an experimental WT, at a reduced size. For most bluff bodies, with clear separation points at sharp edges, the aerodynamic performance is mostly independent of the velocity range, i.e. insensitive with respect to the *Re*. It is sufficient to ensure a mostly constant interval, for *Re* approximately 1×10^4 to 1×10^7, which is characteristic of real-size structures in civil engineering. The more streamlined or curved the shape becomes, the more prone it is to an increased dependency on the *Re* range. Within the current study, the focus was on evaluating various metrics, such as global and local forces as well as flow patterns, for both small-scale and large-scale shapes. The latter sizing implied increasing the domain size and proportionally resizing the actual numerical mesh precisely by a factor of 75 (which keeps all relative nodal distances the same). Tab. 4.1 shows the results for the Rectangle, with no noticable differences across the different scales. Meanwhile, Tab. B.3 provides similar insights for the Bridge, with certain observable differences, such as for the mean lift (which is near zero).

Table 4.1: Aerodynamic coefficients and the *St* for the Rectangle at various geometric scales.

		Small-scale	Large-scale	Bruno et al. (2014)
C_D	Mean	1.070	1.065	1.074 ± 0.129
	SD	0.054	0.054	
C_L	Mean	−0.005	−0.009	-0.014 ± 0.142
	SD	0.739	0.720	0.650 ± 0.374
C_M	Mean	0.031	0.088	
	SD	0.720	0.700	
St_D		0.114	0.115	0.109 ± 0.015

The results from Bruno et al. (2014) show the mean ± the SD of several numerical contributions.

Furthermore, typical flow patterns were also part of the original requirements of the study for the BARC cross-section. According to those definitions, the location of the main vortex (given by x_c and y_c) should be documented, additionally marking the reattachment point L_f and the size of the wake L_w behind the bluff body. These properties are visualized in Fig. 4.14.

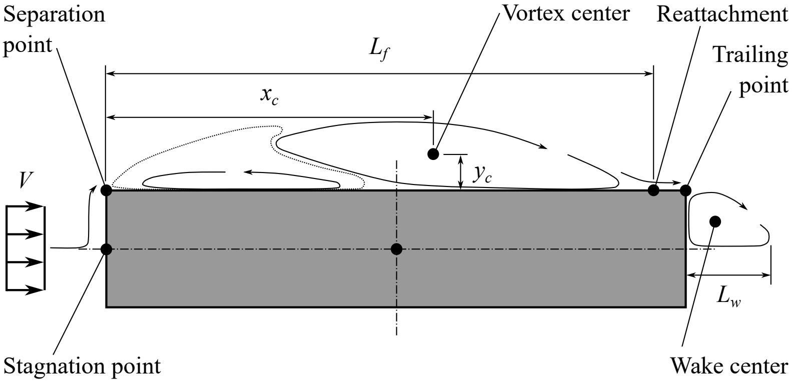

Figure 4.14: Definitions of the flow characteristics, adapted from Bartoli et al. (2020).

Such flow patterns are quantitatively summarized in Tab. 4.2. Here, the values from the top and bottom edge are averaged, being a double-symmetric shape.

Table 4.2: Main flow characteristics of the time-averaged flow field for the Rectangle.

	Small-scale	Large-scale	Bruno et al. (2014)
Average: top and bottom			
x_c/B	0.594	0.603	0.454 ± 0.146
y_c/D	0.335	0.332	0.304 ± 0.033
L_f/B	0.910	0.925	0.950 ± 0.090
Wake			
L_w/D	0.660	0.752	

The results from Bruno et al. (2014) here again show the average ± the SD of several numerical contributions.

For a visual depiction, streamlines are determined in the middle of the domain on the time-averaged velocity field. In case of the Rectangle, there is no observable distinction, as seen in Fig. 4.15.

Aerodynamic force coefficients and flow patterns are consistent between the geometric scales, as well as within the variance of the reference work. This is the case despite typical quality metrics for numerical simulations, such as the Courant–Friedrichs–Lewy Condition number CFL and the y^+ being outside of the optimal range. The former value inherently respects scaling laws, with the current investigation having elements with magnitudes beyond 1.0 at both scales. As the CFD simulations imply the FEM-based VMS treatment of the transient flow, the scheme remains robust and accurate. It should be noted that a more detailed examination would require locating the elements of the mesh with high CFL in discussing its possible effect on the structure itself. Meanwhile, the y^+ value characterizes the mesh refinement near the target boundary, and is affected by scaling. This is due to the fact that the mesh is magnified at the same rate as the domain, such that the relative distances between nodes remain.

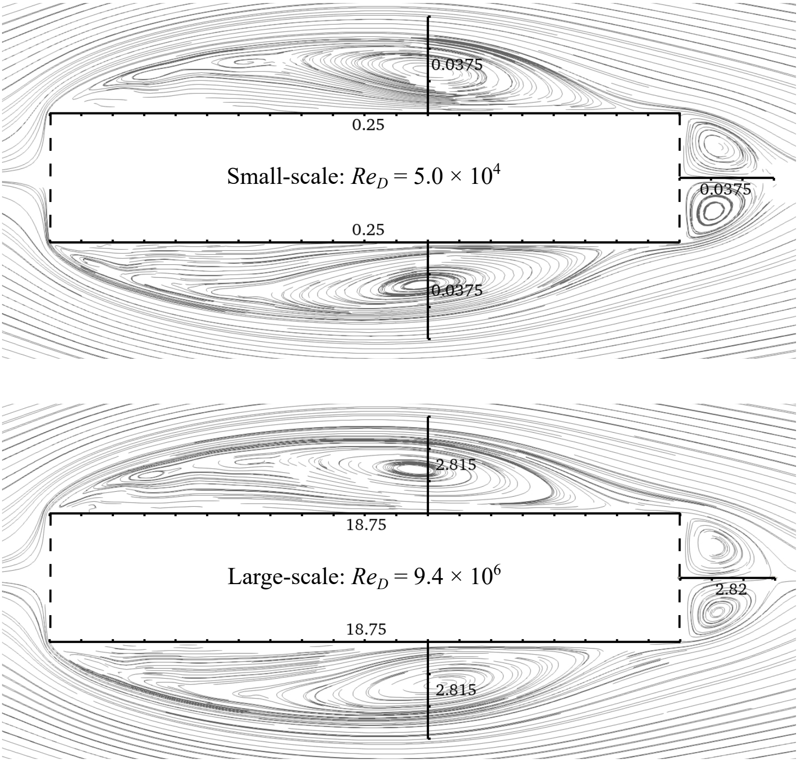

Figure 4.15: Streamlines at small and large geometric scales for the Rectangle.

In Tab. 4.3, high maximum values are observed outside the optimal ranges traditionally used by the CFD community, while the magnitudes for the mean and SD are well within these limits. For the CFL, values less than or equal to 1.0 are generally considered prerequisites for both the accuracy of the solution and the stability of the scheme. The y^+ value can vary from 30 to 300 when applying near-wall treatment. Certain procedures may violate this condition (at least locally) while still providing physically meaningful solutions. However, most of these recommendations and best practices are based on data from simulations using the FVM. Furthermore, the abundance of observations rely on results assessed on small-scale geometries, in an effort to validate numerics with experimental WT data. Accordingly, the most established opinion is heavily influenced by these considerations. As a numerical countermeasure, wall functions are often used to correct the local flow conditions in ensuring a proper boundary layer. Nevertheless, these are models based on empirical relations. The currently used stabilized scheme may not only have a positive effect on modeling turbulence but also implicitly treat near-boundary regions.

Table 4.3: Spatial statistics of the CFL and y^+ metrics obtained on the two geometric scales for the Rectangle.

		Small-scale	Large-scale
CFL			
	Mean	0.247	0.247
	SD	0.209	0.209
	Max	3.521	3.532
	$\# > 1$ [%]	0.918	0.915
	$\# > 2.5$ [%]	< 0.001	< 0.001
y^+			
	Mean	28.4	5298
	SD	27.1	5061
	Max	462.9	86713
	$\# > 5$ [%]	97.9	> 99.9
	$\# > 30$ [%]	32.2	> 99.9

The effect of shape and scaling is also documented for the Bridge. Apart from the very last insights, which are related to numerical quality metrics and are essentially the same, physical outcomes show some changes. These mainly concern the aerodynamic lift coefficient, as in Tab. B.3, and the clarity of the vortical structures from the separation points, as in Fig. B.5 and Tab. B.4.

4.2.4 Flutter derivatives using forced motion

For establishing the main aerodynamic characteristics, I focused on the Rectangle cross-section. This decision was influenced by the abundance of data as well as the challenge of establishing a workflow on a double-symmetric shape. Conversely, there seems to be more research activity related to flutter derivatives on bridge-like shapes. Presumably the use case of identifying the onset of this MIE promotes corresponding work. Consequently, this led to a shift in focus onto the Bridge geometry for the content dedicated to flutter. Validation efforts are summarized in Fig. 4.16, whereby the derivatives are determined by the traditional single-frequency forced motion approach. Sixteen simulations were required to cover the range of the reduced velocity $V^{red} = 0$ to 20.

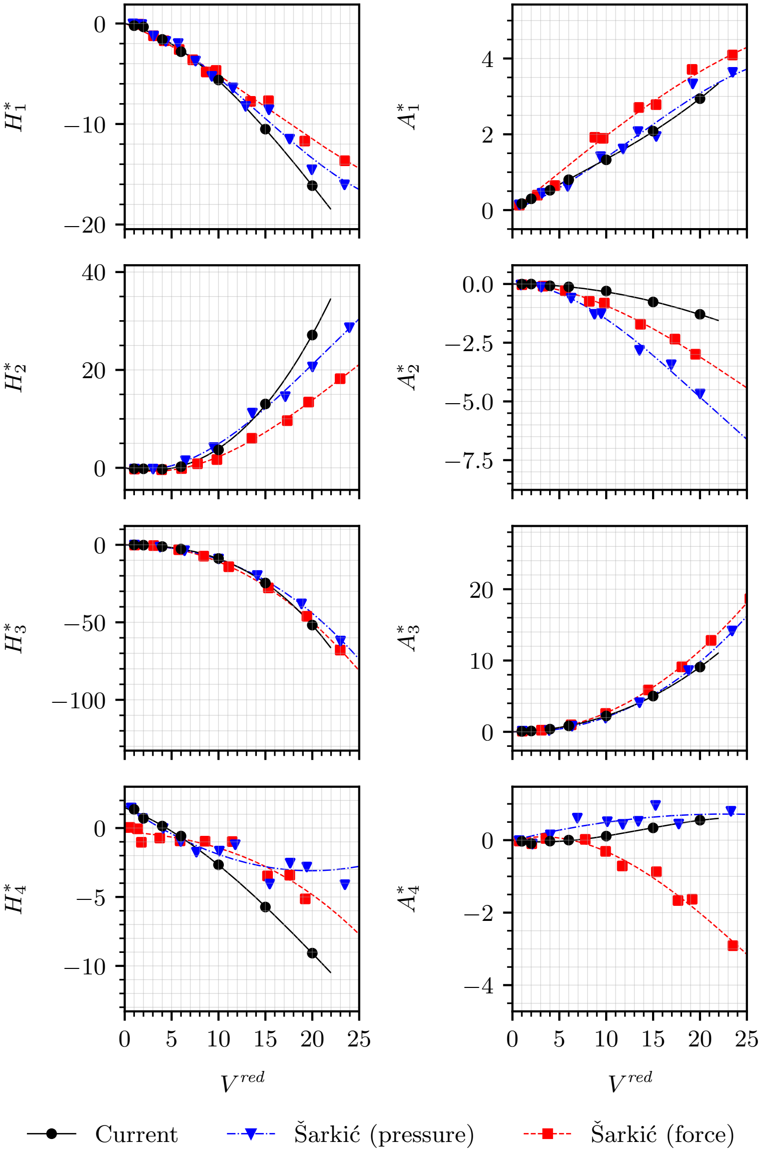

Figure 4.16: Flutter derivatives for the Bridge obtained from single-frequency forced oscillations.

Šarkić et al. (2012) provide data using an experimental WT, including by forced motion. Derivatives were obtained from either pressures or forces. This reference publication states that “the separation of the small signals of the aeroelastic forces acting on the bridge deck model from the larger signals due to inertial forces of the model itself is crucial”. This required a reference measurement in still air, under the same prescribed oscillations, which helps to identify the mechanical properties of the model, i.e. inertia effects. These are later subtracted from the total resultant during wind flow, with the difference representing the actual motion-induced components.

A certain selection of derivatives is of primary interest, with the pair (H_1^*, H_4^*) being the main driver for the heave-related flutter branch, whereas (A_2^*, A_3^*) critically influences pitch. Interestingly, for the two referenced experimental results there are noticeable discrepancies, particularly in case of A_4^*. Analogously, the outcome for the Rectangle cross-section is shown in Fig. B.7.
The meaning of the derivatives is visually substantiated in Fig. 4.17. It is a depiction showing which flutter derivatives are linked to the amplitude of the prescribed motion, and which to the rate of it. When isolating pure heave caused by lift only, or pure pitch triggered by the moment only, the main pairs of derivatives are clearly identifiable.

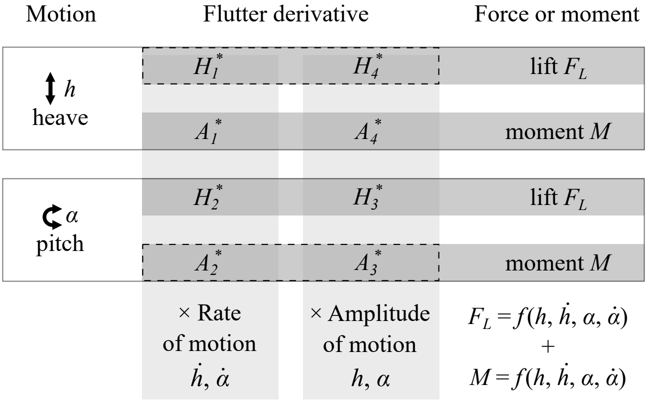

Figure 4.17: Meaning of the flutter derivatives in relation to the amplitude of motion and its rate of change.

The flutter derivatives receive significance in the depiction using the real and imaginary axes. In Fig. 4.18, imposed heave is revisited, linking it to the appropriate flutter derivatives. These are proportional to the arising force. With the motion being sinusoidal, the assessed force is expected to be similar, accompanied by a phase shift. A wave with the amplitude $F_{L,0}$, angular frequency ω and phase ϕ has an equivalency with a complex number. This is shown in Fig. 4.19, where three planes are introduced to support the discussion. Evolution in time and the complex and real planes complement the polar plot.

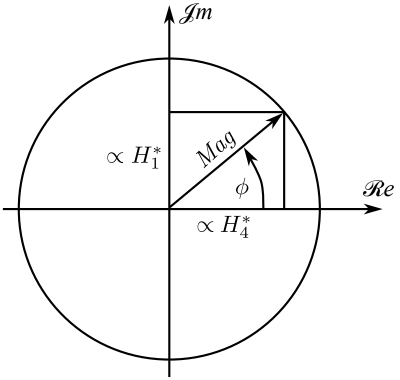

Imposed heave

$$h = h_0 \sin(\omega t)$$

$$\dot{h} = \omega h_0 \cos(\omega t)$$

Resulting lift

$$F_L = F_{L,0} \sin(\omega t + \phi)$$

$$F_L \propto H_1^*, H_4^*$$

$$Mag \propto \sqrt{{H_1^*}^2 + {H_4^*}^2}$$

$$\phi = \tan^{-1}\left(\frac{H_1^*}{H_4^*}\right)$$

Figure 4.18: Exemplifying flutter derivatives for pure heave in the polar representation.

$$F_L = F_{L,0}\left[\cos(\omega t) + i \sin(\omega t)\right]$$

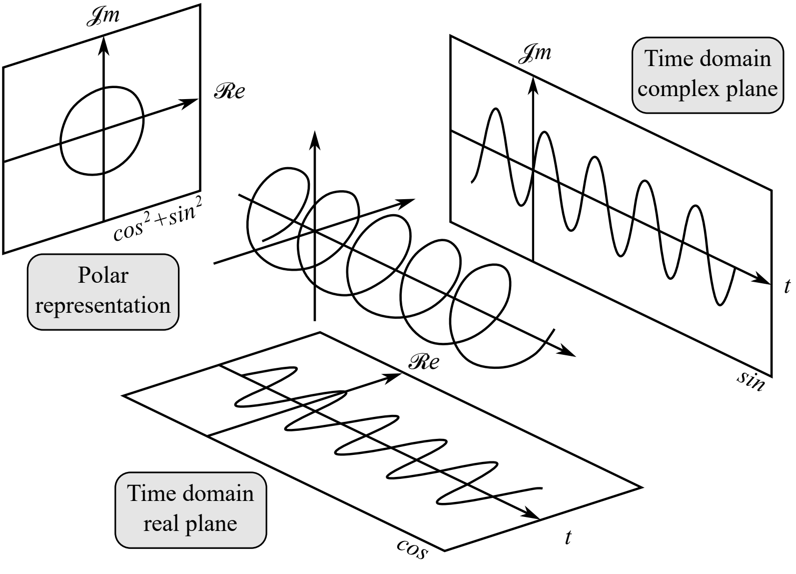

Figure 4.19: Defining the force using three representations, adapted from Duncan (1988).

Duncan (1988) discusses this equivalency relation, where the three-dimensional evolution is called a Heyser spiral or corkscrew. A Hilbert transform connects the real and imaginary parts, which is related to the Fourier transform.

4.2.5 Combined multi-frequency and -direction approach

Combining multiple frequencies, amplitudes, and directions proposes several benefits. It increases efficiency by reducing the number of simulations and offers a more realistic scenario, as bridges naturally oscillate at multiple frequencies with mode shapes superimposed. This may better capture potential interference. The simplest approach is to impose multiple amplitudes and frequencies for each direction, which mathematically results in a summation, as shown in Tab. 4.4.

Table 4.4: Various possibilities for forced motion.

Motion	Single frequency	Multi-frequency	Multi-direction
heave h	$h_0 \sin\left(\omega_h t\right)$	$\sum_{h_i} h_0^i \sin\left(\omega_h^i t\right)$	$\sum_{h_i} (\ldots) + \sum_{\alpha_j} (\ldots)$
pitch α	$\alpha_0 \sin\left(\omega_\alpha t\right)$	$\sum_{\alpha_j} \alpha_0^j \sin\left(\omega_\alpha^j t\right)$	

Directions can also be combined, for example in an alternating manner. Fig. 4.20 illustrates this, potentially reducing sixteen simulations to two.

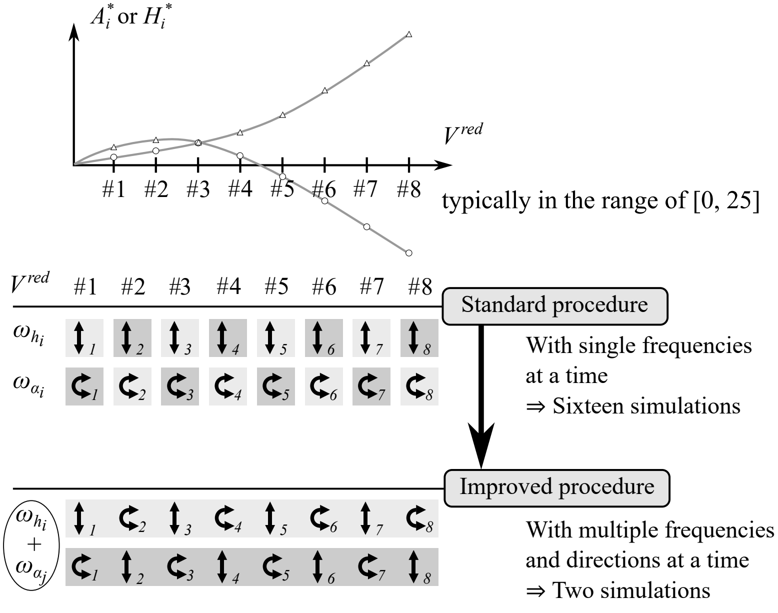

Figure 4.20: Various procedures to determine flutter derivatives using forced motions.

However, it is important to address the reduction in the number of computational runs by considering the total time for the signals, which is necessary to achieve the required amount of data for convergence (i.e. statistical stationarity). The final chosen simulation time should be based on how the frequencies relate to each other. For series of limited duration, this research shows that choosing harmonics (also labeled doubles) is more beneficial than non-harmonics (i.e. primes) as far as the resulting flutter derivatives go. A duration reflecting the least common multiple is a sound choice. In Fig. 4.21, this concept is aided visually. In theory, choosing primes should lead to clearly distinguishable signals. This would apply for series of infinite lengths. Current experience seems to support the notion that the frequency identification based on the Fourier transform of finite temporal data is more accurate when opting for doubles. Here, identifying the series with an integer number of cycles for the transformation is straightforward. Nonetheless, windowing (National Instruments, 2023) should improve the so-called leakage effect when considering primes by reducing the significance of the amplitudes at the boundaries.

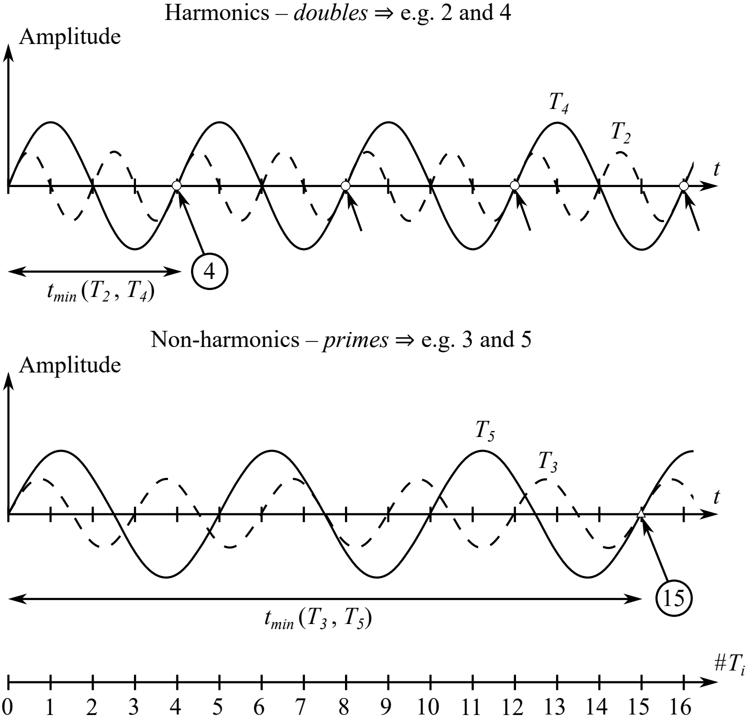
Harmonics – *doubles* ⇒ e.g. 2 and 4

Non-harmonics – *primes* ⇒ e.g. 3 and 5

Figure 4.21: Possible signal lengths for discrete series.

Multi-frequency forced motion is achieved by combining magnitudes selected using the standard approach. Amplitudes are chosen to sum to the value applied during single-frequency investigations, which can be considered as an acceptable limit. For heave, the vertical motion is often taken to be $h_0 < B/20$ or approximately $h_0 < D/(4-5)$, whereas pitch is typically at $\alpha_0 < 5°$. With these magnitudes, the assumptions for using forced motion in obtaining flutter derivatives are maintained. Going from single to multiple frequencies in the time domain is shown in Fig. 4.22.

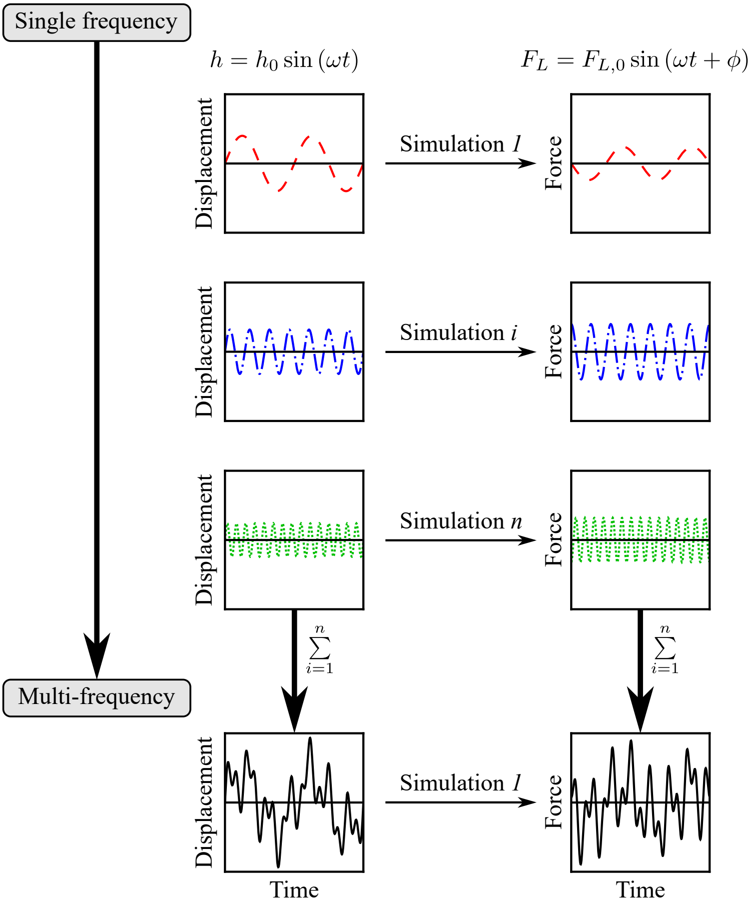

Figure 4.22: Superposing displacement signals and obtaining force time series.

The time-frequency duality is also represented as the basis for signal analysis. Decomposing series is depicted in Fig. 4.23.

$$a(t) = \sum_{i=1}^{n} a_i(t) = \sum_{i=1}^{n} a_{i,0} \sin\left(2\pi f_i t\right)$$

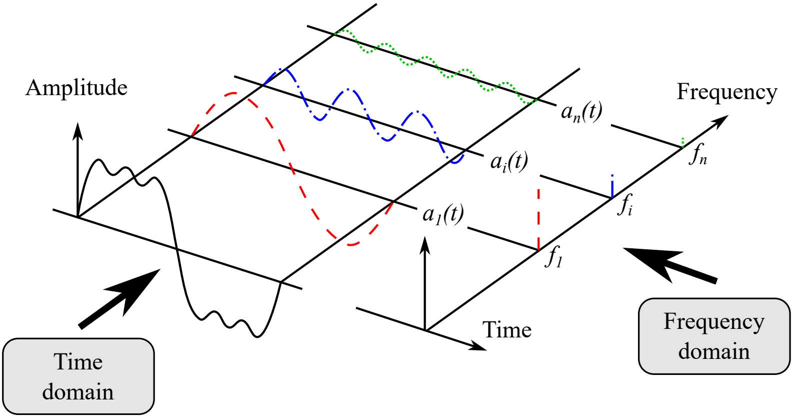

Figure 4.23: Duality of time and frequency of signals.

Mesh moving plays an important role in being able to numerically obtain flutter derivatives by forced motion. Essentially, in addition to a CFD simulation, the grid must be moved appropriately in a robust and accurate manner, which implies the use of ALE-VMS. This FEM-based formulation shows to support the good quality of the outcome, as to be observed in the results of the current thesis. Additionally, Helgedagsrud et al. (2019) discuss multiple aspects related to this numerical approach and possible variations to it when used to compute derivatives. Based on my experience, the additional effort necessary for mesh moving is less than a factor of 1.5 compared to the computation of fluid flow alone. Conversely, running FSI simulations with TWC is at least three times more computationally expensive than pure CFD due to the needed iterations. This increased computational requirement applies both to direct identification and to free vibration tests in wind flow, representing the other indirect manner.
Flutter derivatives were also determined according to an improved procedure, combining frequencies and directions. A pair of simulations lead to all required values assuming frequencies being doubles, while the other combination implied primes. Each run alternated between heave and pitch, for a total of eight frequencies covered, such that derivatives can be obtained for the typical necessary interval. In Fig. 4.24, the outcome is included, here focusing on the Bridge. It is noteworthy that the three approaches produced very similar results, with the primes showing some discrepancy only for the derivatives H_4^* and A_4^*. Derivatives for the Rectangle can be seen in Fig. B.8. Plot lines represent the polynomial fit of order three.

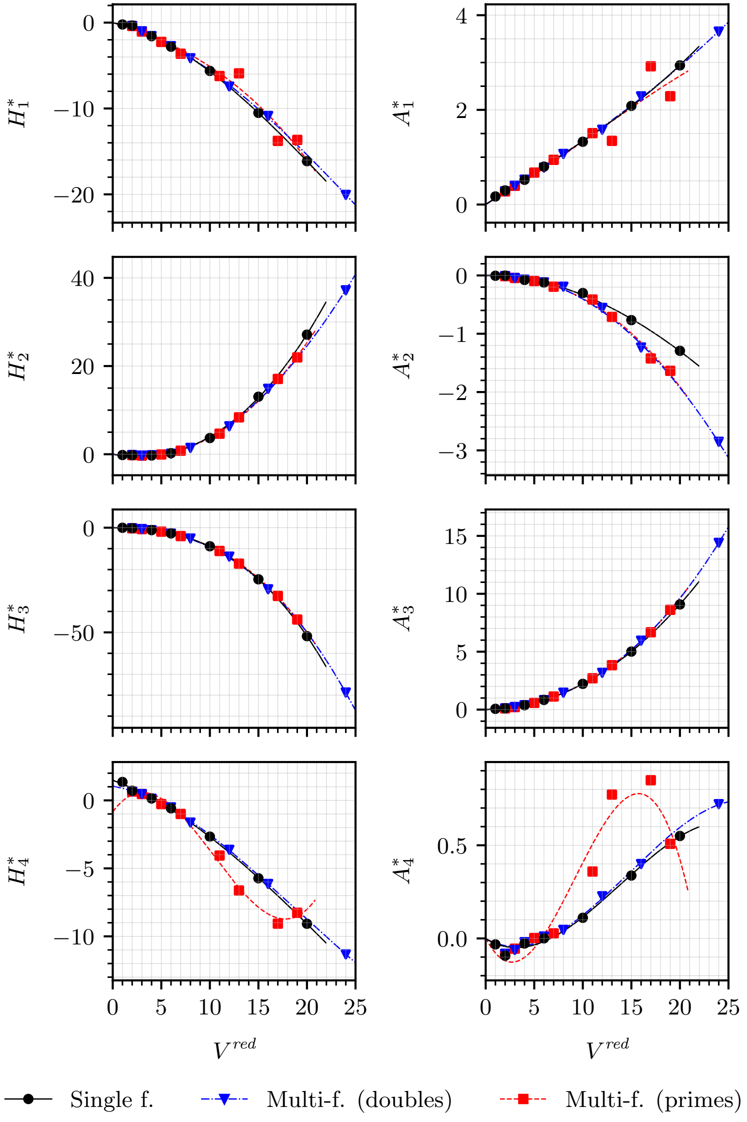

Figure 4.24: Flutter derivatives for the Bridge obtained from multiple frequencies and directions (eight primes or doubles).

The results are very promising with the approach deemed to be adequate for numerical computations. Huang and Liao (2011) presented early data using multiple frequencies, and naming it the Multi-Frequency Vibration Method (MFVM). The scope was limited to a two-dimensional approach of the flow applying a $k-\epsilon$ turbulence model, i.e. a Unsteady Reynolds-Averaged Navier-Stokes (URANS) simulation. The bounding of the amplitude was proposed based on kinetic energy considerations, which from the perspective of the current work might not be necessary. Magnitude can be chosen by limiting the summed contribution to be same as the recommended value by simply dividing equally. Further developments mainly focused on synchronously extracting flutter derivatives for three DoFs, i.e. in lateral, vertical and torsional directions. Xu et al. (2014) reported the need for only one-third of the simulations with this option compared to the standard way. A further improvement is represented by the work of Siedziako et al. (2017). Herein, the authors reported an improved experimental rig, which is capable of the three-DoF motion, concurrently overlaid with white noise. Siedziako and Øiseth (2019) discuss the superposition principle in bridge aerodynamics by investigating bi-harmonic and random motion. Their conclusions support combining frequencies and modes for lift and pitch, but not drag. My findings related to pitch and heave further substantiate such observations. Cross-combining types of motions and superposing multiple frequencies clearly improves simulation efficiency while maintaining accuracy. As the campaign used an LES approach, the high spatial and temporal resolution provides added value.

4.2.6 Direct determination of flutter onset

This workflow also includes the direct determination of flutter. Corresponding work implied FSI simulations with target velocities chosen to be around the estimated critical onset. Such an approach highlights the instability for a particular set of structural properties under certain well-defined wind flow conditions. Two respective solution procedures are compared in Fig. 4.25. Herein, a clear distinction can be made between the direct outcome and the derived quantities, depending on the chosen path. This comparison includes the two versions relevant for the current thesis. Identifying flutter directly is the most intuitive way, yet it is computationally expensive and it only results in the onset conditions identifiable for one cross-section and one set of structural parameters. Indirectly investigating onset based on forced motion generates time histories of forces, which in turn lead to flutter derivatives. This is a model assumption, relying on certain prescribed amplitudes of the motion, as well as the dependence of the force on the motion and its rate of change, while discarding higher order time derivatives. For the former, FSI simulations are needed, typically for several velocity values below and above the predicted onset. For the latter, the number of simulations was described in the previous section.

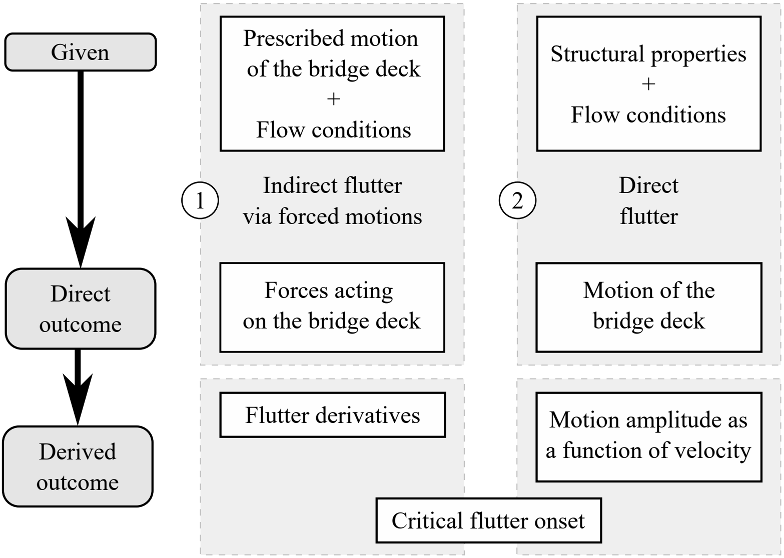

Figure 4.25: Solution procedures for flutter identification.

FSI simulations highlight the onset of flutter for the Bridge at $V^{crit} = 10.79\,\mathrm{m/s}$, as seen in Fig. 4.26.

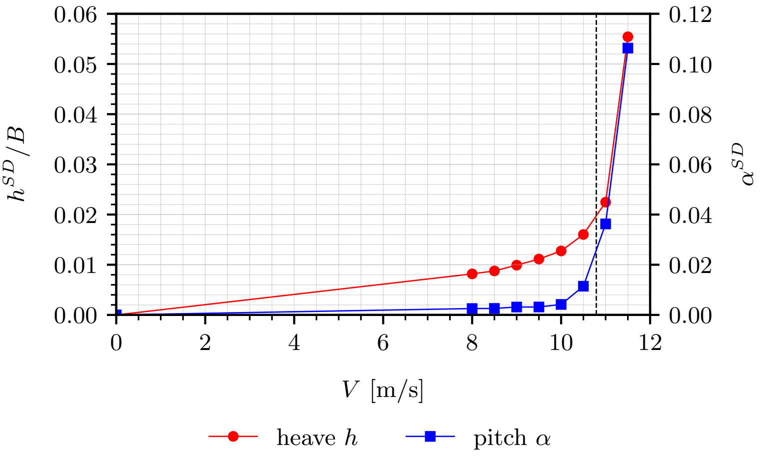

Figure 4.26: Direct flutter identification for the Bridge.

This is based on observing the amplitude of the rotation α as well as displacement h, the latter additionally normalized by B. On the vertical axis, the SD over the same amount of time $t = 3.58\,\mathrm{s}$ is plotted. This implies approximately ten oscillations of the cross-section. As velocities are spaced evenly on the horizontal axis, a superlinear growth can be well observed on the vertical axis once critical onset conditions are met. Similar graphical results for the Rectangle can be seen in Fig. B.6. Furthermore, Tab. 4.5 provides an overview of the structural parameters, as well as the outcomes of flutter identification with the indirect and the direct approaches.

Table 4.5: Summary of the critical onset velocity for various approaches.

		Rectangle		Bridge	
		Structural parameters			
Size					
	B [m]	0.25		0.366	
	D [m]	0.05		0.066	
	L [m]	0.75		1.098	
Translational: *heave*					
	Mass [kg]	3.70		3.48	
	Frequency [Hz]	6.30		1.27	
	Damping ratio [%]	0.16		0.30	
Rotational: *pitch*					
	Inertia [$\mathrm{kg\,m^2}$]	0.0183		0.0526	
	Frequency [Hz]	12.44		3.53	
	Damping ratio [%]	0.55		0.30	
		Flutter onset			
Indirect flutter onset					
	Reference 1	12.05	11.59	11.40	2.64
	Reference 2	12.63	11.91	13.41	2.10
	Single f.	14.89	11.88	9.97	2.92
	Multi-f. (8 doubles)	15.39	11.86	10.45	2.85
	Multi-f. (8 primes)	15.60	11.85	10.45	2.82
Direct flutter onset		14.62	11.80	10.79	2.88
		V^{crit} [m/s]	f^{crit} [Hz]	V^{crit} [m/s]	f^{crit} [Hz]

A rigid body model was set up for the Rectangle based on the properties by Bartoli and Righi (2006), scaling properties to the size used for this study. Similarly, the Bridge assumed sectional parameters from Diana et al. (2020), with values being adapted from large-scale to small-scale. Flutter onset was also included by calculating the critical values using derivatives from other authors. References 1 and 2 denote the works of Matsumoto (1996) and Nieto et al. (2015) for the Rectangle. Analogously, pressure and force-based data from Šarkić et al. (2012) were used for the Bridge. It is notable that all three of the own campaigns for determining flutter using derivatives result in very similar predicted flutter onset. These are within approximately 10% of the observations regarding the direct approach. Other values based on referenced works are within 20%, apart from an outlier in case of the Bridge with experimental WT values using pressure measurements. Onset frequency f^{crit} is presented. For the indirect approach based on derivatives, this signifies the lowest value for which a solution of the instability problem is found. In case of direct flutter, heave and pitch motion is characterized by such oscillations. The value is close to the natural frequency of the rotational DoF, signalling that the pitch branch is triggering the MIE.

4.3 Summary

An LES-type approach was a viable way to analyze the transient loading on bridge decks by wind flow. Current developments covered the entire workflow, ranging from capturing static aerodynamic characteristics at AoAs using CFD to determining the onset of flutter directly with FSI simulations. The novelty was represented by the developments for the multi-frequency approach, where directions of forced motion were also combined. This could deliver the same degree of accuracy as the traditional manner by one frequency at a time. Correspondingly, a reduction of the numerical effort by a factor of four could be achieved. Initial investigations were needed to provide the validation of the domain, meshing and choice of time step. By introducing mesh moving according to an ALE formulation, this was extended to determining the flutter derivatives. Fully-coupled simulations concluded the work, as the highest complexity of numerical investigations. Herein, the results also served for building up valuable data supporting FEM-based multiphysics computations, in particular flow-related events. Moreover, these advances were developed to best exploit HPC. For example, the various AoAs relied on a certain meshing for 0°, while during job farming on-the-fly mesh moving for the target angle represented a pseudo-analysis step. While carrying out the forced motion campaign, this movement of the grid continuously occurred. Such a numerical approach permitted the extension of imposing motions flexibly, while the challenges were shifted to choosing the proper numerical setup. This was necessary, such that amplitudes and time steps conformed to the possibilities of the mesh moving and solution procedure for the flow. Many of the outcomes were in this sense observational and related to best practices in planning and setting up comparable investigations. Additional challenges arose for signal analysis, while assessing force time series. The quality of flutter derivatives was affected by corresponding considerations, such as the choice of combining frequencies or the length of the time series. Similarly, the final step for determining the critical flutter onset relied on quality data and respective polynomial fitting.

Complementary work could focus on FSI phenomena below the onset of MIEs. Most research appears to concentrate on either the aerodynamic performance at various AoAs or identifying flutter derivatives, in addition to directly assessing the onset of this instability. Nonetheless, there is a lack of an extensive overview of oscillating cross-sections under various other flow conditions. Another topic worth pursuing is the detailed analysis of the minimum necessary signal length during forced motion, including confidence intervals. Combined with more insight into the maximum number of superposed frequencies, this could further substantiate the improved methodology for practical usage. Investigations by URANS may also provide additional significant reduction if the approach proves to remain accurate for this specific numerical formulation of the NSEs.

Chapter 5

Wind-structure interaction for lightweight structures

Lightweight structures are prone to wind-induced effects. Numerical means permit the complex modeling necessary to capture these. This chapter focuses on corresponding considerations and various advances, motivated by related challenges. As preliminary content, I include the case of a membrane to outline its characteristics. The shape of such structures is mechanically determined, making the modeling of relevant properties critical. Minimal surfaces and form finding are briefly introduced. Prestress is key in achieving a sound structural state as well as influencing the response to any type of loading. These deliberations are followed by the presentation of a digital workflow for investigating the ABL wind around a unique stadium, with its effects. Content covers sources necessary to construct realistic models for the terrain and the structure, also in recreating the appropriate flow conditions. Multiple numerical treatments are necessary to make these simulation-ready. In particular, aspects for HPC machines are addressed. This case study is included in the broader picture of an integrated CAD and CAE toolchain.

5.1 Fundamentals

5.1.1 Mechanically-determined shapes

All structures deform under load, including self-weight. There is a category that typically exhibits particularly large changes in shape. Cables and technical membranes are such construction elements, which are characterized by practically no bending stiffness, including no resistance to compression, with their load-bearing behavior depending entirely on tensile strength. Fig. 5.1 illustrates this principle. For chains and cables, the shape is usually described by a catenary curve, which assumes own weight in an idealized case. As for the included example, clothes act as concentrated forces F_i (with $i = 1$ to 6), typically unequal, which determine the deformation for an equilibrium state. $R_{H,j}$ and $R_{V,j}$ are the horizontal and vertical reaction forces, whereas s marks the cable sag.

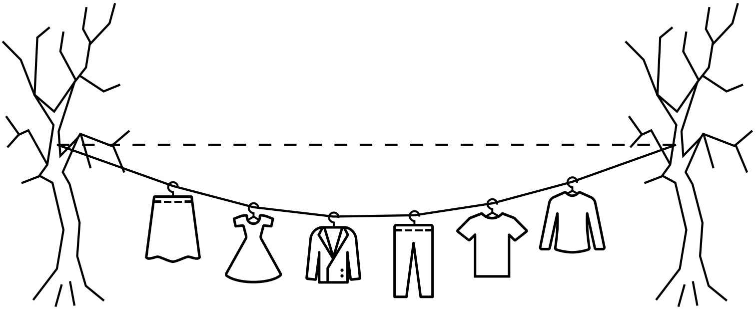

An equivalent structural mechanical system

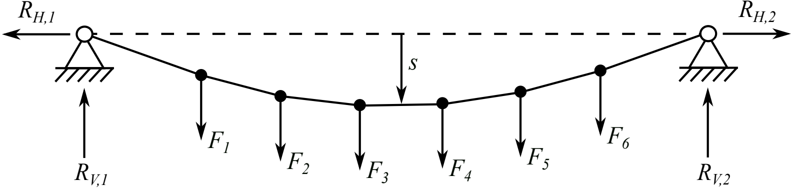

Figure 5.1: Large deformations of a cable under load, adapted from Berger (2005) as cited in Dieringer (2014, Ch. 3).

Fig. 5.2 expands this scenario, ranging from a cable with a single load F in the middle, leading to the internal tension $N_{T,1}$ and $N_{T,2}$, to a couple of cables acting on each other. This latter case results in four internal forces, $N_{T,1}$, $N_{T,2}$, $N_{T,3}$ and $N_{T,4}$. Assuming that there is a fixed connection between the two elements, so these cannot slide, the actual position of this point will depend on the exact value of these internal forces. Consequently, one can control the shape by modifying these components, labeled as prestress. Generalizing the idea leads to a cable net. It is crucial to have alternating high and low points for the corners for a stable and stiff system.

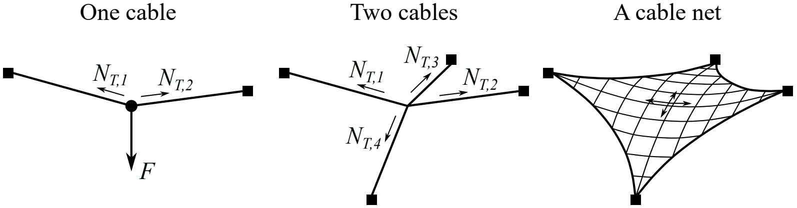

Figure 5.2: From a cable to a cable net.

Cables and membranes are often used in combination to attain function, as well as strength. This is depicted in Fig. 5.3, for the same topology of the so-called hypar or four-point sail. As far as the load-bearing structure goes, it can be a pure cable net, a pure membrane patch, or a combination of both, with varying degrees of connection between the two. The level of interaction depends on the particular technicality of how the elements are joined.

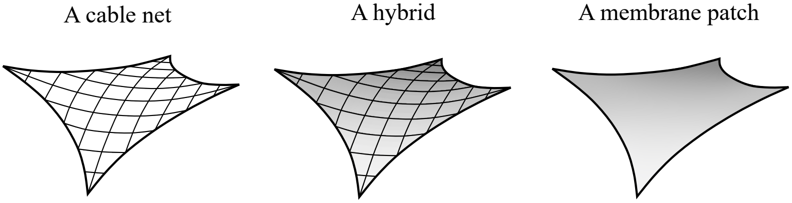

Figure 5.3: From a cable net to a membrane.

From a geometric perspective, such spatial curved shapes can be described by their curvature κ as being the inverse of the radius R describing it:

$$\kappa = \frac{1}{R}. \tag{5.1}$$

In three-dimensional space, we need to consider two radii, R_1 and R_2. Fig. 5.4 highlights a classification, depending on how these relate to each other, in particular their direction, captured by the sign in case of vector notation. The Gaussian curvature $\mathscr{K}$ is a descriptor to relate the principal curvatures κ_1 and κ_2, as the sign of their products, shown in Eq. (5.2). Fig. 5.4 shows the three main categories of synclastic, anticlastic and monoclastic types. From these, the discussion will focus on the middle one, i.e. those with a negative Gaussian curvature, as doubly-curved surfaces are often encountered for lightweight structural shapes.

$$\mathscr{K} = \kappa_1 \kappa_2 \tag{5.2}$$

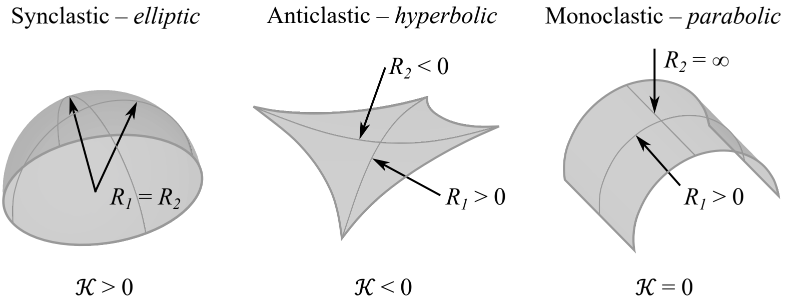

Figure 5.4: Types of shapes characterized by curvature.

The mean curvature is marked by $\mathscr{H}$ and defined as:

$$\mathscr{H} = \frac{\kappa_1 + \kappa_2}{2}, \tag{5.3}$$

which is equal to zero for minimal surfaces, a condition that is relevant for form finding.

Shape is interdependent with forces, defining the load-bearing behavior. Cables and technical membranes are elements that perform well where tensile strength is needed. There is practically no bending or compressive resistance, so external actions, including out-of-plane, are internally resisted by in-plane stresses. In Fig. 5.5, the respective components are highlighted. σ_{11} and σ_{22} mark those along the principle directions 1 and 2, whereas τ_{12} and τ_{21} are linked to shear[*]. These in-plane components are considered constant throughout the thickness, where perpendicular contributions are taken to be negligible.

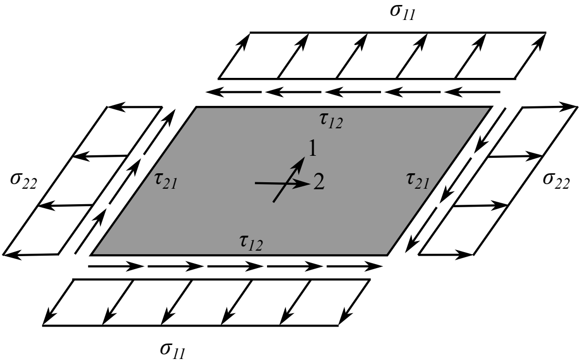

Figure 5.5: Stress state of a membrane element.

---

[*] In the FE methodology, we distinguish between plates in membrane (in-plane) and bending (out-of-plane) action, whereas shells imply a combined formulation.

Lightweight structures made out of technical membrane fabrics are often used to construct doubly-curved roof canopies, with a negative Gaussian curvature. A technical solution typically involves edge cables, providing additional strength. This approach also allows for control of the stress state and the corresponding shape. Fig. 5.6 depicts this aspect on a common saddle surface, where the force in the cable is noted as N^{cab} and the in-plane principal stress in the membrane as n^{mem}.

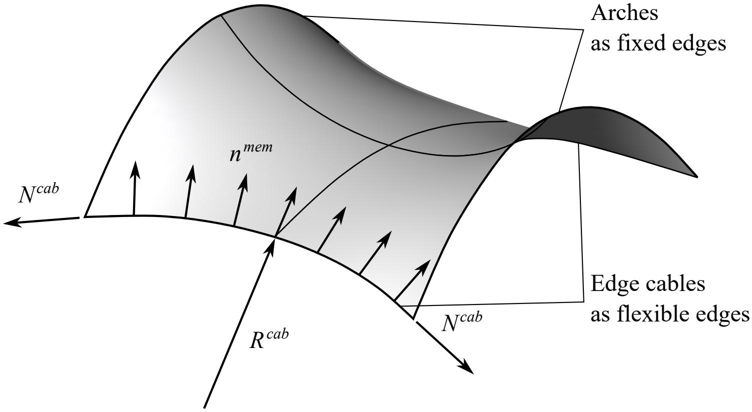

Figure 5.6: Relationship between the stresses in the membrane and the adjacent edge cable.

The relation is marked in Eq. (5.4):

$$N^{cab} = n^{mem} R^{cab}. \tag{5.4}$$

These spatial shapes can be formulated in a parametric space using a two -dimensional description, as shown in Fig. 5.7.
Correspondingly, the surface parameters θ^1 and θ^2 along the parameter lines are sufficient for the characterization in parameter space. The actual shape in three-dimensional Euclidean space is obtained through mapping, an operation based on the Jacobian $J_{X,\theta}$, which connects the two-dimensional parameter space and the three-dimensional geometric space. The undeformed geometry $\mathbf{X}$ and the deformed geometry $\mathbf{x}$ correspond to the reference and current configurations, respectively. The deformed geometry $\mathbf{x}(t)$ is achieved by adding the displacement $\mathbf{u}(\theta^1, \theta^2, t)$ to the reference geometry $\mathbf{X}$ at a specific time instance t. The position $\mathbf{r}$ of a point in three-dimensional Euclidean space, defined by two-dimensional surface parameters θ^1 and θ^2, is expressed using the unit basis vector $\mathbf{e}_i$ as follows:

$$\mathbf{r}\left(\theta^1, \theta^2\right) = x^i\left(\theta^1, \theta^2\right)\mathbf{e}_i = \begin{bmatrix} x\left(\theta^1, \theta^2\right) \\ y\left(\theta^1, \theta^2\right) \\ z\left(\theta^1, \theta^2\right) \end{bmatrix}, \tag{5.5}$$

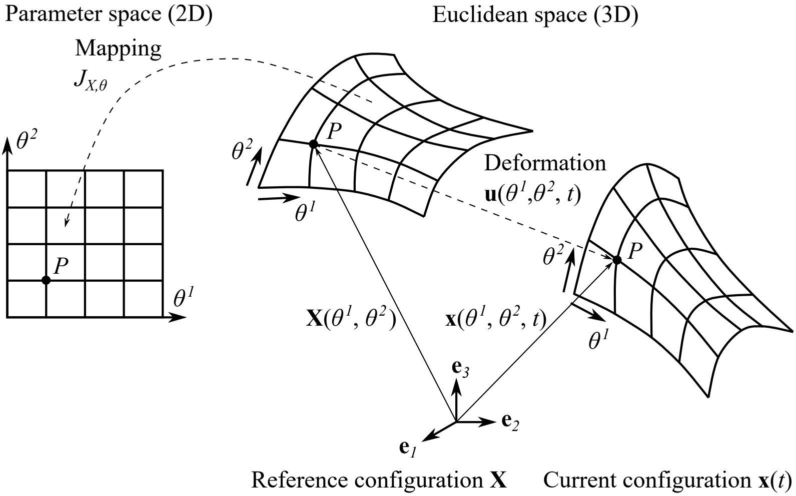

Figure 5.7: Definition of mappings and configuration states in the corresponding parameter and Euclidean spaces.

whereas the mapping of the surface area between these descriptions is defined by the determinant of the Jacobian matrix:

$$J_{X,\theta} = \left\| \frac{\partial \mathbf{X}}{\partial \theta^1} \times \frac{\partial \mathbf{X}}{\partial \theta^2} \right\|. \tag{5.6}$$

A specific deformation describes the difference between the current and the reference configuration:

$$\mathbf{u}(\theta^1,\theta^2,t) = \mathbf{x}\left(\theta^1,\theta^2,t\right) - \mathbf{X}\left(\theta^1,\theta^2\right). \tag{5.7}$$

The previous content described possible geometries and how they can be defined and represented. It is important to highlight the steps leading to the creation of such shapes. While many applications in civil and structural engineering focus on assessing deformations under various loads, it is sometimes desirable to establish a specific geometry that corresponds to a particular stress state. This is the primary function of form finding: to determine a geometry where a given internal stress state and, if applicable, external loading are in equilibrium while satisfying prescribed BCs. Form finding can thus be interpreted as an inverse problem from both engineering and mathematical/mechanical perspectives. This leads to challenges due to the complexity involved in finding a solution. The nature of inverse problems often implies that a unique solution may not exist, so the solving procedure needs to be accurate and stable in providing a feasible answer.

Form finding in membrane structures can be effectively imagined through the behavior of a soap film. This demonstrates how natural forces act to find a minimal surface, closely mirroring the process applied in engineering. A wireframe provides the geometric boundary conditions, i.e., the restrictions on the edges. When dipped into a soap solution – a liquid characterized by surface tension – a shape of minimal area is formed. The surface tension acts uniformly across the film, creating a balanced stress state. This efficient shape is optimal for the given ICs and BCs, as well as the surface tension properties of the liquid. These considerations are observational and provide the basis for experimental scale models as well as various numerical solution procedures.

In the numerical approach, one starts with an arbitrary initial geometry, considered the reference configuration, and iteratively solves the nonlinear problem using computational methods to arrive at the current configuration. The two-dimensional stress state of membranes is inherently statically indeterminate, as internal stresses (tensile forces) are not solely determined by BCs. A proper shape cannot be uniquely determined without additional information. Compatibility between normal strains and shear deformations must also be considered. The following discussion applies in a continuous sense, independent of the discretization used. Fig. 5.8 conceptually highlights the key steps, showing a starting geometry on the left from which a mechanically-determined shape is achieved via form finding. This is contrasted with a typical CAD-created shape[*], which is a purely geometric operation not subject to mechanical considerations. Such a difference can be challenging to distinguish visually. A simple test can help identify the two: a mechanically-determined shape will not deform under the prestress and external loads for which it was designed, whereas a geometrically-constructed model will typically exhibit noticeable deformations under the same loading. This comparison highlights the practical difference between how geometries are constructed in this context.

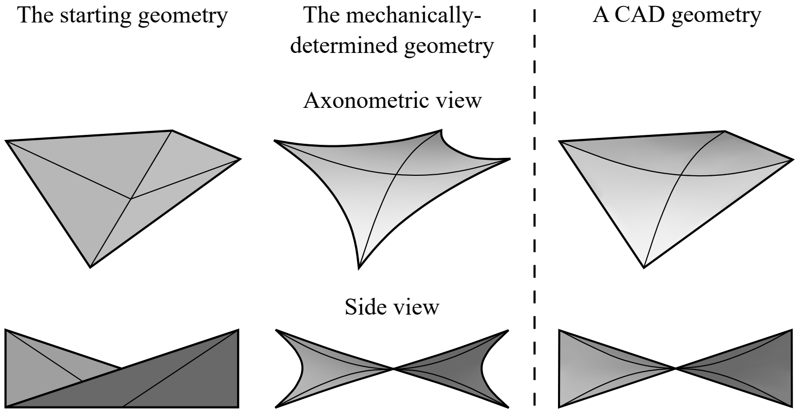

Figure 5.8: Various states of the geometry during form finding alongside a CAD-constructed shape.

---

[*] Straight contour lines can represent valid BCs for form finding. However, in this particular depiction, they are merely a geometric artifact without any mechanical significance.

Numerical methods provide effective means for determining minimal surfaces, leading to an optimization problem from a mathematical perspective, which represents the main interest for the current discussion. The result is a shape characterized by constant and invariant surface stresses. Eq. (5.8) represents a simplified symbolic formulation of the minimization problem for the surface area A. This is achieved by setting the variation of the surface area δA to zero:

$$\delta A = \delta \int_A dA = 0. \tag{5.8}$$

The mechanical equilibrium can be stated using the PVW, similar to the insights in Ch. 2. Assuming a typical case where the self-weight of the membrane is negligible compared to the prestress and aiming to determine a shape without considering external loads, the following integral relation holds in a weak form:

$$\delta W = \int_A \boldsymbol{\sigma}_0 : \delta \mathbf{e} dA = 0, \tag{5.9}$$

where $\boldsymbol{\sigma}_0$ represents the prestress tensor and $\delta\mathbf{e}$ denotes the variation in the strain tensor. The importance of prestress is highlighted, with more detailed discussions available in the works of Sautter (2022, Ch. 3 and App. H) and Bletzinger (2019, Ch. 6). For a comprehensive discussion on deriving form finding, see Dieringer (2014, Ch. 3).

In the numerical context of form finding, the procedure involves solving an inverse problem, which is inherently ill-posed. Due to the nature of the formulation, the solution is non-unique, requiring additional treatment. Spatial discretization is a key factor, as there is an infinite number of ways to approximate the shape using the nodes of a mesh. Within the FEM framework, these nodes can move tangentially to the surface without generating strain energy, except for those on geometric boundaries. Various methods exist to address this challenge, such as modifying the problem's linearization, applying dynamic relaxation, or using homotopy methods. Among the latter, the Updated Reference Strategy (URS), as introduced by and detailed in Bletzinger and Ramm (1999), is noteworthy. This method can be viewed as an enhancement of the Force Density Method (FDM), which was originally developed for designing the cable net structures of the Olympic Stadium in Munich (Linkwitz and Schek, 1972; Gründig et al., 2000). Such approaches help overcome issues related to singularity and ensure that the formfinding process converges to a valid shape that satisfies the required equilibrium conditions.

5.1.2 Coupled effects

The design of lightweight structures can take place in two steps. Often, initially form finding and respective analysis is carried out on the cable net or membrane. This also results in the corresponding reaction forces at the corners. In a second phase, the other parts of the supporting structure are additionally considered. For a specific corner, two elements in tension T and one in compression C represent a skew basis, for the previously determined reaction to be projected onto. The exact placement and length of these supporting elements is up to the design engineer, as any three axes (as long as these are concurrent and non-overlapping) represent a valid basis. In the last phase, the construction is viewed in its entirety.

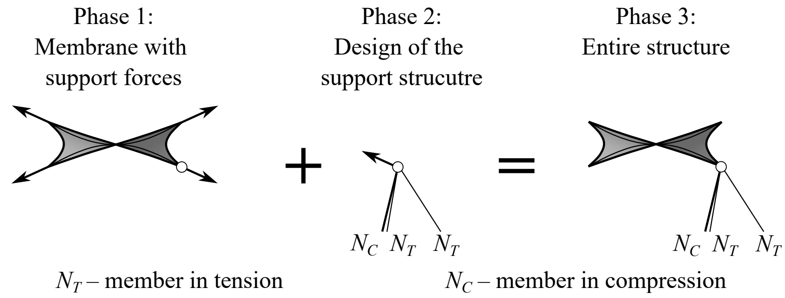

Figure 5.9: Various phases in the preliminary design of a hypar (four-point sail), illustrated for a specific corner point.

Figure 5.10 shows an exemplary hypar with columns and anchoring cables.

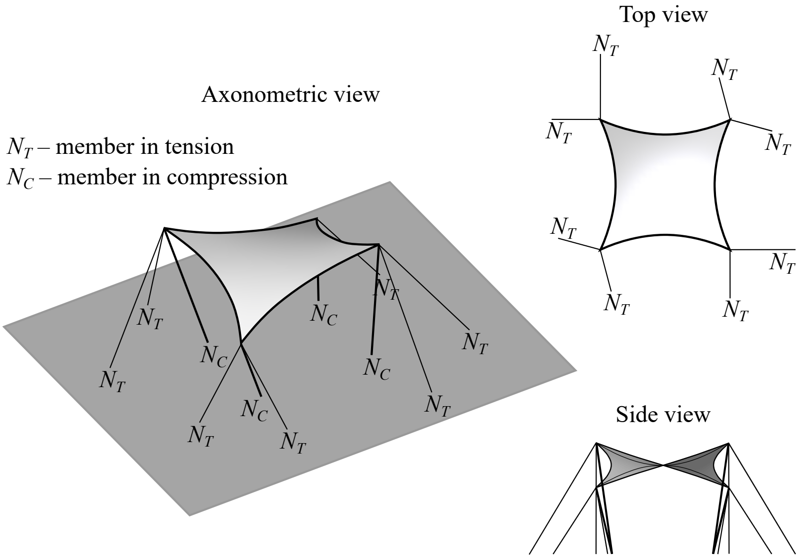

Figure 5.10: Entire structure of a hypar (four-point sail).

For this case, the reaction forces from the corners considering the initial step are now represented by the forces acting in these elements. Their value can be determined by changing the components of each total corner force in the Euclidean base into a skewed reference system, defined by the actual location of the columns and cables. Other constructive solutions are possible, such as implying a single cable tangent (i.e. along) the orientation of the reaction itself. Form and force mutually influence each other, as highlighted in Fig. 5.11. Herein Tryggvason (1979) exemplifies the change of curvature and the change of the cable prestress, caused by internal pressure for a pneumatic structure. This consideration holds for other types of external loads, and the total actual stiffness is strongly dependent on the actual configuration.

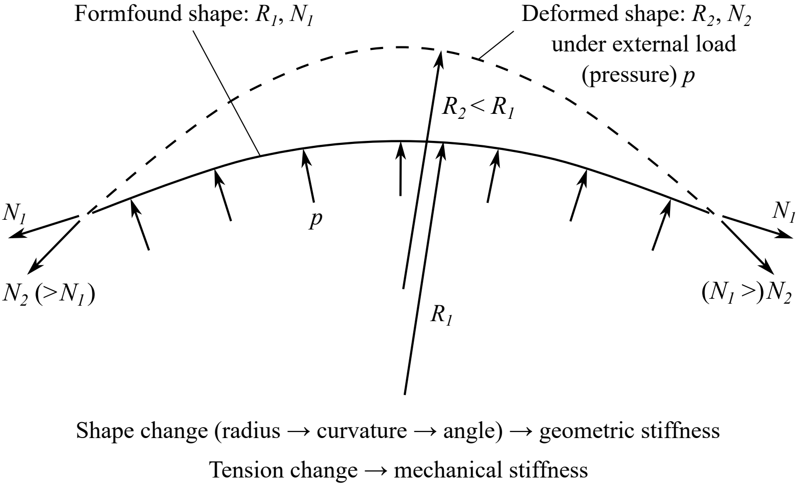

Figure 5.11: Increase in stiffness due to deformation, adapted from Tryggvason (1979).

Furthermore, Petersen and Werkle (2017, Ch. 8) discuss the dynamic properties and vibration modes for chords and cables, which substantiate the dependency of the shape, prestress and respective attributes. The linear theory refers to small vibration amplitudes, which permit the prestress to be considered independent of these, with the sag from self-weight also being negligible. Eq. (5.10) provides the relation to determine the natural frequency:

$$f_{n,i} = \frac{i}{2}\sqrt{\frac{N}{\mu l^2}} \quad \text{with} \quad i = 1 \text{ to } \infty, \tag{5.10}$$

where l marks the length of the segment, μ is the mass per length, and i the order of the mode. A geometric nonlinear view is necessary once the vibration amplitude increases. Consequently, the prestress will become a function of it, with N_0 being the initial value:

$$N\left(\hat{y}\right) = N_0 + \Delta N\left(\hat{y}\right). \tag{5.11}$$

For the first natural frequency, the previous relation is updated to Eq. (5.12):

$$f_1 = \sqrt{1 + \frac{\pi^2 EA}{4N_0}\left(\frac{\hat{y}}{l}\right)^2}\,\frac{1}{2l}\sqrt{\frac{N_0}{\mu}}, \tag{5.12}$$

where $\hat{y}$ notes the vibration amplitude in the middle of the cable. This relation holds for a sinusoidal deformation and small amplitudes. Considerations need to be further detailed when sag under self-weight becomes relevant. The exact shape defines the stiffness characteristics, with stiffness increasing for higher deformation, i.e. a lower radius.
Corresponding lightweight structures are characterized by reduced mass while covering large areas. From a certain extent, the added influence of surrounding air becomes significant. This effect is schematically shown in Fig. 5.12, which marks additional sources of mass, damping and stiffness. Changes of coefficients in the EoM for an SDoF system highlight their influence.

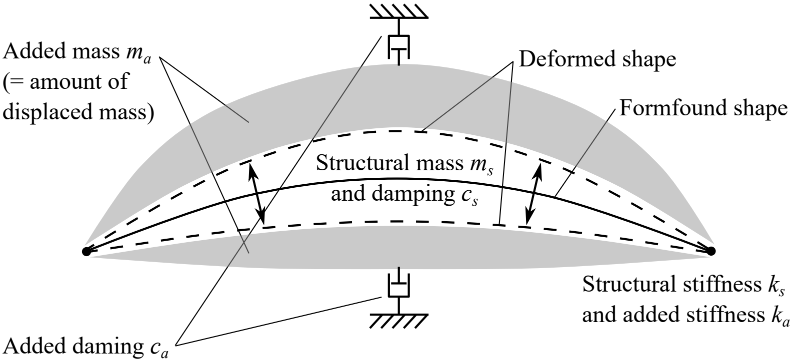

Figure 5.12: Added mass, damping and stiffness for a membrane in motion.

Naudascher and Rockwell (1994, Ch. 3) categorize fluid loading and induced vibrations on body oscillators highlighting these added attributes. The external force is assumed to be split into a mean F^{mean} and fluctuating part $F^{fluct}(t)$. The latter component depends on the wind flow conditions, but also the motion of the oscillator. A simplified view leads to the expression of this force as a linear combination, with terms in phase with acceleration $\ddot{x}$, velocity $\dot{x}$ and displacement x:

$$F^{fluct}(t) = -A\ddot{x} - B\dot{x} - Cx. \tag{5.13}$$

Adapting the notation to clearly mark the added quantities, the coefficients become $m_a = A$, $c_a = B$ and $k_a = C$. This leads to the following EoM:

$$(m_s + m_a)\,\ddot{x} + (c_s + c_a)\,\dot{x} + (k_s + k_a)\,x = 0. \tag{5.14}$$

The expression for the first eigenfrequency in a fluid (whether stagnant or in motion) is derived correspondingly, in comparison to the expression in a vacuum:

$$f_n^{actual} = \frac{1}{2\pi}\sqrt{\frac{k_s + k_a}{m_s + m_a}} \quad \text{and} \quad f_n^{vacuum} = \frac{1}{2\pi}\sqrt{\frac{k_s}{m_s}}. \tag{5.15}$$

A change in frequency can be additionally noted as the respective ratio. Whereas the added stiffness k_a might be considered negligible, Naudascher and Rockwell (1994, Ch. 3) also note that without a complete theoretical model, the effect of added stiffness is impossible to separate from that of the added mass. Consequently, the exciting force is expressed without the dependence on displacement, leading to:

$$\frac{f_n^{actual}}{f_n^{vacuum}} = \sqrt{\frac{1}{1 + m_a/m_s}}. \tag{5.16}$$

The complexity of such coupled phenomena makes it challenging to determine expressions that are valid for a broad selection of structures. Consequently, reference works typically focus on certain examples determining empirical relations. Goldbach (2015) provides an appropriate literature review, summarizing various models and contributing with own observations. Most analytical values provide an accurate description for the behavior in vacuum, which are substantiated by CSM simulations. Other conceptual models attempt to describe this coupling, such as the vortex sheet model, which provides a specific manner of viewing vibrating membranes (Minami, 1998). It considers vortices appearing at the edges, opposite to the direction of the oscillation, as depicted in Fig. 5.13. Herein, a plane membrane is suspended horizontally, vibrating in a half-sine fundamental mode. The challenge lies in the dependency of the added values on the size and shape of the sheet, amplitude of vibration, with additional influence of surface roughness and potential porosity. Bodies oscillating in a fluid displace mass, which are considered to be the additional component. Certain investigations start out with the thin airfoil theory, which can be considered suitable for a flat membrane.

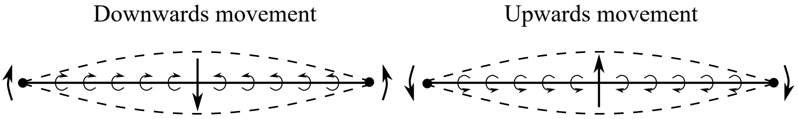

Figure 5.13: Principle of the vortex sheet model for vibrating membranes, adapted from Minami (1998).

Jensen (1972) reports about an experimental setup to quantify these added effects. His work deals with a four-point sail in three configurations: a cable net, a hybrid solution without a strong link between the cables and the membrane, and a solution where the cable net and the membrane constitute a strongly interlinked structural element. The first natural vibration mode is excited by hanging additional weights (denoted as mass m_{ad}) on certain locations of the net and releasing them, provided as a ratio to the own mass m_s. Fig. 5.14 collates important outcomes of this reference work. It can be observed that the added effects for the cable net alone are fairly reduced, whereas the presence of the membrane amplifies these. A reduction of the peak response of approximately 2.5 can be observed, while the eigenfrequency decreases by about 20%, with such changes attributed to c_a and m_a.

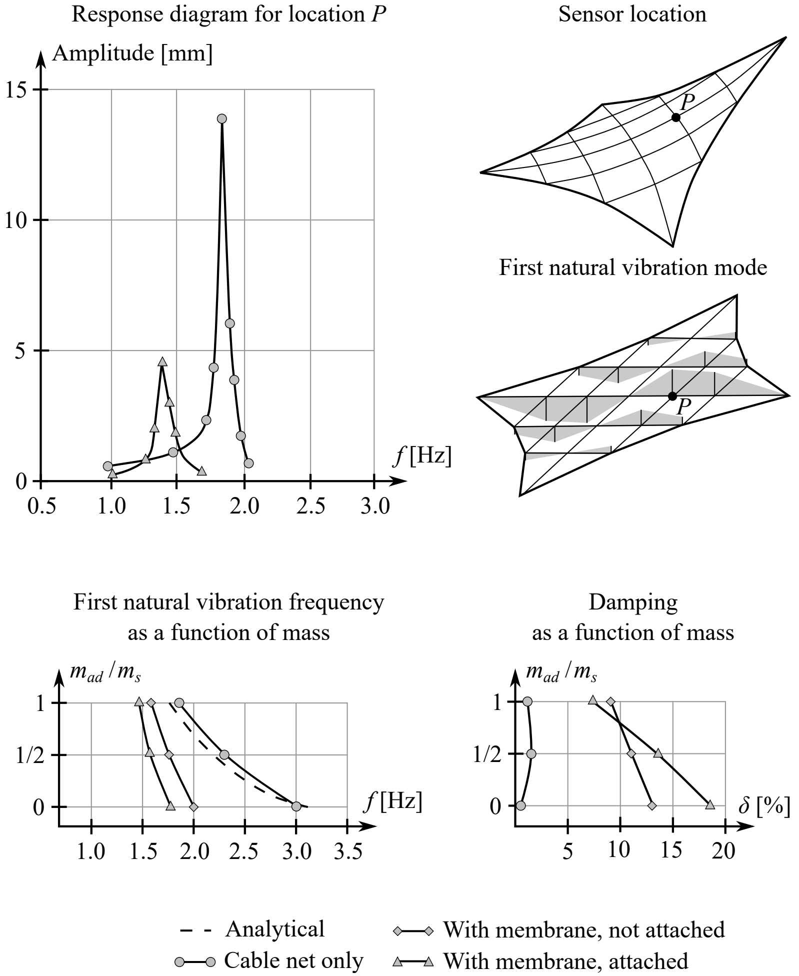

Figure 5.14: Added effects quantified for a four-point sail, adapted from Jensen (1972).

Traditionally, scaled dynamic models are used to capture wind-structure interaction, using the experimental WT. Adapting the geometry for such investigations also defines how structural properties are modified. Accordingly, typical reductions in size of 1 : 25 – 1 : 100 affect thickness. In these conditions, matching the unscaled dynamic attributes is very difficult to achieve for cables and technical membranes. A few controlled tests have been previously carried out at real scale, without the aim of attempting a thorough wind engineering study, but rather focusing on describing the behavior in still air. This is compared to results from analytical models, mostly valid in a vacuum. The numerical WT can provide additional insight by validating this latter aspect as well as enabling fully-coupled analysis without the need to change the geometric scale.

5.1.3 Standardizing wind loading

Codes and standards provide a basic legal and technical framework for assessing the effect of loads on structures. Specific provisions focus on wind-related aspects on various types of common structures. Nonetheless, the shapes and structural properties characterizing membrane roof canopies are not yet thoroughly investigated nor appropriately documented. The TensiNet work group determined representative shapes and noted the importance of a focused study to quantify wind loading, as shown in TensiNet (2015). Fig. 5.15 includes these geometries, which could be the basis for design, including for grouped or combined configurations.

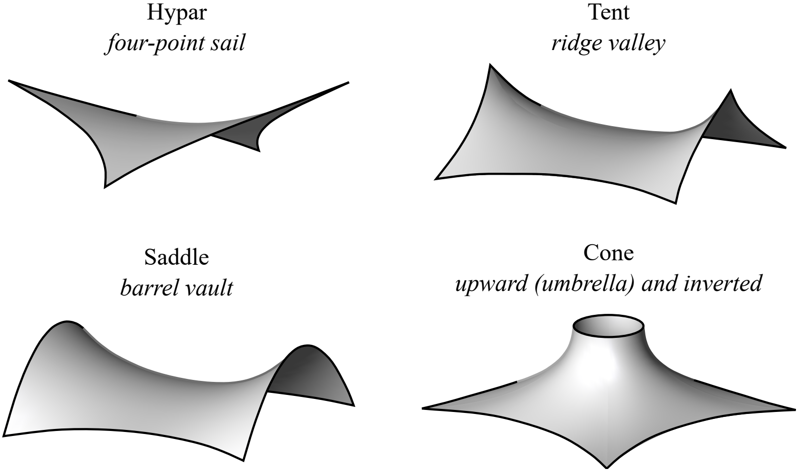

Figure 5.15: Representative shapes for freestanding membrane roof canopies, as identified by TensiNet (2015) and with intermediate results reported in Colliers et al. (2016).

Standardizing wind loading is challenging, as it is exemplified by the recommendations for the circular cylinder. The mean drag coefficient C_D^{mean} and the dimensionless frequency component *St* are summarized in Fig. 5.16. This is an overview of results as collected by Sockel (1984, Chs. 4, 5 and 12) and Hucho (2011, Ch. 3).

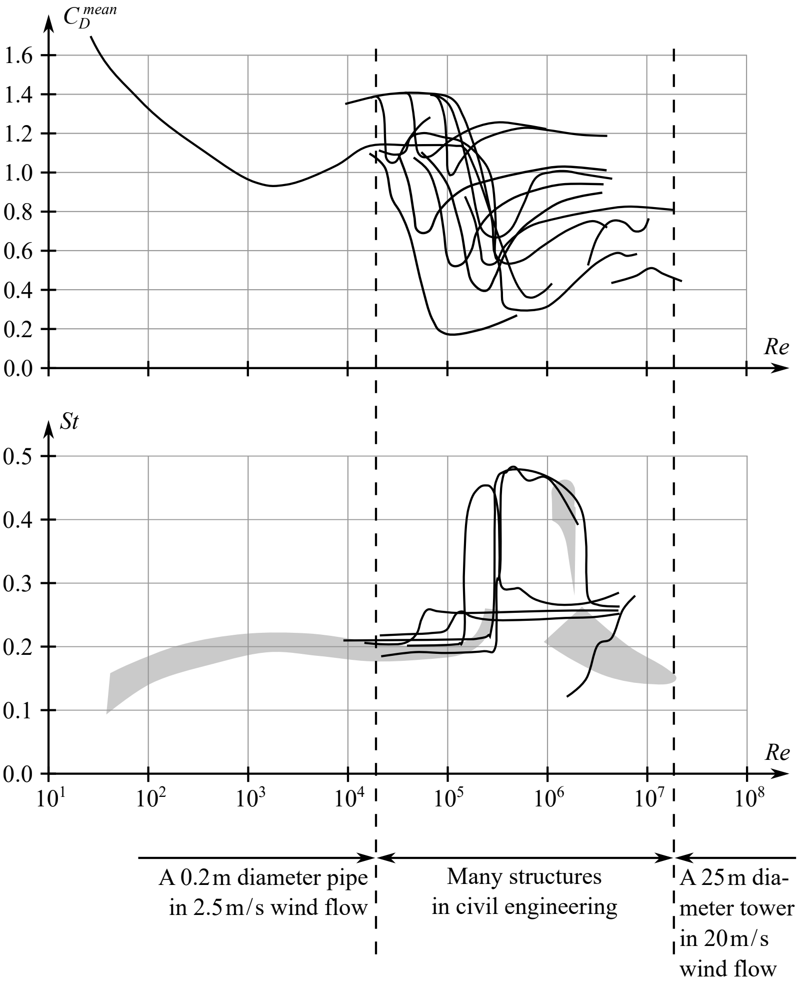

Figure 5.16: Challenges in standardizing wind loading for a circular cylinder, highlighted by a collocation of results from multiple authors, adapted from Sockel (1984, Chs. 4, 5 and 12) and Hucho (2011, Ch. 3).

Variations occur depending on turbulence conditions, surface roughness and the geometric scale. Some insights were gained on real size structures vibrating in wind flow. Crucially, most changes happen in the range of 10^4 *Re* to 10^7 *Re*, which is relevant for the bulk of structures in civil engineering. The drag force is typically of less concern for planning, whereas the correct assessment of the fluctu-

ating cross-flow force is important. For the design of membranes, surfaces are curved in two directions, with the geometry often being characterized by non-straight edges. This raises the necessity for more studies on parametrized shapes of this type to evaluate the degree of sensitivity on the *Re*.
Sockel (1984, Ch. 16) also presents the values for the amplitude of the cross-wind (i.e. lateral) force $C^{lat} = C_{sh}^{RMS}$, with input from scientific studies as well as the resulting proposal for standardization*. Fig. 5.17 notes the actual results and the envelope currently used for design. These values are often key for pipes, chimneys and circular towers with the theoretical magnitude of the fluctuating force being defined by its frequency and amplitude.

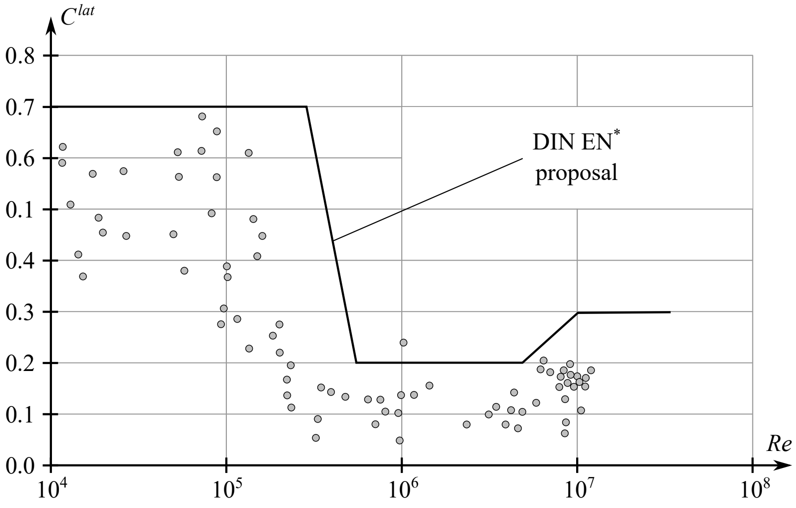

Figure 5.17: Example proposal and current provisions for the cross-wind force coefficient for a circular cylinder, as described by Sockel (1984, Ch. 16) and to be found in the European Committee for Standardization (2010, Ann. E).

Such provisions are available for various bluff bodies, including the detailed information related to a circular cylinder. It is yet to be determined how much transferability exists for usage with mechanically-determined membrane shapes. For high levels of prestress, these structures may be considered rigid. Nonetheless, the degree of roundedness, amount of surface roughness and various other considerations require further research.
Current recommendations for curved roofs are shown in Fig. 5.18. These include a monoclastic and a synclastic shape, and imply an enclosed building canvas. Pressure zones are identified and provided in tables. For the case of vaulted roofs, a fairly clear zoning $A - B - C$ can be identified. It is critical to note that the coefficient value for A can be negative.

---

* DIN stands for the Deutsche Industrie-Norm and EN for the European Norm.

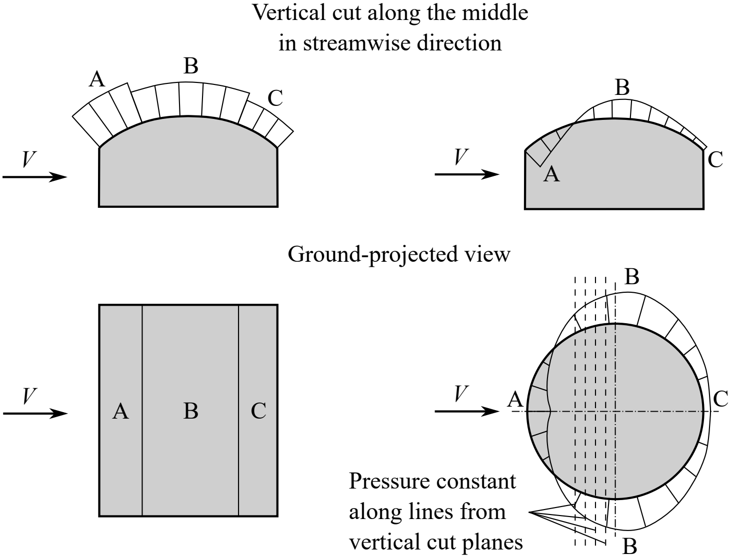

Figure 5.18: Provisions for pressure distribution on vaulted roofs and domes, adapted from the European Committee for Standardization (2010, Sec. 7).

A regional complementary work is represented by the Consiglio Nazionale delle Richerche (2019), which serves as a local enhancement and user's manual for the European Committee for Standardization (2010) in Italy. This includes additional provisions on enclosed structures, with hyperbolic paraboloid roofs. External pressure from wind loading is tabulated for rectangular, circular and elliptic floor plans. While these provide more insights for saddle-type shapes, the usage is limited to one-sided (i.e. from above) action, while considering the surface rigid.

Dealing with freestanding roof canopies is shown in Fig. 5.20, as current codes and standards cover this aspect. Considerations refer to double-pitched solutions, in certain configurations, including depending on the degree of obstruction for the flow below them.

The works of Wüchner (2006), Colliers (2014), and Colliers (2020) cover multiple investigations on the four-point sail, with insights towards categorization and standardization. Michalski (2010) details various efforts on the inverted cone shape. Studies on hyperbolic paraboloid roofs are included in Rizzo et al. (2012) and Rizzo et al. (2021), to name a few. Such selected references highlight existing efforts, yet standardizing wind loading currently only addresses a limited set of aspects. More insight would be needed for lightweight structures, specifically doubly-curved surfaces, using flexible cables nets and technical membranes. These mechanically-defined shapes represent a constructive solution for which ensuring structural resilience needs to be adequately supported during design. Apart from standard ABL wind, the susceptibility to various special storm events should also hold interest.

Definitions
for a hyperbolic paraboloid
of circular plane contour

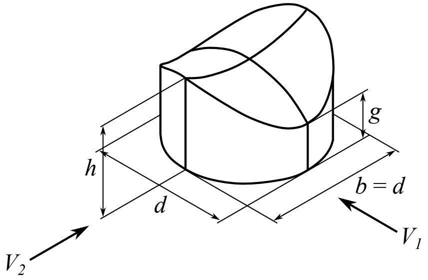

Vertical cut along the middle
in streamwise direction

Ground-projected view

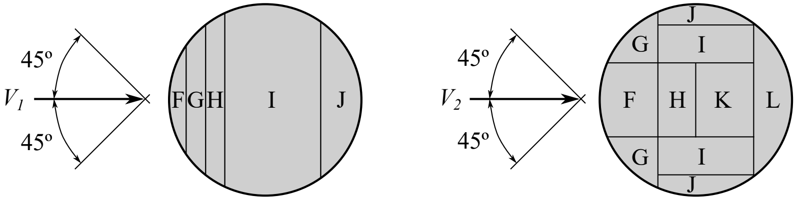

Figure 5.19: Provisions for pressure distribution on hyperbolic paraboloids, adapted from the Consiglio Nazionale delle Richerche (2019, App. H).

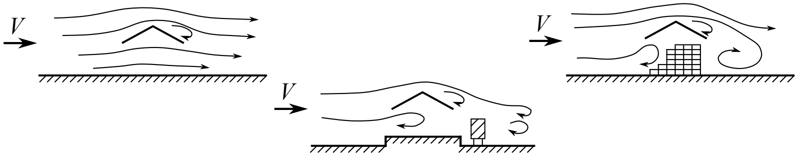

Figure 5.20: Considerations for dealing with freestanding roof canopies, adapted from the European Committee for Standardization (2010, Sec. 7).

5.2 Research and development

The Olympic Stadium in Munich has motivated multiple engineering advances since the activities leading up to the Summer Olympics in 1972. For my current research, the corresponding efforts related to the numerical form finding and analysis of this lightweight structure are of particular interest. It is a unique construction, inspired by the Tanzbrunnen in Köln (1957)[*] and structure of the German Pavilion for the World Expo in Montreal (1967)[†]. Large surface area is covered by a cable net structure, cladded with transparent acrylic sheets. This results in a lightweight roof, with stiffness achieved by anticlastic curvature and prestress. Due to its size, it is a landmark of Munich, with its characteristic shape marking the skyline, as shown in Fig. 5.21.

Figure 5.21: Roof of the Olympic Stadium in Munich (on 01.09.2023).

The Olympic Park is located approximately 5 km northwest of the Munich city center. Notably, the Olympic Swimming Pool, the Olympic Hall, and the Olympic Stadium define this area, featuring similar roof designs. These structures are ordered according to their size and enumerated counter-clockwise from east to west. Additionally, the Olympic Tower oversees the venue, standing at 290 m tall (Winterstein, 2020, Ch. 4).
I focus on covering the necessary steps in defining a realistic and complex numerical model for the structure as well as the wind flow. The latter aspect is only briefly covered by the original activities, many of which are summarized in Leonhardt and Schlaich (1973). Considerations at that time were predominantly related to the structural concept and constructive solution to build the stadium. The influence of the environment was addressed within the scope that was technically possible 50 years ago, and in the manner according to construction normatives and standards. Herein, there were some provision related to loads from snow and wind. My work includes various numerical developments, which extend the possibilities provided by the numerical WT. Whereas the original planning activities were linked to determining a geometry for a target prestress state, as discussed in Sec. 5.1, the current research approached this from

---

[*] www.sl-rasch.com/de/projekte/tanzbrunnen.

[†] www.archdaily.com/623689/ad-classics-german-pavilion-expo-67-frei-otto-and-rolf-gutbrod.

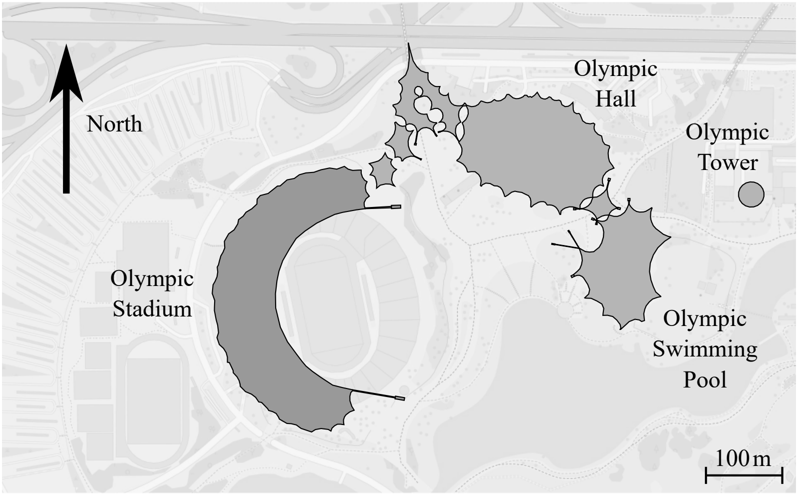

Figure 5.22: Map of the Olympic Park in Munich and its main constructions, based on OpenStreetMap.

an inverted perspective. Namely, after identifying a realistic geometry based on various sources, the aim was to find a feasible prestress state. This served as the prerequisite for CFD and FSI simulations in an HPC environment. Accordingly, possibilities of structural analyses are shown in Fig. 5.23.

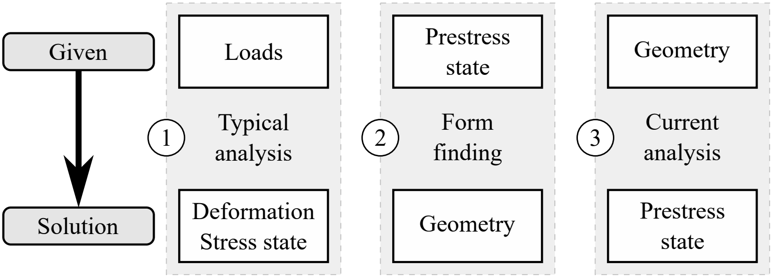

Figure 5.23: Typical possibilities of analyses with the input and the outcome.

5.2.1 Structural concept of the Olympic Stadium in Munich

The roof of the Olympic Stadium covers the western tribune. Its load-bearing structure is made up of nine fields (also called patches), numbered clockwise from south to north. These are connected to each other, forming almost half of a ring. A ring cable sustains the inner edge, towards the sports track, anchored by concrete blocks. Each patch is essentially a cable net, with edge cables forming the contour. Fields 2 to 8 are almost identical. An overview of the structural concept is shown in Fig. 5.24.

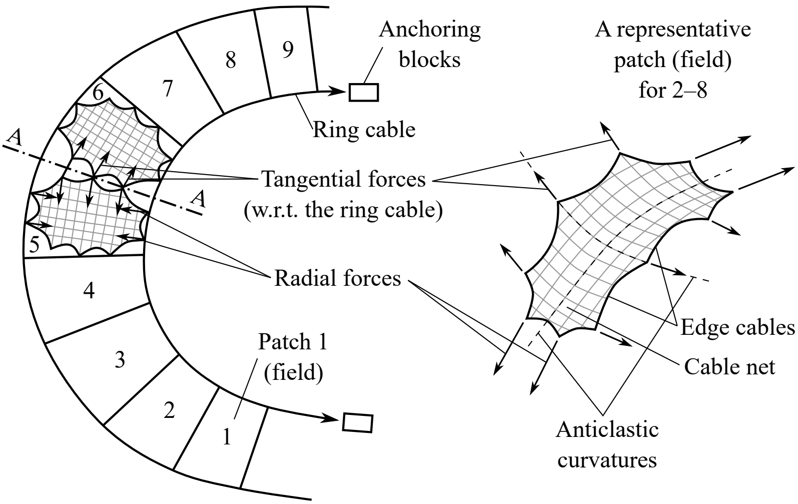

Figure 5.24: Overview of the roof structure, adapted from Leonhardt and Schlaich (1973).

There are various key structural components for the representative patches. Tension is transferred from the cable net within each field, through the edge cables bound them, to the main supporting structure. Pylons, floating supports and the rigid links are members under compression. The main cables transmit forces to the foundation points through tension. Additionally, short cables directly anchor patches to the ground. These concepts are highlighted in Figs. 5.25 and 5.26.

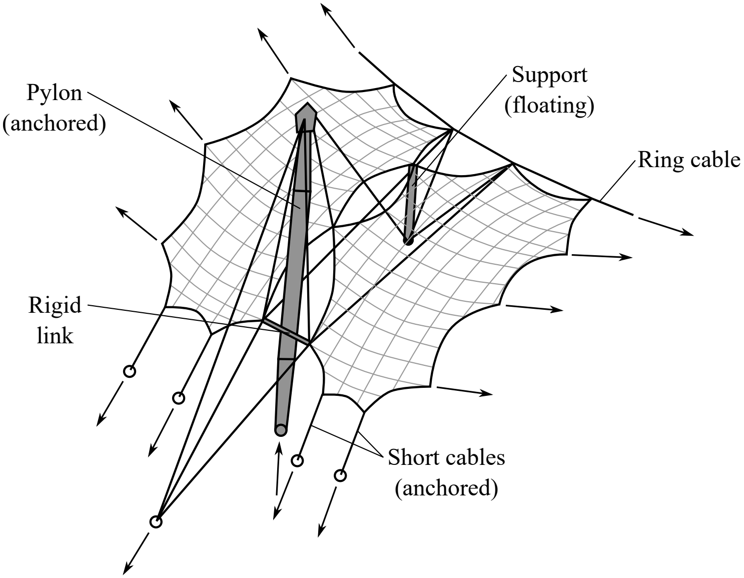

Figure 5.25: Key structural components for a representative patch, adapted from Leonhardt and Schlaich (1973).

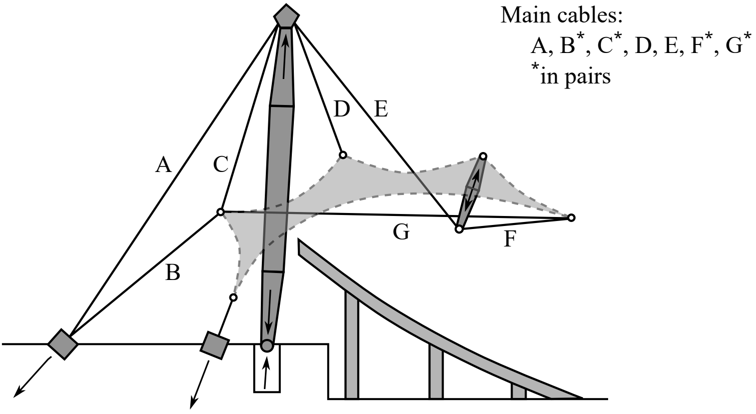

Figure 5.26: Load-bearing for a representative section A–A (see Fig. 5.24), adapted from Leonhardt and Schlaich (1973).

5.2.2 Identifying and modeling a realistic geometry

The realistic geometry results from various sources. An iterative workflow is shown in Fig. 5.27 as it leads up to the initial geometry.

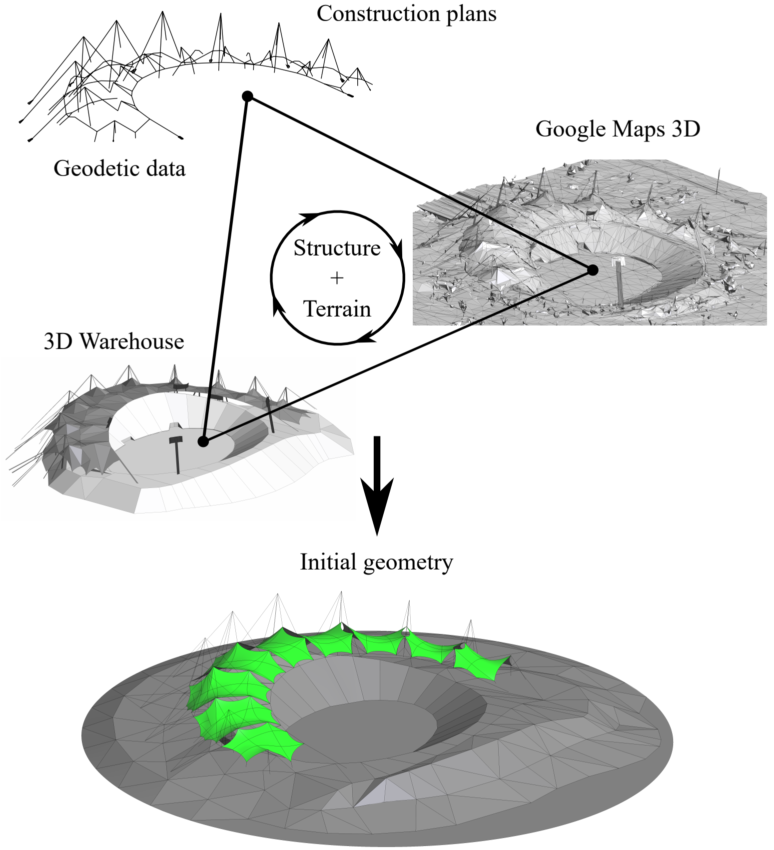

Figure 5.27: Iterative workflow for creating the geometry for the Olympic Stadium, including its surroundings.

Herein, geodetic measurements (Archivraum Olympiapark München, 2010) represent the highest quality source, with data characterizing the built construction. These are available for the anchor points, tops of pylons, endpoints of the floating supports, as well as some points in the middle of fields 2 to 8. Construction plans (Leonhardt and Andrä, 1969) aid identifying curvatures, albeit projected in the horizontal plane and related to the design state. This information is sufficient for the roof, with some uncertainty related to the curvature of edgecables inside the patches. A complementary workflow[*] based on extracting information from Google Maps 3D supports these findings. Characteristic points seem to be accurate to within 5 m. The added value is contributed by defining the surrounding terrain. Similarly, 3D Warehouse[†] contributes with beneficial aspects in shaping the area influencing the wind flow field.

For the CFD simulation, all surfaces affecting flow are relevant to model properly. According to this remark, main cables and compressive elements are not explicitly included. The influence of the line-like members on the flow field is deemed minimal. Conversely, the CSM model contains all of these parts, as they are key in analyzing the structure. Fig. 5.28 includes the characteristic dimensions of these numerical models.

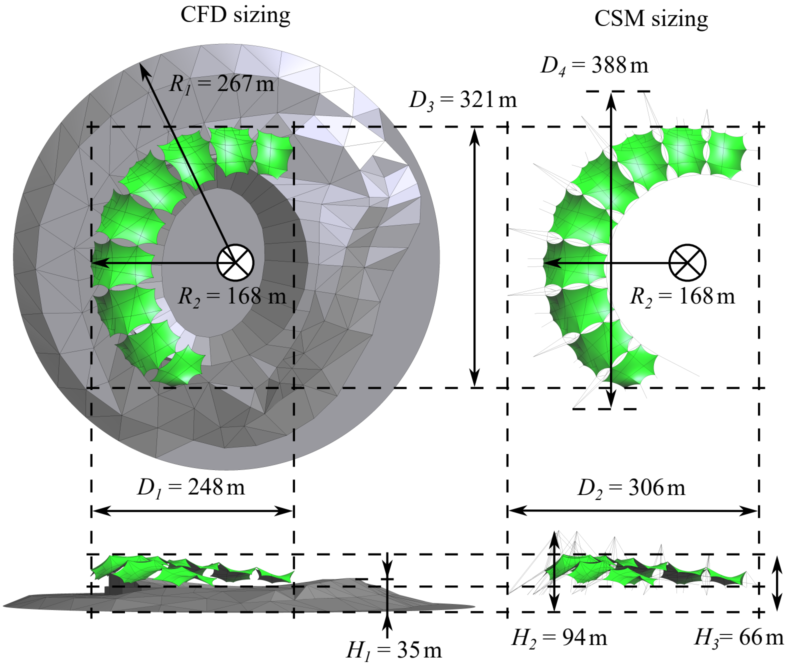

Figure 5.28: Realistic geometry for CFD and CSM simulations.

Terrain is captured up to a radius of $R_1 = 267$ m from an approximately identifiable center, while the outer edge of the patches is located at $R_2 = 168$ m from this point. The top of the middle patches reaches up to the height $H_3 = 66$ m above ground level. Identified as an initial geometry, this representation also serves as the target, for which a prestress state is to be determined.

---

[*] github.com/eliemichel/MapsModelsImporter.

[†] 3dwarehouse.sketchup.com.

5.2.3 Computational methods for model improvement

Various methods were needed to enhance the constructed models. Consequently, utilities were developed to smooth the surface mesh, as well as to improve the volumetric one. Such interventions need to be accompanied by additional steps. The entire workflow is illustrated in Fig. 5.29. For CSM, only step 1 and 2 are necessary, whereby the surface is smoothened, and the prestress state is optimized. CFD starts out similarly by improving the transition between the triangular elements of the meshed roof. This is followed by a necessary mesh update, as moving the near-boundary nodes is necessary, representing step 3. A last improvement of the entire volumetric grid is achieved by optimizing for element quality, according to step 4. Resulting numerical models are labeled as final, ensuring a realistic geometry that is mechanically feasible.

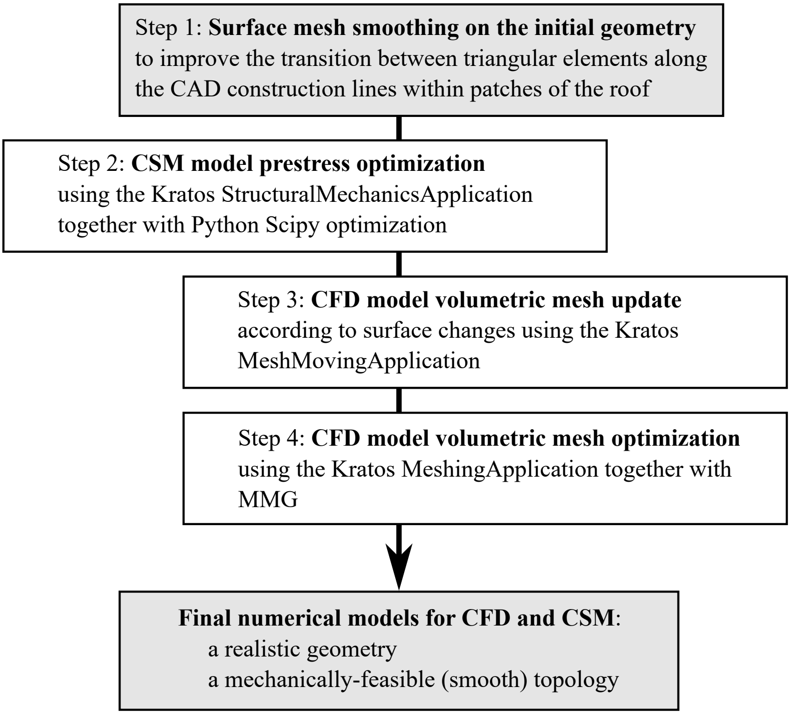

Figure 5.29: Workflow for improving the CFD and CSM models.

Edge detection and smoothing is a relevant geometric handling of the initially constructed CAD shape. The inner lines within the patches are workflow-related artifacts. Continuity* between the curved surfaces is ensured in the C^0 sense, yet

---

* Continuity refers to different levels of smoothness, with C^0 indicating a corner point and C^1 ensuring a common tangent at that specific location.

tangents could not be enforced, failing to ensure the C^1 condition. Edges were identified and handled, as outlined in Fig. 5.30.

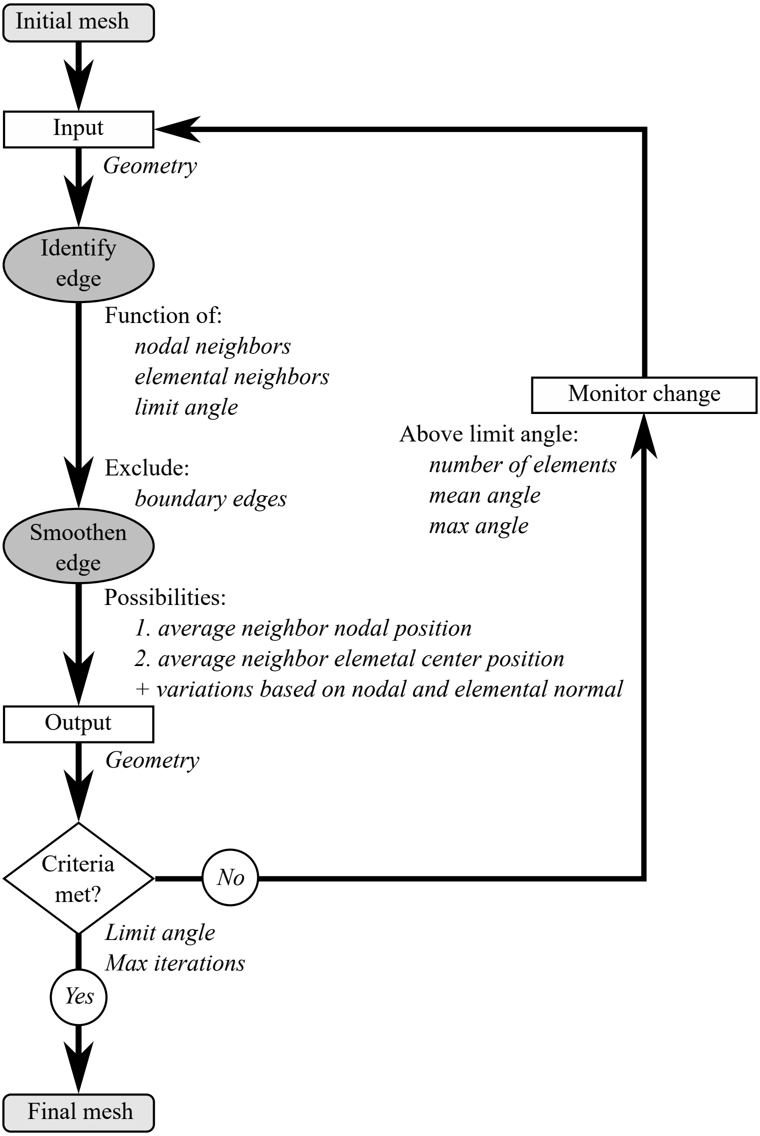

Figure 5.30: Edge detection and smoothing as part of model improvements.

This routine started out with an initial mesh, which served as the input geometry. Edges were identified by marking nodes above a certain limit angle. Smoothening took place by adopting one of many possibilities. Essentially, all ensured a local impact, without a risk of lowering the curvature globally. The starting state as well as the updated mesh are shown in Fig. 5.31. Herein, results for the final mesh resolution are included and the outcome highlighted for patch 4. Identifiable edges within the fields, which are the result of the CAD geometry construction, fade out. However, some corner areas are difficult to treat, which leaves certain regions with high angles between neighboring elements. It is an iterative process, which propagates these artifacts from along certain inner lines to corner areas, whereby the number of affected elements only moderately decreases. Average and maximum angles are meanwhile critically reduced.

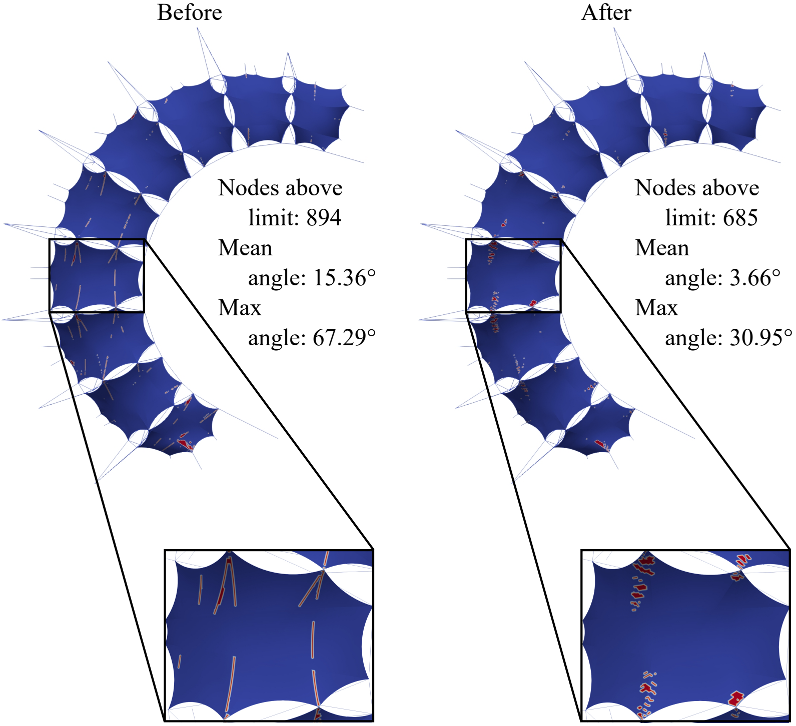

Figure 5.31: Result of the edge smoothing for the final mesh resolution, with limit angle 2° and red marking elements above it.

5.2.4 Determination of a feasible prestress state

The key structural simplification was represented by considering an equivalent membrane instead of the detailed cable net inside the patches. Fig. 5.32 shows a typical segment from the roof, as displayed at the Technical University of Munich.

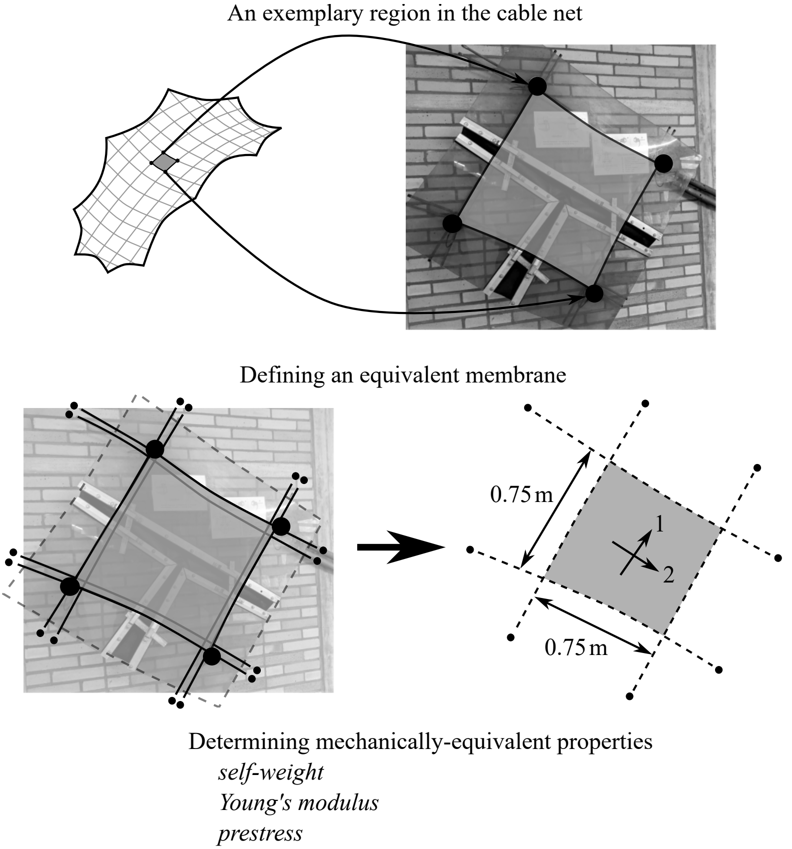

Figure 5.32: Concept for preparing an equivalent membrane instead of an actual cable-net structure.

It was necessary to derive mechanical properties, such that the behavior matched in both cases. Detailing of the structural concept, as can be found in Leonhardt and Schlaich (1973), provided information characterizing this part. Structural strength is ensured by cable strands 0.75 m apart. Assuming a certain thickness for the equivalent membrane lead to the Young's modulus and prestress, converted for this numerical realization. Self-weight was defined accordingly. The prestress was taken isotropic. Moreover, exactly matching the material flexibility of the cable net resulted in a range for the Young's modulus causing challenges for the numerical solution, while resulting in smaller prestress values in the later optimization step. Adopting a lower value for this coefficient ensured numerical convergence for static, eigen and dynamic solving procedures, as well as leading to a realistic prestress distribution. This was one of the key considerations in leading up to an optimization loop. In Fig. 5.33, the procedure is outlined. This was necessary to determine a prestress state given certain initial values.

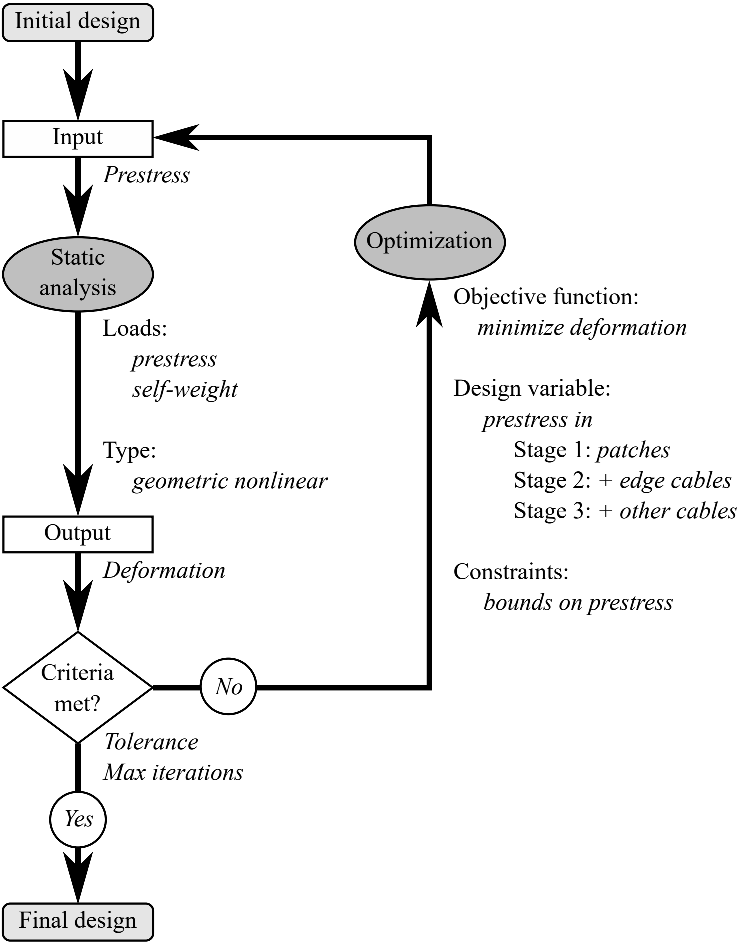

Figure 5.33: Optimization loop for the prestress of the CSM model.

Leonhardt and Andrä (1971) and Leonhardt and Schlaich (1973) provided the initial values for prestress characterizing most components in tension. However, for the fields, no exact values were given, and only the allowable limits are stated clearly. An optimization loop iteratively determined an improved state. This happened in a multi-stage manner, as depicted in Fig. 5.34.

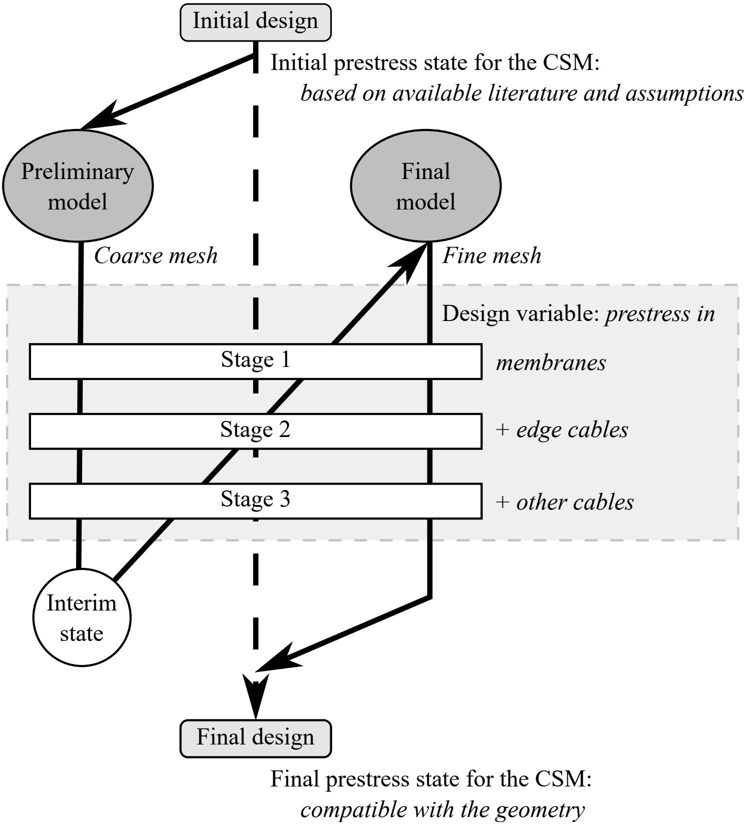

Figure 5.34: Multi-stage strategy for optimizing the prestress of the CSM model.

Correspondingly, multiple stages at two mesh levels were required. The objective function was to minimize deformation as the mean square magnitude of nodal values. For minimal surfaces, the shape under self-weight and prestress has to be equal to the input geometry, i.e. zero nodal deformations. This loop was part of a broader optimization strategy. Accordingly, the workflow started out on a preliminary model, meaning a coarse numerical mesh. Membrane patches, edge cables and further cables were included at various stages, with bounds becoming stricter. A compatible geometry resulted by adopting these steps for a final model with a fine mesh. Summarizing the optimization mathematically follows:

$$\begin{aligned} &\text{Objective function:} \quad f\left(\sigma_0^j\right) = \left(|D_i|^2\right)^{mean} = \frac{\sum_i^{n^{nodes}} \left(d_{i,x}^2 + d_{i,y}^2 + d_{i,z}^2\right)}{n^{nodes}}, \\ &\text{Optimization problem:} \quad \min_{\sigma_0^j \in \text{DS}} f\left(\sigma_0^j\right). \end{aligned} \tag{5.17}$$

The mean square of the nodal deformations D_i is quantified by the objective function f. It depends on the prestress of elements σ_0, for each category j, which can be varied within the Design Space (DS). An outcome for the membrane patches is represented in Fig. 5.35. Peak values are observed in the central fields, being close to the initial design variables. This can be interpreted as the geometry in this region and the starting prestress already being compatible, whereas patches closer towards the extremities are less mechanically-feasible in their initial shape. Similar insights are provided for the edge cables and main cables in Figs. C.5 and C.6.

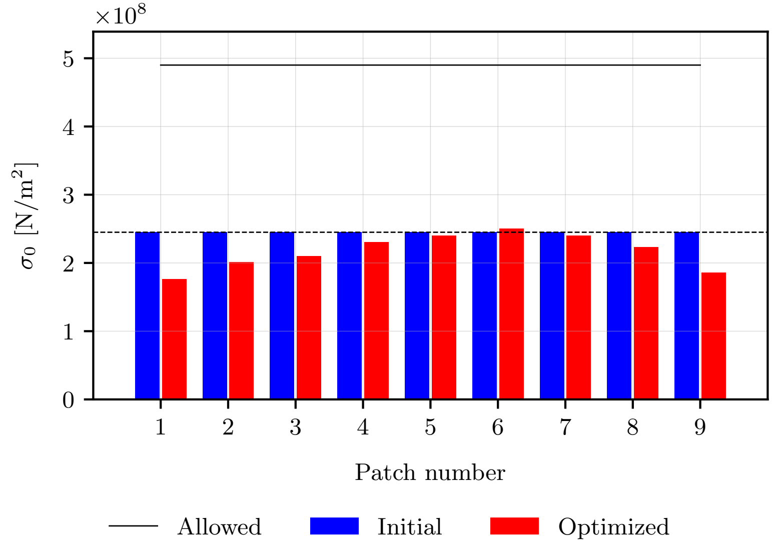

Figure 5.35: Outcome of the prestress optimization for the patches.

I remark that the geometry and accompanying prestress determined are plausible states. The resulting computational models are complex and represent a version, which is realistic without the claim to reproduce the actual state at its full accuracy.

5.2.5 Enabling adequate wind conditions

An adequately sized and properly meshed CFD domain supported high-quality simulations. ABL turbulent flow was generated using the functionality provided by *WindGen*. Fig. 5.36 shows respective considerations and qualitatively the velocity distribution at a certain time step. A quantitative evaluation happened at particular sampling lines, once at the inlet, and the other halfway downstream to the center of the model, noted SL_1 and SL_2.

There are multiple sources available for defining the wind conditions. European Committee for Standardization (2010) provides the general provisions according to codes and standards, with Deutsches Institut für Normung – Normenausschuss Bauwesen (2010) including particularities for Germany. Accordingly, Munich is situated in wind zone 2, with a base mean wind velocity $V_{b,0}^{mean} = 25\,\mathrm{m/s}$. This value is representative for open terrain, i.e. category II. With the Olympic Stadium being situated inside the city, a transitional category between III-IV is deemed appropriate. The respective multiplying factors of the base mean wind profile are 0.77 and 0.56, by taking their average leading to a realistic target magnitude of the mean velocity of approximately $V^{mean} = 16\,\mathrm{m/s}$. This value is characteristic at 10 m elevation, and does not take into consideration any directionality effects, nor seasonality, roughness or orography. Similarly, for a transitional category, by averaging, the roughness length $z_0 = 0.68\,\mathrm{m}$ and the mean wind profile exponent $\alpha = 0.26$ are determined. The reference scientific work on these special structures, Leonhardt and Schlaich (1973), mentions wind velocities of up to 40 m/s to 50 m/s at elevation above 50 m. However, it omits a differentiated reflection regarding mean, gust and maximum values. Such values rather correspond to the gust wind profile in open terrain, according to Deutsches Institut für Normung – Normenausschuss Bauwesen (2010). Winterstein (2020, Ch. 4) includes a detailed analysis, focusing on the Olympic Tower. Herein, the mean wind values of approximately 14 m/s, 18 m/s and 24 m/s are reported for the heights above ground 10 m, 65 m and 200 m. Moreover, this work provides realistic values for turbulence intensity and respective integral turbulence length scale at the reference height $h^{ref} = 65\,\mathrm{m}$, which corresponds to the top of the highest roof patch. Choosing final values and generating wind numerically was additionally based on a detailed evaluation of local wind conditions. This used recorded weather data, as discussed in Sec. C.1. Actual evaluated data from the numerical simulation is included in Fig. 5.37 with dots indicating the targeted reference values. Mean streamwise velocity V_x^{mean} is close to the magnitudes of 15 m/s at 10 m height and 25 m/s at h^{ref}. Turbulence intensity TI_{V_x} reaches 21 % at h^{ref}, with the integral turbulence length scale L_{V_x} being approximately 150 m at that elevation. Turbulent energy is preserved by the numerical scheme up to the cutoff frequency $f^{co} = 1\,\mathrm{Hz}$, and adheres to the evolution of the Kaimal spectrum up to that point. One of the advantages of the numerical WT lies in its ability to enable detailed flow visualization, with vortical structures being of particular interest. A depiction of vortices using the Q-criterion is shown in Fig. C.7.

CFD wind flow domain sizing

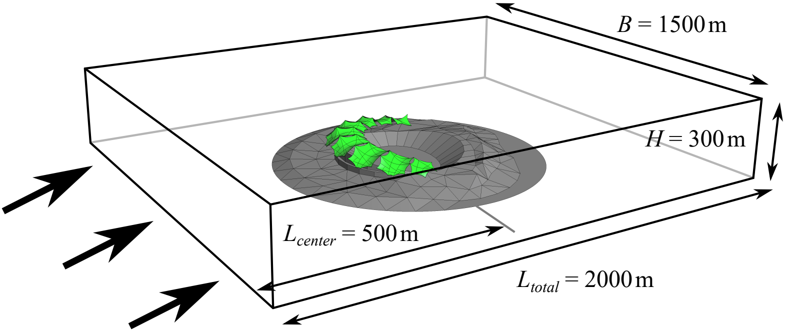

Snapshot of the ABL turbulent flow
on the boundary of the CFD domain

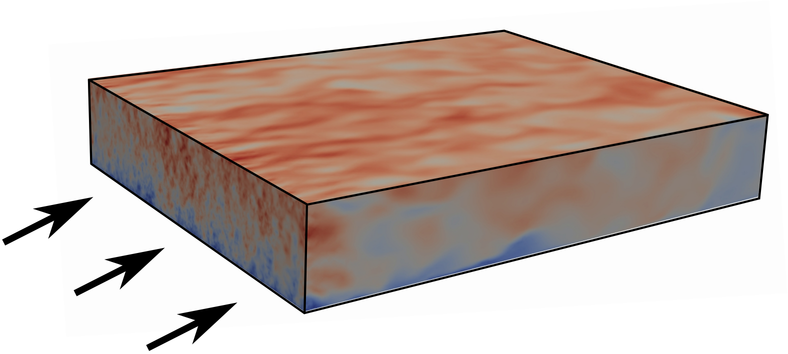

Horizontal cut through the middle of the CFD domain
with ABL turbulent flow and the definition of sampling lines

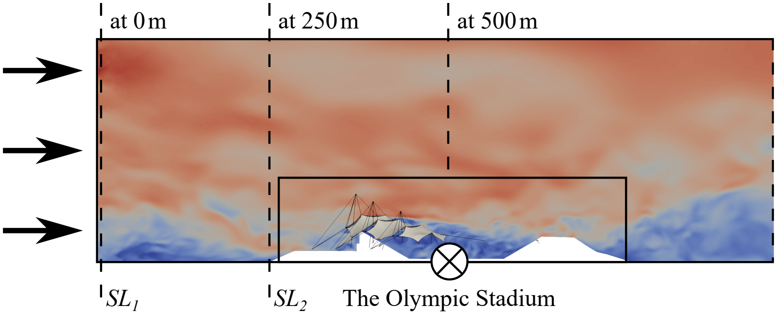

Figure 5.36: Wind flow domain for CFD, including ABL conditions.

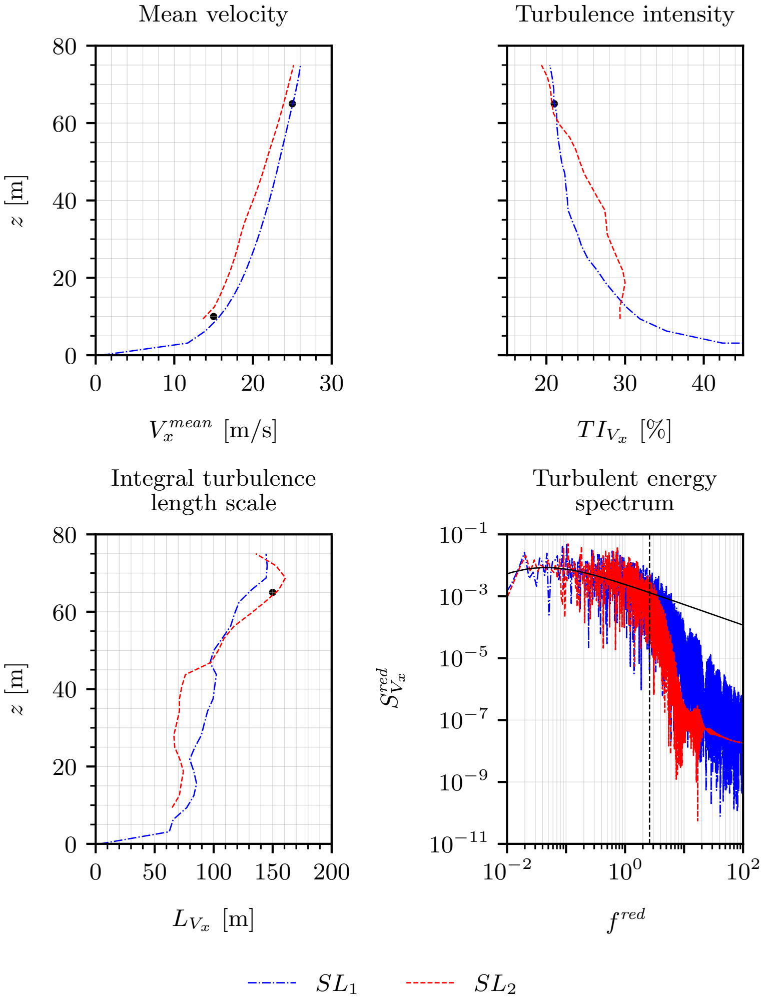

Figure 5.37: Quantification of the local wind conditions.

5.2.6 High-performance numerical simulations

Various simulations strategies were adopted to capture the effect of wind on the roof of the Olympic Stadium. Forces obtained by pure CFD were transferred to the structure to simulate dynamic effects, without transferring the deformations of the roof back to the flow domain, according to the OWC strategy. FSI was carried out in the weak as well as the strong sense. All simulations were split into four initial phases in reaching the full transfer of forces and displacements. Additionally, for the flow domain the inlet velocity was ramped up to its target profile, similarly to the increase of self-weight and prestress for the structure. The weak approaches failed even before coupling took place at its full extent, whereas the strong TWC remained stable and ran successfully. Tab. 5.1 summarizes key metrics of the simulations on the HPC facility. Models are fairly large, whereas the total time of $t = 700\,\text{s}$ was simulated, with the time step $\Delta t = 0.01\,\text{s}$.

Table 5.1: Summary of the HPC simulation data for the Olympic Stadium.

	Model size	
	CFD	CSD
# elements	4.5×10^7	2.3×10^5
# nodes	7.7×10^6	5.8×10^4
	Numerical iterations	
	OWC	TWC
CFD solver	3	
CSD solver	2	
FSI coupling	1	5

In Fig. 5.38, one can see three types of forces, which represent the resultant on the entire roof: the wind loading as captured in the flow domain by CFD, these forces were mapped and transferred to the outer hull of the construction, and the reactions of the structure assessed by CSD. In the bottom row, the necessary coupling iterations n^{iter} for the TWC-FSI are included. Phase 1 for $t = 0\,\text{s}$ to $30\,\text{s}$ implied the wind conditions reaching full extent, as seen for the F_x and F_z components. At the same time, self-weight and prestress were applied with a linear increase, clearly observable for F_z[*]. Phase 2 was used to let both flow and structural behavior stabilize during $t = 30\,\text{s}$ to $40\,\text{s}$. Throughout phase 3 the wind loading was applied, increased gradually over $t = 40\,\text{s}$ to $70\,\text{s}$. Similarly, between $t = 70\,\text{s}$ to $100\,\text{s}$ displacement were mapped, with the coupling reaching its completeness during phase 4. The number of iterations clearly highlighted the need for coupling starting in the middle of this last stage. From there onwards, $n^{iter} = 5$ were required on average. On-the-fly statistics started after phase 4, and the results were eval-

---

[*] The self-weight of $G = 18 \times 10^6\,\text{N}$ was actually subtracted for this depiction, such that the magnitude of the F_z component becomes comparable for the three cases.

uated until the end of the simulation, such that 10 min* worth of data could be recorded. This was deemed representative for natural wind events.

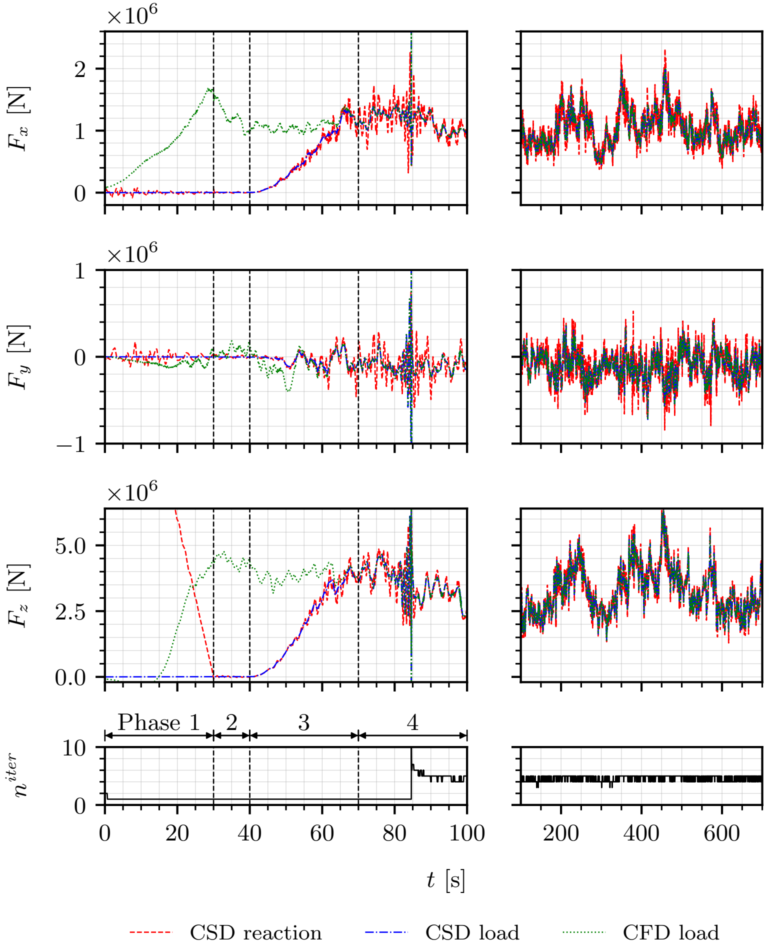

Figure 5.38: Forces and reactions alongside coupling iterations during a strong TWC-FSI simulation.

---

[*] A duration of 10 min typically allows for capturing sufficient statistically converged data to describe a wind event relevant for standard design purposes. European Committee for Standardization (2010) relies on a base mean wind velocity as the characteristic value for this time period, similar to other codes and standards.

The mean and variance of the displacement are shown in Fig. 5.39. For the former, the effect is still dominated by the self-weight and prestress, with peaks in patches 1 and 9. The latter is clearly linked to wind-related effects, with the highest variation in fields 3 to 5, caused by fluctuations of the F_z component. For this middle region, the time-averaged values are still in the order of 1 m, with the SD being approximately one-third of this.

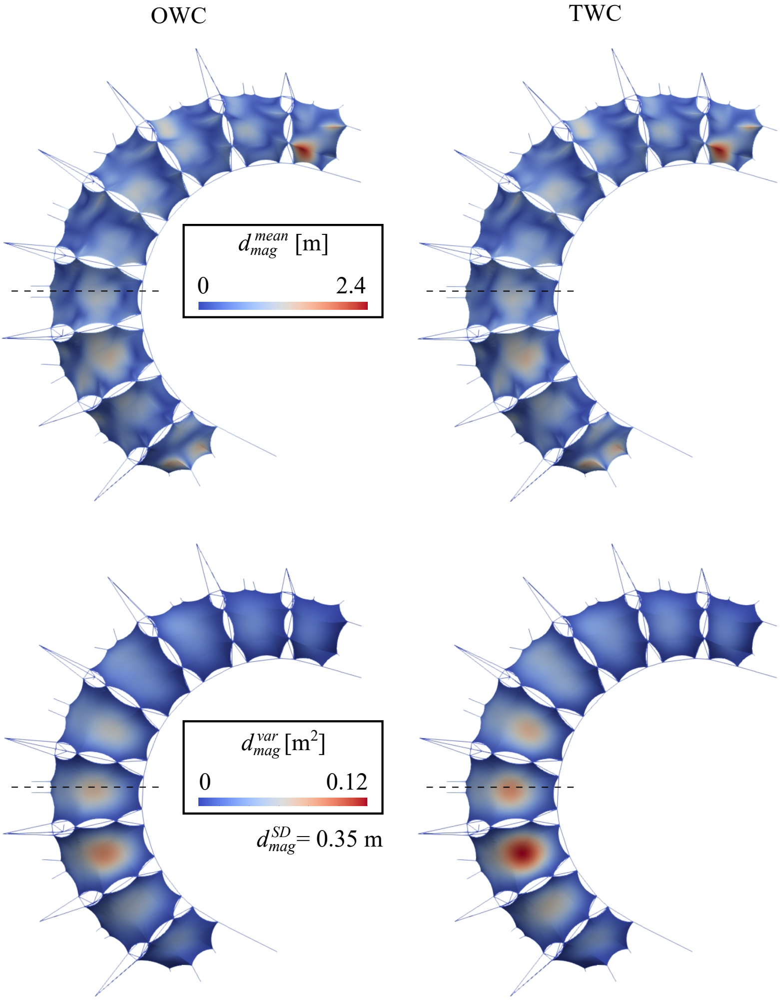

Figure 5.39: Mean and variance of the displacement during OWC and TWC.

Fig 5.40 details the deformations by magnifying the mean and variance of the displacement magnitude d_{mag} along the midline of patch 4. There is 5% difference for the time-averaged value and 20% in the fluctuating component, being higher in case of TWC.

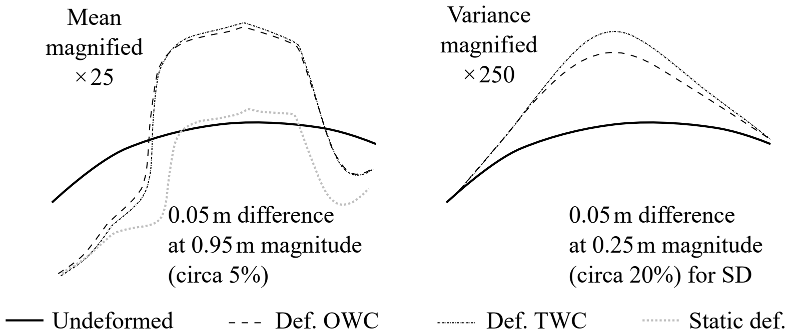

Figure 5.40: Detailing the deformation for the middle of patch 4.

The velocity field enriched by streamlines and the pressure distribution are contained in Fig. 5.41. Deformation is consistent with the pressure on the roof.

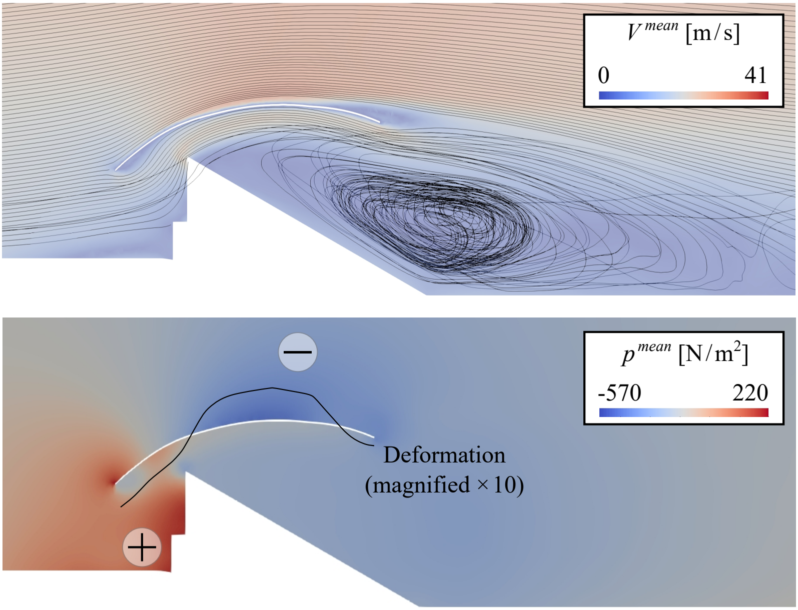

Figure 5.41: Mean velocity and pressure fields during FSI for patch 4.

The mean pressure range in the CFD domain is $-570\,\mathrm{N/m^2}$ to $220\,\mathrm{N/m^2}$. This acts on both the upper and lower surfaces of the roof, which are treated as separate entities in the flow field. In Fig. 5.42, the effect of the wind is assessed on the structural model (i.e. the mid-plane of the roof), where the contributions from the top and bottom surfaces are summed. This results in a pressure range of $-610\,\mathrm{N/m^2}$ to $460\,\mathrm{N/m^2}$, with the positive magnitude approximately double that in the domain. As an additional plausibility check, the mean pressure coefficient, the mean pressure coefficient C_p^{mean} is included. This was calculated with the mean reference velocity at the height of the roof. These values are again within realistic magnitudes. Such depictions can be used to create pressure maps, suitable for zoning in a typical structural engineering design process.

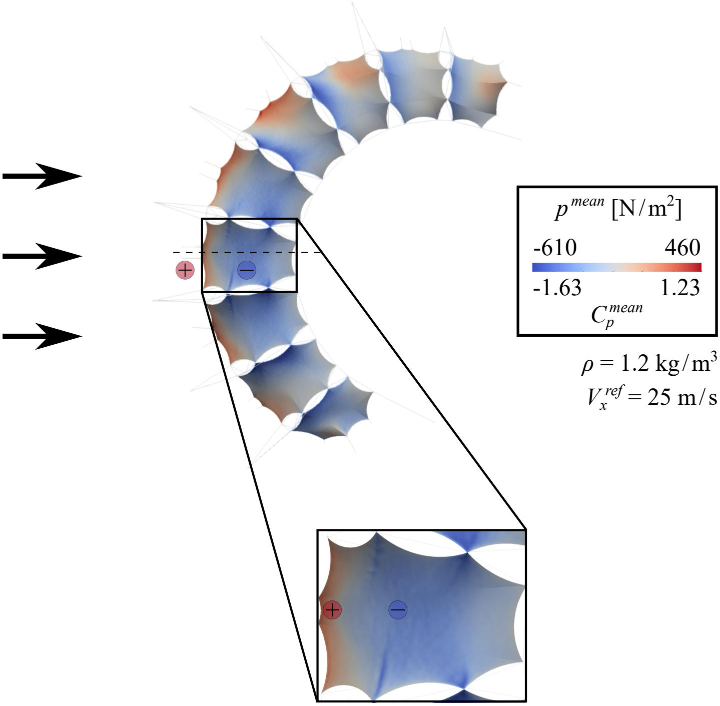

Figure 5.42: Mean pressure for the roof of the Olympic Stadium.

5.3 Summary

The detailed numerical simulation of the Olympic Stadium in Munich was accomplished by a workflow tuned for HPC. The results showed that careful and detailed modeling are clear prerequisites for a high-quality outcome. Preparatory steps included an iterative process for creating a target geometry. This was accompanied by identifying a plausible initial state for the prestress and generating ABL wind conditions. Additionally, for this unique structure, multiple developments were necessary to enable a TWC-FSI simulation. These included surface smoothing, mesh optimizing and determining an improved prestress state. Coupling happened in various phases until the CFD and CSD systems were interacting to their full extent. Using the numerical WT enabled determining a high resolution pressure field on the roof, and, in a first step represented by CFD and OWC, the structural response under these loads. Such results by other means would have been almost impossible, as mapping local loads on highly curved thin roofs in an experimental setting is limited. Moreover, fully-coupled FSI permitted capturing additional effects triggered by the flexibility of the structure. These could be seen as differences mostly in the measured deformation when comparing OWC and TWC. All of these insights enabled a plausibility check. Such inspections were necessary for this unique construction investigated in a special scenario, for which no validation or baseline data was available. Computational means provided a possibility for a thorough assessment.

The current model is a representation of the main load-bearing structure. As an enhancement, the gaps between patches should be connected. Furthermore, the tribune is for now represented by a vertical wall on the outer perimeter, which is a simplification. Similar geometric improvements could also be made for the surroundings. Such changes would render the flow field even more realistic. Additionally, a smooth geometry of the patches could be achieved by form finding. The current target geometry and compatible prestress state would represent adequate ICs for this to be carried out. A detailed modeling by a cable net, at least prototypically for a selected part, would be also worth exploring.

Chapter 6

Conclusions and outlook

This work focused on recent computationally-enabled developments for the numerical (i.e. digital) WT. I addressed multiple aspects relevant to CWE in the broadest sense. Revisiting the motivation of the thesis, the discussion began with a brief historical overview of experimental (i.e. analog) WT, and continued with a detailed deliberation on its numerical counterpart. Key contributed advances were those relevant to modern computer-oriented workflows.

The numerical WT can rely on partitioned schemes successfully. While this has been standard for enabling FSI simulations for a long time, the extended workflow based on multi-coupling represents a modular and robust development. Investigations showed that this approach performs well when assessing the structural response under wind load. The inclusion of added devices such as TMDs and TSDs is crucial for design purposes, whether in early phases or as a retrofitting measure. I concentrated on two passive damping systems with vastly different governing physics. The ability to study such strongly-coupled phenomena with full interaction between modules is a significant advantage of the presented numerical approach. This is not bound by the physical limitations of traditional experimental devices, nor is it affected by typical challenges related to model building at a reduced geometric scale.

Computationally-enabled advances could drastically reduce the effort required to diagnose the onset of flutter. Contributed insights outlined improvements to the combined multi-frequency approach. This work first established a validated setup by thoroughly covering aerodynamic investigations. Subsequent steps focused on the theoretical background and methodological developments for more effective determination of flutter derivatives. The forced-motion approach displayed additional advantages for usage in a computational context. Complementary data was included on the FSI simulation, being related to direct identification. This resulted in establishing a complete workflow using the specific FEM-based VMS formulation.

Lightweight structures are challenging to assess, yet numerical tools provide a viable alternative to existing approaches. The discussed examples clearly substantiate the need for detailed and complex modeling, as well as careful considerations. Recent contributions in developments and simulation cases highlight capabilities, such as realistic wind conditions, the inclusion of terrain, considering the nonlinear structural behavior with the ability to control prestress, etc. It remains crucial to establish more solid grounds for generic shapes of smaller dimensions, according to the preliminary deliberations on these types of structures in wind. Ultimately, for the unique case of the chosen stadium, there was no reference data available. This will continue being the typical situation for many constructions to be designed in the future. Here, one must rely on the predictive capabilities of computational tools, which should be supported by extensive validation cases addressing a broad spectrum of scenarios to ensure the trustworthiness of simulated outcomes.

As a direct continuation to my work, I see the need for open databases with well documented numerical campaigns. Such data collections exist for experimental WT measurement campaigns, including those from NIST[*], TPU[†] and NatHaz[‡]. It could be beneficial to unify or connect various open-source development projects and provide a collection of tools, similar to the efforts from NHERI SimCenter[§]. Corresponding activities would enhance the credibility of computational capabilities. Another aspect is effectively steering software development to ensure it runs as intended on HPC infrastructures, with appropriate scaling and robustness. This implies profiling of respective codes, improvements in data types and structures, to achieve considerable computational speed. At the modeling level, further research should be concerned with connecting even more modules. For the fluid domain, this might imply the usage of embedded methods and lower fidelity formulations for regions of less interest, with body-fitted grids and explicitly modeling turbulence around important zones. Synthetic turbulent inlet can be applied more efficiently near these locations. Better ICs can help to achieve convergence faster. All of these aspects would have the immediate effect of reaching the required accuracy while becoming more resource-efficient. While these enumerated components have been studied, there is a lack of widespread use, and the technical intricacies connecting all of these numerical treatments should not be underestimated. These can be summarized in multistage analysis with the proper combination of various hierarchical modules. Additionally, there exists a lot of data historically, mostly from experimental WT campaigns, but also numerical simulations. The setup of new investigations could benefit from these existing efforts by properly exploiting methods using automated physics-based learning.

---

[*] The National Institute Of Standards and Technology, U.S. Department of Commerce, in collaboration with The Boundary Layer Wind Tunnel Laboratory at the University of Western Ontario, www.nist.gov/el/materials-and-structural-systems-division-73100/nist-aerodynamic-database.

[†] Tokio Polytechnic University, wind.arch.t-kougei.ac.jp/system/eng/contents/code/tpu.

[‡] The Natural Hazard (NatHaz) Modeling Laboratory at the University of Notre Dame, www3.nd.edu/~nathaz/projects.html.

[§] The Computational Modeling and Simulation Center (SimCenter) as part of the Natural Hazards Engineering Research Infrastructure (NHERI) program, simcenter.designsafe-ci.org.

In general, I see future developments in software and hardware continuing to attract increased effort toward similar endeavors while also enabling new possibilities. The numerical WT will become increasingly well-established, ultimately serving as a strong complement to its experimental counterpart in a hybrid setup. For many use-cases, the modern, computer-oriented approach will possibly replace the currently more established alternative. I have already highlighted several of the underlying reasons related to the strengths and potentials of numerical means. The outlook will strongly depend on further key factors such as availability, inclusivity, costs, etc. Recalling the early days of WT measurements, devices and people were linked to a clear location, whether we think about a particular facility or institute. The infrastructure required a significant up-front investment, resources for operational costs, and specialized engineers and scientists to manage it. Knowledge and personnel were concentrated, connected in meaning and function to a close association of craftsmen. Working with the experimental WT retains these characteristics to this day. The numerical alternative strongly depends on software and hardware. For the former, open-source alternatives developed by a large community represent a feasible option. For the latter, cloud-based on-demand computing is similarly a viable choice. Therefore, developers, users and infrastructure are no longer bound to the same location. There are no large up-front costs to write off. Financial aspects will remain crucial for how fast and broad this technology will be adopted. At present, neither the required level of expertise of the human component nor the running costs on HPC systems are low. The evolution of such facets will strongly influence the directions in which all types of computer simulations will head.

I await with excitement to see new activities and how the potentials of numerical methods unfold. Hopefully, these will be accompanied by sound judgement. The following quote provides an appropriate closing tone, applicable to all computational approaches:

> “Industrial users of commercial CFD [and in general CWE] codes should especially be careful, as the optimism of salesmen [as well as of software developers] is legendary. Wonderful color pictures make a great impression, but are of no value if they are not quantitatively correct. Results must be examined very critically before they are believed.”(Ferziger, Perić, and Street, 2020, Ch. 2)

Appendix A

Simulating vibration mitigation

A.1 Summary of the numerical models

Tab. A.1 provides the mesh and time step sizing, characteristic of the implied numerical simulations.

Table A.1: Complexity of the numerical models – Part 1.

Type of simulation	Number of elements	nodes	Total time [s]	Time step size [s]	number
Turbulent wind CFD	7.0×10^6	1.3×10^6	645	0.02	3.2×10^4
Smooth flow CFD	4.0×10^6	0.7×10^6	200	0.01	2.0×10^4
Structure CSD	2.1×10^6	6.0×10^4	Will depend on what the structure or AMDs are coupled to		
TSD CFD	7.5×10^4	3.9×10^4			
TMD CSD	2	1			

In. Tab. A.2, the type of simulation is brought in relation with the number and type of nodal variables, leading to the number of DoFs.

Table A.2: Complexity of the numerical models – Part 2.

Type of simulation	Nodal variables name & type	DoFs per node	total
Turbulent wind CFD	Pressure (scalar) and velocity (vector)	4	5.2×10^6
Smooth flow CFD	Pressure (scalar) and velocity (vector)	4	2.8×10^6
Structure CSD	Displacement and rotation (vector)	6	3.6×10^5
TSD CFD	Pressure (scalar) and velocity (vector)	3	1.2×10^5
TMD CSD	Displacement (vector)	2	2

Appendix B

Numerical workflows for bridge decks

B.1 Convergence study and domain sizing

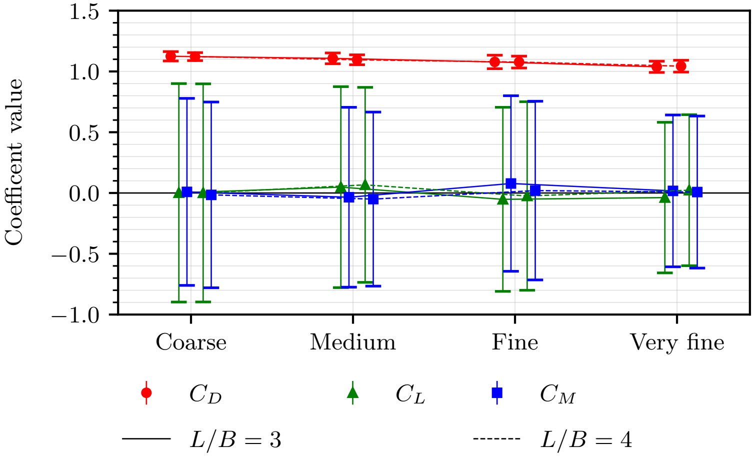

Figure B.1: Convergence study of the aerodynamic coefficients (displaying the mean ± SD) for the Rectangle.

Table B.1: Mesh sizing and setup parameters for the Rectangle.

	Coarse	Medium	Fine	Very fine
Mesh sizing				
Domain [m]	0.24	0.15	0.12	0.12
Structure [m]	0.007	0.005	0.003	0.0025
Resulting mesh				
# elements [$\times 10^6$]	0.95	1.51	2.92	7.63
# nodes [$\times 10^6$]	0.16	0.26	0.51	1.32
Dimensions				
B [m]	0.25			
D [m]	0.05			
B/D [–]	5.0			
L/B [–]	3.0 and 4.0			
Setup				
V [m/s]	15.26			
t^{total} [s]	5.74			
Δt [$\times 10^{-4}$ s]	2.50	2.00	1.20	0.80

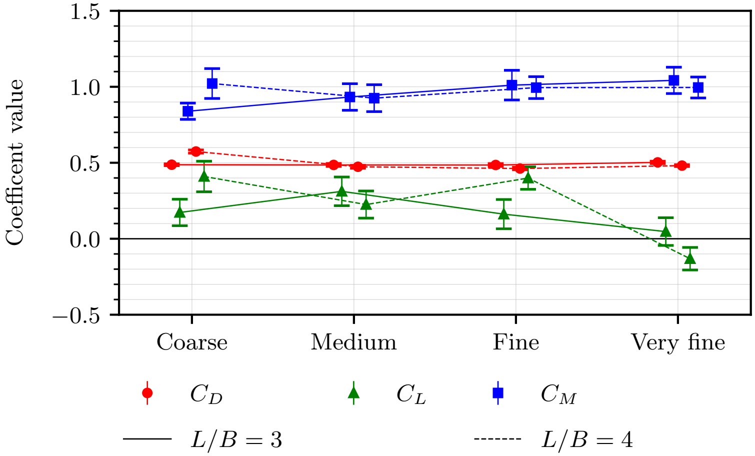

Figure B.2: Convergence study of the aerodynamic coefficients (displaying the mean ± SD) for the Bridge.

Table B.2: Mesh sizing and setup parameters for the Bridge.

		Coarse	Medium	Fine	Very fine
Mesh sizing					
	Domain [m]	0.32	0.24	0.16	0.16
	Structure [m]	0.01	0.0075	0.005	0.0035
Resulting mesh					
	# elements [$\times 10^6$]	1.11	1.52	2.71	8.67
	# nodes [$\times 10^6$]	0.19	0.26	0.47	1.5
Dimensions					
	B [m]	0.366			
	D [m]	0.0666			
	B/D [–]	5.5			
	L/B [–]	3.0 and 4.0			
Setup					
	V [m/s]	11.46			
	t^{total} [s]	10.08			
	Δt [$\times 10^{-4}$ s]	4.50	3.00	2.00	1.50

Coefficient values are provided in flow-attached orientation and normalized by the cross-section height D. The final setup used $L/B = 3$ and the meshing strategy between *Fine* and *Very fine*.

B.2 Pressure distribution as local loads

Fig. B.3 shows the mean and the SD of the pressure coefficient, C_p^{mean} and C_p^{SD}. The range provided in Bruno et al. (2014) is used for comparison. The median value from the benchmark study is marked by a horizontal line, while the gray bars represent the distribution between the 25th and 75th percentile. Values are plotted along the running coordinate s, starting at the middle of the leading face.

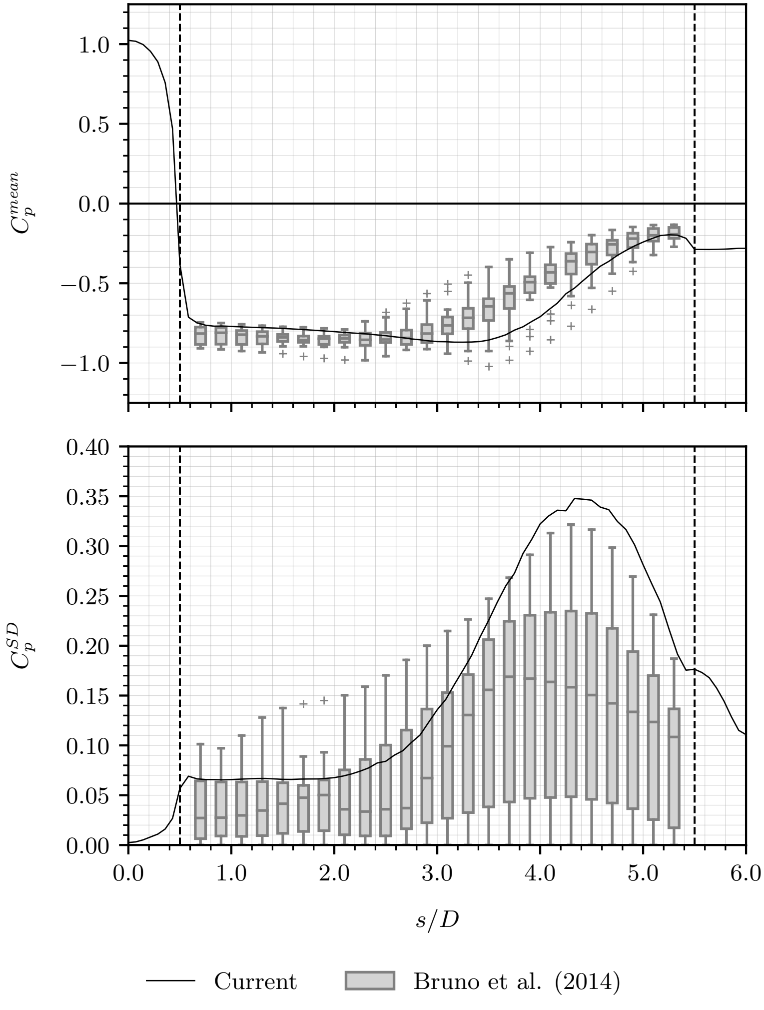

Figure B.3: Distribution of the pressure coefficient for the Rectangle.

In Šarkić (2014, Ch. 7), the distribution of the pressure coefficient is presented on the top and bottom side. Values are plotted along the running coordinate *s*, starting at the leading edge. Here, only the mean values are included in Fig. B.4 for brevity.

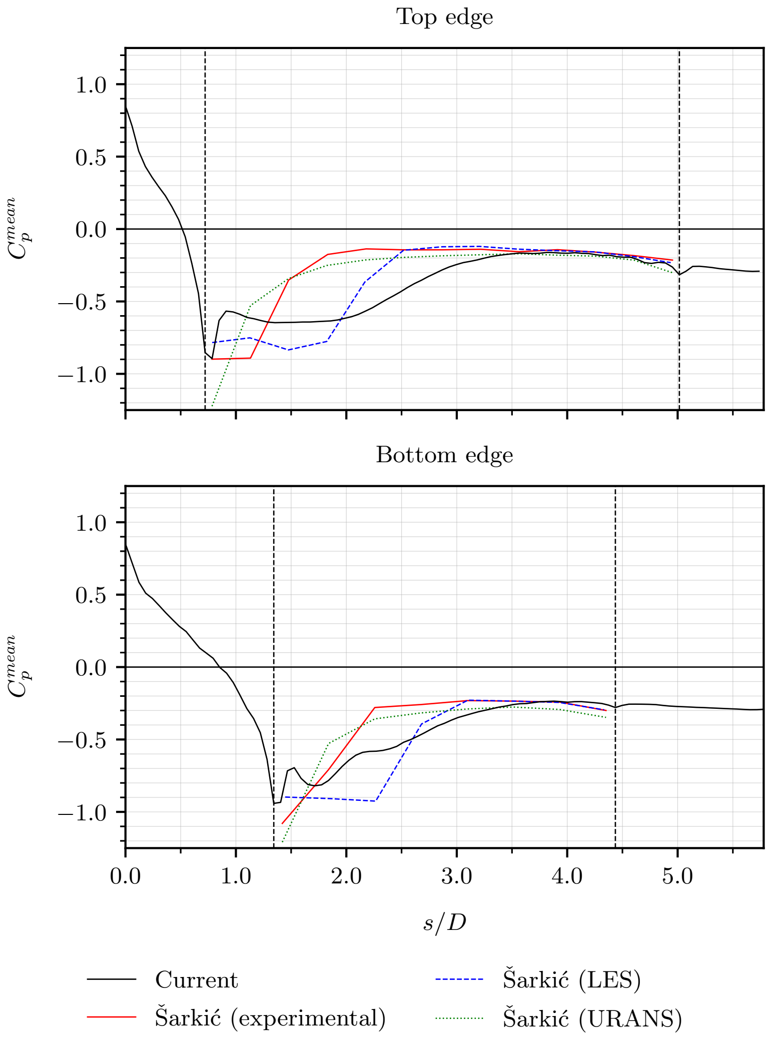

Figure B.4: Distribution of the pressure coefficient for the Bridge.

B.3 Effect of geometric scaling for the Bridge

Tab. B.3 includes the mean and SD of the aerodynamic coefficients when the geometry is scaled. The results from Šarkić et al. (2015) are used for comparison, with one set of data representing force balance measurements in an experimental WT and the other using a numerical approach based on LES. The sign and magnitude of the lift component seems challenging to validate as well as more scale-dependent, while the rest of the components are less sensitive.

Table B.3: Aerodynamic coefficients and the *St* for the Bridge at various geometric scales.

		Small-scale	Large-scale	Šarkić (force)	Šarkić (LES)
C_D	Mean	0.462	0.462	0.488	0.521
	SD	0.009	0.008	0.061	0.111
C_L	Mean	0.075	0.050	−0.222	−0.261
	SD	0.089	0.244	0.405	
C_M	Mean	0.994	0.993	0.646	2.245
	SD	0.087	0.308	0.461	
St_D		0.220	0.221	0.235	0.240

Flow patterns are assessed on the time-averaged velocity field, using the definition presented for the Rectangle. The outcome is quantitatively summarized in Tab. B.4, while Fig. B.5 provides qualitative insight.

Table B.4: Main characteristics of the time-averaged velocity flow field for the Bridge.

	Small-scale	Large-scale
Top side		
x_c/B	0.259	0.252
y_c/D	0.133	0.131
L_f/B	0.399	0.397
Bottom side		
x_c/B	0.193	0.189
y_c/D	0.057	0.052
L_f/B	0.328	0.340
Wake		
L_w/D	1.006	0.935

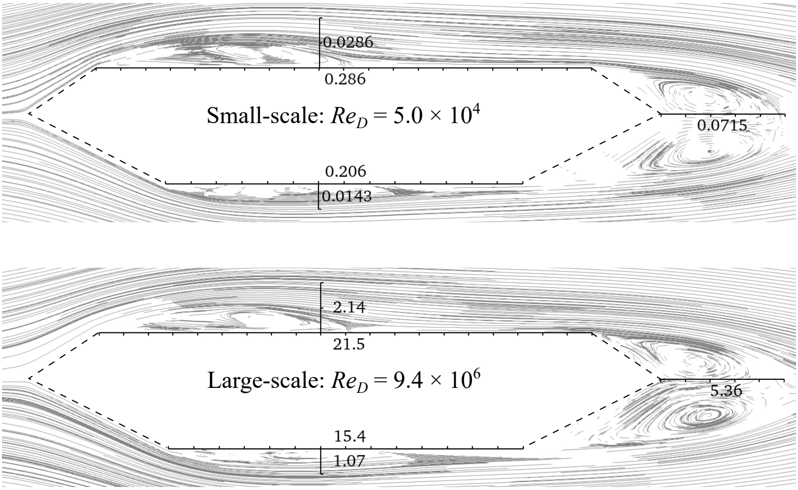

Figure B.5: Streamlines at small and large geometric scales for the Bridge.

B.4 Flutter assessment for the Rectangle

Direct flutter is observed to happen just below 15 m/s, as plotted in Fig. B.6. The amplification is measured during the same amount of time for all simulations, namely $t = 2.83$ s. Such a time frame captures approximately 33 oscillations of the cross-section.

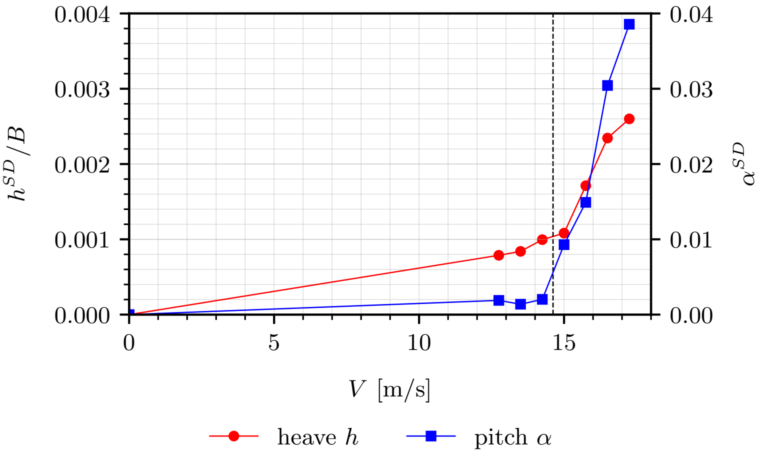

Figure B.6: Direct flutter identification for the Rectangle.

For the Rectangle, reference flutter derivatives were taken from Matsumoto (1996) and Nieto et al. (2015). These are included in Fig. B.7, while establishing the current research benchmark by the standard forced-motion approach. The improved procedure by combined frequencies and directions leads to the outcome in Fig. B.8.

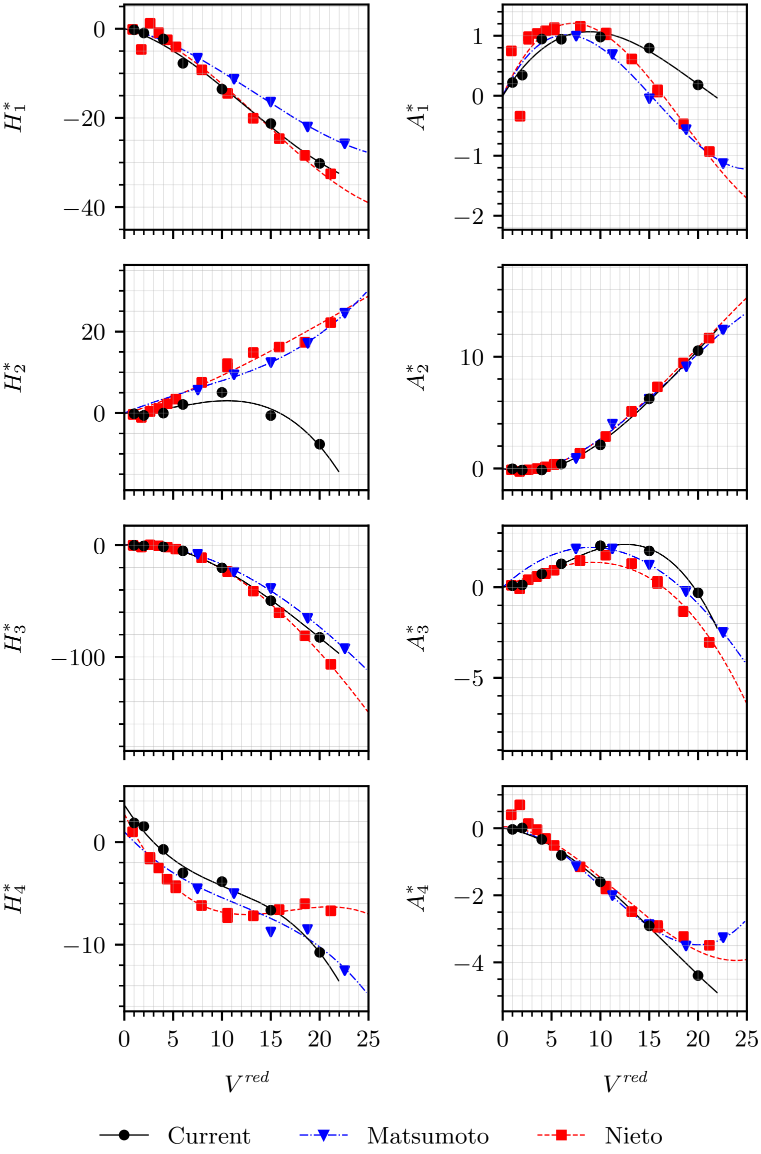

Figure B.7: Flutter derivatives for the Rectangle obtained from single-frequency forced oscillations.

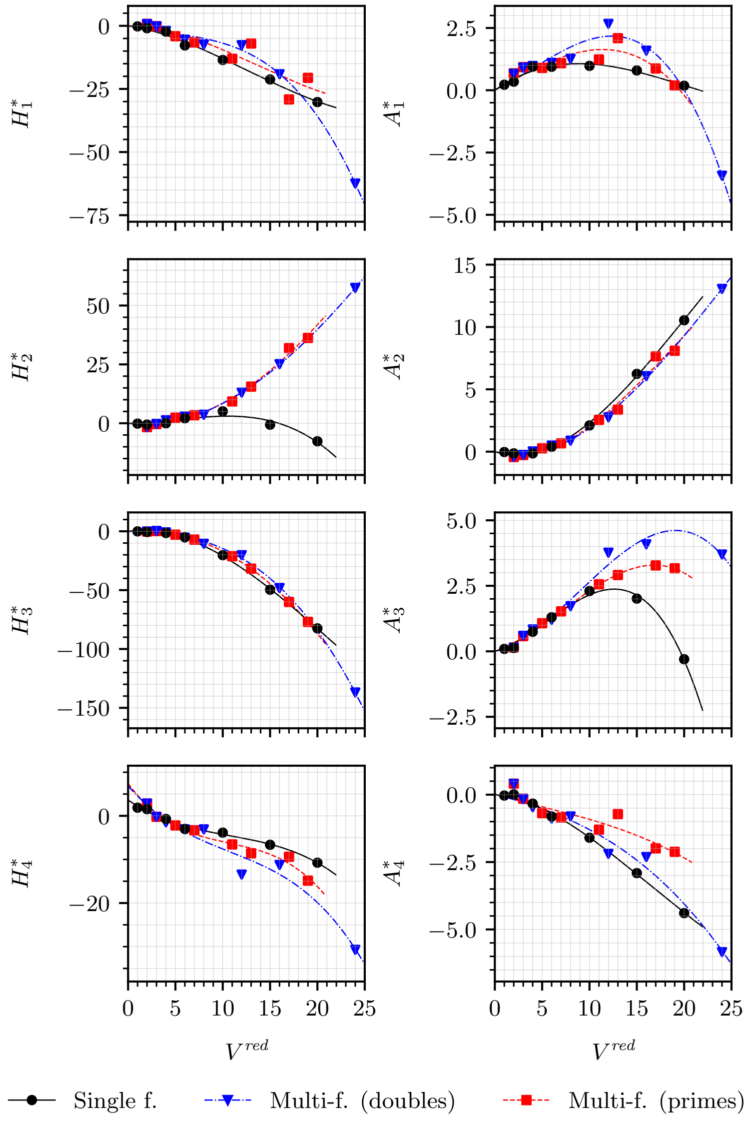

Figure B.8: Flutter derivatives for the Rectangle obtained from multiple frequencies and directions (eight primes or doubles).

Appendix C

Considerations for the Olympic Stadium in Munich

C.1 Wind characteristics in and around Munich

Wind characteristics in the region of interest are recorded at two locations: Munich Airport, which is approximately 30 km northeast of the city center, and within the city at the office building of the German Weather Service, known in German as Deutscher Wetterdienst (DWD). The latter is located circa 4 km northwest from the center. For determining wind conditions at the Olympic Stadium, data from both locations was evaluated. The main outcome is summarized in several figures. Fig. C.1 depicts the locations on the map, as based on OpenStreetMap*, as well as the wind rose highlighting dominant flow directions. The AoA of 250° is clearly prevailing. Information is based on the 10-minute monthly mean. Herein, it is also visible that velocities over 17.5 m/s are possible although unlikely. More precisely, for the location inside the city, over 10^6 measurements were taken between 1997 and 2022, of which 26 fell between 15 m/s and 17.5 m/s, with only 10 exceeding this range. The evaluation uses open data from the DWD†, provided through their Climate Data Center (CDC).

Statistics related to mean and extreme winds is covered in detail in Fig. C.2, representing the location in Munich City (meaning the DWD office). The *mean* and *max* labels imply the 10-minute (monthly) mean and 10-minute (monthly) max, respectively. One plot shows the time history of non-directional magnitude of the wind velocity. The Probability Density Function (PDF) of these series is fitted to a Generalized Extreme Value (GEV) model. Velocity values representing the highest probability density are marked. Finally, the extreme values are estimated by Gumbel's method, according to the steps in Holmes (2015, Ch. 2). Assuming a design for wind loading with a Recurrance Interval (RI) $T_{RI} = 50$ years, respective values are determined, reaching approximately 12.5 m/s. While mean and max show similar distribution types, these statistical models are to be used for the latter.

Seasonality of wind magnitude is shown in Fig. C.3. Germany is known for its winter storms, with this claim being also backed up by this included data, where values peak in March.

Tab. C.1 summarizes technical details related to the measurements provided by the DWD, of which mean and max are used here.

---

[*] www.openstreetmap.org.

[†] www.dwd.de.

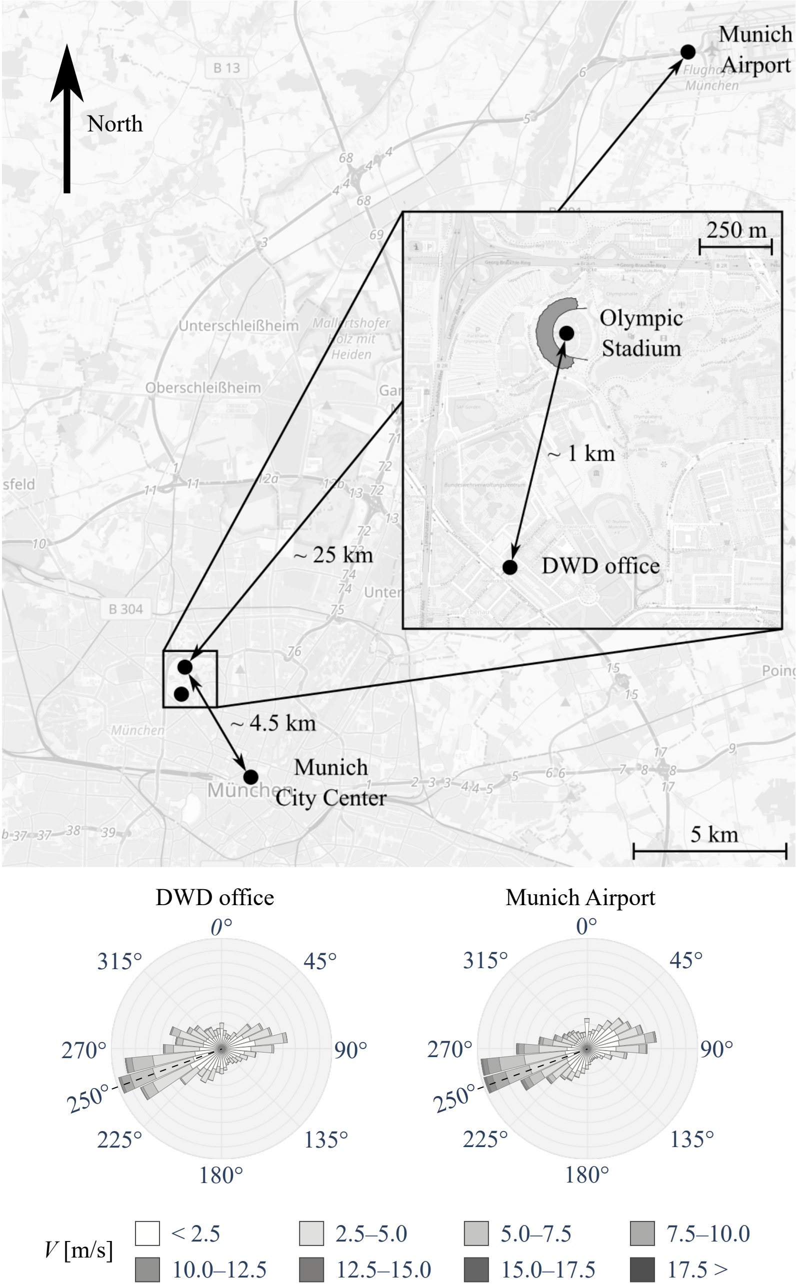

Figure C.1: Weather stations and conditions in and around Munich.

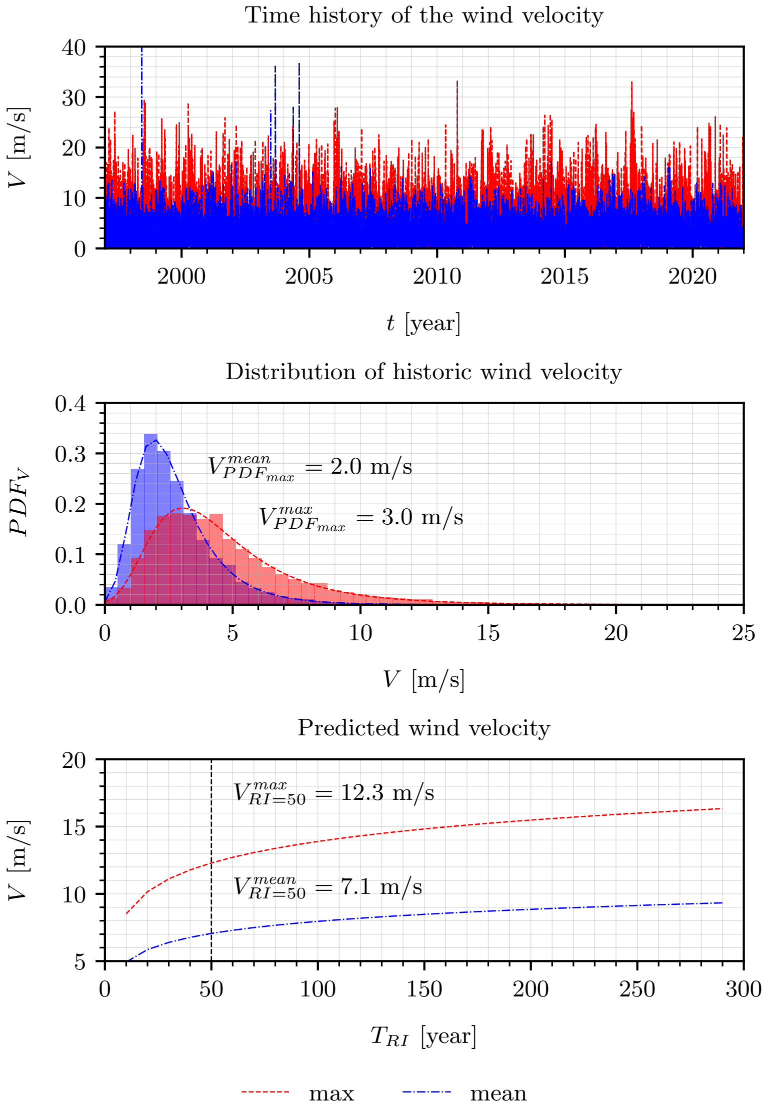

Figure C.2: Mean and gust wind conditions at Munich City.

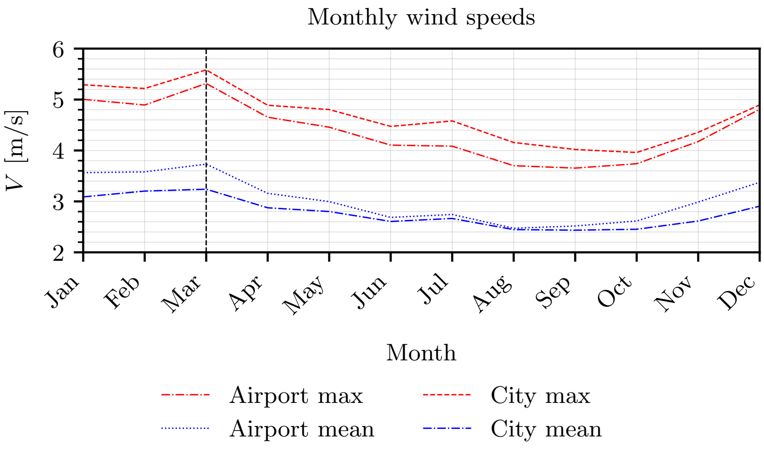

Figure C.3: Monthly winds in and around Munich.

Table C.1: Details of the DWD data.

Recorded values and definitions

Hourly values

hourly mean: average of the six 10-minute means from the previous hour

10-minute values

10-minute mean: mean wind speed during the previous 10 minutes

10-minute max: maximum of wind speed during the previous 10 minutes

3-s gust of 10-minutes: mean 3-second maxima of the wind speed during the previous 10 minutes

Location details

Location	Munich Airport	Munich City
Location ID	01262	03379
Geographic coordinate	48°09’47.5”N 11°32’34.4”E	48°20’51.7”N 11°48’48.2”E
Automatic measurement years	1992–2022	1997–2022
Measurement elevation	10 m	30 m[*]

[*] The elevation in the city implies circa 20 m as it is placed on a building and the additional 10 m for the measuring instrumentation.

C.2 Complementary insights into prestress optimization

Optimization followed a multi-stage strategy, as presented in Fig. 5.34. Steps 1 to 3 were first completed on the coarse mesh, whereas the last phase – including all design variables – was carried out on the final mesh as well. This stage used the results from the last step on the lower-resolution model as initial values for the high-resolution one. The evolution of the objective function and that of the maximum deformation in [m] of the entire roof are shown in Fig. C.4. A cut through the midline of patch 4 further highlights the actual values along this specific section, showing a decrease from 0.40 m to 0.10 m. The COBYLA* method was used in combination with the *StructuralMechanicsApplication* of *Kratos Multiphysics* to obtain this outcome. While Fig. 5.35 displays the achieved prestress in the considered patches, Figs. C.5 and C.6 include those related to edge and main cables, respectively.

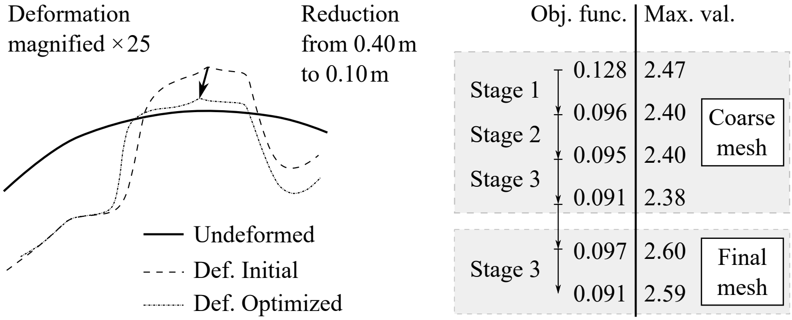

Figure C.4: Detailing the intermediate steps and presenting the outcome of the prestress optimization by showing the deformation in the midline of patch 4.

---

[*] The Constrained Optimization By Linear Approximation (COBYLA) algorithm as part of the Python-SciPy package, docs.scipy.org/doc/scipy/reference/optimize.minimize-cobyla.html.

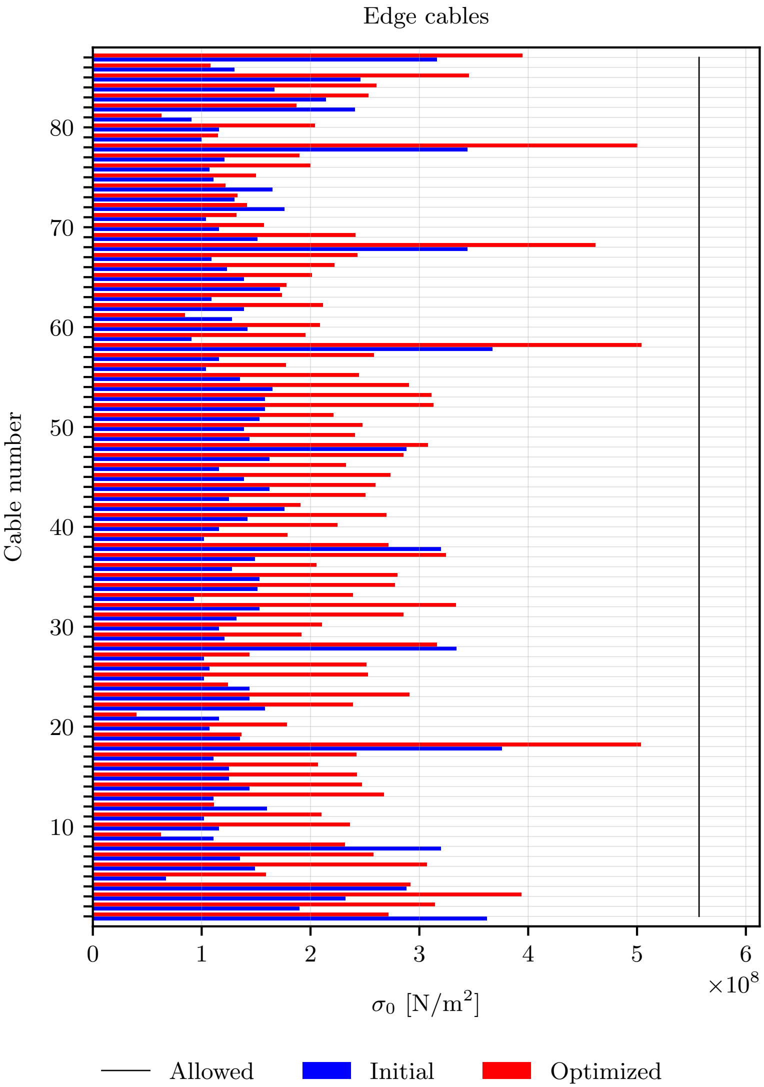

Figure C.5: Outcome of the prestress optimization for the edge cables.

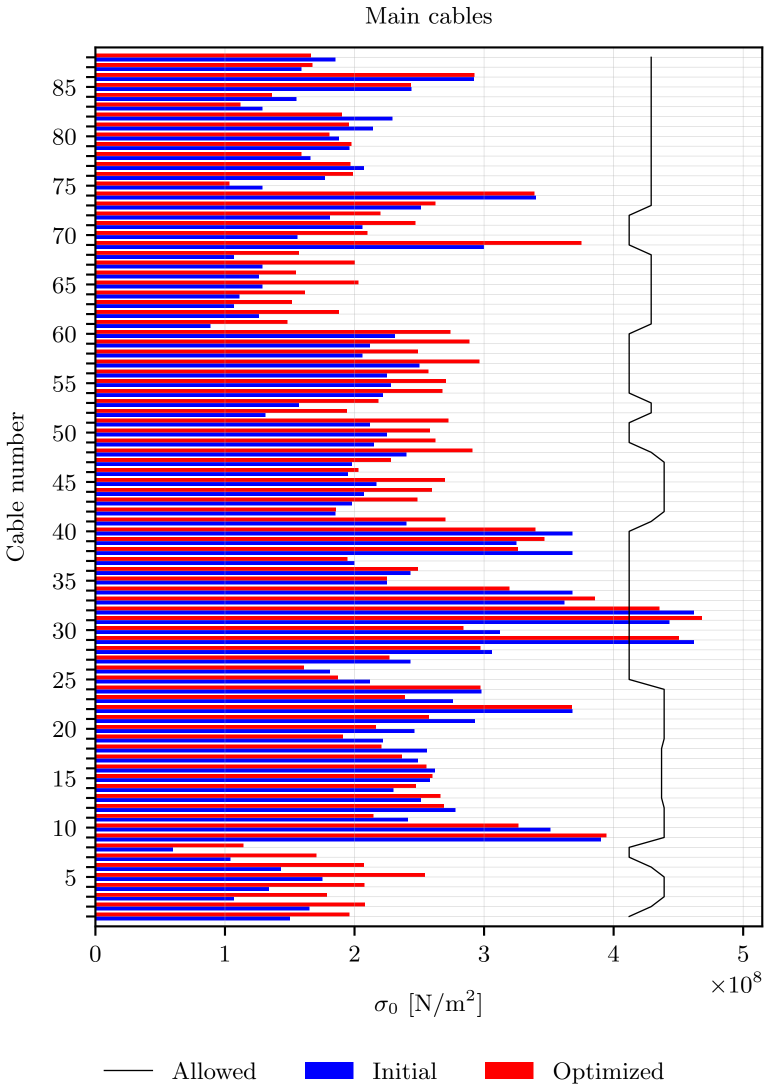

Figure C.6: Outcome of the prestress optimization for the main cables.

C.3 Vorticity visualization

Top view

Side view

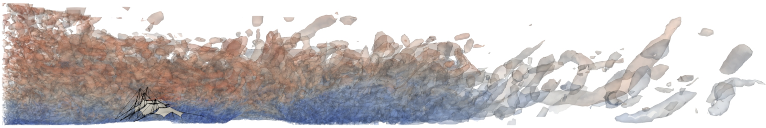

Figure C.7: Visualizing instantaneous vorticity using the Q-criterion (with isosurfaces for $Q = 0.02\,\mathrm{s}^{-2}$ at a certain time step).

List of Figures

List of Tables

Bibliography

[1] M. Andre. “Aeroelastic Modeling and Simulation for the Assessment of Wind Effects on a Parabolic Trough Solar Collector”. Doctoral dissertation. Chair of Structural Analysis, Technical University of Munich, 2018. ISBN: 978-3-943683-50-9. URL: mediatum.ub.tum.de/?id=1426694.

[2] M. Andre. *WindGen.* A synthetic wind simulation library. 2023. URL: www.github.com/msandre/WindGen.

[3] M. Andre, M. Péntek, K.-U. Bletzinger, and R. Wüchner. “Aeroelastic simulation of the wind-excited torsional vibration of a parabolic trough solar collector”. In: *Journal of Wind Engineering and Industrial Aerodynamics* 165 (2017), pp. 67–78. DOI: 10.1016/j.jweia.2017.03.005.

[4] Archivraum Olympiapark München. *Archived records: Documentation of the measurements of the main points of the stadium roof, conducted during the construction phase (1971 and 1972).* Collected and compiled by M. J. Mair (2010) as part of his Bachelor’s thesis at the Chair of Structural Analysis, Technical University of Munich. 2010.

[5] Ö. Avşar. “Determination of Flutter Derivatives from Free Vibration Test Results”. Master’s thesis. Chair of Structural Analysis, Technical University of Hamburg-Harburg, 2003. DOI: 10.13140/RG.2.2.25860.53124.

[6] G. Bartoli, L. Bruno, A. Cimarelli, C. Mannini, L. Patruno, F. Ricciardelli, and M. V. Salvetti. *BARC: Requests for computational simulations.* 2020. URL: www.aniv-iawe.org/barc-home.

[7] G. Bartoli and M. Righi. “Flutter mechanism for rectangular prisms in smooth and turbulent flow”. In: *Journal of Wind Engineering and Industrial Aerodynamics* 94.5 (2006), pp. 275–291. DOI: 10.1016/j.jweia.2006.01.014.

[8] D. Baumgärtner, J. Wolf, R. Rossi, R. Wüchner, and P. Dadvand. *Contribution to the fluid-structure interaction analysis of ultra-lightweight structures using an embedded approach.* Monographs of the International Centre for Numerical Methods in Engineering, 2015. ISBN: 978-84-943307-6-6. DOI: 10.13140/RG.2.1.1079.8561.

[9] Y. Bazilevs, K. Takizawa, and T. E. Tezduyar. *Computational Fluid-Structure Interaction: Methods and Applications*. John Wiley & Sons, 2012. ISBN: 978-0-4709-7877-1. DOI: 10.1002/9781118483565.

[10] S. Bhattacharyya, J. P. Abraham, L. Cheng, and J. Gorman. “Introductory Chapter: A Brief History of and Introduction to Computational Fluid Dynamics”. In: *Applications of Computational Fluid Dynamics Simulation and Modeling*. IntechOpen, 2021. DOI: 10.5772/intechopen.97235.

[11] K.-U. Bletzinger. *Statik 2 – Manuskript zur Vorlesung*. Chair of Structural Analysis, Technical University of Munich. 2019.

[12] K.-U. Bletzinger and E. Ramm. “A General Finite Element Approach to the Form Finding of Tensile Structures by the Updated Reference Strategy”. In: *International Journal of Space Structures* 14.2 (1999), pp. 131–145. DOI: 10.1260/0266351991494759.

[13] B. Blocken. “50 years of Computational Wind Engineering: Past, present and future”. In: *Journal of Wind Engineering and Industrial Aerodynamics* 129 (2014), pp. 69–102. DOI: 10.1016/j.jweia.2014.03.008.

[14] L. Bruno, M. V. Salvetti, and F. Ricciardelli. “Benchmark on the Aerodynamics of a Rectangular 5:1 Cylinder: An overview after the first four years of activity”. In: *Journal of Wind Engineering and Industrial Aerodynamics* 126 (2014), pp. 87–106. DOI: 10.1016/j.jweia.2014.01.005.

[15] P. Bucher. “Development and Implementation of a Parallel Framework for Non-Matching Grid Mapping”. Master’s thesis. Chair of Structural Analysis, Technical University of Munich, 2017.

[16] H.-J. Bungartz, F. Lindner, B. Gatzhammer, M. Mehl, K. Scheufele, A. Shukaev, and B. Uekermann. “preCICE – A fully parallel library for multi-physics surface coupling”. In: *Computers & Fluids* 141 (2016). Advances in Fluid-Structure Interaction, pp. 250–258. DOI: 10.1016/j.compfluid.2016.04.003.

[17] H.-J. Bungartz, F. Lindner, M. Mehl, and B. Uekermann. “A plug-and-play coupling approach for parallel multi-field simulations”. In: *Computational Mechanics* 55 (2015), pp. 1119–1129. DOI: 10.1007/s00466-014-1113-2.

[18] B. Chanetz. “A century of wind tunnels since Eiffel”. In: *Comptes Rendus Mécanique* 345.8 (2017), pp. 581–594. DOI: 10.1016/j.crme.2017.05.012.

[19] A. G. Chowdhury and P. P. Sarkar. “A new technique for identification of eighteen flutter derivatives using a three-degree-of-freedom section model”. In: *Engineering Structures* 25.14 (2003), pp. 1763–1772. DOI: 10.1016/j.engstruct.2003.07.002.

[20] J. Chung and G. M. Hulbert. “A Time Integration Algorithm for Structural Dynamics With Improved Numerical Dissipation: The Generalized-α Method”. In: *Journal of Applied Mechanics* 60.2 (1993), pp. 371–375. DOI: 10.1115/1.2900803.

[21] J. Colliers. “Wind Loading on Tensile Surface Structures – Experimental Approach”. Master’s thesis. Faculty of Engineering, Vrije Universiteit Brussel, 2014.

[22] J. Colliers. “Wind-structure interactions of tensile surface structures: evaluating the wind load distributions over and the steady aeroelastic responses of hyperbolic paraboloid roofs and canopies”. PhD thesis. Faculty of Engineering, Vrije Universiteit Brussel and Faculty of Engineering and Architecture, Ghent University, 2020. URL: biblio.ugent.be/publication/8674838.

[23] J. Colliers, M. Mollaert, J. Vierendeels, and L. De Laet. “Collating Wind Data for Doubly-curved Shapes of Tensioned Surface Structures (Round Robin Exercise 3)”. In: *Procedia Engineering* 155 (2016). TensiNet – COST TU1303 International Symposium 2016 "Novel structural skins – Improving sustainability and efficiency through new structural textile materials and designs", pp. 152–162. DOI: 10.1016/j.proeng.2016.08.016.

[24] Consiglio Nazionale delle Richerche. *Istruzioni per la valutazione delle azioni e degli effetti del vento sulle costruzioni*. CNR-DT 207 R1/2018. 2019.

[25] J. Cotela, E. Oñate, and R. Rossi. *Applications of turbulence modeling in civil engineering*. International Centre for Numerical Methods in Engineering, 2016. URL: www.scipedia.com/public/Cotela_2016.

[26] P. Dadvand, R. Rossi, and E. Oñate. “An Object-oriented Environment for Developing Finite Element Codes for Multi-disciplinary Applications”. In: *Archives of Computational Methods in Engineering* 17 (2010), pp. 253–297. DOI: 10.1007/s11831-010-9045-2.

[27] A. G. Davenport. “The Buffeting of Large Superficial Structures by Atmospheric Turbulence”. In: *Annals of the New York Academy of Sciences* 116 (1 1964), pp. 135–160. DOI: 10.1111/j.1749-6632.1964.tb33943.x.

[28] A. G. Davenport and M. Novak. “Vibration of Structures Induced by Wind”. In: *Harris’ Shock and Vibration Handbook*. Ed. by C. M. Harris and A. Piersol. McGraw-Hill, 2002. Ch. 29, pp. 935–960. ISBN: 978-0-07-137081-3.

[29] J. Degroote, R. Haelterman, S. Annerel, P. Bruggeman, and J. Vierendeels. “Performance of partitioned procedures in fluid-structure interaction”. In: *Computers & Structures* 88.7 (2010), pp. 446–457. DOI: 10.1016/j.compstruc.2009.12.006.

[30] J. P. Den Hartog. *Mechanical Vibrations*. Dover Publications, 1985. ISBN: 978-0-486-64785-2.

[31] W. G. Dettmer, D. Kadapa, C. Perić, R. Liang, and M. Loosten. *On Partitioned Solution Strategies for Computational Fluid-structure Interaction*. Presentation at the Technical University of Munich. 2015.

[32] W. G. Dettmer and D. Perić. “A new staggered scheme for fluid-structure interaction”. In: *International Journal for Numerical Methods in Engineering* 93 (1 2012), pp. 1–22. DOI: 10.1002/nme.4370.

[33] Deutsches Institut für Normung – Normenausschuss Bauwesen. *Nationaler Anhang – National festgelegte Parameter – Eurocode 1: Einwirkungen auf Tragwerke – Teil 1-4: Allgemeine Einwirkungen – Windlasten*. DIN EN 1991-1-4/NA. 2010.

[34] G. Diana, S. Bruni, A. Cigada, and A. Collina. “Turbulence effect on flutter velocity in long span suspended bridges”. In: *Journal of Wind Engineering and Industrial Aerodynamics* 48.2 (1993), pp. 329–342. DOI: 10.1016/0167-6105(93)90144-D.

[35] G. Diana, S. Stoyanoff, K. Aas-Jakobsen, A. Allsop, M. Andersen, T. Argentini, M. C. Montoya, S. Hernández, J. Á. Jurado, H. Katsuchi, I. Kavrakov, H.-K. Kim, G. Larose, A. Larsen, G. Morgenthal, O. Øiseth, S. Omarini, D. Rocchi, M. Svendsen, and T. Wu. “IABSE Task Group 3.1 Benchmark Results. Part 1: Numerical Analysis of a Two-Degree-of-Freedom Bridge Deck Section Based on Analytical Aerodynamics”. In: *Structural Engineering International* 30.3 (2020), pp. 401–410. DOI: 10.1080/10168664.2019.1639480.

[36] F. H. Dieringer. “Numerical Methods for the Design and Analysis of Tensile Structures”. Doctoral dissertation. Chair of Structural Analysis, Technical University of Munich, 2014. ISBN: 978-3-943683-26-4. URL: mediatum.ub.tum.de/?id=1197480.

[37] J. Donea, S. Giuliani, and J. P. Halleux. “An arbitrary lagrangian-eulerian finite element method for transient dynamic fluid-structure interactions”. In: *Computer Methods in Applied Mechanics and Engineering* 33.1 (1982), pp. 689–723. DOI: 10.1016/0045-7825(82)90128-1.

[38] G. W. A. Dummer. *Electronic Inventions and Discoveries: Electronics from Its Earliest Beginnings to the Present Day*. Institute of Physics Publishing, 1997. ISBN: 978-0-7503-0493-1.

[39] A. Duncan. “The Analytic Impulse”. In: *Journal of the Audio Engineering Society* 36.5 (1988), pp. 315–327. URL: aes2.org/publications/elibrary-page/?id=5153.

[40] European Committee for Standardization. *Eurocode 1: Actions on structures – Part 1-4: General actions – Wind actions*. EN 1991-1-1-4. 2010.

[41] C. Farhat, M. Lesoinne, and P. Le Tallec. “Load and motion transfer algorithms for fluid/structure interaction problems with non-matching discrete interfaces: Momentum and energy conservation, optimal discretization and application to aeroelasticity”. In: *Computer Methods in Applied Mechanics and Engineering* 157.1 (1998), pp. 95–114. DOI: 10.1016/S0045-7825(97)00216-8.

[42] C. A. Felippa and K. C. Park. “Staggered transient analysis procedures for coupled mechanical systems: Formulation”. In: *Computer Methods in Applied Mechanics and Engineering* 24.1 (1980), pp. 61–111. DOI: 10.1016/0045-7825(80)90040-7.

[43] C. A. Felippa, K. C. Park, and C. Farhat. “Partitioned analysis of coupled mechanical systems”. In: *Computer Methods in Applied Mechanics and Engineering* 190.24 (2001), pp. 3247–3270. DOI: 10.1016/S0045-7825(00)00391-1.

[44] J. H. Ferziger, M. Perić, and R. L. Street. *Computational Methods for Fluid Dynamics*. Springer Cham, 2020. ISBN: 978-3-319-99691-2. DOI: 10.1007/978-3-319-99693-6.

[45] R. G. J. Flay. “Bluff Body Aerodynamics”. In: *Advanced Structural Wind Engineering*. Ed. by Y. Tamura and A. Kareem. Springer Tokyo, 2013. Ch. 3, pp. 59–84. ISBN: 978-4-431-54336-7. DOI: 10.1007/978-4-431-54337-4.

[46] W. Ford. *Numerical Linear Algebra with Applications – Using MATLAB*. Academic Press, 2014. ISBN: 978-0-12-394435-1. DOI: 10.1016/C2011-0-07533-6.

[47] H. W. Försching. *Grundlagen der Aeroelastik*. Springer Berlin, Heidelberg, 1974. ISBN: 978-3-642-48286-1. DOI: 10.1007/978-3-642-48285-4.

[48] Y. Ge and H. Tanaka. “Long-Span Bridge Aerodynamics”. In: *Advanced Structural Wind Engineering*. Ed. by Y. Tamura and A. Kareem. Springer Tokyo, 2013. Ch. 4, pp. 85–120. ISBN: 978-4-431-54336-7. DOI: 10.1007/978-4-431-54337-4.

[49] A.-K. Goldbach. “Numerical Investigations of the Added Mass Effect on the Dynamic Response of Membrane Structures”. Master’s thesis. Chair of Structural Analysis, Technical University of Munich, 2015.

[50] L. Gründig, E. Moncrieff, P. Singer, and D. Ströbel. “A history of the principal developments and applications of the force density method in Germany 1970–1999”. In: *Fourth International Colloquium on Computation of Shell & Spatial Structures (IASS–IACM 2000)*. Ed. by M. Papadrakakis, A. Samartin, and E. Oñate. 2000. URL: api.semanticscholar.org/CorpusID:54047499.

[51] B. Gustafsson. *Scientific Computing: A Historical Perspective*. Ed. by T. J. Barth, M. Griebel, D. E. Keyes, R. M. Nieminen, D. Roose, and T. Schlick. Vol. 17. Texts in Computational Science and Engineering. Springer Cham, 2018. ISBN: 978-3-319-69846-5. DOI: 10.1007/978-3-319-69847-2.

[52] T. A. Helgedagsrud, Y. Bazilevs, A. Korobenko, K. M. Mathisen, and O. A. Øiseth. “Using ALE-VMS to compute aerodynamic derivatives of bridge sections”. In: *Computers & Fluids* 179 (2019), pp. 820–832. DOI: 10.1016/j.compfluid.2018.04.037.

[53] P. Hémon and F. Santi. “On the Aeroelastic Behaviour of Rectangular Cylinders in Cross-Flow”. In: *Journal of Fluids and Structures* 16.7 (2002), pp. 855–889. DOI: 10.1006/jfls.2002.0452.

[54] M. Heroux, R. Bartlett, V. Howle, R. Hoekstra, J. Hu, T. Kolda, R. Lehoucq, K. Long, R. Pawlowski, E. Phipps, A. Salinger, H. Thornquist, R. Tuminaro, J. Willenbring, and A. Williams. *An Overview of Trilinos*. Tech. rep. Sandia National Laboratories, 2003. URL: mperego.github.io/trilinos.github.io/pdfs/TrilinosOverview.pdf.

[55] J. Hines. “A Comparative Study of the SIMPLE and Fractional Step Time Integration Methods for Transient Incompressible Flows”. Master’s thesis. Mechanical Engineering, University of Waterloo, 2008. URL: uwspace.uwaterloo.ca/bitstream/handle/10012/4162/Hines_Jonathan.pdf.

[56] J. D. Holmes. *Wind Loading of Structures*. 3rd ed. CRC Press, 2015. ISBN: 978-1-4822-2922-6. DOI: 10.1201/b18029.

[57] L. Huang and H. Liao. “Identification of Flutter Derivatives of Bridge Deck Under Multi-Frequency Vibration”. In: *Engineering Applications of Computational Fluid Mechanics* 5.1 (2011), pp. 16–25. DOI: 10.1080/19942060.2011.11015349.

[58] W.-H. Hucho. *Aerodynamik der stumpfen Körper.* Vieweg+Teubner Verlag Wiesbaden, 2011. ISBN: 978-3-8348-1462-3. DOI: 10.1007/978-3-8348-8243-1.

[59] S. R. Ibrahim and E. C. Mikulcik. “A method for the direct identification of vibration parameters from the free response”. In: *The Shock and Vibration Bulletin 47, part 4.* 1977, pp. 183–198.

[60] International Association for Wind Engineering. *Benchmark Buildings for an International HFFB Comparison.* 2007. URL: www.iawe.org/committees/HFBB-spec.pdf.

[61] M. Iwamoto and Y. Fujino. “Identification of flutter derivatives of bridge deck from free vibration data”. In: *Journal of Wind Engineering and Industrial Aerodynamics* 54–55 (1995), pp. 55–63. DOI: 10.1016/0167-6105(94)00029-D.

[62] A. Jameson. “Computational Fluid Dynamics: Past, Present and Future”. In: *Future Direction in CFD Research.* 2012. URL: www.cespr.fsu.edu/people/myh/CFD-Conference/Session-1/Tony-Jameson-Presentation.pdf.

[63] J. J. Jensen. “Das dynamische Verhalten eines vorgespannten Kabelnetzes”. In: *IABSE congress report* 9 (1972), pp. 419–425. DOI: 10.5169/seals-9585.

[64] J. C. Kaimal, J. C. Wyngaard, Y. Izumi, and O. R. Coté. *Spectral Characteristics of Surface-Layer Turbulence.* Tech. rep. AD0748543. Air Force Cambridge Research Laboratories (LYB), 1972. URL: apps.dtic.mil/sti/pdfs/AD0748543.pdf.

[65] A. Kareem, E. Bernardini, and S. M. J. Spence. “Control of the Wind Induced Response of Structures”. In: *Advanced Structural Wind Engineering.* Ed. by Y. Tamura and A. Kareem. Springer Tokyo, 2013. Ch. 14, pp. 377–410. ISBN: 978-4-431-54336-7. DOI: 10.1007/978-4-431-54337-4.

[66] G. Karypis and V. Kumar. *METIS: A Software Package for Partitioning Unstructured Graphs, Partitioning Meshes, and Computing Fill-Reducing Orderings of Sparse Matrices.* Tech. rep. Computer Science & Engineering Technical Reports. University of Minnesota Digital Conservancy, 1997. URL: hdl.handle.net/11299/215346.

[67] Kratos Multiphysics Contributors. *Kratos Multiphysics.* A framework for building parallel multidisciplinary simulation software. 2023. URL: www.github.com/KratosMultiphysics/Kratos.

[68] U. Küttler and W. A. Wall. “Fixed-point fluid-structure interaction solvers with dynamic relaxation”. In: *Computational Mechanics* 43 (2008), pp. 61–72. DOI: 10.1007/s00466-008-0255-5.

[69] K. C. S. Kwok. “Wind-Induced Vibrations of Structures: With Special Reference to Tall Building Aerodynamics”. In: *Advanced Structural Wind Engineering*. Ed. by Y. Tamura and A. Kareem. Springer Tokyo, 2013. Ch. 5, pp. 121–155. ISBN: 978-4-431-54336-7. DOI: 10.1007/978-4-431-54337-4.

[70] A. Lago, D. Trabucco, and A. Wood. *Damping Technologies for Tall Buildings*. Butterworth-Heinemann, 2018. ISBN: 978-0-12-815963-7. DOI: 10.1016/C2017-0-01327-7.

[71] F. Leonhardt and W. Andrä. *XX: Olympische Spiele 1972 München – Überdachung der Sportstätten: Seilkräfte – Vorpsannung*. Leonhardt & Andrä Bürogemeinschaft Beratende Ingenieure VBI Stuttgart. 1971.

[72] F. Leonhardt and W. Andrä. *XX: Olympische Spiele 1972 München – Überdachung der Sportstätten: Übersicht – Grundriss*. Leonhardt & Andrä Bürogemeinschaft Beratende Ingenieure VBI Stuttgart. 1969.

[73] F. Leonhardt and J. Schlaich. “Vorgespannte Seilnetzkonstruktionen – Das Olympiadach in München”. In: *Sonderforschungsbereich (SFB)* (1973). Universität Stuttgart.

[74] K. Linkwitz and H.-J. Schek. “Über eine Methode zur Berechnung vorgespannter Seilnetze und ihre praktische Anwendung auf die Olympiadächer München”. In: *IABSE congress report* 9 (1972), pp. 393–397. DOI: 10.5169/seals-9580.

[75] J. Mann. “Wind field simulation”. In: *Probabilistic Engineering Mechanics* 13.4 (1998), pp. 269–282. DOI: 10.1016/S0266-8920(97)00036-2.

[76] C. Mannini, A. M. Marra, L. Pigolotti, and G. Bartoli. “The effects of free-stream turbulence and angle of attack on the aerodynamics of a cylinder with rectangular 5:1 cross section”. In: *Journal of Wind Engineering and Industrial Aerodynamics* 161 (2017), pp. 42–58. DOI: 10.1016/j.jweia.2016.12.001.

[77] M. Matsumoto. “Aerodynamic damping of prisms”. In: *Journal of Wind Engineering and Industrial Aerodynamics* 59.2 (1996), pp. 159–175. DOI: 10.1016/0167-6105(96)00005-0.

[78] M. Matsumoto. *International Advanced School on Wind-Excited and Aeroelastic Vibrations of Flutter*. Department of Structural and Geotechnical Engineering University of Genova. 2000.

[79] H. G. Matthies and J. Steindorf. “Partitioned strong coupling algorithms for fluid-structure interaction”. In: *Computers & Structures* 81.8 (2003), pp. 805–812. DOI: 10.1016/S0045-7949(02)00409-1.

[80] A. F. Melaku and G. T. Bitsuamlak. “A divergence-free inflow turbulence generator using spectral representation method for large-eddy simulation of ABL flows”. In: *Journal of Wind Engineering and Industrial Aerodynamics* 212 (2021), p. 104580. DOI: 10.1016/j.jweia.2021.104580.

[81] W. H. Melbourne. “Comparison of measurements on the CAARC standard tall building model in simulated model wind flows”. In: *Journal of Wind Engineering and Industrial Aerodynamics* 6.1 (1980), pp. 73–88. DOI: 10.1016/0167-6105(80)90023-9.

[82] A. Michalski. “Simulation leichter Flächentragwerke in einer numerisch generierten atmosphärischen Grenzschicht”. Doctoral dissertation. Chair of Structural Analysis, Technical University of Munich, 2010. ISBN: 978-3-8322-9317-8. URL: mediatum.ub.tum.de/?id=813117.

[83] H. Minami. “Added Mass of a Membrane Vibrating at Finite Amplitude”. In: *Journal of Fluids and Structures* 12.7 (1998), pp. 919–932. DOI: 10.1006/jfls.1998.0175.

[84] A. Mini. “Implementation and evaluation of mesh-updating strategies for computational fluid-structure interaction”. Master’s thesis. Chair of Structural Analysis, Technical University of Munich, 2014.

[85] National Instruments. *Instrument Fundamentals: Complete Guide – Understanding FFTs and Windowing*. 2023. URL: ni.com/instrument-fundamentals.

[86] E. Naudascher and D. Rockwell. *Flow-Induced Vibrations: An Engineering Guide*. Dover Publications, 1994. ISBN: 978-0-486-44282-2.

[87] F. Nieto, J. S. Owen, D. M. Hargreaves, and S. Hernández. “Bridge deck flutter derivatives: Efficient numerical evaluation exploiting their interdependence”. In: *Journal of Wind Engineering and Industrial Aerodynamics* 136 (2015), pp. 138–150. DOI: 10.1016/j.jweia.2014.11.006.

[88] M. Novak. “Galloping Oscillations of Prismatic Structures”. In: *Journal of the Engineering Mechanics Division* 98 (1 1972), pp. 27–46. DOI: 10.1061/JMCEA3.0001575.

[89] D. W. Olson, S. F. Wolf, and J. M. Hook. “The Tacoma Narrows Bridge collapse”. In: *Physics Today* 68.11 (2015), pp. 64–65. DOI: 10.1063/PT.3.2991.

[90] E. Oñate. “A stabilized finite element method for incompressible viscous flows using a finite increment calculus formulation”. In: *Computer Methods in Applied Mechanics and Engineering* 182.3 (2000), pp. 355–370. DOI: 10.1016/S0045-7825(99)00198-X.

[91] M. Péntek, A. Riedl, K.-U. Bletzinger, and F. Weber. “Investigating the Vibration Mitigation Efficiency of Tuned Sloshing Dampers Using a Two-Fluid CFD Approach”. In: *Applied Sciences* 229.14 (2022), p. 111569. DOI: 10.3390/app12147033.

[92] M. Péntek, A. Winterstein, M. Vogl, P. Kupás, K.-U. Bletzinger, and R. Wüchner. “A multiply-partitioned methodology for fully-coupled computational wind-structure interaction simulation considering the inclusion of arbitrary added mass dampers”. In: *Journal of Wind Engineering and Industrial Aerodynamics* 177 (2018), pp. 117–135. DOI: 10.1016/j.jweia.2018.03.010.

[93] C. Petersen and H. Werkle. *Dynamik der Baukonstruktionen*. Springer Vie-weg Wiesbaden, 2017. ISBN: 978-3-8348-1459-3. DOI: 10.1007/978-3-8348-2109-6.

[94] S. Piperno, C. Farhat, and B. Larrouturou. “Partitioned procedures for the transient solution of coupled aeroelastic problems Part I: Model problem, theory and two-dimensional application”. In: *Computer Methods in Applied Mechanics and Engineering* 124.1 (1995), pp. 79–112. DOI: 10.1016/0045-7825(95)92707-9.

[95] N. Ploskas and N. Samaras. *GPU Programming in MATLAB*. Morgan Kaufmann, 2016. ISBN: 978-0-12-805132-0. DOI: 10.1016/C2015-0-00281-7.

[96] F. Rizzo, P. D’Asdia, F. Ricciardelli, and G. Bartoli. “Characterisation of pressure coefficients on hyperbolic paraboloid roofs”. In: *Journal of Wind Engineering and Industrial Aerodynamics* 102 (2012), pp. 61–71. DOI: 10.1016/j.jweia.2012.01.003.

[97] F. Rizzo, G. A. Kopp, and G. F. Giaccu. “Investigation of wind-induced dynamics of a cable net roof with aeroelastic wind tunnel tests”. In: *Engineering Structures* 229 (2021), p. 111569. DOI: 10.1016/j.engstruct.2020.111569.

[98] H. Ruscheweyh. “Practical experiences with wind-induced vibrations”. In: *Journal of Wind Engineering and Industrial Aerodynamics* 33.1 (1990), pp. 211–218. DOI: 10.1016/0167-6105(90)90036-C.

[99] H. Ruscheweyh. “Vortex Excited Vibrations”. In: *Wind-Excited Vibrations of Structures. International Centre for Mechanical Sciences, Nr. 335*. Ed. by H. Sockel. Springer-Verlag Wien, 1994, pp. 51–84. ISBN: 978-3-211-82516-7. DOI: 10.1007/978-3-7091-2708-7_2.

[100] L. Sabat and C. K. Kundu. “History of Finite Element Method: A Review”. In: *Recent Developments in Sustainable Infrastructure*. Ed. by B. B. Das, S. Barbhuiya, R. Gupta, and P. Saha. Springer, Singapore, 2021. ISBN: 978-981-15-4576-4. DOI: 10.1007/978-981-15-4577-1_32.

[101] P. P. Sarkar, N. P. Jones, and R. H. Scanlan. “Identification of Aeroelastic Parameters of Flexible Bridges”. In: *Journal of Engineering Mechanics* 120.8 (1994), pp. 1718–1742. DOI: 10.1061/(ASCE)0733-9399(1994)120:8(1718).

[102] P. P. Sarkar, N. P. Jones, and R. H. Scanlan. “System identification for estimation of flutter derivatives”. In: *Journal of Wind Engineering and Industrial Aerodynamics* 42.1 (1992), pp. 1243–1254. DOI: 10.1016/0167-6105(92)90131-S.

[103] A. Šarkić. “Validated numerical simulation of fluid-structure interactions of bridge girders in turbulent wind fields”. Doctoral dissertation. Fakultät für Bau- und Umweltingenieurwissenschaften, Ruhr-Universität Bochum, 2014. URL: hss-opus.ub.ruhr-uni-bochum.de/opus4/frontdoor/index/index/year/2018/docId/4043.

[104] A. Šarkić, R. Fisch, R. Höffer, and K.-U. Bletzinger. “Bridge flutter derivatives based on computed, validated pressure fields”. In: *Journal of Wind Engineering and Industrial Aerodynamics* 104–106 (2012), pp. 141–151. DOI: 10.1016/j.jweia.2012.02.033.

[105] A. Šarkić, R. Höffer, and B. Stanko. “Numerical simulations and experimental validations of force coefficients and flutter derivatives of a bridge deck”. In: *Journal of Wind Engineering and Industrial Aerodynamics* 144 (2015), pp. 172–182. DOI: 10.1016/j.jweia.2015.04.017.

[106] K. B. Sautter. “Modeling and Simulation of Flexible Protective Structures by Coupling Particle and Finite Element Methods”. Doctoral dissertation. Chair of Structural Analysis, Technical University of Munich, 2022. ISBN: 978-3-943683-68-4. URL: mediatum.ub.tum.de/?id=1650279.

[107] R. H. Scanlan. “On flutter and buffeting mechanisms in long-span bridges”. In: *Probabilistic Engineering Mechanics* 3.1 (1988), pp. 22–27. DOI: 10.1016/0266-8920(88)90004-5.

[108] R. H. Scanlan and J. J. Tomko. “Airfoil and Bridge Deck Flutter Derivatives”. In: *Journal of the Engineering Mechanics Division* 97 (6 1971), pp. 1717–1737. DOI: 10.1061/JMCEA3.0001526.

[109] B. Siedziako. “Modelling of the self-excited forces for bridge decks subjected to random motions: an experimental study”. PhD thesis. Norwegian University of Science and Technology, 2018. URL: www.researchgate.net/publication/323345003.

[110] B. Siedziako and O. Øiseth. “Superposition principle in bridge aerodynamics: Modelling of self-excited forces for bridge decks in random vibrations”. In: *Engineering Structures* 179 (2019), pp. 52–65. DOI: 10.1016/j.engstruct.2018.10.072.

[111] B. Siedziako, O. Øiseth, and A. Rønnquist. “An enhanced forced vibration rig for wind tunnel testing of bridge deck section models in arbitrary motion”. In: *Journal of Wind Engineering and Industrial Aerodynamics* 164 (2017), pp. 152–163. DOI: 10.1016/j.jweia.2017.02.011.

[112] E. Simiu and R. H. Scanlan. *Winds Effects on Structures: Fundamentals and Applications to Design*. 3rd ed. Wiley, 1996. ISBN: 978-0-471-12157-2.

[113] E. Simiu and D. Yeo. *Wind Effects on Structures: Modern Structural Design for Wind*. John Wiley & Sons, 2019. ISBN: 978-1-119-37588-3. DOI: 10.1002/9781119375890.

[114] H. Sockel. *Aerodynamik der Bauwerke*. Vieweg+Teubner Verlag Wiesbaden, 1984. ISBN: 978-3-528-08845-3. DOI: 10.1007/978-3-322-89735-0.

[115] G. Solari. *Wind Science and Engineering: Origins, Developments, Fundamentals and Advancements*. Springer Tracts in Civil Engineering. Springer Cham, 2019. ISBN: 978-3-030-18814-6. DOI: 10.1007/978-3-030-18815-3.

[116] U. Starossek. *Brückendynamik: Winderregte Schwingungen von Seilbrücken*. Vieweg+Teubner Verlag Wiesbaden, 1991. ISBN: 978-3-322-83188-0. DOI: 10.1007/978-3-322-83187-3.

[117] U. Starossek, H. Aslan, and L. Thiesemann. “Experimental and numerical identification of flutter derivatives for nine bridge deck sections”. In: *Wind and Structures* 12 (6 2009), pp. 519–540. DOI: 10.12989/was.2009.12.6.519.

[118] E. Stein. “History of the Finite Element Method – Mathematics Meets Mechanics – Part I: Engineering Developments”. In: *The History of Theoretical, Material and Computational Mechanics – Mathematics Meets Mechanics and Engineering*. Ed. by E. Stein. Springer, Berlin, Heidelberg, 2014, pp. 399–442. ISBN: 978-3-642-39904-6. DOI: 10.1007/978-3-642-39905-3_22.

[119] E. N. Strømmen. *Theory of Bridge Aerodynamics*. Springer, Berlin, Heidelberg, 2006. ISBN: 978-3-540-30604-7. DOI: 10.1007/3-540-30604-8.

[120] G. Szabó. “Hídpályák kísérleti és numerikus alapú aerodinamikai stabilitásvizsgálata”. PhD thesis. Tartószerkezetek Mechanikája Tanszék, Budapesti Műszaki és Gazdaságtudományi Egyetem, 2013. URL: hdl.handle.net/10890/5596.

[121] Z. J. Taylor and M. T.L. Browne. “Hybrid pressure integration and buffeting analysis for multi-row wind loading in an array of single-axis trackers”. In: *Journal of Wind Engineering and Industrial Aerodynamics* 197 (2020), p. 104056. DOI: 10.1016/j.jweia.2019.104056.

[122] TensiNet. *Round Robin Exercise 3 (RR3)*. 2015. URL: www.tensinet.com.

[123] T. Theodorsen. *General theory of aerodynamic instability and the mechanism of flutter*. Tech. rep. 496. National Advisory Committee for Aeronautics, Langley Aeronautical Lab, 1949. URL: ntrs.nasa.gov/citations/19930090935.

[124] B. V. Tryggvason. “Aeroelastic Modeling of Pneumatic and Tensioned Fabric Structures”. In: *5th International Conference on Wind Engineering*. Ed. by J. E. Cermak. Pergamon Press, 1979. ISBN: 978-008-02-4745-8.

[125] M. Van Dyke. *An Album of Fluid Motion*. Parabolic Press, Stanford, 1982. ISBN: 978-0915760022.

[126] B. J. Vickery and R. I. Basu. “Across-wind vibrations of structures of circular cross-section. Part I. Development of a mathematical model for two-dimensional conditions”. In: *Journal of Wind Engineering and Industrial Aerodynamics* 12.1 (1983), pp. 49–73. DOI: 10.1016/0167-6105(83)90080-6.

[127] W. A. Wall. “Fluid-Struktur-Interaktion mit stabilisierten Finiten Elementen”. Doctoral dissertation. Institut für Baustatik und Baudynamik der Universität Stuttgart, 1999. DOI: 10.18419/opus-127.

[128] W. A. Wall, D. P. Mok, J. Schmidt, and E. Ramm. “Partitioned Analysis of Transient Nonlinear Fluid Structure Interaction Problems Including Free Surface Effects”. In: *Multifield Problems: State of the Art*. Ed. by A. M. Sändig, W. Schiehlen, and W. L. Wendland. Springer Berlin Heidelberg, 2000, pp. 159–166. ISBN: 978-3-642-08693-9. DOI: 10.1007/978-3-662-04015-7_18.

[129] R. L. Wardlaw and G. F. Moss. “A Standard Tall Building Model for the Comparison of Simulated Natural Wind in Wind Tunnels”. In: *CAARC, CC 662m Tech* (1970).

[130] A. Winterstein. “Modeling and simulation of wind-structure interaction of slender civil engineering structures including vibration mitigation systems”. Doctoral dissertation. Chair of Structural Analysis, Technical University of Munich, 2020. ISBN: 978-3-943683-61-5. URL: mediatum.ub.tum.de/1542819.

[131] A. Winterstein, C. Lerch, R. Wüchner, and K.-U. Bletzinger. “Computational closed-loop control of fluid-structure interaction FSCI for lightweight structures”. In: *Special Issue: Joint 87th Annual Meeting of the International Association of Applied Mathematics and Mechanics (GAMM) and Deutsche Mathematiker-Vereinigung (DMV)*. Ed. by V. Bach and H. Fassbender. Vol. 16. Wiley, 2016, pp. 15–18. DOI: 10.1002/pamm.201610005.

[132] R. Wüchner. “Mechanik und Numerik der Formfindung und Fluid-Struktur-Interaktion von Membrantragwerken”. Doctoral dissertation. Chair of Structural Analysis, Technical University of Munich, 2006. ISBN: 978-3-8322-6391-1. URL: mediatum.ub.tum.de/doc/601102.

[133] F. Y. Xu, X. Y. Ying, and Z. Zhang. “Three-Degree-of-Freedom Coupled Numerical Technique for Extracting 18 Aerodynamic Derivatives of Bridge Decks”. In: *Journal of Structural Engineering* 140 (11 2014). DOI: 10.1061/(ASCE)ST.1943-541X.0001009.

[134] B. W. Yan and Q. S. Li. “Inflow turbulence generation methods with large eddy simulation for wind effects on tall buildings”. In: *Computers & Fluids* 116 (2015), pp. 158–175. DOI: 10.1016/j.compfluid.2015.04.020.

[135] O. C. Zienkiewicz and R. L. Taylor. *The Finite Element Method for Solid and Structural Mechanics*. Elsevier Butterworth-Heinemann, 2006. ISBN: 978-0-7506-6321-2.

Bisherige Titel der Schriftenreihe

Band	Titel
1	Frank Koschnick, *Geometrische Lockingeffekte bei Finiten Elementen und ein allgemeines Konzept zu ihrer Vermeidung*, 2004.
2	Natalia Camprubi, *Design and Analysis in Shape Optimization of Shells*, 2004.
3	Bernhard Thomee, *Physikalisch nichtlineare Berechnung von Stahlfaserbetonkonstruktionen*, 2005.
4	Fernaß Daoud, *Formoptimierung von Freiformschalen – Mathematische Algorithmen und Filtertechniken*, 2005.
5	Manfred Bischoff, *Models and Finite Elements for Thin-walled Structures*, 2005.
6	Alexander Hörmann, *Ermittlung optimierter Stabwerkmodelle auf Basis des Kraftflusses als Anwendung plattformunabhängiger Prozesskopplung*, 2006.
7	Roland Wüchner, *Mechanik und Numerik der Formfindung und Fluid-Struktur-Interaktion von Membrantragwerken*, 2006.
8	Florian Jurecka, *Robust Design Optimization Based on Metamodeling Techniques*, 2007.
9	Johannes Linhard, *Numerisch-mechanische Betrachtung des Entwurfsprozesses von Membrantragwerken*, 2009.
10	Alexander Kupzok, *Modeling the Interaction of Wind and Membrane Structures by Numerical Simulation*, 2009.
11	Bin Yang, *Modified Particle Swarm Optimizers and their Application to Robust Design and Structural Optimization*, 2009.
12	Michael Fleischer, *Absicherung der virtuellen Prozesskette für Folgeoperationen in der Umformtechnik*, 2009.
13	Amphon Jrusjrungkiat, *Nonlinear Analysis of Pneumatic Membranes – From Subgrid to Interface*, 2009.
14	Alexander Michalski, *Simulation leichter Flächentragwerke in einer numerisch generierten atmosphärischen Grenzschicht*, 2010.

Band	**Titel**
15	Matthias Firl, *Optimal Shape Design of Shell Structures*, 2010.
16	Thomas Gallinger, *Effiziente Algorithmen zur partitionierten Lösung stark gekoppelter Probleme der Fluid-Struktur-Wechselwirkung*, 2011.
17	Josef Kiendl, *Isogeometric Analysis and Shape Optimal Design of Shell Structures*, 2011.
18	Joseph Jordan, *Effiziente Simulation großer Mauerwerksstrukturen mit diskreten Rissmodellen*, 2011.
19	Albrecht von Boetticher, *Flexible Hangmurenbarrieren: Eine numerische Modellierung des Tragwerks, der Hangmure und der Fluid-Struktur-Interaktion*, 2012.
20	Robert Schmidt, *Trimming, Mapping, and Optimization in Isogeometric Analysis of Shell Structures*, 2013.
21	Michael Fischer, *Finite Element Based Simulation, Design and Control of Piezoelectric and Lightweight Smart Structures*, 2013.
22	Falko Hartmut Dieringer, *Numerical Methods for the Design and Analysis for Tensile Structures*, 2014.
23	Rupert Fisch, *Code Verification of Partitioned FSI Environments for Lightweight Structures*, 2014.
24	Stefan Sicklinger, *Stabilized Co-Simulation of Coupled Problems Including Fields and Signals*, 2014.
25	Madjid Hojjat, *Node-based parametrization for shape optimal design*, 2015.
26	Ute Israel, *Optimierung in der Fluid-Struktur-Interaktion – Sensitivitätsanalyse für die Formoptimierung auf Grundlage des partitionierten Verfahrens*, 2015.
27	Electra Stavropoulou, *Sensitivity analysis and regularization for shape optimization of coupled problems*, 2015.
28	Daniel Markus, *Numerical and Experimental Modeling for Shape Optimization of Offshore Structures*, 2015.
29	Pablo Suárez, *Design Process for the Shape Optimization of Pressurized Bulkheads as Components of Aircraft Structures*, 2015.

Band	**Titel**
30	Armin Widhammer, *Variation of Reference Strategy – Generation of Optimized Cutting Patterns for Textile Fabrics*, 2015.
31	Helmut Masching, *Parameter Free Optimization of Shape Adaptive Shell Structures*, 2016.
32	Hao Zhang, *A General Approach for Solving Inverse Problems in Geophysical Systems by Applying Finite Element Method and Metamodel Techniques*, 2016.
33	Tianyang Wang, *Development of Co-Simulation Environment and Mapping Algorithms*, 2016.
34	Michael Breitenberger, *CAD-integrated Design and Analysis of Shell Structures*, 2016.
35	Önay Can, *Functional Adaptation with Hyperkinematics using Natural Element Method: Application for Articular Cartilage*, 2016.
36	Benedikt Philipp, *Methodological Treatment of Non-linear Structural Behavior in the Design, Analysis and Verification of Lightweight Structures*, 2017.
37	Michael Andre, *Aeroelastic Modeling and Simulation for the Assessment of Wind Effects on a Parabolic Trough Solar Collector*, 2018.
38	Andreas Apostolatos, *Isogeometric Analysis of Thin-Walled Structures on Multipatch Surfaces in Fluid-Structure Interaction*, 2018.
39	Altuğ Emiroğlu, *Multiphysics Simulation and CAD-Integrated Shape Optimization in Fluid-Structure Interaction*, 2019.
40	Mehran Saeedi, *Multi-Fidelity Aeroelastic Analysis of Flexible Membrane Wind Turbine Blades*, 2017.
41	Reza Najian Asl, *Shape optimization and sensitivity analysis of fluids, structures, and their interaction using Vertex Morphing Parametrization*, 2019.
42	Ahmed Abodonya, *Verification Methodology for Computational Wind Engineering Prediction of Wind Loads on Structures*, 2020.
43	Anna Maria Bauer, *CAD-integrated Isogeometric Analysis and Design of Lightweight Structures*, 2020.

Band	**Titel**
44	Andreas Winterstein, *Modeling and Simulation of Wind-Structure Interaction of Slender Civil Engineering Structures Including Vibration Mitigation Systems*, 2020.
45	Franz-Josef Ertl, *Vertex Morphing for Constrained Shape Optimization of Three-dimensional Solid Structures*, 2020.
46	Daniel Baumgärtner, *On the Grid-based Shape Optimization of Structures with Internal Flow and the Feedback of Shape Changes into a CAD Model*, 2020.
47	Mohamed Khalil, *Combining Physics-Based Models and Machine Learning for an Enhanced Structural Health Monitoring*, 2021.
48	Long Chen, *Gradient Descent Akin Method*, 2021.
49	Aditya Ghantasala, *Coupling Procedures for Fluid-Fluid and Fluid-Structure Interaction Problems Based on Domain Decomposition Methods*, 2021.
50	Ann-Kathrin Goldbach, *The CAD-Integrated Design Cycle for Structural Membranes*, 2021.
51	Iñigo Pablo López Canalejo, *A Finite-Element Transonic Potential Flow Solver with an Embedded Wake Approach for Aircraft Conceptual Design*, 2022.
52	Mayu Sakuma, *An Application of Multi-Fidelity Uncertainty Quantification for Computational Wind Engineering*, 2022.
53	Suneth Warnakulasuriya, *Development of Methods for Finite Element-Based Sensitivity Analysis and Goal-Directed Mesh Refinement Using the Adjoint Approach for Steady and Transient Flows*, 2022.
54	Klaus Bernd Sautter, *Modeling and Simulation of Flexible Protective Structures by Coupling Particle and Finite Element Methods*, 2022.
55	Efthymios Papoutsis, *On the incorporation of industrial constraints in node-based optimization for car body design*, 2023.
56	Thomas Josef Oberbichler, *A modular and efficient implementation of isogeometric analysis for the interactive CAD-integrated design of lightweight structures*, 2023.
57	Tobias Christoph Teschemacher, *CAD-integrated constitutive modelling, analysis, and design of masonry structures*, 2023.

Band	**Titel**
58	Shahrokh Shayegan, *Enhanced Algorithms for Fluid-Structure Interaction Simulations – Accurate Temporal Discretization and Robust Convergence Acceleration*, 2023.
59	Ihar Antonau, *Enhanced computational design methods for large industrial node-based shape optimization problems*, 2023.
60	Rishith Ellath Meethal, *Hybrid modelling and simulation approaches for the solution of forward and inverse problems in engineering by combining finite element methods and neural networks*, 2023.